

Multi-Domain Modeling of Intersubband Quantum Cascade Devices

Johannes Popp

Vollständiger Abdruck der von der TUM School of Computation, Information and Technology der Technischen Universität München zur Erlangung des akademischen Grades eines

Doktors der Ingenieurwissenschaften (Dr.-Ing.)

genehmigten Dissertation.

Vorsitz:

Prof. Dr.-Ing. habil. Markus Becherer

Prüfende der Dissertation:

- 1. Prof. Dr.-Ing. Christian Jirauschek
- 2. Prof. Dr. rer. nat. habil. Gabriele Schrag

Die Dissertation wurde am 07.11.2024 bei der Technischen Universität München eingereicht und durch die TUM School of Computation, Information and Technology am 16.04.2025 angenommen.

To my beloved wife I	Franziska, and to	my parents Ann	a and Hans.

Contents

AI	ostrac	JI	XIII
Κι	ırzfas	ssung	χV
Li	st of	Contributed Publications	xvi
1	Intro	oduction	1
	1.1	Quantum Cascade Laser	2
	1.2	Quantum Cascade Detector	4
	1.3	Nonlinear Optical Effects	6
	1.4	Nonclassical Laser Theory	9
	1.5	Overview of this Work	10
2	Fun	ctional Engineering of Intersubband Quantum Cascade Devices	13
	2.1	Intersubband QC Device Description	13
	2.2	Schrödinger-Poisson Solver	20
	2.3	Bayesian Optimization and Gaussian Processes	28
	2.4	Summary	29
3	Carı	rier Transport Simulations of Intersubband Quantum Cascade Devices	31
	3.1	Scattering Mechanisms and Carrier Transport Simulations	32
	3.2	Results of Stationary Carrier Transport Simulations	37
	3.3	Dynamical Simulation Setup	40
	3.4	Summary	41
4	Mod	leling of Fluctuations in Dynamical Optoelectronic Devices	43
	4.1	The Quantum Langevin Equations	43
	4.2	The C-Number Langevin Equations	46
	4.3	Generalized Maxwell-Density Matrix Langevin Equations in 1D	50
	4.4	Summary	54
5	An (Open-Source Solver for the Maxwell-Density Matrix Langevin Equations	55
	5.1	Implementations and Extensions of mbsolve	56
	5.2	Numerical Treatment of the Maxwell-Density Matrix Langevin Equations	59
		5.2.1 ADE-FDTD Method for Maxwell's Equations	59
	<i>5</i> 2	5.2.2 Numerical Treatment of the Master Equation	62
	5.3	Parallel Implementation of the ADE-FDTD Method	65
	5.4	Summary	66
6	Veri tion	fication of the Simulation Framework for the Maxwell-Density Matrix Langevin Equass	69
	6.1	Time-Domain Modeling of Terahertz Quantum Cascade Lasers	69
		6.1.1 Reflection Error of PML Absorbing Boundary Conditions	72
		6.1.2 Group Velocity Dispersion in Terahertz Frequency Combs	74
	6.2	Superfluorescence and Amplified Spontaneous Emission	77
	6.3	Summary	78

7	Sim	ulation and Optimization of Photovoltaic Quantum Cascade Detectors	81				
	7.1	Ensemble Monte Carlo Results of Quantum Cascade Detectors	82				
		7.1.1 Mid-Infrared Quantum Cascade Detectors	82				
		7.1.2 Terahertz Quantum Cascade Detector	87				
	7.2	Bayesian Optimization of Quantum Cascade Detectors	90				
		7.2.1 Parameter Set 1	93				
		7.2.2 Parameter Set 2	94				
		7.2.3 Discussion	94				
	7.3	Summary	97				
8	Mult	ti-Domain Modeling of Free-Running Frequency Comb Formation in Quantum Cas-					
	cad	e Lasers	99				
	8.1	Self-Starting Harmonic Mode-Locking in Terahertz Quantum Cascade Lasers	100				
		8.1.1 Influence of Wavefunction Basis Sets on the Coherent Operation in THz HFC QCLs .	100				
		8.1.2 Analysis of Harmonic Mode-Locking Regimes in THz QCL Waveguides	103				
		8.1.3 Noise Characteristics in THz QCL Harmonic Frequency Comb Emission	106				
		8.1.4 Discussion	108				
	8.2	2 Intracavity Terahertz Comb Difference Frequency Generation by Mid-Infrared Quantum Cas-					
		cade Lasers	109				
		8.2.1 Stationary Carrier Transport Simulations	111				
		8.2.2 DFG-QCL Frequency Comb Simulations	115				
	8.3	Summary	121				
9	Con	clusion and Outlook	123				
Α	Арр	pendix	127				
	A. 1	Mbsolve Simulation Setups	127				
		A.1.1 Four Quantum Well Diagonal Transition Design	127				
		A.1.2 Single-Phonon Resonance Depopulation Structure	128				
		A.1.3 Dual-Upper State Active Region	131				
Pu	blica	ations List	135				
Bil	bliog	raphy	139				
Lis	st of	Symbols and Acronyms	163				
Αc	knov	vledaments	173				

List of Figures

1.1 1.2	Coherent radiation in the EM spectrum ranging from microwave to ultraviolet	3
1.3	(a) Operation principle of a QCD and schematic representation of the conduction band structure. (b) Calculated conduction band profile and probability densities of a mid-IR QCD structure N1022 with a detection wavelength of 4.7 µm.	5
1.4	Schematic of a double metal QCL waveguide with THz OFC emission through the laser active region facet	7
1.5	(a) Schematic of the DFG process between the quantized electron states in the conduction band profile of a QCL. (b) Schematic of a distributed feedback/Fabry-Perot configuration for nonlinear THz DFG-QCL frequency comb generation.	8
1.6	Schematic illustration of the coupling of a SCL quantum system and field system and the interaction with their associated reservoirs.	10
2.1	Overview of the <i>monacoQC</i> framework with the three highlighted modules optimizer, setup and solver.	14
2.2	solver	15
2.3	(a) Bandstructure of the direct bandgap semiconductor material $In_{0.53}Ga_{0.47}As$. Band edge energy calculations of the conduction band E_c , heavy-hole (HH) $E_v^{\rm HH}$, light-hole (LH) $E_v^{\rm LH}$ and split-off (SO) valence band $E_v^{\rm SO}$ of $In_xAl_{1-x}As$ grown on a (001) InP substrate under biaxial	
2.4	strain ($k = 0$)	16
2.5	of lattice constant	17
2.6	with (001) orientation. (a) Contour plot of the CBO. (b) Effective mass m^* Schematic illustration of full eigenstate wavefunctions $\Psi_i = \phi_{i,k} u_{c_i,0}$ and envelope wavefunctions $\phi_{i,k}$ in the conduction band of a quantum well consisting of barrier material B and well	19
2.7	material W	21
2.8	Comparison of conduction band profile and probability densities for intersubband QC devices with and without space charge effects. (a) A THz QCL; EMC level occupations used for space charge calculations. (b) A THz QCD; thermally occupied subbands considered for space charge	23
2.9	effects	26 29
3.1	Overview of the <i>monacoQC</i> framework with the three highlighted modules mbsolve, ext. solver and results	32

3.2	(a) The scattering mechanisms in intersubband QC devices can be categorized into three classes: (1) elastic scattering, (2) inelastic scattering and electron-electron scattering (3). (b) Illustration of the carrier transport simulation model based on the density matrix ensemble Monte Carlo method.	34
3.3	(a) Schematic conduction band profile of a QCD. (b) Noise equivalent resistance network of a QCD	36
4.1	Schematic conduction band profile and probability densities of a two-well THz QCL structure, where the upper laser level 3 is populated via resonant tunneling from injector level 1'	44
5.1	Overview of the <i>mbsolve</i> project	55
5.25.3	Schematic of a SCL gain medium setup truncated with two PML boundaries at the facets The standard Yee grid of the ADE-FDTD method combined with the discretization of the density matrix with respect to time and space	60
6.1	Calculated conduction band profile and probability densities of the investigated THz QCL structure at a bias field strength of $11\mathrm{kV}\mathrm{cm}^{-1}$	70
6.2	Simulated spectral gain profile together with the normalized group velocity $v_{\rm g} n_{\rm eff}/c$	72
6.3	Illustration of the two different simulation setups under numerical investigation. Setup 1 describes a THz gain medium with length $L_1 = 5$ mm truncated with a PML boundary containing 200 gridpoints terminated by a PMC layer, setup 2 is based on the same material system with	
	twice the length and two PMC layers at the facets	73
6.4	Reflection error for two PML configurations. (a) Time-domain analysis. (b) Frequency-domain analysis	73
6.5	(a) Real and imaginary part of the permittivity for the Lorentz susceptibility model of the bulk material GaAs. The recorded Gaussian pulse at the second interface of the QCL waveguide is shown in (b) without the explicit dispersion model, and in (c) applying the model	75
6.6	Simulation results of the THz frequency comb and the RF beatnote. Without dispersion: two clear and distinct lobes of one OFC (a) and a sharp beatnote (b). With GVD: broadened comb lobes with reduced intensity (c) and a more distorted beatnote (d)	76
6.7	Electric field envelope at the interface of the laser cavity for the last three simulated round trips. (a) Without bulk and waveguide dispersion. (b) With chromatic dispersion	77
6.8	Simulation results for a superfluorescence test setup in an initially inverted two-level system using the Maxwell-density matrix Langevin equations. (a) Superfluorescence. (b) Amplified spontaneous emission.	78
7.1	Calculated conduction band profile and probability densities of the investigated mid-infrared QCD structure N1021 detecting at 7.6 µm	83
7.2	Simulated responsivity R_p of the QCD structure N1021 as a function of wavenumber in the temperature range	83
7.3	Comparison of simulated and experimental results for the detector structure N1021. (a) Extraction efficiency p_e and peak absorption $\eta_{abs,p}$ as a function of temperature T . (b) Detector resistance-area product A_dR_d as a function of the inverse temperature T^{-1}	84
7.4	Comparison of simulated and experimental results for the predefined figures of merit of the detector structure N1022. (a) Peak responsivity R_p as a function of temperature T . (b) Detector	0.5
7.5	resistance-area product A_dR_d as a function of the inverse temperature T^{-1}	85
7.6	QCD structure N1037 detecting at $4 \mu m$	86
	in the temperature range 100 K to 300 K . (b) Simulated and experimentally measured specific detectivity as a function of temperature T	86

7.7	Calculated conduction band profile and probability densities of the investigated terahertz QCD structure detecting at 84 µm for a lattice temperature of 10 K	87
7.8	Responsivity spectrum R_p as a function of wavenumber for the 3.5 THz QCD structure at a temperature of 10 K, as obtained from the simulation and extracted from experimental photocurrent measurements. Furthermore, a comparison between EMC and NEGF simulation results is	00
7.9	shown for 50 K	88
7.10	obtained from EMC and NEGF including electron-electron scattering simulations for 50 K, 100 K and 150 K.	89
	Detector resistance-area product $A_d R_d$ as a function of the inverse temperature T^{-1} , as obtained from EMC and NEGF simulations and extracted from experimental dark current measurements.	89
	Calculated conduction band profile and probability densities of (a) the investigated mid-IR QCD structure N1022 and the two optimized structures (b) r1_1 and (c) r2_1	91
7.12	Dependence of specific detectivity D^* (a), (b), peak responsivity R_p (c), (d) and resistance-area product A_dR_d (e), (f) on pairs of parameters, starting from the nominal structure N1022 and using the BO results of parameter set 1	92
7.13	Dependence of specific detectivity D^* (a), (b), peak responsivity R_p (c), (d) and resistance-area product A_dR_d (e), (f) on pairs of parameters, starting from the nominal structure N1022 and using the BO results of parameter set 2	95
7.14	(a) Simulated responsivity R_p of the nominal QCD structure N1022 and the optimized structures as a function of wavenumber at 300 K. (b) Sensitivity on the specific detectivity D^* over distance	93
	from the optimum of parameter set 1 and 2	96
8.1	Monte Carlo simulation results of the THz QCL gain medium using extended and localized states. Simulated unsaturated peak gain values (a) and center frequencies (b) are shown as a function of the applied bias V .	101
8.2	Spectrum of the Maxwell-DM simulation setup at a bias of $V = 50 \text{mV/period}$. Inset: Zoom on the radiofrequency beatnote with a numerical frequency resolution of 1 MHz	102
8.3	Comparison of three coherent regimes in a 4 mm long THz QCL device with a metal-metal waveguide at 80 K. Results of a fundamental frequency comb (48 mV/period), harmonic combs of $4 \times f_{rt}$ (50 mV/period) and with a mode spacing of $2 \times f_{rt}$ (54 mV/period) are presented. (a) Intensity spectra of the optical radiation. (b) RF spectra with beatnotes. (c) Time-resolved	104
8.4	electric field amplitudes and calculated instantaneous frequency	104105
8.5	Time evolution of the spectral intensity I for self-starting harmonic mode-locking in three THz HFC QCL waveguide configurations at an applied bias of 50 mV/period and a temperature of	100
8.6	80 K	106
0.0	of 5 FSR in a 4 mm long THz QCL device with a metal-metal waveguide at 80 K and for $V = 50 \text{mV/period}$. (a) Intensity spectra of the optical radiation at the facet. (b) Simulated	
8.7	instantaneous intensity at the facet and calculated instantaneous frequency	107
0 0	HFC emission.	108
8.8	Investigated conduction band profiles and probability densities of the two modeled THz DFG-QCL structures. (a) Single-phonon resonance depopulation scheme based on a strain-balanced In _{0.37} Al _{0.63} As/In _{0.65} Ga _{0.35} As/In _{0.53} Ga _{0.47} As material system at a lattice temperature of 293 K. (b) Bandstructure of the dual-upper state active region based on a strain-compensated	
	$In_{0.6}Ga_{0.4}As/In_{0.44}Al_{0.56}As$ material system at a lattice temperature of 78 K	110

Simulation results of the SPR-depopulation design. (a) Normalized gain vs. wavenumber for	
simulated tight-binding (tb) and extended (ext) states, together with the measured EL curve.	
(b) Simulated level broadening γ_i and relative level occupation ρ_{ii} of the extended states and	
tight-binding states for one QCL energy period as a function of the subband energy	112
Simulation results of the DAU design. (a) Normalized gain as a function of wavenumber	
simulated at an operating temperature of 78 K and 300 K together with the measured EL curve.	
(b) Simulated level broadening γ_i and relative level occupation ρ_{ii} for one QCL energy period	
as a function of the subband energy.	114
Simulation setups for the Maxwell-density matrix simulation of the two considered THz DFG-	
QCL frequency comb setups. (a) FP reference waveguide model. (b) Waveguide model of the	
SPR-depopulation QCL setup including a single-period DFB grating. (c) Waveguide model of	
the DAU QCL design including a single-period DFB grating	115
Simulated mid-IR (a) and THz (b) spectra of the DFG-QCL at a temperature of 293 K and an	
applied bias of $45 \mathrm{kV} \mathrm{cm}^{-1}$	116
Simulation results of the QCL device in a FP waveguide and at a temperature of 293 K. (a)	
Simulated mid-IR intensity spectrum at the facet. (b) Simulated instantaneous intensity at the	
facet and calculated instantaneous frequency.	117
Simulation results of the DFG-QCL device at a temperature of 293 K. The simulation parameters	
<u>-</u>	118
	119
· ·	
	120
¥	
• • • • • • • • • • • • • • • • • • • •	
simulated electric field for the mid-IR FP components (a) and THz components (b)	121
Schematic illustration of the multi-domain simulation approach for intersubband QC devices	124
	simulated tight-binding (tb) and extended (ext) states, together with the measured EL curve. (b) Simulated level broadening γ_i and relative level occupation ρ_{ii} of the extended states and tight-binding states for one QCL energy period as a function of the subband energy Simulation results of the DAU design. (a) Normalized gain as a function of wavenumber simulated at an operating temperature of 78 K and 300 K together with the measured EL curve. (b) Simulated level broadening γ_i and relative level occupation ρ_{ii} for one QCL energy period as a function of the subband energy

List of Tables

4.1	Division of the diffusion matrix into submatrices $D_{\nu}(A_{\nu},t)$ and the corresponding c-number subvectors A_{ν} and noise submatrices $B_{\nu}(A_{\nu},t)$. In order to preserve the physical properties of the quantum system description, we have to interpret noise matrices $B_{\nu}(A_{\nu},t)$ differently for occupation and coherence terms. The differing matrix expressions for the coherence terms are highlighted here in red	51
7.1	Layer sequence with barrier layers in boldface, peak wavelength λ_p , extraction efficiency p_e , peak responsivity R_p , resistance-area product A_dR_d and specific detectivity D^* of the nominal structure N1022 and the optimized structures	93
8.1	Near-resonance DFG triplets of states and resulting second-order nonlinear susceptibility $\chi^{(2)}$ for the SPR-depopulation QCL active gain medium. All parameters are considered for extended states, except the triplet of state (1)', where the tight-binding solutions are presented. Listed are the resonance energy $\hbar\omega_{ij}$, pure dephasing energy $\gamma_{ij,p}$ (interface roughness contribution) in meV and transition dipole moments z_{ij} in nm for the mid-IR pump frequencies (ω_1, ω_2) and the THz mode (ω_{THz})	112
8.2	Near-resonance DFG triplets of states and resulting second-order nonlinear susceptibility $\chi^{(2)}$ for the DAU QCL active gain medium. Resonance energy $\hbar\omega_{ij}$, pure dephasing energy $\gamma_{ij,p}$	
	(interface roughness contribution) in meV and transition dipole moments z_{ij} in nm for the mid-IR pump frequencies (ω_1, ω_2) and the THz mode (ω_{THz}).	114

Abstract

Quantum cascade lasers (QCLs) are special types of semiconductor lasers emitting optical power with a broadband spectrum in the mid-infrared (mid-IR) or terahertz (THz) region and are suitable for the generation of optical frequency combs (OFCs), laser spectra consisting of perfectly equidistant and locked lines. Both in mid-IR and THz the generation of optical frequency combs with QCL sources was already demonstrated in recent years. The property of extremely accurate frequency resolution demonstrates the enormous potential in the area of metrology and spectroscopy and makes QCL frequency combs highly interesting for integration into innovative applications of different fields, e.g. astronomy or healthcare diagnostics. In this thesis, a major focus is on improving the current performance of QCLs by comprehensively investigating existing QCL designs and performing systematic design optimization using accurate QCL modeling approaches. Furthermore, the development of ultrafast detectors with superior noise characteristics in the mid-IR and THz regimes is part of this work. Low-noise detectors based on intersubband transitions are required for the detection of nonclassical features in QCL-based frequency combs. There are two types of detectors, quantum well infrared photodetectors (QWIPs) operating in photoconductive mode and quantum cascade detectors (QCDs) operating in photovoltaic mode. QCDs are especially suited for our purpose since they operate at zero bias and therefore have better noise performance since there is no dark current noise.

In this work, we present the open-source framework *monacoQC* in combination with our in-house Ensemble Monte Carlo (EMC) simulation tool for charge carrier transport. A Schrödinger-Poisson library is also integrated and can be used for the engineering of the quantized electron states in the quantum cascade (QC) heterostructure. Within the EMC approach, no empirical or fitting parameters are required as the scattering is evaluated selfconsistently based on Fermi's golden rule. All relevant scattering mechanisms for intersubband QC devices are considered. Since the currents in QCDs are much smaller than in QCLs, the direct EMC simulation of the photocurrent for the irradiated designs cannot provide sufficient accuracy. To accurately model QCDs, we have developed a robust and compact approach based on a rate equation model and a Kirchhoff resistance network. By exploiting thermodynamic equilibrium relations, we can calculate quantities such as spectral responsivity or specific detectivity. The modeling approach is validated using available experimental results for different QCD designs in the mid-infrared and terahertz range and compared with simulations based on the non-equilibrium Green function method. We additionally present a Bayesian optimization algorithm in combination with the scattering-based modeling approach to increase the operating temperature in photovoltaic QCDs, which is important for commercial applications. Here we focus on optimizing a mature mid-infrared QCD design that detects at 4.7 μ m. Our optimization strategy yields an improvement of specific detectivity by a factor of $\sim 2-3$ at room temperature. Furthermore, we investigate the sensitivity of our approach to manufacturing tolerances and demonstrate the robustness of the optimized designs to growth variations.

Endowing intersubband QC devices with outstanding quantum features like nonclassical emission modes, entanglement among the modes of the comb and parametric generation of comb patterns far from the central emission frequency would lead to applications in quantum networks, including quantum computation, quantum communication and quantum metrology. Since the nonclassical features are directly linked to the noise properties, detailed simulations of the coherent light-matter interaction are required for the development of low-noise optoelectronic quantum sources and detectors. Here, we present a full-wave Maxwell-density matrix modeling approach including c-number stochastic noise terms for the simulation of the spatiotemporal dynamics in active photonic devices. Fluctuations arising from interactions of the optical field and quantum system with their reservoirs are treated within the quantum Langevin theory. The noise implementations are integrated into the semiclassical *mbsolve* simulation framework, which is based on the Lindblad equation for electron dynamics, coupled with Maxwell's equations for the optical propagation in the laser waveguide. Within the *mbsolve* framework, numerically extensive simulations of multilevel systems can be conducted. By combining the two

simulation tools, *monacoQC* and *mbsolve*, we provide a multi-domain modeling approach, which is described here in detail and applied for fully time-dependent and self-consistent simulations of intersubband QC devices.

Recently, coherent OFC mode-locking with large intermodal spacing was demonstrated in QCLs. These self-starting harmonic frequency combs (HFCs) show highly phase-stable operation and promise interesting perspectives toward optical or even quantum communication. We investigate the influence of the chosen eigenstate basis on the gain spectrum and present self-consistent simulation results of stable HFC operation in a double metal terahertz OCL. In our simulations, the studied OCL gain medium shows self-starting harmonic mode-locking for different bias and waveguide configurations, resulting in a mode spacing of up to twelve times the cavity round trip frequency. Furthermore, we characterize the spectral time evolution of the coherent HFC formation process and analyze the effects of noise contributions on the comb characteristics. To date, direct THz QCL frequency comb generation is not achievable at room temperature. However, THz comb generation based on intracavity difference frequency generation (DFG) in mid-IR QCLs is a promising alternative. Dynamical simulations of broadband THz DFG OFC emission in mid-IR QCLs are conducted in this work. All necessary input parameters for the description of the quantum system are determined self-consistently using our in-house EMC approach. Notably, such simulations require a full-wave Maxwell-density matrix solver which does not employ the common rotating wave approximation, as a broadband optical field extending from the THz to the mid-IR region is investigated. Our modeling approach and the obtained simulation results for two THz DFG-QCL comb setups are validated against experimental data, showing reasonable agreement.

Kurzfassung

Quantenkaskadenlaser (QKL) sind spezielle Halbleiterlaser, welche optische Leistung mit einem breitbandigen Spektrum im mittleren Infrarot (IR) oder Terahertz (THz) Bereich emittieren und daher für die Erzeugung von optischen Frequenzkämmen geeignet sind. Die sogenannten Frequenzkämme sind hierbei Spektren, die aus perfekt äquidistanten und gekoppelten Linien bestehen. Sowohl im mittleren IR als auch im THz-Bereich konnte in den letzten Jahren bereits die Erzeugung von optischen Frequenzkämmen mit QKL-Quellen demonstriert werden. Hierbei zeigt die Eigenschaft der extrem genauen Frequenzauflösung ein enormes Potenzial für die Bereiche der Metrologie und Spektroskopie auf und macht QKL-Frequenzkämme hochinteressant für die Integration in innovative Anwendungen verschiedener Bereiche, z. B. in der Astronomie oder der Gesundheitsdiagnostik. Ein Hauptaugenmerk in dieser Arbeit liegt auf der Verbesserung der aktuellen Leistung von QKLn. Wir konzentrieren uns hierbei auf eine umfassende Untersuchung bestehender QKL-Designs und eine systematische Optimierung mithilfe genauer QKL-Modellierungsansätze. Darüber hinaus ist die Entwicklung ultraschneller Detektoren mit ausgezeichneten Rauscheigenschaften im mittleren IR- und THz-Bereich ein entscheidender Punkt in dieser Arbeit. Für die Erkennung von nichtklassischen Merkmalen in QKL-basierten Frequenzkämmen sind rauscharme Detektoren, die auf Intersubband-Übergängen basieren, erforderlich. Wir können diese Detektoren in zwei Arten aufteilen: Quantenquellen-Infrarot-Photodetektoren, die im photoleitenden Modus arbeiten, und Quantenkaskadendetektoren (QKDen), die im photovoltaischen Modus arbeiten. QKDen sind für unseren Zweck besonders geeignet, da sie bei 0V Spannung betrieben werden. Es ergibt sich hierbei kein Dunkelstromrauschen, was ein besseres Rauschverhalten zur Folge hat.

In dieser Arbeit stellen wir das Open-Source-Tool monacoQC in Kombination mit unserem hauseigenen Ensemble Monte Carlo (EMC) Simulationansatz, welcher für die Modellierung des Ladungsträgertransports verwendet wird, vor. Weiterhin ist eine Schrödinger-Poisson-Bibliothek integriert, welche für das Engineering der quantisierten Elektronenzustände in den Quantenkaskaden (QKn) Heterostrukturen verwendet werden kann. Im Rahmen des EMC-Ansatzes sind keine empirischen Parameter erforderlich, da die Streuraten selbstkonsistent auf der Grundlage der goldenen Regel von Fermi berechnet werden. Alle relevanten Streuungsmechanismen für Intersubband-OK-Bauelemente werden hier berücksichtigt. Da die Ströme in OKDen deutlich niedriger sind als in QKLn, liefert die direkte EMC-Simulation des Photostroms in den Detektoren keine ausreichende Genauigkeit. Um QKDen genauer modellieren zu können, haben wir daher einen robusten und kompakten Ansatz entwickelt, der auf einem Ratengleichungsmodell und einem Kirchhoffschen Widerstandsnetzwerk basiert. Unter Ausnutzung thermodynamischer Gleichgewichtsbeziehungen können wir Größen wie die spektrale Empfindlichkeit oder die spezifische Detektivität berechnen. Unser Modellierungsansatz wird hier mithilfe experimenteller Ergebnisse für verschiedene OKD-Designs im mittleren Infrarot- und Terahertzbereich validiert und mit Simulationen basierend auf der Nichtgleichgewichts-Green-Function-Methode verglichen. Darüber hinaus stellen wir einen Bayes'schen Optimierungsalgorithmus in Kombination mit dem streuungsbasierten Modellierungsansatz vor, um die Betriebstemperatur in photovoltaischen QKDen zu erhöhen. Dies ist speziell für kommerzielle Anwendungen wichtig. Wir konzentrieren uns auf die Optimierung eines ausgereiften QKD-Designs, welches im mittleren Infrarotbereich bei einer Wellenlänge von 4.7 µm detektiert. Unsere Optimierungsstrategie führt hierbei zu einer Verbesserung der spezifischen Detektivität um einen Faktor von $\sim 2-3$ bei Raumtemperatur. Darüber hinaus untersuchen wir hier die Empfindlichkeit unseres Ansatzes gegenüber Fertigungstoleranzen und zeigen die Robustheit der optimierten Designs gegenüber Wachstumsvariationen.

Die Ausstattung von Intersubband-QKn-Bauelementen mit herausragenden Quantenmerkmalen wie nichtklassischen Emissionsmoden, Verschränkung zwischen den Moden des Kammes und parametrischer Erzeugung von Kammmustern weit von der zentralen Emissionsfrequenz entfernt können zu Anwendungen in Quantennetzwerken führen. Hier zu nennen sind Anwendungsbereiche wie Quantencomputer, Quantenkommunikation und Quantenmetrologie. Da die nichtklassischen Merkmale direkt mit den Rauscheigenschaften verbunden sind, sind detaillierte Simulationen der kohärenten Licht-Materie-Wechselwirkung für die Entwicklung rauscharmer optoelektronischer Quantenquellen und -detektoren erforderlich. Wir stellen hier einen Vollwellen-Maxwell-Dichtematrix-Modellierungsansatz vor, der komplexzahlige stochastische Rauschterme für die Simulation der räumlich-zeitlichen Dynamik in aktiven photonischen Bauelementen enthält. Fluktuationen, die sich aus den Wechselwirkungen des optischen Feldes und des Quantensystems mit ihren Reservoiren ergeben, werden im Rahmen der Quanten-Langevin-Theorie behandelt. Die Rauschimplementierungen sind in das semiklassische Simulationstool *mbsolve* integriert, welches auf der Lindblad-Gleichung für die Elektronendynamik in Verbindung mit den Maxwell-Gleichungen für die optische Ausbreitung im Laserwellenleiter basiert. Mit Hilfe des *mbsolve*-Tools können numerisch umfangreiche Simulationen durchgeführt werden. Durch die Kombination der beiden Simulationswerkzeuge *monacoQC* und *mbsolve* bieten wir einen Multi-Domain-Modellierungsansatz für vollständig zeitabhängige und selbstkonsistente Simulationen von Intersubband-QKn-Bauelementen an. Dieser wird hier im Detail beschrieben.

Kürzlich wurde kohärente Modenkopplung mit großen intermodalen Abständen in QKLn demonstriert. Diese selbststartenden harmonischen Frequenzkämme (HFKe) zeigen einen sehr phasenstabilen Betrieb und versprechen interessante Ansätze für die optische und sogar Quantenkommunikation. Wir untersuchen den Einfluss der gewählten Eigenzustandsbasis auf das Verstärkungsspektrum und präsentieren selbstkonsistente Simulationsergebnisse des stabilen HFK-Betriebs in einem Doppelmetall-THz-QKL. In unseren Simulationen kann für das untersuchte QKL-Verstärkungsmedium selbststartendes harmonisches Mode-Locking in verschiedenen Spannungs- und Wellenleiterkonfigurationen gezeigt werden. Dies führt zu einem Modenabstand vom bis zum Zwölffachen der Umlauffrequenz des Resonators. Darüber hinaus charakterisieren wir die spektrale Zeitentwicklung des kohärenten HFK-Bildungsprozesses und analysieren die Auswirkungen von Rauschbeiträgen auf die Kammcharakteristik. Bislang ist die direkte Erzeugung eines THz-QKL-Frequenzkamms bei Raumtemperatur nicht möglich. Hierbei ist die Erzeugung von THz-Kämmen auf der Grundlage der Differenzfrequenzerzeugung (DFE) in OKLn, welche im mittleren IR-Bereich emittieren, eine vielversprechende Alternative. In dieser Arbeit werden dynamische Simulationen von breitbandigen DFE-QKL-Frequenzkammspektren präsentiert. Alle notwendigen Eingangsparameter für die Beschreibung des Quantensystems werden selbstkonsistent mit unserem eigenen EMC-Simulationstool bestimmt. Da es sich hierbei um ein breitbandiges optisches Feld, das sich vom THz- bis zum mittleren IR-Bereich erstreckt, handelt, ist für solche Simulationen ein Vollwellen-Maxwell-Dichtematrix-Solver, welcher nicht auf die übliche Rotationswellen-Näherung zurückgreift, erforderlich. Unser Modellierungsansatz und die erzielten Simulationsergebnisse für zwei THz-DFE-QKL-Kammaufbauten werden anhand experimenteller Daten validiert und zeigen gute Übereinstimmung.

List of Contributed Publications

Core Publications

This thesis is based on the following core publications:

- J. Popp, J. Stowasser, M. A. Schreiber, L. Seitner, F. Hitzelhammer, M. Haider, G. Slavcheva, and C. Jirauschek, "Modeling of fluctuations in dynamical optoelectronic device simulations within a Maxwell-density matrix Langevin approach", *APL Quantum*, vol. 1, no. 1, p. 016 109, 2024. DOI: 10.1063/5.0183 828.
- J. Popp, M. Haider, M. Franckié, J. Faist, and C. Jirauschek, "Bayesian optimization of quantum cascade detectors", *Opt. Quant. Electron.*, vol. 53, no. 5, p. 287, 2021. DOI: 10.1007/s11082-021-02885-0.
- J. Popp, L. Seitner, M. A. Schreiber, M. Haider, L. Consolino, A. Sorgi, F. Cappelli, P. De Natale, K. Fujita, and C. Jirauschek, "Self-consistent simulations of intracavity terahertz comb difference frequency generation by mid-infrared quantum cascade lasers", *J. Appl. Phys.*, vol. 133, no. 23, p. 233 103, 2023. DOI: 10.1063/5.0151036.
- J. Popp, L. Seitner, F. Naunheimer, G. Janowski, M. Haider, and C. Jirauschek, "Multi-domain modeling of free-running harmonic frequency comb formation in terahertz quantum cascade lasers", *IEEE Photonics J.*, vol. 16, no. 2, p. 0 600 711, 2024. DOI: 10.1109/JPHOT.2024.3370189.

Further Publications

In addition, findings from the following publications are used in this thesis:

- C. Jirauschek, J. Popp, M. Haider, M. Franckié, and J. Faist, "Ensemble Monte Carlo modeling of quantum cascade detectors", *J. Appl. Phys.*, vol. 130, no. 20, p. 203103, 2021. DOI: 10.1063/5.0065540.
- J. Popp, M. Haider, M. Franckié, J. Faist, and C. Jirauschek, "Monte Carlo modeling of a short wavelength strain compensated quantum cascade detector", in 2021 Conference on Lasers and Electro-Optics Europe & European Quantum Electronics Conference (CLEO/Europe-EQEC), 2021, pp. 1–1. DOI: 10.1109 /CLEO/Europe-EQEC52157.2021.9542111.
- J. Popp, L. Seitner, M. Haider, and C. Jirauschek, "Reducing the reflection error of PML absorbing boundary conditions within a generalized Maxwell-Bloch framework", in 2022 3rd URSI Atlantic and Asia Pacific Radio Science Meeting (AT-AP-RASC), 2022, pp. 1–4. DOI: 10.23919/AT-AP-RASC54737 .2022.9814330.
- L. Seitner, J. Popp, M. Riesch, M. Haider, and C. Jirauschek, "Group velocity dispersion in terahertz frequency combs within a generalized Maxwell-Bloch framework", *J. Phys.: Conf. Ser.*, vol. 2090, no. 1, p. 012 082, 2021. DOI: 10.1088/1742-6596/2090/1/012082.

1 Introduction

The electromagnetic spectrum is depicted in Fig. 1.1 and can be divided into different portions which, thanks to semiconductor technology, enable a wide range of applications. Here, the radio frequency (RF) and microwave regions with frequencies up to 300 GHz are covered by electronic devices such as transistors and are used, for example, in wireless communications or radar applications. Furthermore, semiconductor laser diodes generate coherent light in the range from the near-infrared to the ultraviolet spectrum and are used in various applications, e.g., in fiber-optic communications or consumer electronics. The fundamental working principle of such devices is described by the generation of optical photons through electron-hole recombination within the electrically pumped active gain medium. The optical frequency is determined by the bandgap energy of the chosen semiconductor materials. Unfortunately, the room-temperature performance of conventional interband semiconductor lasers is limited within the adjacent mid-infrared (mid-IR) and terahertz (THz) regions. Indeed, there are materials such as lead salts with an appropriate bandgap energy [1], [2] which, however, have critical operational limitations in terms of thermal runaway effects and thermal recycling due to their softened chemical bonds associated with the small band gap [3], [4]. In recent years, quantum cascade lasers (QCLs) [3]–[7] and interband cascade lasers (ICL) [8]–[10] have emerged as the most important representatives of coherent sources to close this gap.

In the following, we will focus more on the QCL, a special type of semiconductor laser governed by unipolar intersubband transitions in quantum well heterostructures. Kazarinov and Suris [11] first introduced the theoretical description of QCLs in 1971, while the experimental realization was accomplished for the first time in 1994 by Faist et al. [5]. QCLs are suitable for the generation of optical frequency combs consisting of perfectly equidistant and locked lines in the electromagnetic spectrum [12], [13]. Both in mid-IR and THz the generation of optical frequency combs (OFCs) with OCL sources was already demonstrated in recent years [14], [15]. The property of extremely accurate frequency resolution demonstrates the enormous potential in the area of metrology and spectroscopy and makes QCL frequency combs highly attractive for integration into innovative applications of different fields, e.g., astronomy or healthcare diagnostics [16]. The presentday performance of QCLs can be improved by extensive investigations of existing designs and by conducting systematic optimization using accurate QCL modeling approaches [17]-[22]. Furthermore, the development of ultrafast detectors with superior noise characteristics in the mid-IR and THz regimes is of great interest. Lownoise detectors based on intersubband transitions are required for the detection of nonlinear and nonclassical features in QCL emission [23], [24]. Here, we will focus on quantum cascade detectors (QCDs) [25], [26], which operate in the photovoltaic mode and exploit scattering-based extraction along the lines of the closely related QCL. Combining both devices by on-chip integration can serve as a cost-efficient portable sensing application [27], [28].

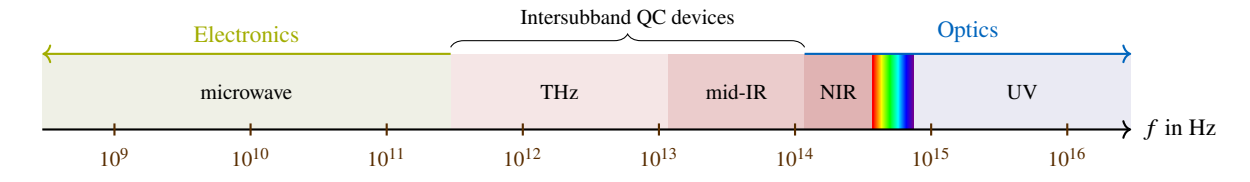


Figure 1.1 Coherent radiation in the EM spectrum ranging from microwave to ultraviolet. Electronic sources cover frequencies below $\sim 0.3\,\text{THz}$ and optical (semiconductor) sources frequencies above $\sim 100\,\text{THz}$. The THz and mid-IR gap between the realms of optics and microwaves can be operated by intersubband QC devices.

Aiming for a full understanding of the physical processes in intersubband quantum cascade (QC) devices and pushing towards higher device performance, a detailed theoretical characterization of the active gain medium consisting of quantum well heterostructures is required. Advanced self-consistent carrier transport models

for QCLs, such as the ensemble Monte Carlo (EMC) method [29], [30], density matrix (DM) [31], [32] or the nonequilibrium Green's function (NEGF) approach [29], [33], [34], are available and offer different levels of physical complexity and numerical efficiency. Electron transport in intersubband QC devices across thick barriers is governed by incoherent tunneling transport. Since semiclassical models, e.g., the EMC method, cannot cover quantum coherence effects, such as resonant tunneling across thick injection barriers, corrections based on the DM formalism have been incorporated. Therefore, incoherent tunneling is treated as an additional "scattering-like" mechanism [35], [36] and gives the EMC method a good balance between computational efficiency and accuracy. In contrast to QCLs, the currents within QCDs are significantly smaller, which makes direct carrier transport simulations using standard QCL modeling techniques unfeasible. Simple models based on scattering rates were introduced in literature [27], [28], [37]–[40]. We have derived an accurate and versatile simulation approach, which is based on a rate equation model and a noise resistance model, to characterize the photodetector signal strength and noise properties [23], [24], [41], [42]. For the calculation of the important figures of merit, e.g., responsivity and detectivity, only the absorption coefficient and intersubband scattering rates are required and can be extracted from carrier transport simulations, e.g., using the density matrix EMC (DM-EMC) modeling approach.

Coherent light-matter interaction plays a significant role in the non-stationary behavior of intersubband QC devices. For the investigation of semiconductor laser dynamics, Maxwell-Bloch (MB) equations offer a compact and efficient modeling approach [29], [43]–[48]. Here, Maxwell's equations for the optical field propagation are coupled with the Bloch equations for two-level quantum systems. A special type of MB equations is given by the effective semiconductor Maxwell-Bloch (ESMB) equations [13], [49]–[53], where certain semiconductor specifications such as asymmetric gain and dispersion profiles are covered by the inclusion of a non-zero linewidth enhancement factor (LEF). Extensions towards multiple quantum states within the generalized DM approach result in a more powerful and sophisticated tool for the quantitative modeling of quantum optoelectronic devices [47], [54]–[59]. Among other active photonic devices, these approaches (MB, ESMB, Maxwell-DM, related (semi-)analysis models) have been applied extensively to QCLs, especially for the dynamical simulation of mode-locking [50], [60]–[67], the investigation of coherent instabilities [45], [68]–[70] and the formation of fundamental and harmonic frequency comb regimes [51], [52], [54]–[56], [59], [66], [67], [71]–[78].

In this chapter, we will start with a small overview of the investigated intersubband QC devices and discuss the basic operating principle of QCLs and QCDs in Section 1.1 and 1.2, respectively. In Section 1.3 we will introduce nonlinear optical effects of different orders exploited in QCLs, e.g., for the coherent THz OFC emission at room temperature by difference-frequency generation (DFG) or harmonic mode-locking triggered by four-wave-mixing (FWM) processes. Exploiting these nonlinear effects opens up potential applications in the area of wireless terahertz communication networks [79], [80] and THz imaging [81], [82]. Then, Section 1.4 addresses a new generation of semiconductor devices endowed with quantum features. Quantum optics experiments based on intersubband QC devices have recently attracted great interest and demonstrate enormous potential for future applications in groundbreaking areas of quantum technologies such as quantum metrology and sensing [83], [84]. Here, we discuss the possibilities for an expansion of the general Maxwell-density matrix equations towards nonclassical effects. Fluctuations arising from interactions of the optical field and quantum system with their reservoirs are treated within the quantum Langevin theory [85]–[88]. Based on that, we can derive fluctuation terms from c-number Langevin equations and consider them in the generalized Maxwell-density matrix Langevin equations [59], [89]. The chapter is concluded in Section 1.5 with a brief overview of the thesis.

1.1 Quantum Cascade Laser

The quantum cascade laser is a peculiar type of semiconductor laser, where the emission frequency is selected by quantum engineering. Here, the optical transition takes place between quantized electron states in the conduction band of a multiple quantum well heterostructure. Unlike other semiconductor devices, where the optical transition occurs between conduction and valence band, the desired transition frequency and other optical and electrical properties such as the dipole moment or electron transport can be designed in QCLs by adjusting the thickness of the corresponding barrier and well layers. For the fabrication of the active QCL medium

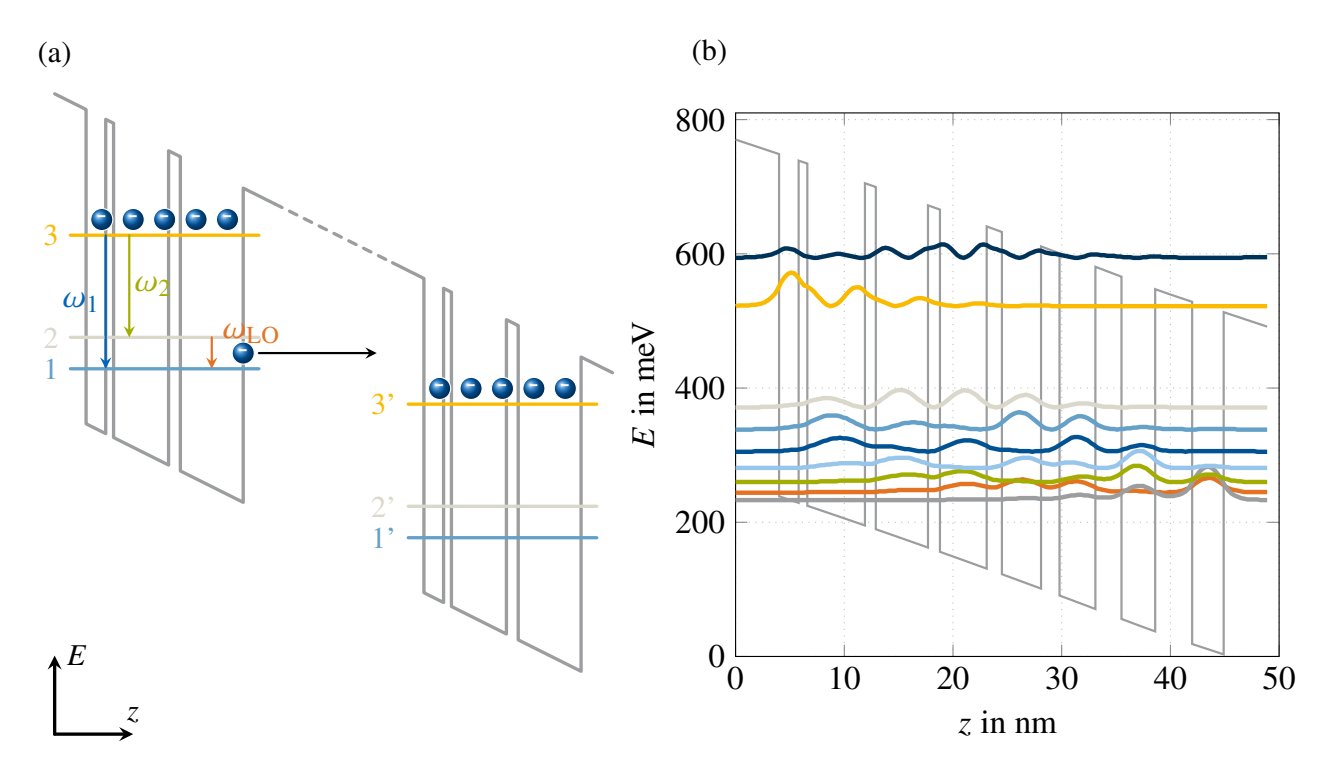


Figure 1.2 (a) Basic operation principle of a QCL and schematic conduction band profile. Each period consists of an active region and an electron injector. Electrons are injected into the ULL, from which they radiatively decay to the LLLs 2 and 1 by emitting photons with frequencies ω_1 and ω_2 , respectively. Subsequently, electrons scatter through the injector region and are injected into the ULL of the next period, where this process is repeated. Adapted from J. Popp, "Self-consistent simulations of intracavity terahertz comb difference frequency generation by mid-infrared quantum cascade lasers" [90] (CC BY 4.0). (b) Conduction band profile and probability densities for a mid-infrared QCL lasing at $\sim 8.5 \,\mu\text{m}$ [91].

molecular beam epitaxy (MBE) or metalorganic chemical vapor deposition (MOCVD) techniques are used. In these devices, electron recycling is accomplished by a multistaged cascade geometry with up to 100 periods and leads to an unprecedented quantum efficiency, as one injected electron can generate multiple photons. The fundamental working principle is schematically described in Fig. 1.2(a), where the conduction band profile of a QCL is qualitatively illustrated [5], [92]. Additionally, we show the conduction band profile of one period together with the calculated probability densities of the quantum states for a diagonal bound-to-continuum (BTC) QCL design emitting at $\sim 8.5 \,\mu m$ in Fig. 1.2(b) [91]. In laser operation, a tilted conduction band profile is obtained by applying a bias of 57 kV cm⁻¹. Electrons are injected into the upper laser level (ULL) 3 and optical transitions by stimulated emission at the frequencies ω_1 and ω_2 are accompanied by the decay of electrons from the ULL 3 to the lower laser levels (LLLs) 2 and 1. Efficient depopulation is achieved by longitudinal optical (LO) phonon scattering to the depopulation level 1. Within the electron injector region, the electrons are transported toward the interface of the next period and will be injected into the next ULL 3' by resonant tunneling. The same process as described above is repeated in successive periods until the electrons reach the anode and are collected.

By selecting a well-suited material system, both the mid-IR and THz region become accessible [5], [93]. For the development of short-wavelength QCLs beyond the conduction band offset (CBO) limit of 0.52 eV in lattice-matched systems, the material composition of the mid-IR QCL material system InGaAs/InAlAs can be strain engineered [94]–[97]. Over the years, multi-watt output powers, continuous wave (CW) operation at room temperature and wallplug efficiencies up to 50 % have been achieved with mid-IR QCL sources [98]–[102]. An appropriate choice for the realization of QCL devices emitting in the THz regime is the material system AlGaAs/GaAs [6], [7]. To access and close the THz gap between microwaves and optics, the QCL is the ideal semiconductor laser source. One major disadvantage of direct THz light generation with QCL sources is the lack of devices operating at room temperature resulting from the complexity of establishing and preserving population inversion between the upper and lower laser levels [7], [103]. This problem arises since the THz

photon energy is around a few meV and thus well below the thermal energy of 26 meV at room temperature. The laser system tends to thermodynamic equilibrium and intrinsically destroys population inversion. Until very recently, the requirement of cryogenic cooling for direct THz QCL operation could only be overcome by THz difference frequency generation [82], [104]. However, the development of THz QCL designs with a maximum operating temperature well above 200 K in pulsed operation opened the door for device applications using less demanding cooling systems, e.g., thermoelectric Peltier cooling [21], [105], [106].

QCLs with a broadband optical emission spectrum are suitable for the generation of optical frequency combs, i.e., laser spectra consisting of perfectly equidistant and phase-locked lines. Both in the mid-IR and THz regime, the generation of optical frequency combs with QCL sources was already demonstrated [14], [15]. In principle, the gain spectrum of these devices can be very broadband, potentially covering one frequency octave, and therefore pointing towards self-referenced emission [107]-[109]. However, the mode-locked comb emission is usually restricted to a rather small dynamic range, at low current densities. Here, the small group velocity dispersion (GVD) allows the FWM processes to effectively lock the cavity modes, without the need for external optical elements. Mode-locking over the entire 1.3 THz gain bandwidth, and across more than 60% of the operational range of a heterogeneous QCL device has been achieved recently by altering its intracavity light intensity [110]. This has been done by reducing the reflectivity of the device back facet to induce higher mirror losses, through coating with an epitaxially-grown multilayer graphene film. Moreover, the extremely accurate frequency resolution recently demonstrated by these miniaturized combs when externally phase referenced [111], shows their enormous potential in the area of metrology and spectroscopy and makes QCL devices highly interesting for the integration into innovative applications of different fields, e.g., astronomy or healthcare diagnostics [16], [112], [113]. In recent years, a main focus of research has been dedicated to the reconstruction of time domain profiles and intermodal phase relations of QCL frequency combs. Based on methods such as the shifted-wave interference Fourier-transform spectroscopy (SWIFTS) [114], [115] or Fourier-transform analysis of comb emission (FACE) [66], [111], [116], the phase stability of the frequency combs could be demonstrated. The coexistence of frequency-modulated (FM) and amplitude-modulated (AM) comb regimes in both mid-IR and THz QCL sources was experimentally retrieved [114], [115], [117], [118], and could be replicated in several theoretical studies based on different simulation models [51], [52], [70], [119]–[123].

1.2 Quantum Cascade Detector

The quantum cascade detector is the counterpart of the well-engineered QCL and therefore consists also of a multiple quantum well heterostructure [25], [26]. In QCLs, lasing is achieved by stimulated emission between quantized states, while in QCDs stimulated absorption is the relevant physical mechanism for photodetection. OCDs do not need external fields due to their asymmetric conduction band profile and work in a photovoltaic detection mode. In Fig. 1.3(a), a schematic of the aforementioned conduction band profile with the subband states of a QCD is represented [28], [124], [125]. The working principle of such devices is based on intersubband transitions, where the absorption transition takes place between the ground state a₁ and the absorption state a₂ in the active quantum well. Photo-excited electrons can be extracted into level b by resonant tunneling, which is specified here by the characteristic Rabi frequency Ω corresponding to the anticrossing energy between the near-resonant states. From level b the electron transport through a staircase consisting of multiple extractor states is governed by LO-phonon-assisted tunneling. An electron then arrives at the ground level a'1 of the next period and will iteratively repeat this process until it gets collected at the cathode. The unilateral charge transport of photoexcited electrons is ensured by the graded quantum well composition of the extraction cascade. In Fig. 1.3(b) we present the conduction band diagram together with the calculated probability distributions of the quantum states for the mid-IR QCD design N1022 with a peak detection wavelength of 4.7 µm [124], [126]. Here we identify two closely aligned absorption levels extending over two wells. The electron transport is governed by resonant tunneling through the thick barrier as indicated above.

Another well-known intersubband detector is the quantum well-infrared photodetector (QWIP), which works in photoconductive operation and consists of multiple periods of quantum wells. Absorbed photons excite electrons within a quantum well from confined to quasi-bound subbands. By applying a bias the electrons

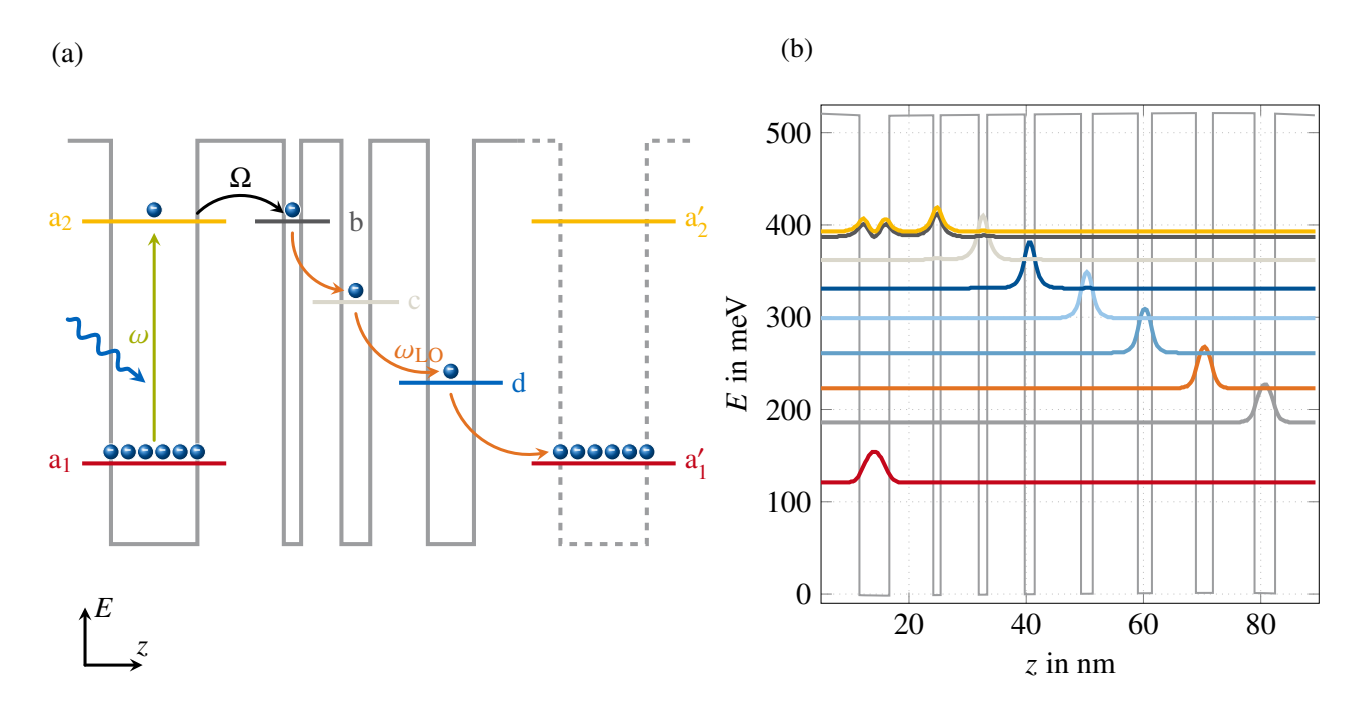


Figure 1.3 (a) Operation principle of a QCD and schematic representation of the conduction band structure. Electrons in the active well a are lifted from the ground level a_1 to the absorption level a_2 by the annihilation of an optical photon with frequency ω. The lifted electrons escape by resonant tunneling to well b and scatter through a quantum cascade by emitting phonons with frequency $ω_{LO}$. They will be collected in the ground state a'_1 of the adjacent period and the photovoltaic process is repeated. (b) Calculated conduction band profile and probability densities of the mid-IR QCD structure N1022 with a detection wavelength of 4.7 μm [126].

can escape into the continuum and contribute to the photocurrent [127], [128]. The unipolar character of both designs (QCDs and QWIPs) brings the advantage of highspeed operation in comparison to interband devices [129]. In QWIPs, the main noise source is dark current noise, whereas QCDs are mainly limited by Johnson noise [26], [126], [130]. Therefore, QCDs offer superior noise behavior, which is especially important for high-temperature operation e.g in mobile applications [38], [130]-[132]. Furthermore, QCDs have the advantage of simple adaption to the matured processing technique of QCLs resulting in an increased design freedom and reliability [131]. In order to optimize the detector performance, different designs have been tested, such as vertical [126], diagonal [40] or coupled quantum well detectors [133]. The relevance of QCDs for on-chip integration with QCLs is growing rapidly. In recent years, high-performance bi-functional quantum cascade devices were introduced, which can be used for monolithic integration on a single chip and demonstrate promising perspectives towards cheap and light-weight portable sensor solutions [132], [134], [135]. A systematic design optimization of QCDs is an essential task for the development and improvement of such devices. Different optimization strategies have already been applied to QCL design processes, e.g., a genetic optimization algorithm [91] or Bayesian optimization (BO) [21]. Franckié and Faist [22] published results for a comparison of the Bayesian optimization algorithm with an "information algorithm with parallel trials" (IAPT) algorithm and the aforementioned genetic algorithm. The three optimization tools were applied to a Gaussian process (GP) model, which was trained for a THz QCL using the QCL gain as a merit function. The BO scheme shows the best performance in terms of convergence and robustness. Therefore, we have decided to use BO in combination with a newly developed QCD modeling approach to optimize the mid-IR QCD design N1022 with respect to the important figures of merits, e.g., detectivity and responsivity. The QCD simulation approach is described in this work and validated against experimental data for both mid-IR and THz QCD designs. Furthermore, in this thesis, we present the BO results of QCDs where structures with improved performance in terms of signal strength and noise performance are obtained.

1.3 Nonlinear Optical Effects

OCLs serve as compact and powerful on-chip sources for coherent OFC emission without the need for external optical elements [12]–[15], [84], [110], [115], [116], [136]–[138]. Furthermore, other promising semiconductor lasers (SCLs) for integrated optical frequency comb technologies spanning from the near-IR to mid-IR regime are available, e.g., quantum dot (QD) lasers [139]–[149], quantum dash (QDash) lasers [150]–[155], and ICLs [9], [10], [156], [157]. The active gain medium of the aforementioned low-dimensional SCLs provides a large thirdorder nonlinearity $\chi^{(3)}$, which gives rise to a broadband FWM process and results in mode proliferation [12], [113]. Here, the complex interplay of parametric gain, FWM nonlinearity, chromatic dispersion and spatial hole burning (SHB) is essential for the frequency comb formation [10], [15], [70], [122], [141], [151], [158]–[160]. For a better understanding and to improve the laser performance, noise and linewidth characteristics of such devices have been extensively studied, both theoretically and experimentally [147], [148], [159], [161]–[169]. Stable and robust OFC operation is assured by a narrow beatnote, which is a measure for the amount of amplitude and phase-noise of the comb lines. Noise accompanying carrier transport and spontaneous emission noise can therefore have a significant impact on the OFC formation and the performance of SCLs. Recently, OFC emission in a novel QCL operating regime was detected, featuring harmonic modes separated by multiples of the cavity roundtrip (rt) frequency. In both the mid-IR and THz spectrum, harmonic frequency comb (HFC) states of varying orders were obtained in QCLs for different bias points and waveguide geometries [73], [79], [81], [83], [170], [171]. Potential applications of HFC QCL setups arise in the area of wireless terahertz communication networks [79], THz imaging [81] and quantum optics experiments [83], [84]. Free-running HFC formation in THz QCLs is mainly based on double-metal waveguide configurations. A schematic of such a THz HFC QCL setup is illustrated in Fig. 1.4, where the active gain medium is sandwiched into a double metal waveguide, and the outcoupled coherent THz light is either specified by a fundamental or a harmonic OFC spectrum depending on the order of the intermodal spacing. Recently, stable self-starting second-order HFC emission could be demonstrated for a single-plasmon THz QCL with a cavity length of 15 mm [172]. Effective coherent emission of harmonic combs is further achieved by active mode-locking [53], [61], [65], or can be controlled and manipulated through external forcing, e.g., macroscopic defects [173]-[175], external cavities [176] or optical seeding [177].

Fully numerical studies have observed HFCs with large comb-line separation (more than $2 \times f_{rt}$ obtained in [52]) in presence of external forcing (macroscopic defects [173]-[175], active modulation [53], or external cavities [13]). Furthermore, analytical models have been derived and predict gain for largely detuned side modes [75], [171], or provide an explanation based on mean-field treatment [122], [123]. However, no direct observation of higher-order HFC combs attributed to the internal laser dynamics in free-running QCL devices could be retrieved by numerical simulations, to the best of our knowledge. Therefore, we have performed a substantial numerical study of THz QCLs based on a diagonal transition design [178], [179] and could demonstrate for the first time self-starting fundamental and harmonic mode-locking with self-assembling of high-order HFCs [73], [180]-[182]. For the characterization of the active gain medium, we have used our in-house open-source monacoQC framework, featuring a versatile wavefunction solver [35], [183], [184] and a stationary carrier transport model, which is based on the DM-EMC method [35]. For the investigation of the dynamical behavior in the THz OCL, we have used the open-source solver tool *mbsolve* for the full-wave generalized Maxwell-DM equation system, which is composed for the modeling of light-matter interaction in multilevel quantum systems without invoking the rotating wave approximation (RWA) [47], [72]. All input parameters for the dynamical simulations can be self-consistently extracted from the quantum cascade device modeling tool monacoQC. A detailed description of the multi-domain simulation approach is presented in this work. As pointed out in several theoretical analyses of QCL gain media, the chosen wavefunction basis has a significant impact on the gain characteristics [35], [36], [179], [184]. In order to analyze the influence of the eigenstate basis set on the laser output state, we calculate the wavefunctions in extended [183] and localized [35], [36], [184] basis. The influence of the basis set on the gain characteristics and the harmonic mode-locking behavior is discussed in Chapter 8.

Unfortunately, the maximum CW operation temperature of direct THz QCL designs is currently limited to 129 K and demands cryogenic cooling [170], [185], [186]. An alternative approach to generate CW THz radiation closer to or even at room temperature is intracavity DFG in dual-wavelength mid-IR QCL sources [80],

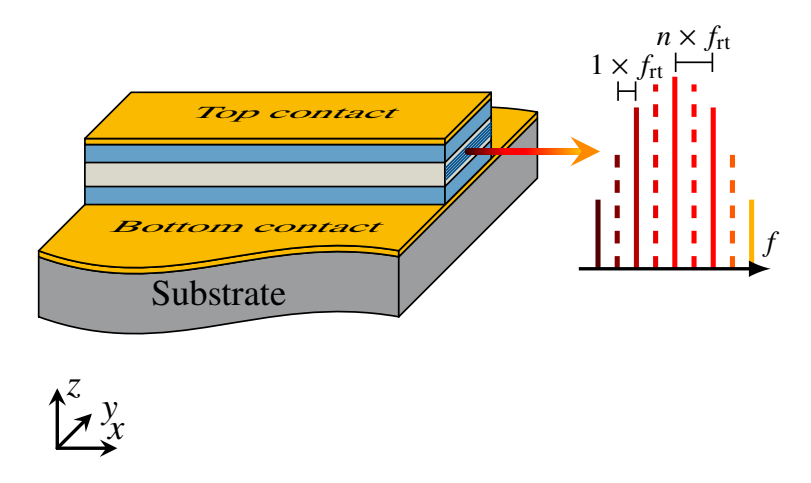


Figure 1.4 Schematic of a double metal QCL waveguide with THz OFC emission through the laser active region facet. Here, the difference between a fundamental OFC and a HFC is illustrated by the varying mode spacings within the emitted comb spectrum. For the fundamental comb the mode spacing corresponds to the roundtrip rate $f_{\rm rt}$, while for the HFC comb spectrum, we obtain a mode spacing of $n \times f_{\rm rt}$, where n is an integer multiple of one. Reprinted from J. Popp *et al.*, "Multi-domain modeling of free-running harmonic frequency comb formation in terahertz quantum cascade lasers" [178] (CC BY 4.0).

[82], [187], [188]. Belkin et al. [189] presented the first so-called THz DFG-QCL device in 2007 and since then great effort has been put into the engineering and development of such devices. The main advantage here is that room temperature operation with such dual-wavelength mid-IR QCLs is well accessible without the necessity of population inversion for a THz transition. The basic working principle of a THz DFG-QCL is described in Fig. 1.5(a). The optical transition of electrons by stimulated emission from the ULL 4 to the LLL 3 and 2 occurs and lasing starts at two mid-IR pump modes ω_1 and ω_2 . A THz mode at frequency ω_{THz} results from the nonlinear mixing process and downconversion of the mid-IR frequencies ω_1 and ω_2 . Here, the DFG triplet is formed by the three states 4, 3 and 2. Subsequently, efficient depopulation is achieved by LO phonon scattering and the electrons are injected into the upper laser level 4' of the adjacent period. The active region has to be designed with a large second-order nonlinear susceptibility $\chi^{(2)}$ to obtain an efficient THz DFG process. Quantum engineering of the QCL active region towards giant nonlinearities is strongly dependent on the coupling of the involved triplets of states. By utilizing a dual-upper state (DAU) active region design instead of a stacked BTC structure a stronger nonlinearity due to additional DFG triplet states is obtained. Additionally, these laser designs exhibit a relatively broad gain spectrum [190]-[193]. The first THz DFG-QCLs consisted of a single waveguide for both mid-IR and THz frequencies and thus suffered from excessive absorption in the THz regime [188], [189], [194]. To overcome this inefficiency in the outcoupling of THz radiation, QCL waveguides with a Cherenkov phase-matching scheme were introduced, and are now standard for THz DFG-QCL devices [190], [195], [196]. Here, the mid-IR pump modes are confined in the laser active region and are outcoupled through the mid-IR waveguide facets, whereas the THz emission is directed towards the semi-insulating (SI) InP substrate, providing comparably low THz loss. Cherenkov emission into the substrate is achieved when the phase velocity of the nonlinear polarization wave within the slab waveguide is faster than in the surrounding medium. As the SI InP provides a higher THz refractive index n_{THz} than the group effective refractive index n_g of the pump modes, the THz radiation exits the active region under the Cherenkov emission angle $\theta_c = \cos^{-1}(n_g/n_{THz})$ [82]. To avoid internal reflection of the Cherenkov wave emission at the substrate/air interface, the front facet has to be polished at an angle between 20° and 30° [80], [82], [187], [188].

Initially, the main research focus was laid on the development and fabrication of widely tunable THz DFG-QCL emission with narrow linewidth in the frequency range of 1 THz to 6 THz [192], [197]–[202]. Here, broadband tuning is either obtained by external-cavity (EC) DFG-QCL setups [200]–[202] or by monolithic electrically tunable THz DFG-QCLs [192], [197]–[199]. Single mode THz operation is established by dual-period, or sampled distributed feedback (DFB) grating approaches with dual-wavelength single mid-IR pump modes [188],

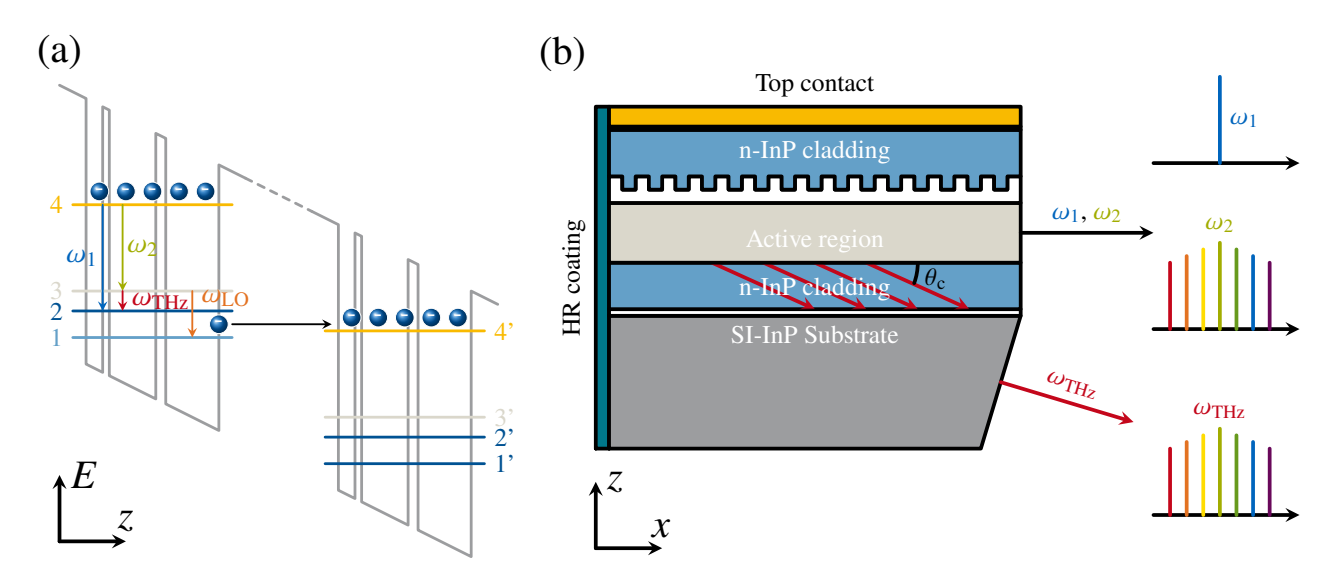


Figure 1.5 Schematics of THz difference frequency generation in mid-IR QCLs. Mid-IR pump frequencies are indicated by ω_2 (green) and ω_1 (blue), THz emission is represented by ω_{THz} (red). (a) Schematic of the DFG process between the quantized electron states in the conduction band profile of a QCL. The energy levels (4,3,2) form a DFG triplet, electron extraction is illustrated by LO phonon scattering into level 1 followed by injection into the adjacent period. Reprinted from J. Popp *et al.*, "Self-consistent simulations of intracavity terahertz comb difference frequency generation by midinfrared quantum cascade lasers" [178] (CC BY 4.0). (b) Schematic of a distributed feedback/Fabry-Perot configuration for nonlinear THz DFG-QCL frequency comb generation. The buried DFB grating is etched into the upper guide layer, which results in a single DFB mode ω_1 frequency detuned from the gain maximum. The FP frequency comb is centered around ω_2 and the THz comb radiation generated by nonlinear mixing is extracted into the substrate, where it gets outcoupled through the polished facet. The back facet is coated with a high-reflection (HR) coating. Reprinted from J. Popp *et al.*, "Self-consistent simulations of intracavity terahertz comb difference frequency generation by mid-infrared quantum cascade lasers" [178] (CC BY 4.0).

[198], [200]. Furthermore, the applicability in high-precision spectroscopy was tested by characterizing the spectral purity and tunability [137], [203]. Recently, broadband THz DFG-QCL frequency combs were generated by mixing a single mid-IR mode, which is selected by an integrated largely frequency-detuned DFB grating, and a frequency comb centered at a second mid-IR frequency in a multimode Fabry-Perot (FP) cavity [82], [191], [204]–[206]. This distributed feedback/Fabry-Perot configuration for nonlinear THz DFG-QCL frequency comb generation is schematically illustrated in Fig. 1.5(b).

To model the nonlinear mixing processes in QCLs, Maxwell-DM equations are a valuable tool, as they offer a relatively compact and numerically efficient model [47]. In Chapter 8, we present THz DFG-QCL OFC results using the open-source solver tool *mbsolve* [72], [207]. Here, the generalized one-dimensional Maxwell-DM equations are treated without invoking the RWA, which is crucial for the simulation of THz DFG-QCL frequency comb setups, as the spectrum spans from the THz region to the mid-IR regime and cannot be resolved within the RWA. Nonlinear and nonclassical effects, like tunneling processes and coherence of the relevant optical transitions, may account for an asymmetric gain and have been included in the system Hamiltonian. Furthermore, all required parameters for the description of the quantum system are also extracted self-consistently from our in-house *monacoQC* approach for stationary carrier transport simulations using the EMC method [29], [35].

1.4 Nonclassical Laser Theory

Significant research efforts are devoted to the generation and deployment of nonclassical features in optical and electronic systems [208]–[213]. Recently, intensity correlations in QCL HFCs were experimentally investigated to develop a new generation of semiconductor devices generating light with nonclassical properties [83]. Endowing commercial devices with outstanding quantum features would pave the way to next generation high-performance applications in the field of quantum networks [214], [215] including quantum computation [216], [217], quantum communication [218], quantum metrology [219]–[221] and quantum simulation [222], [223]. Notably, photonic systems are quite attractive for the investigation and employment of nonclassical features, such as the generation of so-called quantum combs [224]–[226], corresponding to nonclassical states of light with multimode squeezed and/or entangled output. As the emergence of nonlinear and nonclassical features in SCLs is directly linked to the noise properties [83], [227], the development of low-noise SCLs sources based on detailed simulations is an important prerequisite.

The Maxwell-Bloch equations are widely used for spatiotemporal simulations of the optical dynamics in nano-optoelectronic devices [43], [47], [228]. Spontaneous emission plays an important role in such devices, where the resulting recombination can simply be included by nonlinear rate terms for the carrier occupations [229], [230]. However, the corresponding noise contributions are not included in the Maxwell-Bloch model due to its semiclassical nature. For more realistic simulation scenarios, e.g., OFC generation in low-dimensional SCLs, the incorporation of nonclassical fluctuations should be considered. In the semiclassical framework [231], [232], stochastic noise terms are typically implemented using a pseudorandom number generator. The uncorrelated Gaussian-distributed random numbers are added to the optical propagation equation at every gridpoint [44], [233]–[235]. Furthermore, dipole fluctuations have been included in different MB models by adding noise terms to the off-diagonal density matrix elements [230], [236]–[240].

The magnitude of stochastic noise terms can be derived from the quantum Langevin equations [85], [86], [241], [242], which can also be represented by equivalent stochastic c-number equations [44], [89], [243], [244], i.e., evolution equations for operator expectation values with additional stochastic terms. Such c-number Langevin equations have been used in literature [164], [165], [227], [245]–[249] to calculate the intrinsic linewidth and estimate the intensity noise in SCLs. An extension of the stochastic c-number approach to incorporate nonclassical effects has been discussed in [89] and [250]. By virtue of the fluctuation-dissipation theorem, a decay of populations, coherences, or the optical field is generally accompanied by fluctuations, and a Maxwell-Bloch equation model which includes such decay-induced fluctuations has been presented [233], [251], [252]. In Chapter 4, we present an extension of the two-level quantum theory by Drummond and Raymer [89] by including incoherent tunneling injection into the ULL. From this, we have derived the semiclassical noise terms for our generalized Maxwell-density matrix Langevin approach, where we ensure the preservation of

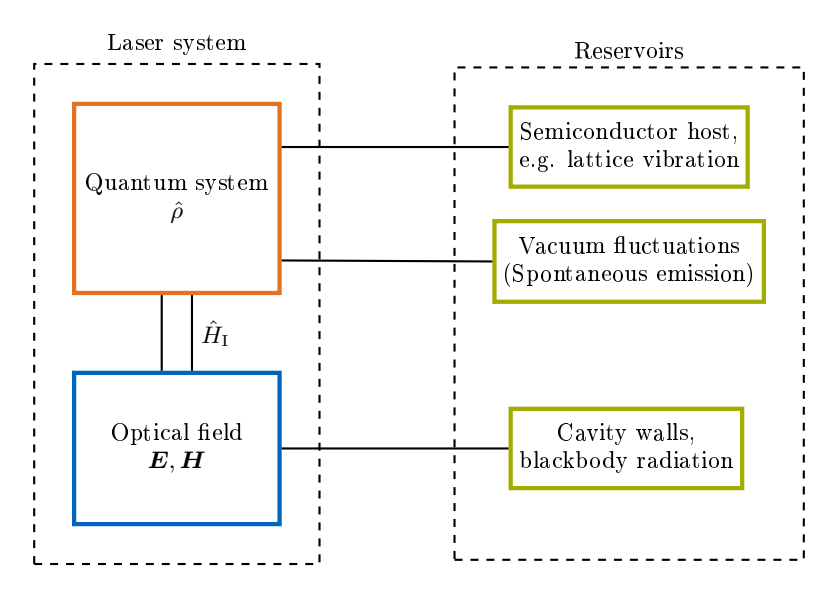


Figure 1.6 Schematic illustration of the coupling of a SCL quantum system and field system and the interaction with their associated reservoirs. Reprinted from J. Popp *et al.*, "Modeling of Fluctuations in Dynamical Optoelectronic Device Simulations within a Maxwell-Density Matrix Langevin Approach" [1] (CC BY 4.0).

the physical properties of the density matrix, i.e., positive definiteness and unit trace. Furthermore, we have incorporated the derived noise terms in our open-source tool *mbsolve* to model the fluctuations accompanying electronic transport and spontaneous emission in the dynamical simulations of light-matter interaction in multilevel quantum optoelectronic systems such as QCLs and QD lasers. Using simulation results of a THz QCL harmonic frequency comb, we discuss the effects of noise contributions on the comb characteristics in Chapter 8.

Our model is illustrated schematically in Fig. 1.6. Here, the structure is described by the density matrix $\hat{\rho}$ and the optical field represented by the electric and magnetic field vectors E, H, which are coupled to each other by the interaction Hamiltonian $\hat{H}_{\rm I}$. For the calculation of drift and diffusion operators in the quantum Langevin theory, we take into account the influence of various reservoirs in our structure. Regarding the quantum system, the reservoir interactions with the semiconductor host, which for example includes phonons associated with (longitudinal- and transverse-optical and -acoustic) thermal lattice vibrations, lattice imperfections in the form of impurities (such as dopants), interface roughness (IF) or atomic disorder in alloys, as well as vacuum fluctuations arising from spontaneous emission are considered. For the optical field, the interaction with noise arising from thermal radiation (blackbody) entering the active waveguide from the cavity walls can be taken into account by external noise sources [253].

1.5 Overview of this Work

In the introduction above the basic operating principles of the investigated intersubband QC devices (QCL, QCD) have been outlined. Additionally, we have briefly introduced nonlinear optical effects of different orders exploited in QCLs, e.g., coherent THz OFC emission at room temperature by DFG and harmonic mode-locking triggered by FWM processes. Finally, we have addressed a new generation of semiconductor devices endowed with quantum features. Here, we have highlighted the enormous potential of intersubband QC devices for future applications in groundbreaking areas of quantum technologies such as quantum metrology and sensing. We have also briefly discussed the generalized Maxwell-density matrix Langevin equations, where the derivation from quantum theory by taking into account the interactions of the optical field and quantum system with their reservoirs is presented in Chapter 4.

In the area of theoretical modeling and numerical simulation of intersubband QC devices, our group provides strong expertise [24], [29], [42], [47], [58], [78], [78], [90]. Here, the open-source *monacoQC* framework for intersubband QC device engineering [254] in combination with the in-house EMC approach for charge-

carrier transport [29] and the open-source solver tool *mbsolve* for light-matter interaction in nonlinear optics [47], [72] have been developed and extended in recent years. In the EMC approach, scattering is self-consistently evaluated based on Fermi's golden rule. Within the *mbsolve* framework, numerically extensive simulations of multilevel systems based on the full-wave Maxwell-density matrix equations can be conducted. Beyond the so-called rotating wave approximation, dynamical simulations of broadband frequency combs or THz difference frequency generation QCL frequency comb setups extending from the mid-IR to the THz spectral range are feasible [47]. In this thesis, a detailed description of the multi-domain simulation approach for intersubband QC devices is presented and the simulation results obtained for the intersubband QC devices are discussed in depth. In the following, we give a brief overview of this work, starting with the theoretical foundations, and continuing with the modeling approaches and the simulation results of intersubband QC setups.

In Chapter 2, we introduce the open-source *monacoQC* framework for QC device engineering. Here, we explain the fundamental physical and optical principles of low-dimensional semiconductors and describe the heterostructure technology. The main focus is on the calculation of important band parameters such as the band gap energy or the effective mass, taking into account the effects of nonparabolicity and strain. All material parameter models presented are included in the setup library and can be used to describe the active QC region and to calculate the simulation parameters. In addition, the Schrödinger-Poisson solver tool for the design and engineering of quantized electron states and the Bayesian optimization tool for QC devices are presented.

In Chapter 3, carrier transport simulation models for intersubband QC devices are described and the integration into the *monacoQC* framework is discussed. Here, our major focus is on the in-house DM-EMC model and a rate equation model for QCDs. We characterize the main scattering mechanisms in quantum well heterostructures and calculate the corresponding scattering rates using Fermi's golden rule. We further describe the stochastic EMC method and explain the density matrix expansion for the inclusion of incoherent tunneling transport. Within the results library, the stationary carrier transport simulation results and the eigenstates, solutions from the SP solver, are stored using class objects. The provided class functions can be used for the analysis and visualization of the simulation results. In order to process the simulation data and to provide a compact quantum system model for the dynamic Maxwell-DM simulations, the class **mbsolve_sim** is introduced.

Furthermore, our recent work about modeling fluctuations in dynamical optoelectronic device simulations within a Maxwell-density matrix Langevin approach is described in Chapter 4. Based on the quantum theory for a three-level quantum system including incoherent tunneling injection we can derive stochastic fluctuation terms and incorporate them in our *mbsolve* tool. Starting from the quantum Langevin equations, we can derive the associated c-number Langevin equations and combine them with the Maxwell-DM equations. Fluctuations that accompany electronic transport and spontaneous emission in optoelectronic multilevel systems can be accurately modeled in dynamic simulations of light-matter interaction. Our Maxwell-DM Langevin modeling approach shows great potential for the theoretical investigation of intermodal intensity correlations in photonic devices and the development of low-noise integrated light emitters, also with regard to the generation of non-classical light.

In Chapter 5, we give an overview of the open-source Maxwell-DM Langevin tool *mbsolve* and describe new implementations, e.g., the truncation of the optical field at the simulation boundaries, the treatment of chromatic waveguide dispersion and the modeling of fluctuations in dynamical optoelectronic device simulations. We give a brief overview of the existing methods and validate the most important parameters, such as numerical performance and long-term stability. Furthermore, the numerical treatment of the Maxwell-DM Langevin equations within the *mbsolve* framework is described in detail. For the truncation of the optical field in lossy and dispersive media, we use the advanced finite-difference time-domain method with auxiliary differential equations. The numerical treatment of the density matrix within the matrix-exponential approach and the evolution of the fluctuation operator are presented. Finally, the main loop of the simulation with the extended generalized update equations is discussed.

The new functional extensions of the mbsolve simulation library are verified in Chapter 6 by using various simulation setups. Here, we conduct a comprehensive study of a THz QCL system, including the characterization of gain and intrinsic dispersion. A sophisticated perfectly matched absorbing boundary condition is used for the truncation of the active QCL gain medium. By taking into account the impedance mismatch effects arising from the internal quantum system, we can avoid detrimental reflection errors. An improved absorbing characteristic

can be demonstrated by comparing the simulation results with the conventional absorbing boundary conditions. We further investigate the influence of group velocity dispersion on the formation of THz frequency combs. Therefore, we use the implemented Lorentz model for the THz QCL OFC setup and can report good agreement with the experimental data. A superfluorescence (SF) setup is used for the validation of our fluctuation implementations. The inclusion of fluctuations is important to reproduce the transition from SF to amplified spontaneous emission (ASE), which is associated with the decrease in dephasing times. Here, the experimental findings can be replicated.

In Chapter 7, we present simulation and optimization results for photovoltaic QCD operation. Using an advanced method for accurate and efficient simulations of photovoltaic QCD structures based on the EMC approach, we show simulation results of QCDs detecting in the mid-IR and THz regimes. The comparison with experimental data and NEGF simulation results yields good agreement and qualifies our approach for systematic optimization of QCDs. Therefore we use the BO approach in combination with our QCD modeling approach to optimize the mid-IR QCD design N1022. The resulting QCD structures show improved performance concerning signal strength and noise characteristics. Using a GP trained with the simulation results of the BO runs, we can make assumptions about the sensitivity of the optimized designs to the manufacturing tolerances. The optimized structures appear to be quite robust to variations in the growth layer.

Multi-domain modeling results of free-running frequency comb formation in quantum cascade lasers are presented in Chapter 8. Therefore, the chapter is divided into two parts, one presenting simulation results for self-starting harmonic mode-locking in a THz QCL and the other showing simulation results of intracavity terahertz comb emission by difference frequency generation. Our results for the THz QCL setup show the self-assembling of high-order HFCs, where the mode-locking results from the internal laser dynamics. The investigation of different basis states reveals their influence on the gain characteristics and the formation of HFC states in THz QCLs. Additionally, we investigate the influence of the applied bias and waveguide geometry on the HFC formation and characterize the spectral time evolution of the self-starting harmonic mode-locking mechanism. We discuss the effects of noise contributions on the THz HFC characteristics. For the THz DFG QCL setup, we present stationary charge carrier transport simulations of the given structures based on the EMC method and compare them with the corresponding experimental data. Based on these results, we conduct dynamic simulations of the light-matter interaction using the open-source Maxwell-density matrix simulation tool *mbsolve*. Within our simulations, we can reproduce the experimental findings, where a THz comb is obtained by nonlinear mixing of a largely detuned DFB mid-IR single mode and a mid-IR FP comb.

Finally, in Chapter 9 we discuss our findings and point out possible future directions.

2 Functional Engineering of Intersubband Quantum Cascade Devices

Quantum cascade devices cover a wide range of the mid-IR and THz frequency spectrum and are therefore suitable for applications in chemical and biological sensing, imaging and communication. Here, we focus on two devices that are characterized by their physical working principle: The quantum cascade laser is a unipolar semiconductor laser and the quantum cascade detector as its counterpart is a unipolar semiconductor detector. In both devices, the lasing/detecting mechanism is achieved by optical intersubband transitions between quantized states in specially designed multiple quantum well heterostructures. A deep theoretical understanding of the physical mechanisms in these structures is required to systematically improve the performance in terms of operating temperature, efficiency and spectral range. The quantum well heterostructure further serves as a versatile model application for the development and improvement of simulation techniques in nano- and optoelectronics.

In this chapter, we focus on a comprehensive description of the QC device specifications and use extensive theoretical models from the literature for the development and optimization of these optoelectronic components. We deal with the fundamental principles of the physical and optical properties of low-dimensional semiconductors and describe the heterostructure technology. Therefore, we have developed the open-source Matlab-based QC device engineering tool *monacoQC*, schematically illustrated in Fig. 2.1 [24], [90]. In the following, we will divide the *monacoQC* framework into the given submodules and describe the specifications of the modules optimizer, setup and solver in this chapter in more detail. The reamining modules mbsolve, ext. solver and results are covered in Chapter 3.

A setup library for the description of the QC active region and the simulation parameters is provided. Taking into account all important parameters in our **device** description, the corresponding wavefunctions ψ_i and system Hamiltonian \hat{H}_s are calculated within a Schrödinger-Poisson (SP) solver library. The numerical approach used for solving the Schrödinger equation is based on the transfer matrix method (TMM) and is implemented in the corresponding class **tm_solver** [29], [183]. Additionally, a class **poisson_solver** takes care of the mean-field treatment of the electron-electron interaction and determines the arising electrostatic potential. Backend classes for the SP (**writer_wf**) and setup module (**fortran_sim**) generate all necessary EMC simulation input files, which are then fed into an external EMC simulation tool for stationary carrier transport simulations. Additionally, a Bayesian optimization module (**BO_sim**) based on Gaussian process regression is integrated into the *monacoQC* framework aiming to engineer and develop high-performance QC devices in a structured manner [24], [255], [256].

The chapter is organized as follows: In Section 2.1, we give an overview of the module setup for the description of intersubband QC devices. The electronic and optical properties of III-V semiconductors, including the physical approaches required to calculate the semiconductor band structure, are presented here. We further give a description of the Schrödinger-Poisson solver tool in Section 2.2. Here, we discuss the numerical solution of the one-dimensional Schrödinger equation, which provides the eigenenergies and wave functions of the energy eigenstates in the QC heterostructure. Furthermore, the inclusion of space charge effects through the solution of the Schrödinger-Poisson equation system is treated. Section 2.3 gives a brief summary of Bayesian optimization and Gaussian processes and explains how to apply this method to the optimization of quantum cascade devices.

2.1 Intersubband QC Device Description

The setup library mainly consists of two classes for the description of the intersubband QC structures. Here, the class **device** includes all important information about the active QC medium and the waveguide. The active

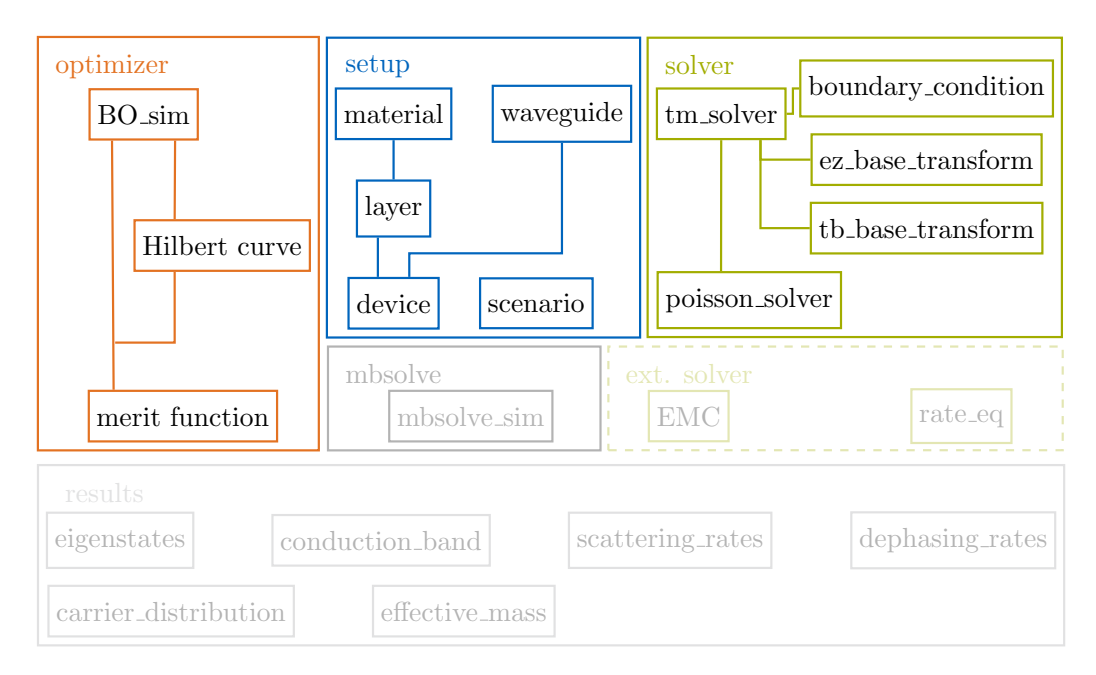


Figure 2.1 Overview of the *monacoQC* framework [254]. The project consists of six modules. In this chapter, we concentrate on the description of the three highlighted modules optimizer, setup and solver. Adopted from J. Popp *et al.*, "Multi-domain modeling of free-running harmonic frequency comb formation in terahertz quantum cascade lasers" [178] (CC BY 4.0).

region is formed by one period consisting of the layer collection with barrier and well materials. Relevant parameters of the waveguide model, e.g., the cavity length L, the linear loss term α_0 , the facet reflectance R and the confinement factor Γ , are summarized in the class **waveguide**. Other relevant environmental simulation parameters, e.g., applied bias or temperature T, describe the simulation scenario and are specified in the corresponding class **scenario**.

To obtain realistic simulation results, an accurate and detailed description of the specific physical properties of the used III-V compound semiconductor material systems is required. The III-V semiconductor compounds crystallize in a zincblende lattice structure, schematically illustrated in Fig. 2.2(a). Here, the unit cell consists of two interpenetrating face-centered cubic unit cells, each containing one specific atom. The reciprocal lattice of the underlying Bravais lattice is a body-centered cubic lattice and its first Brillouin zone is a truncated octahedron, shown in Fig. 2.2(b) with the standard notation for the points of high symmetry. In general, Greek letters are used to describe the points within the zone and Roman letters are used for the points on the surface. The two common material systems, AlGaAs/GaAs for THz QCLs and InGaAs/InAlAs for mid-IR QCLs are also based on the zincblende crystal lattice. In III-V semiconductors 8 outer electrons reside in one unit cell contributing to the chemical bonds. The other electrons are highly bound to the nuclei and will be neglected in our description of the electronic properties near the bandgap. In GaAs, the 8 covalent electrons are summarized by 3 electrons from Ga and 5 electrons from As and hybridize to tetrahedral bonds, e.g., one Ga-atom to its four nearest As-atom neighbors. Here, two electrons form strongly bound s-levels and the remaining six electrons fill the three bonding p-type orbitals. Due to the large number of unit cells, the levels broaden into bands, where the bonding p-orbitals form the valence bands, and the lowest lying empty anti-bonding (often s-level) orbitals the conduction band. In Fig. 2.3(a), the bandstructure of the ternary alloy In_{0.53}Ga_{0.47}As is depicted with a conduction band and three valence bands (heavy-hole (HH), light-hole and split-off (SO)). In general, the band edge of the valence band in III-V semiconductors can be found at the Γ point, which is the center of the Brillouin zone. Spin-orbit coupling is fully dedicated to the anion (As), which means that the spin-orbit split-off band is nearly independent of the cation. If the cation of a binary material is heavier, it is more likely to find the conduction band minimum at the Γ point. The binary material InAs features a direct bandgap at the Γ point, whereas AlAs has an indirect bandgap with the conduction band minimum at the X point. Ternary and quaternary alloys do not have a crystalline arrangement, as the involved atoms are distributed randomly at the sites of the zincblende lattice. To describe the electronic states of these alloys the virtual crystal approximation

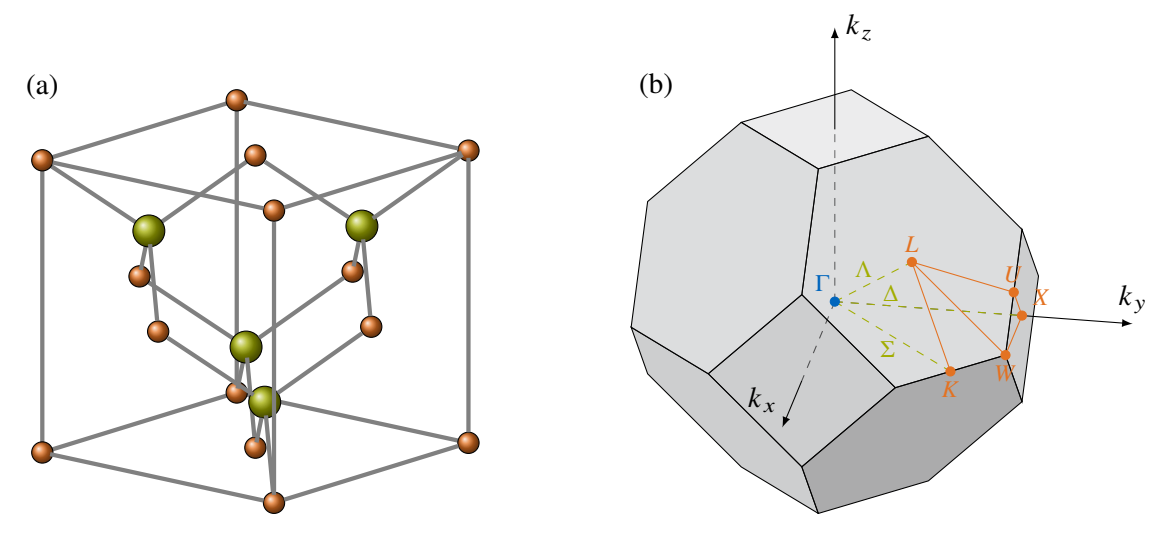


Figure 2.2 (a) Zincblende lattice composed by two face-centered cubic (fcc) primitive cells, where one is shifted by $(\frac{a}{4}, \frac{a}{4}, \frac{a}{4})$ relative to the position of the other resulting in an interpenetration of the two. (b) First Brillouin zone of the face-centered cubic lattice. Special points and directions are highlighted. Solid lines are on the surface and the broken lines are inside the zone.

(VCA) is applied. Here, the actual potential is replaced by an averaged one, which restores the translational invariance. This is required for the Bloch theorem, which is used for the description of wavefunctions in crystals. Furthermore, specific parameters such as the conduction band edge energy E_c or effective masses m^* for the description of semiconductors can be defined. For ternary alloys we can calculate these parameters $T_{A_{1-x}B_xC}$ using a simple quadratic formula [257]

$$T_{A_{1-x}B_xC} = (1-x)B_{AC} + xB_{BC} - x(1-x)C, (2.1)$$

where B_{AC} and B_{BC} are the two involved binaries, x describes the alloy composition and C is the so-called bowing parameter, which accounts for the deviation from the linear interpolation between the two binaries. The physical significance of the bowing parameters results from the disorder effects caused by the presence of the different cations (e.g., In and Al for InAlAs) and anions (e.g., As and P for GaAsP), respectively. Due to the different bandstructures of the binaries, the electronic properties of ternary alloys such as InAlAs vary highly nonlinearly with composition. In contrast to the material InGaAs, which offers a direct bandgap over the full composition range, the conduction band edge for InAlAs changes from the Γ point to the X point for varying compositions, where the crosspoint of the bandgap from direct to indirect is roughly at a composition of x = 0.64 [258]. Even for compound alloys such as AlGaAs, where the lattice periods of the binary components are very similar, there are strong nonlinearities due to the considerable differences in the bandstructure of the individual binary components.

The breakdown of the parabolic dispersion relation between energy and wavenumber in the conduction band of semiconductor materials for higher energy levels has to be considered in the simulation of QCLs. These nonparabolicity effects are treated within the $\mathbf{k} \cdot \mathbf{p}$ perturbation theory [259]–[261]. Here, the bandstructure of semiconductors is described by an energy-dependent effective mass [262], [263]. Within Bloch's theorem a solution for the Schrödinger equation in a periodic lattice potential with the period \mathbf{R} , e.g., in a bulk semiconductor crystal, is given by wavefunctions of the form

$$\Psi_{n,k}(r) = \exp(ikr)u_{n,k}(r), \qquad (2.2)$$

with the periodic Bloch function $u_{n,k}(\mathbf{r}) = u_{n,k}(\mathbf{R} + \mathbf{r})$. The $\mathbf{k} \cdot \mathbf{p}$ theory is used to solve the Schrödinger equation based on perturbation theory. Here, the Schrödinger equation for Bloch wavefunctions in crystals is given by

$$\hat{H}_0(\mathbf{r})\Psi_{n,\mathbf{k}}(\mathbf{r}) = \left[\frac{\hat{\mathbf{p}}^2}{2m_0} + V(\mathbf{r})\right]\Psi_{n,\mathbf{k}}(\mathbf{r}) = E_n(\mathbf{k})\Psi_{n,\mathbf{k}}(\mathbf{r}), \qquad (2.3)$$

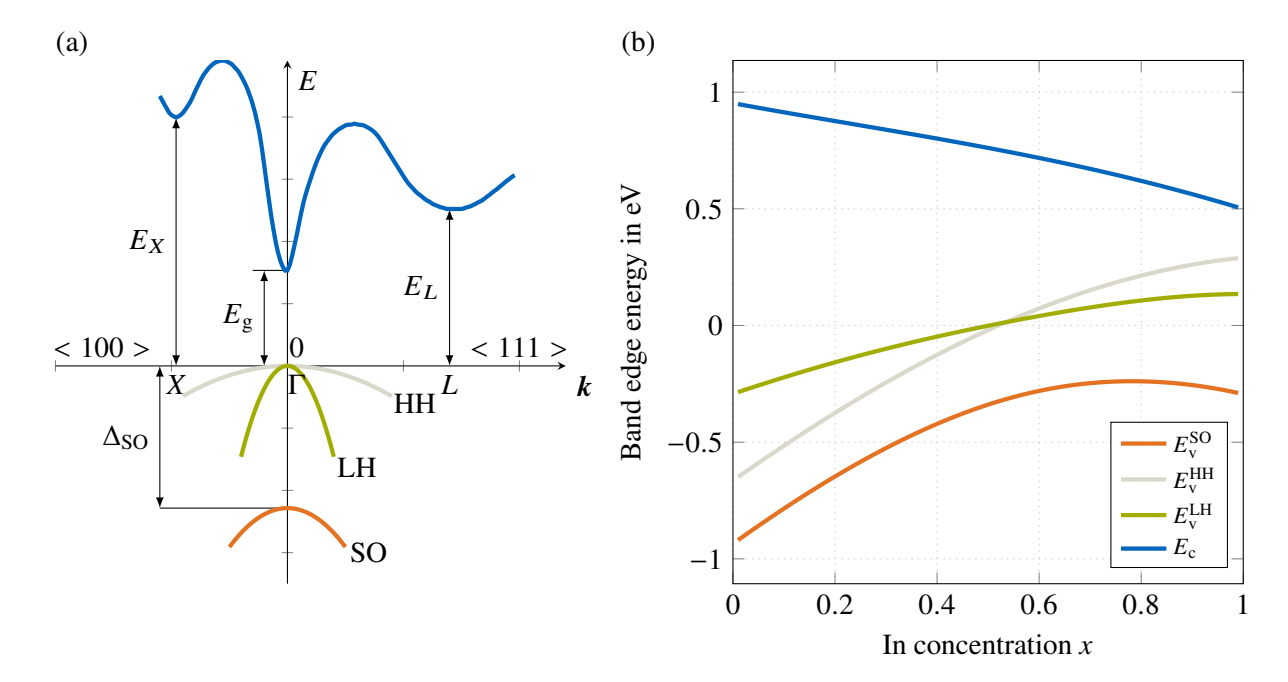


Figure 2.3 (a) Bandstructure of the direct bandgap semiconductor material $In_{0.53}Ga_{0.47}As$. The conduction and valence bands are depicted and the symmetry points X, Γ and L are marked. Reproduced from [264]. (b) Band edge energy calculations of the conduction band E_c , heavy-hole (HH) $E_v^{\rm HH}$, light-hole (LH) $E_v^{\rm LH}$ and split-off (SO) valence band $E_v^{\rm SO}$ of $In_xAl_{1-x}As$ grown on a (001) InP substrate under biaxial strain (k = 0) [265]. The influence of biaxial strain is taken into account and leads to a split-up of heavy and light hole valence band energy [263].

where \hat{p} is the momentum operator, m_0 is the electron mass, V(r) is the crystal potential and E_n denotes the eigenenergies. In general, spin-orbit coupling should be considered in more sophisticated studies of III-V semiconductor materials, but we neglect it here for the introduction to this theory in order to obtain a simplified derivation. For a more detailed description including the spin-orbit coupling, we refer to [262]. Using $\hat{p} = -i\hbar\nabla$ with \hbar being the reduced Planck constant, and substituting the wavefunctions from Eq. (2.2) into Eq. (2.3), we can cancel out the plane wave term $\exp(ikr)$ and obtain for the Bloch functions $u_{n,k}(r)$

$$\left[\frac{\hat{p}^2}{2m_0} + V(r) + \frac{\hbar}{m_0} k \hat{p} + \frac{\hbar^2 k^2}{2m_0}\right] u_{n,k}(r) = E_n(k) u_{n,k}(r), \qquad (2.4)$$

where the total Hamiltonian is divided into a unperturbed Hamiltonian \hat{H}_0 and a momentum-dependent term H'(k). At the Γ -point for k = 0 a solution for the wavefunctions and eigenenergies is obtained as

$$\hat{H}_0 u_{n,0}(\mathbf{r}) = E_n(0) u_{n,0}(\mathbf{r}), \qquad (2.5)$$

which can be used as the basis for the perturbation theory introduced below. The functions $u_{n,k}(r)$ at the vicinity of the band edge are written as

$$u_{n,k}(\mathbf{r}) = \sum_{m} c_m(\mathbf{k}) u_{m,0}(\mathbf{r}),$$
 (2.6)

with the k-dependent coefficients $c_m(k)$. By inserting Eq. (2.6) into Eq. (2.4), we obtain the second-order energy correction for the conduction band (n = c)

$$E_{c}(\mathbf{k}) = E_{c}(0) + \frac{\hbar^{2} \mathbf{k}^{2}}{2m_{0}} + \frac{\hbar^{2}}{m_{0}^{2}} \sum_{m \neq c} \frac{|\langle u_{c,\mathbf{0}}(\mathbf{r}) | \mathbf{k} \cdot \hat{\mathbf{p}} | u_{m,\mathbf{0}}(\mathbf{r}) \rangle|^{2}}{E_{c}(0) - E_{m}(0)},$$
(2.7)

where the momentum matrix elements $\langle u_{c,0}(r)|k\cdot\hat{p}|u_{m,0}(r)\rangle$ describes the energy corrections arising from the coupling strength between the conduction band c and all other considered energy bands m. For example, the

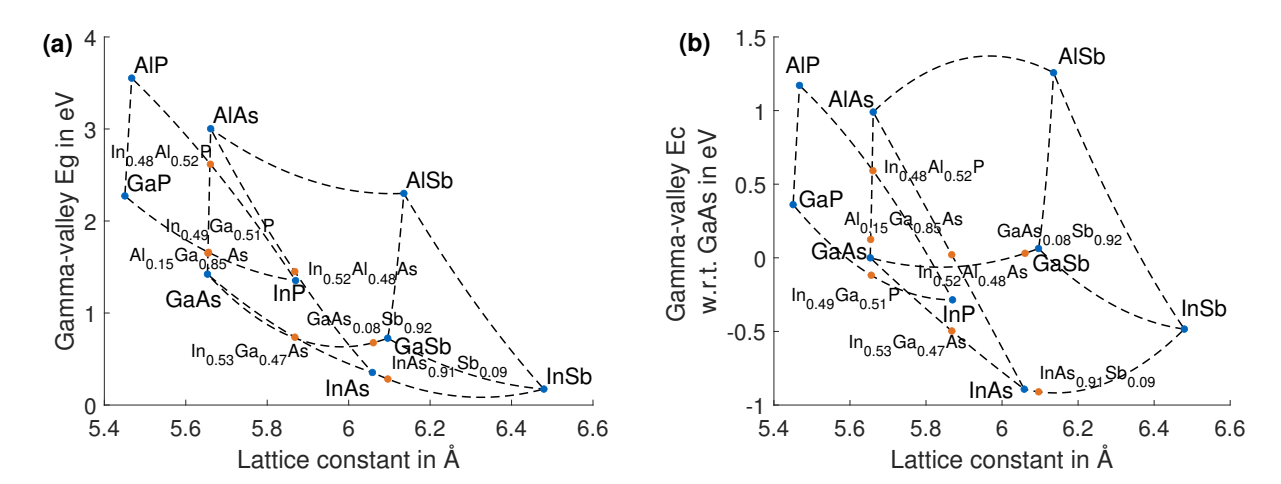


Figure 2.4 (a) Γ-valley bandgap energy E_g as a function of lattice constant for nine III-V binary compound semiconductors (blue points) and their lattice-matched ternary alloys (orange points) for a lattice temperature of 300 K. The dashed lines connect two binaries and represent ternary alloys of varying alloy composition. (b) Γ-valley conduction band edge energies of binaries (blue points) and lattice-matched ternaries (orange points) as a function of lattice constant. Here, the conduction band energy of GaAs was used as the reference value and is set to zero.

matrix element between the conduction band state S, built out of S orbitals, and the valence band state S, built out of S orbitals, is conventionally written as $S \mid \hat{p}_x \mid X = (im_0) \mathbf{P}$. Here, the parameter \mathbf{P} is the momentum matrix element between conduction and valence band and was defined by \mathbf{E} . Kane [260], [261]. From the second-order Taylor expansion, we can define an effective mass S or S orbitals, and the valence band state S, built out of S orbitals, and the valence band state S, built out of S orbitals, and the valence band state S, built out of S orbitals, and the valence band state S, built out of S orbitals, and the valence band state S, built out of S orbitals, and the valence band state S, built out of S orbitals, and the valence band state S orbitals, and the valence S orbitals, and the valence S orbitals S orbitals.

$$\frac{1}{m^*} = \frac{1}{m_0} + \frac{2}{m_0^2 k^2} \sum_{m \neq c} \frac{|\langle u_{c,\mathbf{0}}(r) | k \cdot \hat{p} | u_{m,\mathbf{0}}(r) \rangle|^2}{E_c(0) - E_m(0)}.$$
 (2.8)

In the following, we will focus on multiband $\mathbf{k} \cdot \mathbf{p}$ models, which are nowadays the standard model for bulk semiconductor bandstructure calculations. Well-known models are based on eight bands [258], [266]–[268] and include the spin-orbit coupling. Based on that, the conduction band edge effective mass can be expressed as [258]

$$\frac{1}{m^*} = \frac{1+2F}{m_0} + 2\mathbf{P}^2 \frac{E_{\rm g} + 2\Delta_{\rm SO}/3}{E_{\rm g}(E_{\rm g} + \Delta_{\rm SO})},$$
(2.9)

where $\Delta_{SO} = E_v^{LH} - E_v^{SO} = -E_v^{SO}$ is the spin-orbit splitting, E_g the bandgap energy and F the Kane parameter. The energy-dependent effective mass based on 14-band $\mathbf{k} \cdot \mathbf{p}$ calculations is given by [269]

$$m_{\perp}^{*}(E) = \frac{m_{\perp}^{*}(0)}{2\alpha' E} \left[1 - (1 - 4\alpha' E)^{\frac{1}{2}} \right],$$
 (2.10a)

$$m_{\parallel}^{*}(E) = m_{\parallel}^{*}(0)[1 + (2\alpha' + \beta')E]$$
 (2.10b)

with nonparabolicity parameters α' and β' [29]. Approximately, we can write $\alpha' = (E_g + \Delta_{SO}/3)^{-1}$.

Environmental influences such as temperature or strain on the semiconductor lattice can have a significant impact and have to be taken into account for the calculation of specific material parameters such as the energy band gap E_g or the effective mass m^* . Here, the temperature-dependent energy band gap E_g is fitted using the empirical Varshni formula [270]

$$E_{\rm g}(T) = E_{\rm g}(0) - \frac{\alpha_{\rm v} T^2}{T + \beta_{\rm v}},$$
 (2.11)

where α_v and β_v are the Varshni parameters.

In Fig. 2.4(a) and (b) the Γ -valley energy gap and conduction band edge energy E_c values of nine binary materials and specific lattice-matched ternary alloys are illustrated. Here, the Matlab functions **plot_Eg_materials** and **plot_Ec_materials** included in the *monacoQC* framework are used to generate the presented vector graphics.

All band parameters for the III-V compound semiconductors and their ternary alloys are extracted from [258]. The *monacoQC* framework could be easily extended towards quaternary alloys, e.g., AlGaInAs or GaInAsP, and other parameters, e.g., for the calculation of *X*- and *L*-valley energy gaps, could be incorporated.

An exact determination of the conduction band discontinuity in the quantum well heterostructure is important for the calculation of the eigenenergies E_i and wavefunctions ψ_i of the intersubband QC device system. Hence, to characterize the semiconductor bandstructure and the conduction band discontinuities in the quantum well heterostructure we apply the model-solid theory [271]. It is based on density-functional calculations, where the individual bulk semiconductors are described by ab initio pseudo-potentials. The calculated band energies are aligned on absolute energy values, which makes it possible to calculate CBOs by subtracting the conduction band edge energies of individual well and barrier materials. As bandgap values in density-functional theory cannot be predicted correctly, the experimentally measured bandgap values are used to get a more precise solution of the bandstructure [258]. Effects on the bandstructure due to pseudomorphic strain are intrinsically included in the model-solid theory. For the development of short-wavelength QCLs beyond the CBO limit of 0.52 eV in lattice-matched systems, the material composition of the mid-IR QCL material system InGaAs/InAlAs has to be strain-engineered. In this work, we investigate efficient DFG QCL designs based on strain-compensated InGaAs/InAlAs material systems. These exhibit a reduced thermally activated carrier leakage into continuum states above the barrier potentials and thus have an increased device performance [192]. Therefore, the composition of strain-compensated QC heterostructures during the growth process has to be selected carefully to avoid relaxation defects in the semiconductor lattice. This is achieved by balancing the compressive and tensile strain of well and barrier materials. The relative shift in conduction band energy due to hydrostatic strain is given by [271]

$$P_{\epsilon}^{c} = \Delta E_{c} = a_{c} \frac{\Delta \Omega}{\Omega}, \qquad (2.12)$$

where a_c is the hydrostatic deformation potential of the conduction band. The volume change arising from bi-axial strain $\Delta\Omega/\Omega={\rm Tr}(\epsilon)=2\epsilon_{\parallel}+\epsilon_{\perp}$ is calculated by the trace of the strain tensor ϵ . In a similar manner, the effective change in valence band position is obtained by [271]

$$P_{\epsilon}^{V} = \Delta E_{V} = a_{V} \frac{\Delta \Omega}{\Omega}, \qquad (2.13)$$

with the hydrostatic deformation potential a_v of the valence band. The effective bandgap energy under strain influence is then given by $E_g^s = E_g + P_\epsilon^c + P_\epsilon^v$. The influence of biaxial strain further leads to a split-up of heavy and light-hole valence band energy. This effect is illustrated in Fig. 2.3(b), where the calculated band edge energies of $In_xAl_{1-x}As$ taking into account biaxial strain due to lattice-mismatched growth on (001) InP is illustrated as a function of indium concentration. The relative energy offset for the three valence bands added to the lattice-matched value E_v is calculated by [265]

$$E_{\rm v}^{\rm HH} = -P_{\epsilon}^{\rm v} - Q_{\epsilon} \,, \tag{2.14a}$$

$$E_{\rm v}^{\rm LH} = -P_{\epsilon}^{\rm v} + \frac{1}{2} \left(Q_{\epsilon} - \Delta_{\rm SO} + \sqrt{\Delta_{\rm SO}^2 + 2\Delta_{\rm SO} Q_{\epsilon} + 9Q_{\epsilon}^2} \right), \tag{2.14b}$$

$$E_{\rm v}^{\rm SO} = -P_{\epsilon}^{\rm v} + \frac{1}{2} \left(Q_{\epsilon} - \Delta_{\rm SO} - \sqrt{\Delta_{\rm SO}^2 + 2\Delta_{\rm SO} Q_{\epsilon} + 9Q_{\epsilon}^2} \right)$$
 (2.14c)

with

$$Q_{\epsilon} = -b_{s}(\epsilon_{\parallel} - \epsilon_{\perp}). \tag{2.15}$$

Here, the shear deformation potential b_s is used. In Fig. 2.5(a), the CBO of the material system InAlAs/InGaAs on InP for $x \in [0,1]$ is depicted. As can be seen here, the material composition choice of $In_xAl_{1-x}As$ has a significant influence on the material system CBO value, whereas the indium concentration variation in $In_xGa_{1-x}As$ does not affect the CBO value considerably. In QCL device engineering it would make sense to tune the target CBO value by the $In_xAl_{1-x}As$ composition and balance the strain in the active period by adjusting the indium concentration of the $In_xGa_{1-x}As$ well materials.

Sugawara *et al.* [265] investigated the effects of strain on the effective mass at the conduction band edge and derived a model based on an 8-band $\mathbf{k} \cdot \mathbf{p}$ theory for the calculation of effective masses in strained materials.

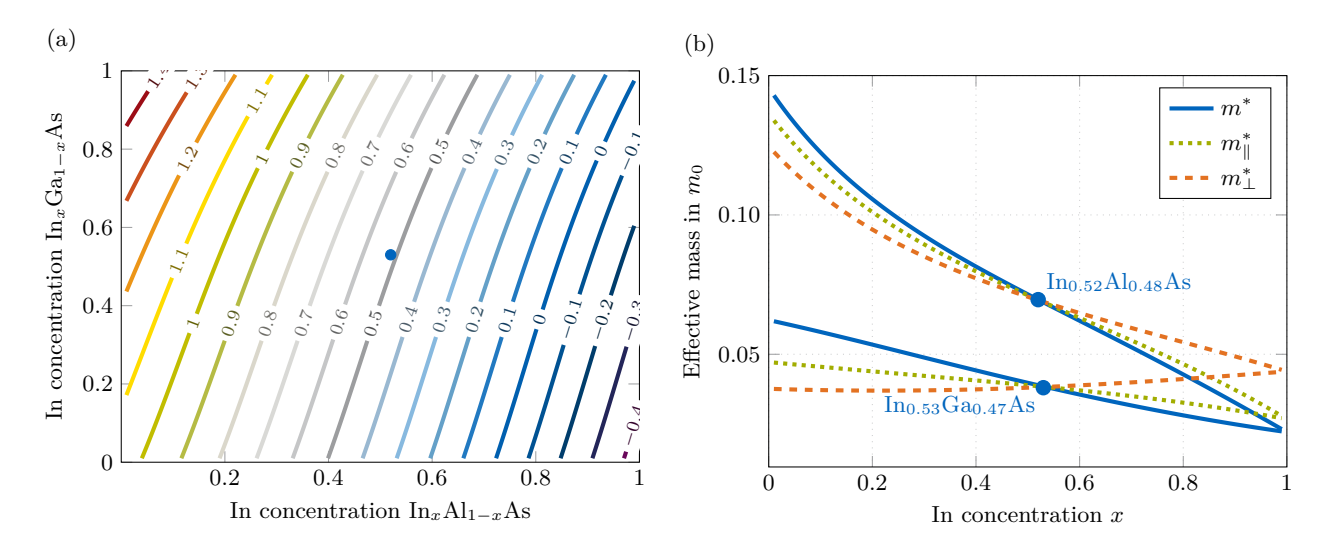


Figure 2.5 Calculated strain effects for the material system InGaAs/InAlAs at 300 K on an InP substrate with (001) orientation. (a) Contour plot of the CBO of the $In_xGa_{1-x}As/In_xAl_{1-x}As$ material system for indium (In) concentrations $x \in [0, 1]$. The lattice-matched material system $In_{0.52}Ga_{0.48}As/In_{0.53}Al_{0.47}As$ is represented by the blue dot. (b) Effective mass m^* at the Γ-point of the materials $In_xGa_{1-x}As$ and $In_xAl_{1-x}As$ for $x \in [0, 1]$. Strain effects lead to an anisotropic effective mass with different values for growth direction m_{\perp}^* and in-plane m_{\parallel}^* values.

Here, it was demonstrated that the electron effective mass at the conduction band edge becomes anisotropic for $In_xGa_{1-x}As/InP$ quantum wells. The effective mass for growth direction m_{\perp}^* and in-plane m_{\parallel}^* effective mass at the conduction band edge are calculated with [265]

$$\frac{1}{m_{\parallel}^*} = \frac{1 + 2F}{m_0} + \frac{2\mathbf{P}^2}{3} \left[\frac{(\sqrt{2}\alpha - \beta)^2}{E_{\rm g} + P_{\epsilon}^c - E_{\rm v}^{\rm LH}} + \frac{(\sqrt{2}\beta + \alpha)^2}{E_{\rm g} + P_{\epsilon}^c - E_{\rm v}^{\rm SO}} \right],\tag{2.16a}$$

$$\frac{1}{m_{\perp}^{*}} = \frac{1 + 2F}{m_{0}} + \frac{\mathbf{P}^{2}}{3} \left[\frac{3}{E_{g} + P_{\epsilon}^{c} - E_{v}^{HH}} + \frac{(\sqrt{2}\alpha + \beta)^{2}}{E_{g} + P_{\epsilon}^{c} - E_{v}^{SO}} + \frac{(\alpha - \sqrt{2}\beta)^{2}}{E_{g} + P_{\epsilon}^{c} - E_{v}^{LH}} \right], \tag{2.16b}$$

where the two variables α and β represent the strain influence. In the case of lattice-matched material systems with $\alpha=1$, $\beta=0$ and $E_v^{\rm HH}=E_v^{\rm LH}=E_v=0$, we obtain an isotropic effective mass at the band edge $(m_{\perp}^*=m_{\parallel}^*)$ and the effective mass calculation gets reduced to the simplified formula of Eq. (2.9). Effective mass m^* calculations at the conduction band edge for the materials ${\rm In}_x{\rm Ga}_{1-x}{\rm As}/{\rm In}_x{\rm Al}_{1-x}{\rm As}$ on an InP substrate at $T=300\,{\rm K}$ are illustrated in Fig. 2.5(b). Biaxial strain leads to a breakdown of the isotropy in effective mass. Moving away from the lattice matched system ${\rm In}_{0.52}{\rm Al}_{0.48}{\rm As}$ and ${\rm In}_{0.53}{\rm Ga}_{0.47}{\rm As}$ on InP results in a divergence of effective mass for growth direction and in-plane effective mass with varying indium concentrations. All functions to calculate the here presented semiconductor parameter properties are defined and implemented in the material classes consisting of a base class **material** and the subclasses for binary compounds and ternary alloys.

In Listing 2.1, an example script for the setup generation of a THz QCL setup [73] used for HFC generation is depicted. Here, we define a ternary barrier material **AlGaAs** with an **Al** concentration of 0.15 and combine it with the binary well material **GaAs**. The active period consists of a sequence of barrier and well materials, where the injection well of length 183 nm is **Si**-doped with 2.3×10^{16} cm⁻³. The active waveguide with a length of 5 mm is specified by an effective refractive index of 3.6 and a power loss coefficient of 13 cm^{-1} . The simulation scenario is specified with a temperature of 80 K, a bias field of 49 kV cm⁻¹ and a simulation endtime of 50 ps. Here, the simulation basis for the Schrödinger-Poisson solver is set to a tight-binding basis, which will be introduced in the following section [35], [36].

Listing 2.1 Code snippet of the Matlab script for the THz HFC-QCL setup in [73].

```
%% define scenario and device
% barrier material
```

```
b = AlGaAs(0.15);
% well material
w = GaAs();
% set up period
period = { ...
    layer(b, 58); ...
    layer(w, 183, 2.3e16); ...
    layer(b, 41); ...
    layer(w, 92); ...
    layer(b, 39); ...
    layer(w, 115); ...
    layer(b, 29); ...
    layer(w, 106); ...
    };
% number of periods
num_periods = 5;
% set up device
d = device(period, num_periods);
% set waveguide
% effective refractive index.
neff = 3.6;
d.n_eff = neff;
r = (neff - 1) / (neff + 1);
w = waveguide(5e-3, 1300, [], 1, r);
d.set_waveguide(w);
% temperature in K
temperature = 80;
% bias field in kV/period
V = 49e-6;
l_period = d.l_period * 1e-8;
% bias field in kV/cm
bias = V / l_period;
% Simulation time in s
t_sim = 5e-11;
% Using tight-binding basis for SP simulations
basis_sp = 'tb';
% Number of wavefunctions
num_wavefct = 5;
% set up scenario
s = scenario(temperature, bias, t_sim, num_wavefct, basis_sp);
```

2.2 Schrödinger-Poisson Solver

Intersubband QC devices consist of multiple quantum wells, where energetic alignment between LLL and ULL in the conduction band is specified by the layer composition of the well and barrier materials. For the development and optimization of such devices with their optical transition at a characteristic wavelength, a careful design of the quantized electron states in the heterostructure is crucial. Here, the optical and non-radiative properties can be analyzed and improved by efficient wavefunction engineering. Using the stationary Schrödinger equation, the eigenenergies and wavefunctions are calculated, and by solving the Poisson equation, one can take into account additional space charge effects.

Bastard [262] derived a concept for heterostructures based on the envelope function model, where the atomic wavefunction is divided into two parts. Firstly, the fast-oscillating Bloch functions $u_{v_i,0}(\mathbf{r})$ in band v have the same periodicity as the crystal potential and are assumed to be the same in the well and barrier layers as

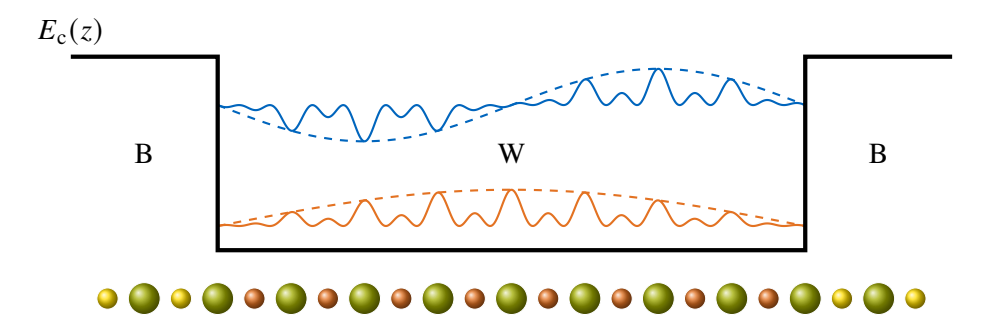


Figure 2.6 Schematic illustration of full eigenstate wavefunctions $\Psi_i = \phi_{i,k} u_{c_i,0}$ (solid) and envelope wavefunctions $\phi_{i,k}$ (dashed) in the conduction band of a quantum well consisting of barrier material B and well material W. Here, the materials B and W consist of two atoms (B: green and yellow; W: green and orange), respectively. The conduction band energy $E_c(z)$ changes depending on the growth direction z.

both materials have a similar lattice constant. Secondly, a slowly varying envelope function $\phi_{i,k}(r)$ is used to describe the impact of the heterostructure. The combination results in the atomic wavefunction, written as

$$\Psi(\mathbf{r}, \mathbf{k}) = \sum_{i} \phi_{i, \mathbf{k}}(\mathbf{r}) u_{\nu_i, 0}(\mathbf{r}). \qquad (2.17)$$

Within the multiple quantum well heterostructure of QC devices, we distinguish between in-growth direction z and in-plane directions $r = [x, y]^T$. Here, charge carriers move freely in xy-plane and are only confined in z-direction. The in-plane wavevector in the xy-plane can be summarized as $k = [k_x, k_y]^T$ and the material composition and thus the potential V and the effective masses m^* only vary in growth direction. With this, we can make the following ansatz for the slowly varying envelope function

$$\phi_{i,k}(\mathbf{r}) = \frac{1}{\sqrt{S}} \psi_{i,k}(z) \exp(ik_x x + ik_y y). \qquad (2.18)$$

Here, $\psi_{i,k}(z)$ is the 1D envelope wavefunction confined in growth direction. S denotes the in-plane cross-sectional area and is required to fulfill the normalization condition $\int |\psi_{i,k}(z)|^2 dz = 1$. In Fig. 2.6, the wavefunctions Ψ_i and corresponding envelope wavefunctions $\phi_{i,k}$ for the two lowest-lying energy eigenstates in the conduction band of a quantum well are schematically illustrated. For the treatment in the vicinity of the Γ -point in the conduction band we utilize the framework of the Ben Daniel-Duke model, where the coupling between conduction and valence band is neglected. The resulting stationary Schrödinger equation is given by

$$\left[\frac{\hbar^2 k^2}{2m^{\parallel}(z)} - \frac{\hbar^2}{2} \partial_z \frac{1}{m^*(z)} \partial_z + V(z) - E_{i,k}\right] \psi_{i,k}(z) = 0, \qquad (2.19)$$

with k-dependent eigenenergies $E_{i,k}$ and wavefunctions $\psi_{i,k}(z)$. By neglecting the z dependence of the in-plane effective mass $m^{\parallel}(z)$, the Schrödinger equation can be simplified to 1D, and is given by

$$\left[-\frac{\hbar^2}{2} \partial_z \frac{1}{m^*(z)} \partial_z + V(z) - E_i \right] \psi_i(z) = 0.$$
 (2.20)

Taking the free in-plane electron motion into account, we obtain for the eigenenergies $E_{i,k} = E_i + E_{kin}$, with the kinetic energy

$$E_{\rm kin} = \frac{\hbar^2 k^2}{2m^{\parallel}} \,. \tag{2.21}$$

Widely used numerical approaches for solving the 1D Schrödinger equation are based on the transfer matrix method [183], [272]–[274] or use the finite difference scheme [275], [276]. Here, two important requirements are fulfilled, namely the robustness and computational efficiency of the numerical approaches. The latter is also very important as we have to investigate different bias points and various QC device configurations for

detailed design optimization. In the following, we will focus on the TMM, since it is easier to include effects like nonparabolicity. Furthermore, one obtains an exact treatment of the potential steps at the well and barrier interfaces of the heterostructures. Within the TMM an arbitrary potential is approximated by dividing it into piecewise constant or linear segments, for which analytical solutions of the 1D Schrödinger equation exist, e.g., complex exponential solutions for piecewise constant segments [272], [273] and Airy functions for linear segments [273]. Biased QCL heterostructures can, in general, be divided into segments of constant effective mass and piecewise linear potential, if we neglect space charge and nonparabolicity effects. The Airy function approach seems to be the appropriate choice here, but proves to be computationally quite complex and poses numerical problems when segments with nearly flat potentials are considered [277], [278].

In our *monacoQC* framework, we have decided to implement the exponential transfer matrix scheme. Here, the structure is divided into segments of piecewise constant potential and the potential jumps that occur between the well and barrier layers are located at the segment boundaries. The wavefunction solution in one segment is given by

$$\psi_n(z) = A_n \exp[ik_n(z - z_n)] + B_n \exp[-ik_n(z - z_n)]. \tag{2.22}$$

Here, the segment n is described using a spatial discretization $z_n \le z \le z_n + \Delta_n = z_{n+1}$ and constant values for $V(z_n) = V_n$ and $m^*(z_n) = m_n^*$. The wavenumber is $k_n = \sqrt{2m_n^*(E - V_n)}/\hbar$ for $E > V_n$ and becomes imaginary $k_n = i\sqrt{2m_n^*(V_n - E)}/\hbar$ for $E < V_n$. Matching conditions have to be specified for potential steps and effective mass discontinuities [29], [183], [263] and can be written as

$$\psi(z_0^+) = \psi(z_0^-), \left[\partial_z \psi(z_0^+)\right] / m^*(z_0^+) = \left[\partial_z \psi(z_0^-)\right] / m^*(z_0^-),$$
(2.23)

with z_0^+ and z_0^- being the positions directly to the right and left of the potential step describing the discontinuity [263]. Using Eq. (2.22) and by applying the matching conditions, the relation between amplitudes $[A_n, B_n]^T$ at neighboring segments are determined as

$$\begin{pmatrix} A_{n+1} \\ B_{n+1} \end{pmatrix} = T_{n,n+1} \begin{pmatrix} A_n \\ B_n \end{pmatrix}. \tag{2.24}$$

Here, we further use a symmetric transfer matrix to improve the accuracy of the exponential matrix scheme, which is given by

$$T_{n,n+1} = T_{n+1} \left(\frac{\Delta_n}{2}\right) T_{n \to n+1} T_n \left(\frac{\Delta_n}{2}\right) = \begin{pmatrix} \frac{\tilde{k}_{n+1} + \tilde{k}_n}{2\tilde{k}_{n+1}} e^{ik_n^+ \Delta_n} & \frac{\tilde{k}_{n+1} - \tilde{k}_n}{2\tilde{k}_{n+1}} e^{-ik_n^- \Delta_n} \\ \frac{\tilde{k}_{n+1} - \tilde{k}_n}{2\tilde{k}_{n+1}} e^{ik_n^- \Delta_n} & \frac{\tilde{k}_{n+1} + \tilde{k}_n}{2\tilde{k}_{n+1}} e^{-ik_n^+ \Delta_n} \\ \frac{\tilde{k}_{n+1} - \tilde{k}_n}{2\tilde{k}_{n+1}} e^{ik_n^- \Delta_n} & \frac{\tilde{k}_{n+1} - \tilde{k}_n}{2\tilde{k}_{n+1}} e^{-ik_n^+ \Delta_n} \end{pmatrix}$$
(2.25)

with $k_n^{\pm} = (k_n \pm k_{n+1})/2$, $k_n = \sqrt{2m_n^*(E - V_n)}/\hbar$ and $\tilde{k}_n = k_n/m_n^*$ [29], [183]. The symmetric transfer matrix can be divided into two submatrices, one for segments of flat potential $T_n(\frac{\Delta_n}{2})$ and one for potential steps at segment interfaces $T_{n \to n+1}$. The former is obtained by

$$T_n(\frac{\Delta_n}{2}) = \begin{pmatrix} e^{ik_n \frac{\Delta_n}{2}} & 0\\ 0 & e^{-ik_n \frac{\Delta_n}{2}} \end{pmatrix}, \tag{2.26}$$

and the latter is given by

$$T_{n \to n+1} = \frac{1}{2\tilde{k}_{n+1}} \begin{pmatrix} \tilde{k}_{n+1} + \tilde{k}_n & \tilde{k}_{n+1} - \tilde{k}_n \\ \tilde{k}_{n+1} - \tilde{k}_n & \tilde{k}_{n+1} + \tilde{k}_n \end{pmatrix}. \tag{2.27}$$

If the structure is divided into N segments, the amplitudes on the left boundary A_N , B_N are calculated from the amplitudes on the right boundary A_0 , B_0 using Eq. (2.24). The result can be written as

$$\begin{pmatrix} A_N \\ B_N \end{pmatrix} = T_{N-1,N} T_{N-2,N-1} \cdots T_{0,1} \begin{pmatrix} A_0 \\ B_0 \end{pmatrix} = \begin{pmatrix} T_{11} & T_{12} \\ T_{21} & T_{22} \end{pmatrix} \begin{pmatrix} A_0 \\ B_0 \end{pmatrix}. \tag{2.28}$$

Finally, an adequate boundary condition for the chosen wavefunction basis has to be selected. Available basis sets in the open-source solver library are extended states (ext) [29], tight-binding states (tb) [35], [36] and

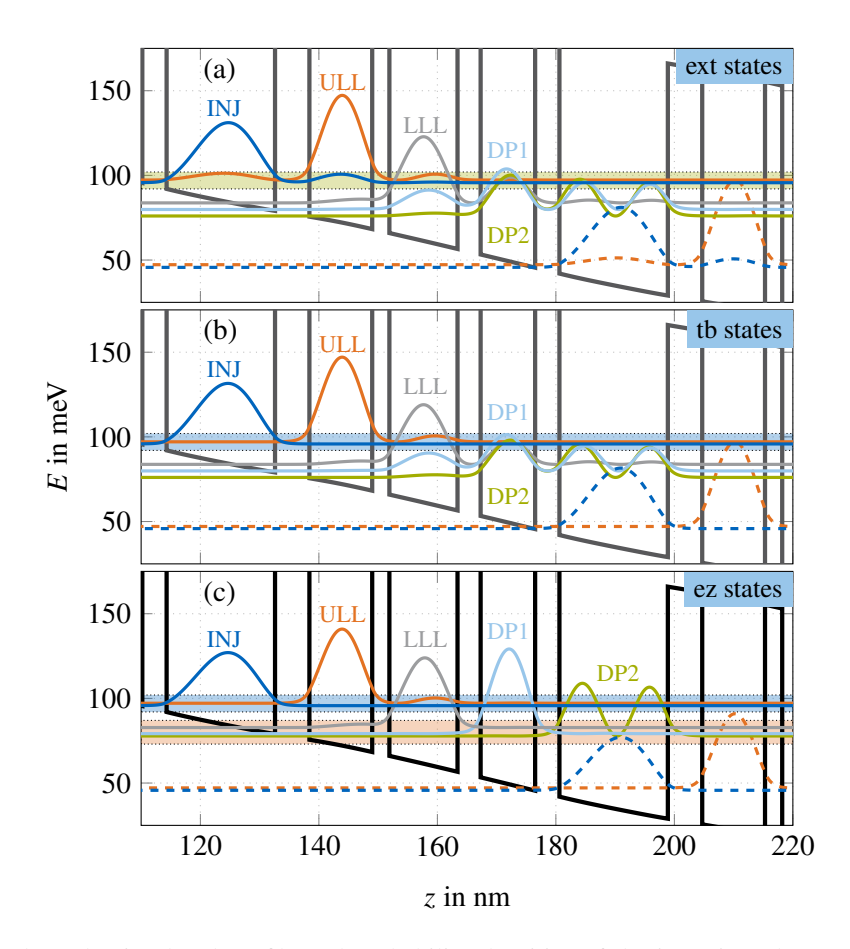


Figure 2.7 Calculated conduction band profile and probability densities of the investigated THz QCL structure based on GaAs/Al_{0.15}Ga_{0.85}As with an optical transition frequency of around 3 THz and for a temperature of 80 K. The layer sequence (in nm) of one active period is 4.1/18.3/5.8/10.6/2.9/11.5/3.9/9.2. Barriers are in boldface, for the underlined layers a doping density of 2.3×10^{16} cm⁻³ (n-type) is assigned and the applied bias is 50 mV/period. Comparison of three Schrödinger-Poisson solutions based on the extended (a) [183] and tight-binding (b) potential [35], [36] and (c) EZ-transformation [184].

EZ-states (ez) [184]. In general, the three basis state configurations represent different levels of wavefunction localization, where an appropriate choice is important to adequately resolve specific effects in carrier transport simulations, such as resonant tunneling across injection barriers in THz QCLs [35], [184]. The transition from extended states to highly localized states is schematically illustrated in Fig. 2.7, where the conduction band profile together with the probability densities in the three basis state configurations (ext, tb, ez) is presented for a THz QCL design featuring a diagonal transition [73]. In comparison to extended states, where the full potential V is used for the calculation of the eigenstates, the QC heterostructure is divided into modules within the tightbinding approach. Each module comprises an active period, which is separated from its neighboring period by the thickest barrier. The wavefunction is then calculated using the so-called tight-binding potential $V_{\rm tb}$, which is schematically illustrated in Fig. 4.1 for a two-well THz QCL design. To model the carrier injection across thick barriers correctly, which is governed by incoherent tunneling between near-resonant states, tight-binding states (highlighted with a blue rectangle in Fig. 2.7(b)) are advantageous against extended states (highlighted with a green rectangle in Fig. 2.7(a)) [35], [36]. Additional coherences arising from closely aligned energetic levels can be taken into account by applying an EZ-transformation [184]. Here, eigenstates separated by an energy of less than 5 meV are summarized within a multiplet of states and the term EZ refers to the energy E and the position z within the subspace of the multiplet. These subsets of eigenstates are diagonalized with respect to the dipole moment operator [184]. A transformed triplet of states within the investigated THz QCL configuration is schematically illustrated in Fig. 2.7(c) by an orange rectangle.

For the simulation of intersubband QC heterostructures, we can restrict ourselves to a limited number of periods, as we can apply periodic boundary conditions within the carrier transport simulations. The default

value for the number of periods within the monacoQC framework is set to **num_periods** = 5 in accordance with the input values for the external EMC tool. For the wavefunction calculations, we can even further reduce the simulation domain to a single period and copy the relevant wavefunctions to the adjacent periods. Using the extended state configuration, for example, all important wavefunctions can be found within an energy period $E_{\rm p}$ corresponding to the bias drop over one period. The wavefunctions of the adjacent periods are then simply obtained by shifting the original wavefunctions in position using a multiple of the period length L_p and the corresponding eigenenergies by adding a multiple of the energy period $E_p = V(z_0) - V(z_0 - L_p)$. At one period right to the simulation window, the wavefunctions are given by $\psi_{i'}(z) = \psi_i(z - L_p)$ and the eigenenergies by $E_{i'} = E_i - E_p$. Furthermore, we have to specify appropriate wavefunction values at the boundaries of our simulation domain. Here, we choose decaying solutions with $A_0 = B_N = 0$, corresponding to $T_{22} = 0$. The remaining energy-dependent matrix elements $T_{11}(E)$, $T_{12}(E)$ and $T_{21}(E)$ can be found for the specific eigenenergies by applying the so-called shooting method. Therefore, we have to divide the energy period E_p into a limited number of subintervals Δ_E and obtain the discrete energy points $E_j = E_0 + j\Delta_E$. Here, E_0 is the starting energy point in the energy grid. To obtain a valid solution at the boundaries of our simulation windows, the eigenenergies must fulfill $B_N(E_i)B_N(E_{i+1}) < 0$ for a given energy interval $E_i \cdots E_{i+1}$. If an energy interval for an eigenenergy solution is found, we apply the root-finding function fzero from the Matlab standard library to obtain a more accurate solution using a finer energy subgrid between $[E_i, E_{i+1}]$.

The aforementioned parameters, e.g., E_p or the values for A_0 , B_0 , are defined in a class **boundary_condition**. Here, we use a plugin structure consisting of an abstract base class **boundary_condition** and different boundary conditions for the solution of extended states (**boundary_condition_ext**), tight-binding states (**boundary_condition_ext**), EZ-states (**boundary_condition_ext**) and for QCDs (**boundary_condition_QCD**). For the creation of a certain boundary condition object the static method **create_instance** must be called. This method expects the simulation scenario including the basis configuration for the boundary condition. Additional input arguments for the specification of important parameters are a device instance and an object of class **sim_constants**, which comprises all simulation constants for the appropriate description of the TMM system, e.g., a vector with the spatial grid z or the potential V. Instances of the two classes **sim_constants** and **boundary_condition** serve as the main properties of the solver class **tm_solver**.

In the predefined energy period E_p , more than the number of relevant wavefunctions could be found. In this case, an automated selection method for the most strongly bound wavefunctions would be useful. Therefore, we can calculate the energy of state i with respect to the conduction band edge

$$\tilde{E}_i = E_i - \int V |\psi_i|^2 \, \mathrm{d}z \tag{2.29}$$

to categorize the wavefunctions ψ_i and obtain a measure for the significance of a state i in the carrier transport simulations.

The electronic properties and thus the functionality of semiconductor materials, e.g., p-type and n-type conductors with different resistivity, can be engineered over a wide range by changing the charge carrier densities. Therefore, charge carriers in intersubband QC devices are provided by doping the active region with a donor material such as Si. By applying a bias voltage the unbound electrons are distributed across the whole active period, while the ionized donor atoms are localized in a relatively small area, e.g., the active well. The separation process of carriers and the resulting space charges can lead to a considerable bending effect of the conduction band, which has a significant influence on the position and shape of eigenstates and will further affect the carrier transport simulation results. The total potential used within Eq. (2.20) is given by

$$V(z) = E_{c}(z) - E_{p}z/L_{p} + \tilde{V}(z), \qquad (2.30)$$

where $E_c(z)$ is the unbiased conduction band profile, E_pz/L_p gives the impact of the applied bias and $\tilde{V}(z)$ is the additional electrostatic potential arising from the space charges. The abstract solver class **poisson_solver** takes care of the mean-field treatment of the electron-electron interaction, referred to as Hartee approximation. Here, the additional electrostatic potential is determined by solving the Poisson equation [274], [279]

$$e^{-1}\partial_z \left[\varepsilon(z)\partial_z \tilde{V}(z) \right] = e \left[n_{\mathcal{D}}(z) - \sum_i n_i^s |\psi_i(z)|^2 \right], \tag{2.31}$$

where e is the elementary charge and $\varepsilon(z)$ is the permittivity, which varies for different material compositions and exhibits periodicity due to the repetitions in multiple heterostructures. Furthermore, the concentration of the positively charged donor ions is given by $n_{\rm D}(z)$ and $n_i^{\rm S}$ denotes the electron sheet density of level i together with the wavefunction $\psi_i(z)$. The electrostatic potential energy fulfills the condition $\tilde{V}(z_0) = \tilde{V}(z_0 + L_{\rm p})$. Furthermore, $\partial_z \tilde{V}(z_0) = \partial_z \tilde{V}(z_0 + L_{\rm p})$ in accordance with the charge neutrality in one period $(\int_{z_0}^{z_0 + L_{\rm p}} \rho \, \mathrm{d}z = 0)$, and therefore has the same periodicity as $E_{\rm c}(z)$. To solve Eq. (2.31), we use the finite difference method, written as [29]

$$\tilde{s}_{n}\tilde{V}_{n-1} - \tilde{d}_{n}\tilde{V}_{n} + \tilde{s}_{n+1}\tilde{V}_{n+1} = e\left[n_{D,n} - \sum_{i} n_{i}^{s} |\psi_{i,n}|^{2}\right], \tag{2.32}$$

with

$$\tilde{s}_{n} = \frac{1}{2e\Delta_{z}^{2}} (\varepsilon_{n-1} + \varepsilon_{n}),
\tilde{d}_{n} = \frac{1}{2e\Delta_{z}^{2}} (\varepsilon_{n-1} + 2\varepsilon_{n} + \varepsilon_{n+1}).$$
(2.33)

Here, we can exploit the periodicity of \tilde{V} and only have to solve Eq. (2.32) for a single period $z \in [z_0, z_0 + L_p]$. The given electrostatic potential energy segment can then be easily copied into the entries of the total potential vector at which the other considered periods are located. The resulting total vector V is inserted back into the Schrödinger equation to find the wavefunction solutions. The equation system can be treated in matrix notation $M\tilde{V} = \rho$, where \tilde{V} and ρ contain the elements \tilde{V}_n and ρ_n and M is a tridiagonal matrix with the finite difference coefficients \tilde{s}_n and \tilde{d}_n . Within the monacoQC framework, this linear equation system is solved using standard Matlab commands.

In QCL structures, the sheet densities n_i^s of the individual levels i used in Eq. (2.31) are usually determined using detailed carrier transport simulations [33]–[35]. To characterize the significance of space charge effects, we compare two simulation scenarios for a terahertz QCL [280]. Firstly, we solve only the Schrödinger equation and neglect the electrostatic potential energy \tilde{V} (dashed lines). Secondly, we solve the full Schrödinger-Poisson equation system by including sheet densities n_i^s extracted from our in-house EMC approach (solid lines). As illustrated in Fig. 2.8(a), considerable band bending effects due to space charge effects are present in the SP solution including the carrier transport simulation results from EMC. Here, the localized positively charged donor ions reside in the well layer around $z = 100 \, \text{nm}$, whereas the electrons are distributed across multiple subbands.

The simulation of photovoltaic QCDs differs from that of QCLs. Here we assume an operation in thermal equilibrium for zero bias and without illumination. Using the 2D density of states $n_i^{\rm 2D} = m_i^{\parallel}/(\pi\hbar^2)$ the electron sheet density in subband i at temperature T is then calculated by

$$n_i^{\rm s} = \frac{m_i^{\parallel}}{\pi \hbar^2} k_{\rm B} T \ln\{1 + \exp[(\mu_{\rm c} - E_i)/(k_{\rm B} T)]\}, \qquad (2.34)$$

with the quantized subband energy E_i , the effective subband masses m_i^{\parallel} containing non-parabolicity effects. Here $k_{\rm B}$ denotes the Boltzmann constant. The chemical potential $\mu_{\rm c}$ can be calculated by

$$n^{s} = \int_{z_0}^{z_0 + L_p} n_{D} dz = \sum_{i} n_{i}^{s}, \qquad (2.35)$$

where the charge neutrality condition within one period holds. Simulation results for a THz QCD [281] are illustrated in Fig 2.8(b). Here, we compare the SP-solver solutions of included space charge effects resulting from thermally filled subbands (solid lines) with no space charge effects (dashed lines) and obtain similar tendencies of band bending effects as for the THz QCL.

For a simulation setup consisting of a **device** and **scenario** object, as specified for a THz-QCL in Listing 2.1, a solver instance can be created with the constructor of the class **tm_solver**. The solution of the SP equation system is obtained with the solver method **solve**. The corresponding Matlab commands are given by

>> solver = tm_solver(d,s); [eig,cond] = solver.solve(emc_dist, eig_old)

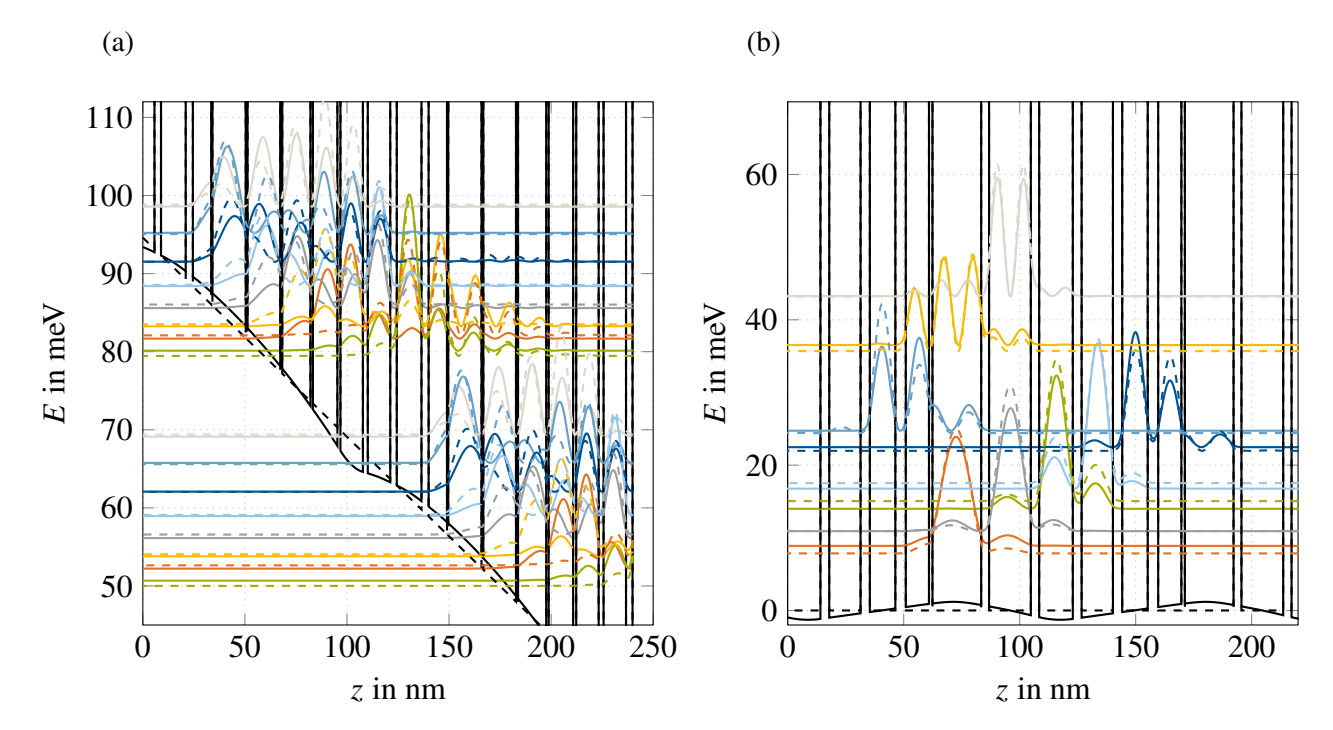


Figure 2.8 (a) Conduction band profile and probability densities of a THz QCL [280]. Shown are the results without considering space charge effects (dashed lines) and for space charge effects taken into account. Here, the level occupations are extracted from EMC simulation results (solid lines). (b) Conduction band profile and probability densities of a THz QCD [281]. Shown are the results without considering space charge effects (dashed lines) and for space charge effects taken into account, assuming thermally occupied subbands (solid lines).

In the following, we will explain the **solve** method in more detail. For better illustration, the original Matlab code snippet is shown in Listing 2.2. Based on the given setup and boundary conditions, this method iteratively solves the Schrödinger-Possion equation system until convergence is reached and returns an object of class **eigenstates** and of class **conduction_band**, respectively.

At the beginning, it is clarified, whether **carrier_distribution** and **eigenstates** instances have been passed as input arguments to the function. Here, we use a function handle **func_carr_distr** with an input argument of type **eigenstates** to generate the **carrier_distribution** instance. The classes **emc_carrier_distribution**, **eqdist_carrier_distribution** and **thermal_carrier_distribution** are available for the generation of predefined carrier distributions, based either on EMC results, an equal or thermal distribution. To facilitate the easy integration of carrier transport simulation results from other approaches, e.g., NEGF, into the Schrödinger-Poisson library, we again use a plugin structure, where the static class method **generate** is inherited from the abstract **frontend** class.

The given objects **func_carr_distr** and **eig_system_old**, e.g., carrier transport simulation results and eigenstate solutions from a previous simulation run, are used to calculate an initial vector containing the charge density. This is done within the static method **get_rho** of the **poisson_solver**. As an additional input argument the **sim_constants** object is required, which contains the vector with the charge density of the localized donors. The loop starts with the calculation of \tilde{V} using the static method **calc_potential** of the **poisson_solver** class. The total potential vector V will be saved in a **conduction_band** instance. The method **calc_wavefcts** takes care of the eigenstates calculation in the central period and returns the wavefunctions ψ , eigenenergies E and the corresponding energies with respect to the conduction band edge \tilde{E} . An important aspect of self-consistent charge carrier transport simulations is the inclusion of nonparabolicity corrections in the scattering rate calculations [29]. This is managed within our in-house EMC approach by the use of an averaged in-plane effective mass for subband i [282], [283]

$$m_i^{\parallel} = \int m^*(z) \{ 1 + [2\alpha'(z) + \beta'(z)] [E_i - V(z)] \} |\psi_i(z)|^2 dz.$$
 (2.36)

The averaged in-plane effective mass vector m^{\parallel} is passed to the class method $\operatorname{gen_eig_system}$ together with the other vectors mentioned. The returned object $\operatorname{eig_system}$ comprises the quantum-mechanical description of the complete systems with, e.g., all wavefunctions ψ , the system Hamiltonian H_s and effective masses m^* in $\operatorname{num_periods} - 1$ periods. The object $\operatorname{cond_profile}$ contains the total potential V consisting of conduction band profile and band bending effects due to space charges. Within the while loop, the SP equation system is solved iteratively until the relative change in charge density

$$\Delta \rho = \frac{\langle \rho - \rho_{\text{old}}, \rho - \rho_{\text{old}} \rangle}{\langle \rho, \rho \rangle}, \qquad (2.37)$$

falls below a certain value. A predefined value 1×10^{-5} is used in the **tm_solver** and is stored in the property **error**. If convergence is reached, the quantum-mechanical description **eig_system** and the total potential information **cond_profile** are returned and can be used as input data for the multi-domain simulation approach.

If the appropriate number of wavefunctions, which is specified in the **scenario**, cannot be found, the **solve** method will throw an error. In this case, one can, for example, adjust the **tm_solver** property **num_E**, which is the number of energy points within the TMM, or modify the energy period **E_period** and the vector index of the minimum energy point **ind_E_min** within the **boundary_condition** instance. A small change in the TMM parameter space can help to find the desired number of wavefunctions.

Listing 2.2 Code snippet of the solve method of the solver class tm_solver.

```
function [eig_system, cond_profile] = ...
                  solve(obj, func_carr_distr, eig_system_old)
 % Function handle for carrier distribution.
 if ~exist("func_carr_distr")
    func_carr_distr = @(eig_st) ...
    eqdist_carrier_distribution. ...
    generate(obj.sim_const.num_wavefct);
  end
 % Eigenstate instance from the previous simulation run.
 if ~exist('eig_system_old', 'var')
    eig_system_old = [];
  end
 % Calculate vector with charge density.
 rho = poisson_solver.get_rho(obj.sim_const, ...
    func_carr_distr, eig_system_old);
 % Setting up convergence parameter.
  err = 2 * obj.error;
 % SP loop
  while (err > obj.error)
   % Solve Poisson equation: additional electrostatic potential.
    dV = poisson_solver.calc_potential(obj.sim_const, rho);
   % Calculate total potential in J.
    V = obj.sim_const.vec_V_0 + dV;
   % Generate object of conduction band profile.
    cond_profile = conduction_band(obj.sim_const.vec_z_tm, V);
   % Calculate eigenenergies and wavefunctions.
    [psi, E, m_E_eff, E_bound_CB0] = obj.calc_wavefcts(V);
   % Check the number of found wavefunctions.
    if (length(E_bound_CBO) < obj.sim_const.num_wavefct)</pre>
      error(['Could_not_find_the', ...
        '_appropriate_number_of_wavefunctions!']);
    end
```

```
% Returns object of system eigenstates.
eig_system = obj.gen_eig_syst(psi, E, m_E_eff, ...
    E_bound_CBO, cond_profile);

rho_old = rho;
% Calculate updated charge density from new eigenstates.
rho = poisson_solver.get_rho(obj.sim_const, ...
    func_carr_distr, eig_system);
% Termination condition (relative change in sheet density).
err = sum((rho - rho_old).^2) / sum(rho.^2);
disp(num2str(err));
end
end
```

2.3 Bayesian Optimization and Gaussian Processes

For the optimization of quantum cascade devices, the existing simulation tools (e.g., DM-EMC or NEGF) can be used [18], [21], [22], [24]. Since these modeling approaches are highly complex and accurate, an efficient optimization strategy is required. The input space in such simulations can range from different layer variations of the active QC period to changes in the doping density or material compositions. Therefore, the Bayesian optimization algorithm is a suitable statistical tool since it is generally applicable to an unknown objective function f(x), which can be time and computationally expensive. The algorithm is characterized by the search for the global minimum of the objective function f(x) on a high-dimensional input space $x \in \mathbb{R}^d$ [256]. Bayesian optimization consists of two main elements, a surrogate model and an acquisition function. The surrogate model is a Gaussian process, which is trained by function evaluations. The acquisition function acts as a utility function and thus helps to interpret the posterior function distribution, and makes a decision for the next data points to be evaluated [255]. In the following, we will give a short overview of the main elements of Bayesian optimization and describe the monacoQC optimization toolbox in more detail.

A Gaussian process is interpreted as a Gaussian distribution over functions, and fully described by its mean $\mu(x)$ and covariance function k(x,x') [284]. It specifies a collection of random variables forming a joint Gaussian distribution. For randomly chosen input values x_i , the function values can be drawn by the prior distribution of function values $f(x_i)$, which is a Gaussian distribution. An appropriate choice for a simple covariance function k(x,x') is the squared exponential covariance function

$$k(x, x') = \sigma_0^2 \exp\left(-\frac{1}{2}\sigma_1^2|x - x'|^2\right),\tag{2.38}$$

where σ_1^2 is the characteristic length scale and σ_0^2 the covariance amplitude. GPs account for noisy function values $f(x) + \epsilon_n$ by an additional uncorrelated Gaussian noise term ϵ_n with variance σ_n^2 . After the evaluation of the objective function f at some input points \mathbf{x}^* , the posterior probability distribution is calculated by conditioning the joint distribution on the function evaluations $\mathbf{y}^* = f(\mathbf{x}^*)$ as

$$p(y|x, \mathbf{x}^*, \mathbf{y}^*, \theta) \sim \mathcal{N}(\mu, k),$$
 (2.39)

with mean $\mu = k(x, \mathbf{x}^*)[k(\mathbf{x}^*, \mathbf{x}^*) + \sigma_n^2 \mathbf{I}]^{-1}\mathbf{y}^*$, covariance matrix $\mathbf{K} = k(x, x) - k(x, \mathbf{x}^*)[k(\mathbf{x}^*, \mathbf{x}^*) + \sigma_n^2 \mathbf{I}]^{-1} \times k(\mathbf{x}^*, x)$ and hyperparameters $\theta = (\sigma_0, \sigma_1, \sigma_n)$. The training data from all previous iterations are summarized in $(\mathbf{x}^*, \mathbf{y}^*)$. New function values y can thus be drawn for new random test inputs x. By maximizing the marginal likelihood $p(\mathbf{y}^*|\mathbf{x}^*, \theta)$, the optimal values of hyperparameters θ to describe the training data can be found.

The acquisition function a(x) is a measure for the yield of the next evaluation input point x_n and is defined as $x_n = \arg \max_x a(x)$. As an example, we will introduce here the common acquisition function *Expected Improvement* (EI) that provides a precise balance between exploration and exploitation. The EI acquisition function is defined as

$$EI(x) = \langle (t - y)_{+} \rangle = \int_{-\infty}^{\infty} (t - y)_{+} p(y|x, \theta) dy, \qquad (2.40)$$

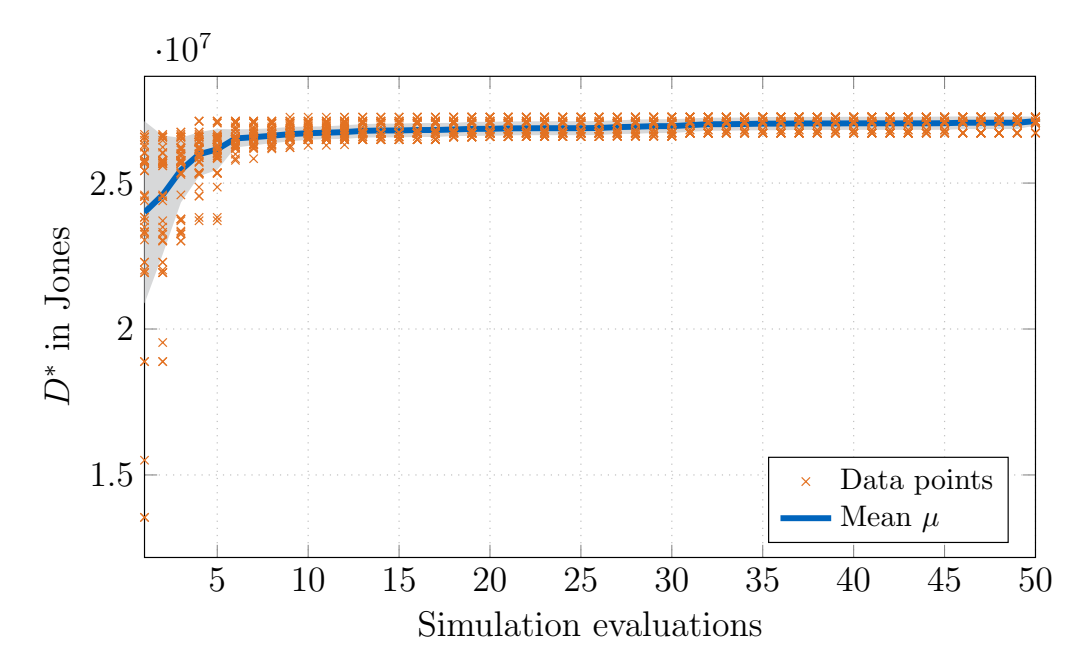


Figure 2.9 The optimized specific detectivity D^* of the QCD test structure N1022 [126]. Here, the blue line exhibits the mean value of 50 BO runs together with the data points (orange crosses). The gray area represents one standard deviation σ from the mean μ . The Bayesian optimization of each run was stopped after 50 evaluations. Reprinted from J. Popp *et al.*, "Bayesian optimization of quantum cascade detectors" [24] (CC BY 4.0).

with $(t-y)_+ = \max(0, t-y)$, where t is a target value and is usually set to be the maximum of the pre-evaluated function values. The term exploration refers to the investigation of areas in the input space with high uncertainty, while exploitation refers to the evaluation of the expected maximum of the predictive mean value [285]. To summarize, EI exhibits high function values for inputs x either with high predictive mean $\mu(x)$ or high predictive variance $\sigma^2(x)$, or both.

In the optimizer toolbox, a class **BO_sim** for the Bayesian optimization of QC devices is implemented. Here, the QC base period, the layer sequence under test and the length variation interval have to be provided as input parameters for the constructor. The class function **bayes_opt** is used for the BO process and is based on the standard implementation of the BO algorithm, which is part of the Statistics and Machine Learning ToolboxTM from Matlab. Here, a suitable function for the figure of merit (**merit_fun**) has to be provided. This function takes care of the carrier transport simulation and returns the calculated figure of merit. The helper function **evaluate_next_device** is called within the BO process to generate the simulation parameters, e.g., device object, for the next QC setup under test and to evaluate the merit function for the given input space.

The validity of BO_sim as an appropriate tool for the optimization of QC devices was tested and the results are illustrated in Fig. 2.9. Here, we performed 50 BO runs of the nominal QCD structure N1022 [126] to characterize the convergence rate and uncertainty of the optimization. The specific detectivity D^* converges quite fast to a global maximum, which makes it also practical to use time-demanding simulation approaches, e.g., EMC or NEGF, for efficient design optimization.

2.4 Summary

In this chapter, we have introduced our open-source Matlab-based QC device development tool *monacoQC*. The main goal is to provide a versatile platform for the development and improvement of optoelectronic QC devices. Therefore, we have addressed the fundamental principles of physical and optical properties of low-dimensional semiconductors and heterostructure technology.

Firstly, the band structure in III-V semiconductors is described. Here, a comprehensive model is provided to derive the important band parameters such as the band gap energy or the effective mass. Based on the $\mathbf{k} \cdot \mathbf{p}$ perturbation theory, a formula for the energy-dependent effective mass is derived and accounts for

nonparabolicity effects in III-V semiconductors. Furthermore, an 8-band $\mathbf{k} \cdot \mathbf{p}$ model by Sugawara *et al.* [265] is used to investigate the effects of strain on the effective mass at the conduction band edge. Subsequently, the semiconductor band structure and the conduction band discontinuities in quantum well heterostructures are characterized using model-solid theory. All material parameter models presented here are included in the setup library and can be used to describe the active QC region and the simulation parameters.

Secondly, we have introduced the Schrödinger-Poisson solver tool. An efficient wavefunction engineering is required to analyze and improve the optical and non-radiative properties of QC structures. We have started with the description of the 1D Schrödinger equation in the framework of the Ben-Daniel-Duke model. The transfer matrix method is used to derive a numerical solution of the 1D Schrödinger equation and the Possion equation is used to take into account space charge effects. Carrier injection plays a crucial role in modeling QC structures. Therefore, we have provided different wavefunction basis configurations in the solver library to appropriately account for specific carrier transport effects. These configurations are characterized by the order of wave function localization. The calculated self-energies and wave functions can be used as input parameters for the carrier transport simulations and serve as a description of the quantum system in dynamical Maxwell-density matrix Langevin simulations.

Finally, the Bayesian optimization tool for QC devices is described. Since the carrier transport models for QC devices are complex and numerically demanding, an efficient optimization method is beneficial. The two main elements of Bayesian optimization, the surrogate model and the acquisition function, have been characterized and the main properties of the Gaussian process surrogate model and the EI acquisition function are highlighted. The section is concluded by a validation of the BO model using a mid-IR QCD structure.

3 Carrier Transport Simulations of Intersubband Quantum Cascade Devices

Aiming for a full understanding of the physical mechanisms in QCLs or the analysis of noise characteristics in QCDs, a detailed theoretical characterization of the active QC medium is required. The systematic design optimization of optical and electronic properties can be accomplished using advanced self-consistent carrier transport models offering different levels of complexity and numerical efficiency. The EMC method is a widely used statistical method for the numerical evaluation of the carrier transport in low-dimensional semiconductor devices, such as quantum cascade structures [29], [30], [286]. A more general quantum transport approach, which has been applied to the simulation of intersubband QC devices, is given by non-equilibrium Green's functions [29], [33], [34], [42], [287], [288]. Those simulation approaches are self-consistent three-dimensional (3D) approaches taking into account intrasubband processes between different kinetic energies within a subband and do not rely on empirical or fitting parameters as input.

In general, the NEGF approach contains the full quantum information of scattering and dephasing effects and is therefore superior to semiclassical methods such as the EMC method. However, the numerical simulation of the NEGF solution is expensive, if incoherent scattering within the self-consistent Born approximation is taken into account. To reduce the numerical costs, NEGF simulations are typically executed by neglecting electron-electron scattering beyond the Hartree approximation. For the modeling of energy transfer during electron-electron scattering, the implementation of exchange terms would be required, which makes the actual carrier transport simulation unfeasible from a numerical point of view. In addition, the density matrix equation can be used to model the charge carrier transport in intersubband QC devices [289]. In the literature, 1D and 3D models of optical dynamics and charge transport in QCL structures are available [29], [32], [54], [68], [90], [290]–[296]. The 1D approach can be seen as a quantum-mechanical generalization of the simple rate equation model, where resonant tunneling and dephasing are taken into account.

Since semiclassical models, e.g., the EMC method, cannot cover quantum coherence effects, such as resonant tunneling across thick injection barriers, e.g., in THz QCLs, quantum corrections based on the density matrix formalism have been incorporated. Therefore, incoherent tunneling is treated as an additional "scattering-like" mechanism [35], [36], and gives the DM-EMC method a good balance between computational efficiency and accuracy.

In this chapter, we discuss the remaining three modules within the *monacoQC* framework, namely the ext. solver, mbsolve and results. Generally, each available carrier transport simulation tool can be integrated into the *monacoQC* framework by providing a suitable interface class. We have therefore focused on the in-house DM-EMC solver and a rate equation solver, which can be used for the characterization of simpler simulation problems. Both solver tools have been developed over the last 20 years in the Computational Photonics group. In this work, the existing tools were used and integrated into the monacoQC framework. It should be mentioned here that the module ext. solver with the two solver classes is not included in the GitHub repository. The simulation results, e.g., wavefunctions and conduction band profiles from the SP solver or carrier transport properties such as scattering rates, dephasing rates and level occupations from the EMC solver, can be integrated and processed. The stationary carrier transport simulation results can be summarized in the backend class **mbsolve_sim** and serve as input for the dynamical Maxwell-DM equation solver. The base library together with selected carrier transport simulation results can be found on GitHub [254].

The chapter is organized as follows: Section 3.1 characterizes the main scattering mechanisms in intersubband QC devices and presents the two simulation methods based on the self-consistent DM-EMC method and the more simplistic rate equation model. In the *monacoQC* toolbox, results extracted from the SP solver and from the stationary carrier transport simulations can be summarized and stored in objects of different classes. Here, interesting microscopic and macroscopic quantities, e.g., the spectral gain or the level occupations, can be

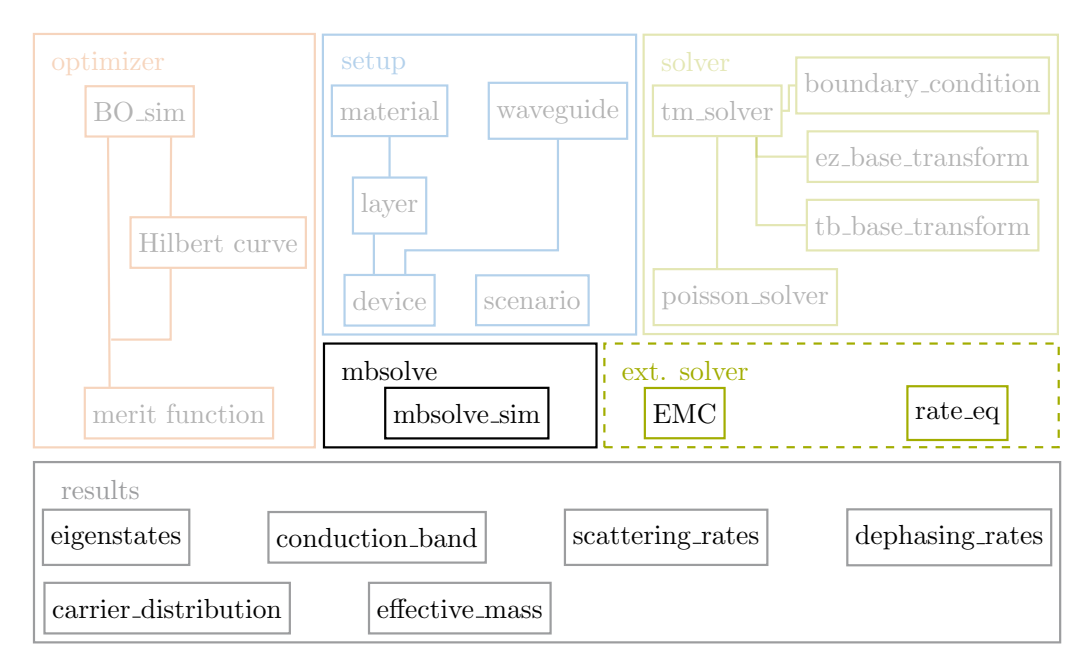


Figure 3.1 Overview of the *monacoQC* framework [254]. In this chapter, we concentrate on the three highlighted modules mbsolve, ext. solver and results. Adopted from J. Popp *et al.*, "Multi-domain modeling of free-running harmonic frequency comb formation in terahertz quantum cascade lasers" [178] (CC BY 4.0).

analyzed with the help of visualization methods. The result classes and their functionalities will be discussed in Section 3.2. The third module, which is dealt with in this chapter, contains the backend class **mbsolve_sim** and will be presented in Section 3.3. Here, a reduced quantum system model can be composed from the comprehensive carrier transport simulation results and can then be extracted as a simulation setup for the dynamical Maxwell-density matrix Langevin approach *mbsolve*. The chapter concludes with a short summary.

3.1 Scattering Mechanisms and Carrier Transport Simulations

The transition of an electron in a quantum well heterostructure from one quantized level to another is described by a scattering process. The corresponding scattering rate is derived from a perturbation potential V, which is either static or time-dependent. Taking into account the different perturbations, we have to distinguish between three categories of scattering processes as illustrated in Fig. 3.2(a). Elastic processes are described by a time-constant potential, where the energy of the involved carrier is conserved (Schematic (1) in Fig. 3.2(a)). In Schematic (2) of Fig. 3.2(a), the inelastic scattering process is illustrated, which is described by a harmonic time-dependent potential ($V \propto \cos(\omega_0 t)$). Here, absorption or emission leads to a change in the energy of a particle by $\pm\hbar\omega_0$. The third process, depicted in Schematic (3) of Fig. 3.2(a), describes a special class corresponding to carrier-carrier scattering. In the case of intersubband QC devices, it refers to a process, where two electrons are involved. Based on Fermi's golden rule, the scattering rate from the initial state $|i\mathbf{k}\rangle$ to the final state $|j\mathbf{k}'\rangle$ is determined by [263]

$$W_{j\mathbf{k'},i\mathbf{k}} = \begin{cases} \frac{2\pi}{\hbar} |V_{j\mathbf{k'},i\mathbf{k}}|^2 \delta(E_{j\mathbf{k'}} - E_{i\mathbf{k}}), & \text{elastic}, \\ \frac{2\pi}{\hbar} |V_{j\mathbf{k'},i\mathbf{k}}^{\mp}|^2 \delta(E_{j\mathbf{k'}} - E_{i\mathbf{k}} \pm \hbar\omega_0), & \text{inelastic}. \end{cases}$$
(3.1)

In intersubband QC devices, the initial and final state i and j describe subbands and the wavevectors k and k' are the in-plane wavevectors. Total energy conversion including the conservation of the in-plane energy is ensured by the Dirac δ function. The potential matrix element $V_{jk',jk}$ for elastic scattering processes is given by

$$V_{j\mathbf{k'},i\mathbf{k}} = \langle j\mathbf{k'}|V|i\mathbf{k}\rangle$$

$$= S^{-1} \int_{S} \int_{-\infty}^{\infty} V \psi_{j}^{*} \psi_{i} \exp[i(\mathbf{k} - \mathbf{k'})\mathbf{r}] \mathbf{d}^{2} r \, dz,$$
(3.2)

with the constant potential V. For elastic scattering processes, we obtain a harmonic potential $V = V_0 \exp(i\mathbf{Q}x - i\omega_0 t) + V_0^* \exp(-i\mathbf{Q}x + i\omega_0 t)$, where \mathbf{Q} is, for example, the phonon wave vector. The matrix element is then given by

$$\begin{pmatrix} V_{jk',ik}^{+}(Q) \\ V_{jk',ik}^{-}(Q) \end{pmatrix} = \langle jk' | \begin{pmatrix} V_0 \exp(iQx) \\ V_0^* \exp(-iQx) \end{pmatrix} | ik \rangle
= S^{-1} \int_{S} \int_{-\infty}^{\infty} \psi_j^* \psi_i \begin{pmatrix} V_0 \exp(iQx) \\ V_0^* \exp(-iQx) \end{pmatrix} \exp[i(k-k')r] \mathbf{d}^2 r \, dz.$$
(3.3)

We treat the QC active medium as an infinitely extended periodic heterostructure and integrate over $-\infty$ to ∞ in z-direction. This is valid under the assumption of bound wavefunctions $\psi_{i,j}$ in Eqs. (3.2) and (3.3). Furthermore, the integration in x and y direction can be extended from $-\infty$ to ∞ for the scattering rates calculations, if we assume a macroscopic in-plane cross-section S.

In the following, we will briefly summarize the most important non-radiative scattering processes in intersubband QC devices. For detailed information about the perturbation potentials and the calculation of individual scattering mechanisms, we refer to [29] and [297].

The relevant elastic mechanisms in intersubband devices are impurity, interface roughness and alloy scattering. Ionized donors in quantum well heterostructures have been introduced in the previous chapter for the calculation of the space charge effects within the mean-field treatment. Besides this, ionized donors act as charged impurities and have to be considered for the scattering of electrons. Impurity scattering processes are described by the Coulomb potential and can be the dominant elastic scattering process in intersubband QC devices, such as QCLs [298]–[300]. Furthermore, the performance of QCLs can be changed significantly due to scattering arising from imperfect interfaces [301]-[304]. Here, the layer-by-layer growth can result in fluctuations of the compositions at the interfaces between the well and barrier material. Typically, the interface roughness scattering is specified by a Gaussian auto-correlation function with a characteristic standard deviation Δ and correlation length Λ . Alloy scattering has to be considered in ternary semiconductor alloys such as AlGaAs, where the Al and Ga atoms are randomly distributed in the zincblende structure. The perturbation potential is given by the difference of real conduction band energy $E_c(z)$ and the VCA conduction band energy $E_{c,VCA}(z)$, introduced as average potential in Section 2.1. As the wavefunctions are mostly localized in the well layers, alloy scattering usually only has to be taken into account for the well materials [262]. Alloy scattering is particularly important for short-wavelength QCLs, where the electron mobility of the highly pure samples is limited at low temperatures [303].

In intersubband QC devices, lattice vibrations lead to a harmonic perturbation potential, resulting in an additional inelastic scattering mechanism called phonon scattering. Here, a phonon is a quasi-particle and represents an excited state of the quantized vibrational modes. There are two types of phonons: acoustic and optical phonons. Acoustic phonons are sound waves, where two consecutive modes move in the same direction. Optical phonons describe optical waves, where two adjacent atoms in the same unit cell move in opposite directions. Dependent on the wave propagation, we speak about transverse or longitudinal optical/acoustic phonons. Nonpolar phonon scattering based on acoustic and transverse optical phonons is present in all crystals, whereas the phonon scattering based on longitudinal optical phonons occurs only in polar materials, such as III-V semiconductors. Here, a strong local dipole moment caused by the out-of-phase movement of neighboring atoms results in an oscillating perturbative electric field. The dominant non-radiative scattering mechanism in intersubband QC devices is LO phonon scattering. Efficient carrier extraction in intersubband QC devices is achieved by matching the separation energy between the levels in the extraction cascade to the LO phonon energy, e.g., $\hbar\omega_{\rm LO}\approx 36$ meV in GaAs [305].

Many-electron effects are already included in the Poisson equation using the Hartee potential. Furthermore, the collision of electrons can be included in semiclassical models as an additional scattering mechanism and is typically implemented as a two-electron process [29], [306], [307]. Electron-electron scattering has an important influence in k-space resolved transport models for, e.g., the description of thermalization effects of electrons in subbands [308], [309].

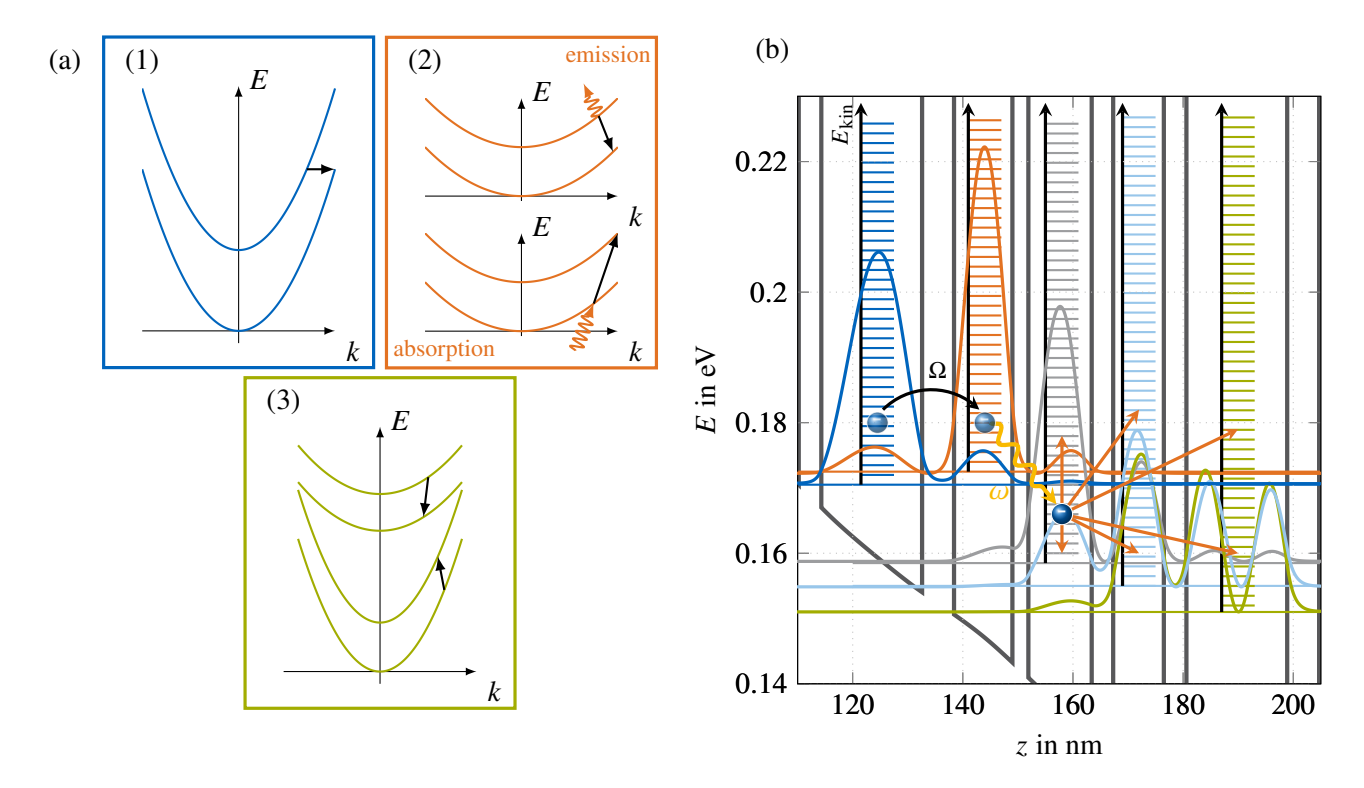


Figure 3.2 (a) The scattering mechanisms in intersubband QC devices can be categorized into three classes: (1) elastic scattering, (2) inelastic scattering and (3) electron-electron scattering. (b) Illustration of the carrier transport simulation model based on the density matrix ensemble Monte Carlo method. Here, the electron transport is scattering-induced and occurs between subbands in the conduction band of a biased diagonal transition THz QCL heterostructure [73].

In Fig. 3.2(b), a theoretical description of the DM-EMC model is illustrated for a diagonal transition THz QCL gain medium. The scattering-induced transport of electrons between quantized levels is modeled semiclassically by evaluating the Boltzmann equation

$$\partial_t f_{i,\mathbf{k}} = \sum_{s} \sum_{i,\mathbf{k}} \left(W_{i\mathbf{k},j\mathbf{k}'}^{(s)} f_{j,\mathbf{k}'} - W_{j\mathbf{k}',i\mathbf{k}}^{(s)} f_{i,\mathbf{k}} \right), \tag{3.4}$$

where s sums over the individual contributions of the scattering mechanisms, $W_{jk',ik}$ denotes scattering rate from state $|ik\rangle$ to $|jk'\rangle$ and $f_{i,k}(t)$ is the distribution function, which indicates the probability that the state $|ik\rangle$ is occupied at a certain time t. Here, all relevant mechanisms such as LO and acoustic phonon, electron-electron, impurity, interface roughness, and alloy scattering are considered. The corresponding rates are calculated self-consistently at the beginning of the simulation using Fermi's golden rule. For the initialization of the simulation, an ensemble of electrons is distributed over the different states characterized by the subband index i and in-plane wavevector k. According to the Monte Carlo method, the QCL system will converge to the stationary solution by stochastically evaluating the scattering events. The density matrix EMC approach includes elements of the density matrix formalism to account for tunneling across thick injection barriers, described by the Rabi frequencies Ω_{ij} [29], [35], [184]. The corresponding single-electron tunneling rate is given by

$$r_{ij,k}^t = \frac{2\Omega_{ij}^2 \gamma_{ij,k}}{\omega_{ij}^2 + \gamma_{ij,k}^2},$$
(3.5)

where $\omega_{ij} = (E_i - E_j)/\hbar$ denotes the resonance frequency between states $|i, k\rangle$ and $|j, k\rangle$ and $\gamma_{ij,k}$ is the dephasing rate.

If the external solver library is integrated into the *monacoQC* framework, the EMC executables can be built by following the build instructions. Here, we use the build automation tool CMake to build and install the tools. Additionally, a Matlab wrapper function **sim_stat_solver** exists to solve the self-consistent stationary

simulation system. The SP solver and the DM-EMC approach are iterated until convergence is achieved. The relative change of the unsaturated gain curve is used as a convergence criterion. The following command will start the simulation of the diagonal transition THz QCL illustrated in Fig. 3.2(b):

\$cd monaco/setups/tests; matlab -batch "addpath(genpath('../../monaco/'));
[d, s] = forrer2021('ez'); [cond_band, eigen, curr_dens, carr_dist, deph, sc,
gain, count] = sim_stat_solver(s, d, pwd), save('forrer2021_ez.mat')"

In this configuration, we use the EZ-configuration for the wavefunction solution. The simulation results consisting of **conduction_band**, **eigenstates**, **current_density**, **carrier_distribution**, **dephashing_rates** and **scattering_rates** objects are saved in a mat-file. Additionally, a class object with the k-resolved gain results is returned.

Unfortunately, the direct QCD modeling based on the standard QCL simulation approaches is unfeasible due to the significantly smaller currents in photovoltaic mode. Therefore, we have developed an alternative method, providing a robust and compact approach to determine the figures of merit of QCDs [42]. Detector signal strength and noise characteristics are obtained utilizing a rate equation model and a Kirchhoff resistance network, illustrated in Fig. 3.3. As inputs only the absorption coefficient and intersubband scattering rates, extracted from the EMC carrier transport simulations or calculated using Fermi's golden rule, are required. Assuming a periodic QCD structure with N subbands per period, the transition rates from subband j to i can be written as $r_{ij} = r_{i+N,j+N}$. In the stationary case, the rate equation for a reference period including also the transitions to and from the left- and the right-neighboring period can be written as [29], [42], [310]

$$Qp = b. (3.6)$$

Here, Q is the transition rate matrix with the elements $q_{ii} = -\sum_{j \neq i} \left(r_{j+N,i} + r_{ji} + r_{j,i+N} \right)$ for i = 1..(N-1), $q_{Nj} = 1$ for j = 1..N, and $q_{ij} = r_{i,j+N} + r_{ij} + r_{i+N,j}$ otherwise. The subband occupation probabilities p_i are summarized in vector p, and the vector elements of b are given by $b_i = \delta_{iN}$ with the Kronecker delta δ_{iN} . The photon-induced rate r_p due to incident light has to be added as an additional rate δr_{ag} from the ground level g to the absorption level g. The resulting matrix g has non-zero elements g and g are g are g from the ground level g to the stationary level occupations and by taking into account stimulated photon transitions we obtain the modified equation system

$$(\mathbf{Q} + \delta \mathbf{Q})(\mathbf{p} + \delta \mathbf{p}) = \mathbf{b}. \tag{3.7}$$

For moderate intensities, i.e., if the QCD operates in the linear response regime, we can neglect the higher order term $\delta Q \delta p$ and under consideration of Eq. (3.6) a second rate equation in the form

$$Q\delta p = -\delta Q p \tag{3.8}$$

is obtained. The solution of Eq. (3.8) gives the population changes δp in the irradiated structure. By applying Cramer's rule one obtains individual-level occupation changes by

$$\delta p_i = \frac{|Q_i|}{|Q|} (p_a - p_g) r_p, \qquad (3.9)$$

where |...| denotes the matrix determinant, and Q_i is the matrix obtained by replacing the *i*-th column of Q by the vector v with two non-zero elements $v_g = -1$ and $v_a = 1$. As illustrated in Fig. 3.3(b), we can model the detector noise using a noise equivalent resistances network, where the subbands within the QCD heterostructure act as nodes [311]. The total QCD resistance R_d can be calculated by solving Kirchhoff's equations. For unbiased QCDs, the conductance per unit area is dominated by Johnson noise at elevated temperatures and can be written as [311]

$$\sigma_{ij} = \sigma_{ji} = \frac{e^2 n^s}{2k_B T} \left(r_{ij} p_j + r_{ji} p_i \right). \tag{3.10}$$

By setting $\sigma_{ii} = 0$, we can formulate Kirchhoff's law for a node i as

$$\sum_{j} \sigma_{ij} \left(u_i - u_j \right) = 0. \tag{3.11}$$

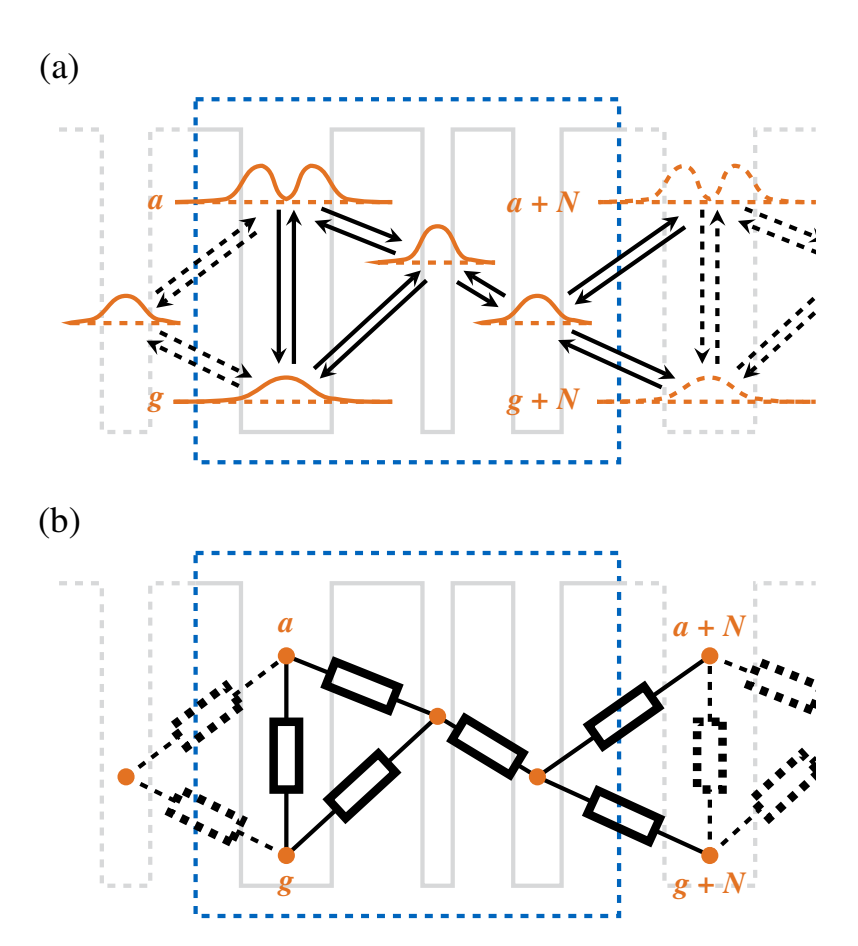


Figure 3.3 (a) Schematic conduction band profile of a QCD. Photovoltaic operation is ensured by absorption from ground level g to absorption level a and consecutive scattering through the extractor levels in the quantum cascade. Reprinted from J. Popp *et al.*, "Bayesian optimization of quantum cascade detectors" [24] (CC BY 4.0). (b) For the characterization of noise in QCDs, the quantum well heterostructure with quantized states can be represented by an equivalent resistance network.

In Fig. 3.3(b) it is easy to see that $\sigma_{ij} = \sigma_{i+N,j+N}$ applies in periodic QCDs and we can greatly reduce the numerical cost by exploiting the periodicity of the conductance network. We further assume that the voltages of equivalent nodes in adjacent periods are related by $u_{i+N} = u_i + u_p$. Here, u_p is the voltage drop per period. For QCDs with several periods, we can neglect the boundary conditions at the end contacts and derive from Eq. (3.11) for a reference period [42]

$$Gu = u_p d. (3.12)$$

Here, we also have to account for transitions to and from the left- and the right-neighboring period, and obtain the conductance matrix elements

$$g_{ij} = \begin{cases} \sigma_{ij} + \sigma_{i,j+N} + \sigma_{i+N,j}, & i \neq j, \\ -\sum_{\substack{n=1\\n\neq i}}^{N} (\sigma_{in} + \sigma_{i,n+N} + \sigma_{i+N,n}), & i = j. \end{cases}$$
(3.13)

The elements of d are

$$d_{i} = \sum_{n=1}^{N} (\sigma_{i+N,n} - \sigma_{i,n+N}). \tag{3.14}$$

No independent solution can be found for the linear equation system given in Eq. (3.12), since the zero potential u = 0 can be chosen arbitrarily. Therefore, we set the voltage u_n corresponding to an arbitrary subband n to zero and eliminate the nth equation from Eq. (3.12). The order of G and length of u and u are reduced to u if u is the number of subbands per period. In accordance with the rate equation system, we can apply Cramer's rule to Eq. (3.12) and obtain the individual solution u_i

$$u_i = u_p \frac{|G_i|}{|G|},\tag{3.15}$$

where G_i is the matrix obtained by replacing the *i*-th column of G by vector d. The model, which includes the equations (3.11) and (3.12), was published in [42] and is an extension of a resistance model based on LO phonon scattering [312].

3.2 Results of Stationary Carrier Transport Simulations

In the *monacoQC* framework, the results library contains different classes for the post-processing and visualization of carrier transport simulation results, e.g., based on the DM-EMC approach. Here, interesting microscopic and macroscopic quantities, e.g., electron distribution, current, gain and absorption, device resistance, photo response, etc. can be analyzed. In the following, we will give a short overview of the library classes and their functionalities.

The classes **conduction_band** and **eigenstates** were already introduced in Section 2.2. The former contains information about the total potential profile V of the investigated QC structure. Here, the methods **plot_profile** and **write_cond_profile** can be used to either plot the potential profile or save the position and potential vector z and V in a CSV-file. The latter is used for the description of the quantum system and contains information about the wavefunctions ψ , the system Hamiltonian H_s , effective masses m^* and the dipole matrix d. In the following, we will give a short overview of the calculation of the individual dipole matrix element d_{ij} . Here, we start with the evaluation of the expectation value of the momentum operator \hat{p} . With the eigenstate wave functions $\Psi_i = \phi_{i,k} u_{c_i,0}$ in the conduction band, which are shown in Fig. 2.6, the matrix element can be expressed as [263]

$$\langle \Psi_i | \hat{\boldsymbol{p}} | \Psi_i \rangle \approx \langle \phi_{ik} | \phi_{ik} \rangle \langle u_{ci0} | \hat{\boldsymbol{p}} | u_{ci0} \rangle + \langle u_{ci0} | u_{ci0} \rangle \langle \phi_{ik} | \hat{\boldsymbol{p}} | \phi_{ik} \rangle. \tag{3.16}$$

The first term vanishes due to $\langle u_{c_i,0} | \hat{p} | u_{c_i,0} \rangle = 0$, and with $\langle u_{c_i,0} | u_{c_i,0} \rangle = 1$ we obtain the simplified formula

$$\langle \Psi_i | \hat{\boldsymbol{p}} | \Psi_i \rangle \approx \langle \phi_{i,k} | \hat{\boldsymbol{p}} | \phi_{i,k} \rangle. \tag{3.17}$$

By the insertion of the slowly varying envelope function from Eq. (2.18), we can further simplify to $\langle \phi_{i,k} | \hat{p} | \phi_{j,k} \rangle = \langle \psi_i | \hat{p}_z | \psi_j \rangle \delta(k, k')$, which means that in quantum well heterostructures there is only one non-vanishing dipole

moment \hat{p}_z in the direction of growth z. Light-matter interaction is present if an electric field component perpendicular to the semiconductor layers exists and is referred to as the polarization selection rule. In THz QC devices, for example, we can neglect nonparabolicity effects and assume a k independent optical transition energy $E_i(k) - E_i(k) = E_i - E_j$. On this basis, it can be shown that the equivalence applies

$$\langle \Psi_i | \hat{\boldsymbol{p}}_z | \Psi_j \rangle = \frac{\mathrm{i} m^* (E_i - E_j)}{\hbar} \langle \Psi_i | z | \Psi_j \rangle. \tag{3.18}$$

The dipole matrix element between an initial state $\phi_{j,k}$ and a final state $\phi_{i,k}$ is then given by

$$\mathbf{d}_{ij} = \langle \psi_i | \hat{\mathbf{d}} | \psi_j \rangle = -e \mathbf{e}_z \int \psi_i^* z \psi_j \, \mathrm{d}z.$$
 (3.19)

Here, e_z denotes the unit vector in z direction. The class **eigenstates** provides a member function **get_dipole _element**. With the help of the wavefunctions ψ_i , ψ_j the individual dipole matrix elements d_{ij} are calculated. Furthermore, a function **plot_wavefunctions** with an instance **conduction_band** as input can be used to plot the conduction band profile and the probability densities of the stored wavefunctions ψ_i . Based on the wavefunction numbering displayed in the Matlab figure legend, one can specify wavefunctions, which can then be extracted using the function **write_wavefcts**. Those wavefunctions will then be stored in a separate CSV file. Additionally, the Rabi frequencies Ω_{ij} and resonance frequencies ω_{ij} can be extracted from the system Hamiltonian H_s , the corresponding methods are **get_rabi_freq** and **get_resonance_freq**.

The class **carrier_distribution** contains the subband occupation probabilities and the electron distribution within each subband. The steady-state electron distributions $\rho^0_{ii,k'}$ within one subband i are well described by either the Fermi-Dirac or Maxwell-Boltzmann distribution, where the characteristic subband electron temperatures can significantly exceed the lattice temperatures [29], [313]. The methods **get_electron_temperature** and **fit_distribution** are provided to return the subband electron temperatures and fit the k resolved subband electron distributions to the predefined carrier distribution function. One can specify the carrier distribution function using the class method **set_fit_carr_dist** and the distribution name ("Maxwell Boltzmann" (default), "Fermi Dirac") as input argument.

The k-dependent scattering rates $r_{jk'\to ik}$, which were extracted e.g., from self-consistent DM-EMC simulations or calculated with the help of Fermi's Golden Rule [29], are stored in the class **scattering_rates**. A map is provided, which contains all important scattering mechanisms present in intersubband QC devices, e.g., LO and acoustic phonon scattering, electron-electron scattering, impurity scattering, interface roughness scattering and alloy scattering. Under the assumption of moderate temporal variations of intersubband electron distributions $\rho_{jj,k}$, averaged scattering rates r_{ij} can be calculated by [47], [71]

$$r_{ij} = \sum_{\mathbf{k}, \mathbf{k'}} r_{j\mathbf{k'} \to i\mathbf{k}} \rho_{jj, \mathbf{k'}}^0 \left| \sum_{\mathbf{k}} \rho_{jj, \mathbf{k'}}^0 \right|. \tag{3.20}$$

Based on the requirements, one can extract the scattering rate matrix including transitions between levels within the active period, or transitions to and from the left- and the right-neighboring period. The function **get_scattering_matrix** returns the specific scattering matrix dependent on the input variable **direction** ("left", "center", "right").

The class **dephasing_rates** includes a map with all considered pure dephasing contributions and level broadenings with respect to the kinetic energy of each subband. The calculated dephasing rates $\gamma_{ij,k}$ are based on Ando's model [314]–[316] and the level broadenings are calculated from the DM-EMC scattering rates [29], [35], [317]. For off-diagonal density matrix elements, which generally vary strongly with time, no clearly defined concept is given for the k averaging and thus the calculation of effective dephasing rates γ_{ij} from $\gamma_{ij,k}$. Particularly for QCLs, in which the electron temperature of the different subbands fluctuates greatly and the individual subbands have a highly non-thermal distribution, the ratio $\rho_{ii,k}^0/\rho_{jj,k}^0$ is strongly k dependent [29]. By averaging over the inversion between the subbands, the effective dephasing rates γ_{ij} can be determined as [300], [317]

$$\gamma_{ij} = \sum_{k} \gamma_{ij,k'} |\rho_{ii,k}^{0} - \rho_{jj,k}^{0}| / \sum_{k} |\rho_{ii,k}^{0} - \rho_{jj,k}^{0}|.$$
(3.21)

The functions **get_dephashing_rate**, **get_pure_dephashing_rate** and **get_lt_broadening** can be used to extract individual dephasing rates γ_{ij} , pure dephasing rates $\gamma_{ij,p}$ and lifetime broadening $\frac{1}{2} \left(\frac{1}{\tau_i} + \frac{1}{\tau_j} \right)$. Here, τ_i is the lifetime of level i.

Based on that, we can now calculate key figures of merit for the performance characterization of intersubband QC devices. For the QCD, the frequency-dependent responsivity is defined by the generated detector photocurrent I_{out} per incident optical power P_{in} and is written as

$$R_{\rm p}(\omega) = \frac{I_{\rm out}(\omega)}{P_{\rm in}(\omega)} = \frac{e}{\hbar \omega} \frac{p_{\rm e}}{N_{\rm p}} T_{\rm f} [1 - \exp(-\alpha_{\rm p} n_{\rm p} N_{\rm p} L_{\rm p} \sin \theta)], \tag{3.22}$$

where $T_{\rm f}$ is the facet transmittance, $\alpha_{\rm p}$ the power absorption coefficient, $n_{\rm p}$ the number of passes of the optical field through the absorbing region, $N_{\rm p}$ the number of periods in the active region, $L_{\rm p}$ the length of one period and $\omega = 2\pi c/\lambda$ the angular frequency [38]. In general, a mesa-structure with a double-pass waveguide is considered for the characterization of such detector devices. Here, the two facets are polished into 45° wedges. The light beam exhibits a propagation angle $\theta = 45^{\circ}$ relative to the growth direction to meet the quantum-mechanical polarization rule. The ratio between the current change over the period to change in current from ground to upper level is given by the extraction efficiency $p_{\rm e}$ and can be calculated, as published in [42], by

$$p_{e} = (p_{g}r_{p})^{-1} \sum_{i=1}^{N} \sum_{j=1}^{N} (r_{j+N,i} - r_{j,i+N}) \delta p_{i}.$$
(3.23)

Using Eq. (3.9), we obtain in the linear regime

$$p_{e} = \frac{p_{a} - p_{g}}{|\mathbf{Q}| p_{g}} \sum_{i=1}^{N} \sum_{j=1}^{N} (r_{j+N,i} - r_{j,i+N}) |Q_{i}|,$$
(3.24)

where the photon-induced rate r_p cancels out. Thus, when evaluating Eq. (3.8) with a linear equation system solver rather than using Cramer's rule, r_p can be set to a numerically convenient value. If in a QCD structure, more than one optical absorption transition is present [126], the occupation change δp_i in Eq. (3.23) is obtained by summing over the individual contributions. Furthermore, we have to account for the individual contributions by an effective p_e ,

$$p_{\rm e} = \sum_{a} c_a p_{\rm e,a} \,, \tag{3.25}$$

where the $p_{e,a}$ for each of the absorption levels a has been separately computed and c_a is the relative absorption contribution of level a.

Another key figure of merit is the specific detectivity D^* serving as a measure for the signal-to-noise ratio in photodetectors. In QCDs, the detectivity is limited by Johnson noise and is given by [126]

$$D^* = R_{\rm p} \sqrt{\frac{A_{\rm d} R_{\rm d}}{4k_{\rm p} T}},\tag{3.26}$$

where A_d is the detector area and R_d the detector resistance. The unit of D^* is Jones, which correspond to $\text{cm}\sqrt{\text{Hz}}/\text{W}$. The detector resistance in Eq. (3.26) is given by

$$R_{\rm d} = N_{\rm p}/(\sigma_{\rm p}A)$$

where A is the in-plane cross-section area of the quantum wells, which coincides with the detector area A_d in Eq. (3.26) if the facet is in the in-plane direction. The conductance per unit area of a single QCD period can be calculated from the ratio of net current density flowing between adjacent periods to the voltage drop per period [42],

$$\sigma_{p} = u_{p}^{-1} \sum_{i=1}^{N} \sum_{j=1}^{N} \sigma_{i,j+N} (u_{j} + u_{p} - u_{i})$$
(3.27a)

$$= \sum_{i=1}^{N} \sum_{j=1}^{N} \sigma_{i,j+N} \left(\frac{|G_j|}{|G|} + 1 - \frac{|G_i|}{|G|} \right), \tag{3.27b}$$

where Eq. (3.27b) has been obtained by inserting Eq. (3.15). As can be seen from Eq. (3.27b), σ_p only depends on the σ_{ij} , and can thus be calculated self-consistently using Eqs. (3.6) and (3.10) with EMC intersubband scattering rates.

3.3 Dynamical Simulation Setup

The stationary carrier transport simulation results, as needed for the dynamical Maxwell-density matrix Langevin approach [59], [90], can be summarized in the backend class **mbsolve sim**. Here, the resonant tunneling and required optical transitions for mid-IR ($\omega_{\text{mid-IR}}$) and THz (ω_{THz}) frequencies have to be identified. By the use of various helper methods, a reduced model, which describes the quantum system adequately, can be retrieved. Furthermore, methods, e.g., calc_gain, calc_suscept_2 for calculations of the gain characteristics and secondorder susceptibility $|\chi^{(2)}|$, are provided in the class **mbsolve_sim**. The class method **generate** composes a Python script of the quantum-mechanical description in *mbsolve* syntax, which can be directly used as input script for a *mbsolve* simulation via its Python interface [72]. The quantum-mechanical description comprises the level occupations ρ_{ii} , the system Hamiltonian matrix H_s with eigenenergies E_i and anticrossing energies $\hbar\Omega_{ij}$, the dipole moment matrix d_z , the dephasing rates γ_{ij} and the scattering rates r_{ij} . For the one-dimensional dynamic Maxwell-DM simulations, the energy-resolved dephasing rates are simulated within the EMC approach and have to be averaged over the population inversions of the involved subbands, as described in detail in the previous section. The base library together with carrier transport results in extended and EZ-configuration for the THz HFC QCL setup illustrated in Fig. 2.7 can be found on GitHub [254]. As an example, the quantummechanical description for the THz-HFC-QCL setup at a bias voltage of 50 mV per period with one optical and one tunnel junction is illustrated in Listing 3.1.

Listing 3.1 Code snippet of the Python script for the THz HFC QCL setup at a bias voltage of 50 mV given in [73].

```
import mbsolve.lib as mb
import mbsolve.solvercpu
import mbsolve.writerhdf5
import mbsolve.readerhdf5
import math
import time
# Hamiltonian
energies = [ 0.0097 * mb.E0, 0.0082 * mb.E0, -0.0047 * mb.E0,
-0.0083 * mb.E0, -0.0097 * mb.E0
off_diagonales = [ 0.0005 * mb.E0, 0, 0, 0, 0, 0, 0, 0, 0]
H = mb.qm_operator(energies, off_diagonales)
# dipole moment operator
off_dipoles = [ 0, -2.9500e-09 * mb.E0, 0, 0, 0, 0, 0, 0, 0] diag_dipoles = [ 0, 0, 0, 0, 0 ]
u = mb.qm_operator(diag_dipoles, off_dipoles)
# relaxation superoperator
# scattering rate matrix R
rates = [ [ 0, 1.8815e+09, 2.1290e+10, 4.0984e+09, 5.6000e+09 ],
          [ 3.5006e+09, 0, 3.2437e+08, 2.2854e+10, 2.0029e+12 ],
          [ 6.5578e+10, 6.2829e+08, 0, 8.0333e+11, 6.1577e+09 ],
          [ 6.8416e+09, 3.6845e+08, 6.6107e+11, 0, 4.7378e+12 ],
          [ 5.2192e+08, 6.7259e+10, 4.7554e+09, 4.7726e+12, 0 ] ]
# pure dephasing rates
pure_deph = [ 3.5857e+12, 9.3257e+11, 0, 0, 0, 0, 0, 0, 0, 0]
relax_sop = mb.qm_lindblad_relaxation(rates, pure_deph)
# initial density matrix
rho_init = mb.qm_operator([ 0.3705, 0.4937, 0.0741, 0.0333, 0.0285])
```

To classify the efficiency of nonlinear mixing processes and the potential for broadband THz comb emission, we have investigated the gain spectrum of QCL setups emitting in the mid-IR and THz spectrum [90], [178]. Here, the optical gain using the method **calc_gain** is calculated by [29]

$$g(\omega) = \frac{\omega}{\varepsilon_0 c n_{\text{eff}}} \sum_{i,j} d_{ij}^2 \frac{\gamma_{ij}}{\gamma_{ij}^2 + (\hbar \omega - \hbar \omega_{ij})^2} (p_i - p_j), \qquad (3.28)$$

where c is the vacuum speed of light and n_{eff} is the effective refractive index. Moreover, $\hbar\omega_{ij}=(E_i-E_j)$ denotes the resonance energy between level i and j. The transition linewidth broadening is given by [35]

$$\gamma_{ij} = (\gamma_i + \gamma_j)/2 + \gamma_{ij,p}, \qquad (3.29)$$

where γ_i corresponds to the level broadening of level i and $\gamma_{ij,p}$ represents the pure dephasing contribution.

We further have characterized the strength of the nonlinearity in the active gain region important for THz frequency comb emission in DFG QCLs via nonlinear mixing [90]. The second-order nonlinear susceptibility $\chi^{(2)}$ within the method **calc_suscept_2** is calculated by [318]

$$\chi^{(2)}(\omega_{\text{THz}} = \omega_{1} - \omega_{2}) = -\frac{e^{3}}{\varepsilon_{0}} \sum_{i,j,k} N_{i} z_{ij} z_{jk} z_{ki} \left\{ \left[\frac{1}{(\hbar \omega_{ki} - i\gamma_{ki} - \hbar \omega_{\text{THz}})} + \frac{1}{\hbar \omega_{kj} + i\gamma_{kj} + \hbar \omega_{\text{THz}}} \right] \times \right.$$

$$\times \left[\frac{1}{(\hbar \omega_{ji} - i\gamma_{ji} + \hbar \omega_{2})} + \frac{1}{\hbar \omega_{ji} - i\gamma_{ji} - \hbar \omega_{1}} \right] - \left[\frac{1}{(\hbar \omega_{kj} - i\gamma_{kj} - \hbar \omega_{\text{THz}})} + \frac{1}{\hbar \omega_{ki} + i\gamma_{ki} + \hbar \omega_{\text{THz}}} \right] \times \left. \left[\frac{1}{(\hbar \omega_{ij} - i\gamma_{ij} + \hbar \omega_{2})} + \frac{1}{\hbar \omega_{ij} - i\gamma_{ij} - \hbar \omega_{1}} \right] \right\}, \quad (3.30)$$

where the levels with indices i, j, k build a DFG triplet. Here, all combinations of involved upper and lower laser levels are taken into account. A detailed and more sophisticated Monte Carlo analysis of the second-order nonlinear susceptibility can be found in the literature ([318], [319]), where also the effects of the intrasubband kinetic electron distribution were included. By taking into account only the dominant DFG triplets near resonance to the mid-IR design frequencies ω_1 and ω_2 , a significantly reduced number of terms in Eq. (3.30) remains [104], [192], [200], [318].

3.4 Summary

In this chapter, we have discussed the carrier transport simulation models provided in the *monacoQC* framework. We have started with a short overview of the carrier transport approaches widely used in literature. In general, all of these models can be easily integrated into the *monacoQC* framework by providing a suitable interface class. However, we restrict ourselves here to the in-house DM-EMC model and a rate equation model for the modeling of QCDs. A strong focus was put on the evaluation of the simulation results and the creation of a reduced quantum model, which can then be used as input setup for the dynamic Maxwell-density matrix Langevin simulation approach *mbsolve*.

First, we have characterized the main scattering mechanisms in the quantum well heterostructure, which consist of elastic, inelastic and carrier-carrier scattering. With the help of Fermi's golden rule, we can determine the scattering rate between the initial and final states caused by a perturbation. Here, the individual state is characterized by its state number and the in-plane wave vector. The calculated scattering rates are then used as input for the EMC method, resulting in a self-consistent simulation approach. We also describe the stochastic EMC method and explain its density matrix extension, which includes incoherent tunneling. Since direct EMC modeling of photovoltaic QCDs is not feasible, we have developed a robust and compact approach based on a rate equation model and a Kirchhoff resistor network to calculate the key figure of merits.

Secondly, the results library of the *monacoQC* framework has been introduced. In this library, the results of the stationary carrier transport simulations and the eigenstate solutions of the SP solver are saved in corresponding class objects. The classes **eigenstates**, **conduction_band**, **carrier_distribution**, **scattering_rates** and **dephasing_rates** are introduced and their class functions, which can be used to visualize and analyze the

simulation results, are described. Using the intersubband electron distributions, we can determine the effective intersubband scattering and dephasing rates from the k-resolved scattering rates, as an abstraction of the extensive carrier transport simulations. The evaluation of the intraband dipole matrix element is explained by calculating the expected value of the momentum operator. Furthermore, we discuss the computation of the main figure of merit for the characterization of QC device performance in more detail.

Based on the carrier transport results, we can create a reduced quantum system model, which serves as input for the dynamic Maxwell-density matrix Langevin simulations. The corresponding class **msolve_sim** is used to derive a suitable quantum-mechanical description of the QC model. It provides some helper functions for the characterization, e.g., calculation of the gain spectrum or the second-order nonlinearity. Here, the most important tunneling transitions and optical transitions have to be identified to create a compact model. The quantum-mechanical description can then be extracted as a Python input script for the *mbsolve* approach.

4 Modeling of Fluctuations in Dynamical Optoelectronic Devices

For the modeling of the optical dynamics in miniaturized photonic devices, the Maxwell-Bloch equations are widely used since they form a relatively compact and numerically efficient model and thus allow for spatiotemporal simulations of the laser dynamics over many optical roundtrips [43], [47], [228]. Here, the Bloch equations are used for simulating the evolution of the quantum system and its coherent light-matter interaction with the optical field in the active medium. Additionally, the optical field propagation is treated classically within Maxwell's equations, where the coupling with the quantum system arises from the macroscopic polarization term [47]. The density matrix formalism can be extended and adapted by adding further quantized states in addition to the laser levels and tunneling between states. The inclusion of fluctuations accompanying electronic transport and spontaneous emission in dynamic simulations is of crucial importance.

Low-dimensional active photonic devices such as QCLs and QD structures can open up fascinating perspectives in quantum science. Since the nonclassical features are directly linked to the noise properties, detailed simulations of the coherent light-matter interaction are required for the development of low-noise optoelectronic quantum sources. Fluctuations arising from interactions of the optical field and quantum system with their reservoirs are treated within the quantum Langevin theory. Here, the fluctuations are included by adding stochastic c-number terms to the Maxwell-density matrix equations.

In the following, we restrict ourselves to optoelectronic devices where the optical field can be well modeled using 1D Maxwell's equations. This for example applies to semiconductor lasers with longitudinally invariant waveguide geometries, where the 3D Maxwell's equations can be reduced to an effective 1D model [47]. The focus lies on the inclusion of noise arising for example from spontaneous emission and fluctuations associated with the electron transport. First, we introduce the quantum Langevin equations using a simple three-level resonant tunneling QCL system in Section 4.1. Here, the reservoir variables are eliminated and replaced by drift and fluctuation terms within the Heisenberg equation of motion. The quantum Langevin equations can be transformed into associated c-number Langevin equations, as explained in Section 4.2. From this, we can derive the stochastic noise terms incorporated into the full-wave Maxwell-density matrix equation system. The resulting Maxwell-density matrix equations are described in Section 4.3. Finally, we give a short summary.

4.1 The Quantum Langevin Equations

The quantum Langevin equations are introduced by using a simple three-level resonant tunneling QCL system as depicted in Fig. 4.1 [55], [294]. The QCL exploits optical transitions between quantized states in the conduction band of a quantum well heterostructure, where the properties can be controlled by quantum design rather than being determined by the bulk material. This not only applies to the gain and lasing wavelength but also to the nonlinear optical properties such as FWM. Besides confinement provided by the quantum wells, another important quantum effect is tunneling through the separating barriers, which significantly influences carrier transport, in addition to the incoherent scattering-induced transitions due to phonons, crystal imperfections and electron-electron interactions [29], [35]. Regarding non-stationary QCL operation as is the case for OFC emission, coherent light-matter interaction as a further quantum effect plays a significant role in the dynamic

This chapter is largely based on Section II of J. Popp, J. Stowasser, M. A. Schreiber, *et al.*, "Modeling of fluctuations in dynamical optoelectronic device simulations within a Maxwell-density matrix Langevin approach", *APL Quantum*, vol. 1, no. 1, p. 016109, 2024. DOI: 10.1063/5.0183828, an open access article published under the terms of the Creative Commons Attribution 4.0 International License, which permits unrestricted use, distribution, and reproduction in any medium, provided the original author and source are credited.

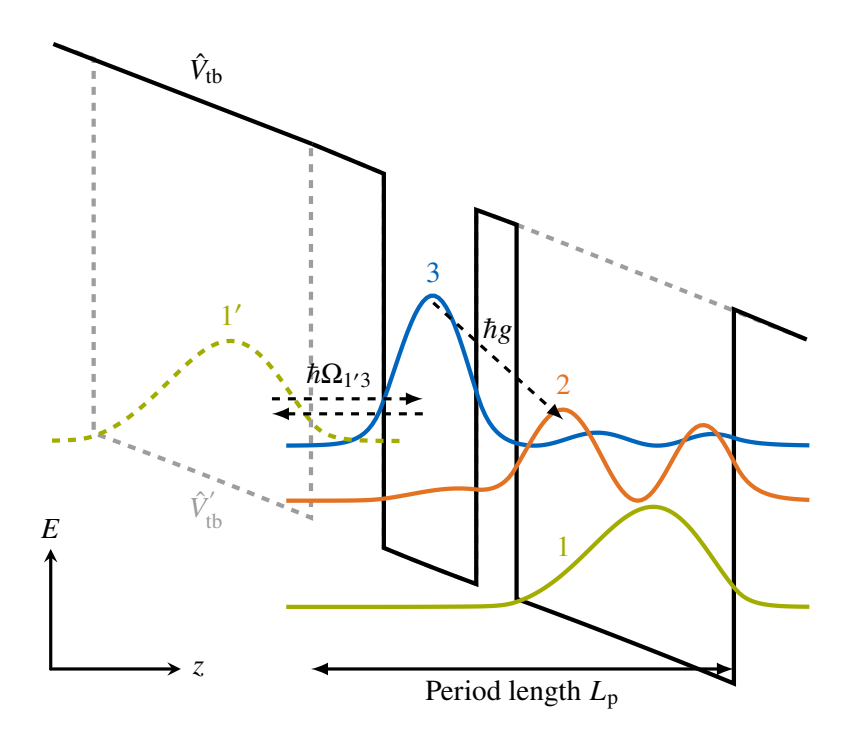


Figure 4.1 Schematic conduction band profile and probability densities of a two-well THz QCL structure, where the upper laser level 3 is populated via resonant tunneling from injector level 1'. Depopulation occurs through LO-phonon scattering from the lower laser level 2 to the depopulation level 1. Reprinted from J. Popp *et al.*, "Modeling of fluctuations in dynamical optoelectronic device simulations within a Maxwell-density matrix Langevin approach" [59] (CC BY 4.0).

behavior, e.g., leading to Rabi flopping [68], i.e., oscillations of the electron population between the upper and lower laser levels driven by the resonant optical field. Dephasing due to incoherent scattering has to be taken into account for a realistic description, as it greatly affects tunneling and coherent light-matter interaction.

For the structure shown in Fig. 4.1, the lasing transition occurs between the upper laser level $|3\rangle$ and the lower laser level $|2\rangle$. Depopulation takes place via level $|1\rangle$ and electrons are injected from the depopulation level $|1'\rangle$ of the adjacent period via resonant tunneling. The resonant tunneling across thick injection barriers in THz QCLs is treated within the tight-binding model [29], [32], [36], [71], [294], [295]. Here, the tunneling between a doublet of states at the thick injection barrier is described by the coupling strength $\Omega_{ij} = -\hbar^{-1} \langle i | \hat{V}_{\text{ext}} - \hat{V}_{\text{tb}} | j \rangle$, with the extended conduction band potential \hat{V}_{ext} and the tight-binding potential \hat{V}_{tb} . The coupling strengths Ω_{ij} between the states $|3\rangle$, $|2\rangle$, $|1\rangle$ within the active period are zero [32].

In general, the QCL system is then described by the reduced system Hamiltonian [87], [246], [320]

$$\begin{split} \hat{H}_{\mathrm{s}} &= \hat{H}_{\mathrm{F}} + \hat{H}_{0} + \Delta \hat{V}_{\mathrm{tb}} + \hat{H}_{\mathrm{I}} \\ &= \hbar \omega_{0} \hat{a}^{\dagger} \hat{a} + \sum_{i} E_{i} |i\rangle \langle i| - \hbar \Omega_{1'3} (|1'\rangle \langle 3| + |3\rangle \langle 1'|) + \hbar g(|3\rangle \langle 2| + |2\rangle \langle 3|) \Big(\hat{a} + \hat{a}^{\dagger} \Big) \,, \end{split} \tag{4.1}$$

where \hat{H}_F is the Hamiltonian of the optical field, \hat{H}_0 is the Hamiltonian of the quantum system with $\Delta \hat{V}_{tb}$ describing the coupling of electron states in two adjacent periods within the tight-binding model, and \hat{H}_I constitutes the interaction Hamiltonian between quantum system and optical field. Here, ω_0 is the single mode lasing angular frequency, $\hat{a}^{\dagger}(\hat{a})$ denotes the creation (annihilation) operator of the radiation field, E_i is the energy of level $|i\rangle$ and $\hbar\Omega_{1'3}$ the anticrossing energy gap between levels $|1'\rangle$ and $|3\rangle$. The dipole coupling constant g can be written in terms of the dipole matrix element, $d_{z,23} = q\langle 2|\hat{z}|3\rangle$, as [86], [320]

$$g = -\sqrt{\frac{\omega_0}{2\hbar\epsilon_r \epsilon_0 V_p}} d_{z,23}, \qquad (4.2)$$

where ϵ_r is the relative permittivity, ϵ_0 is the vacuum permittivity and V_p is the volume of each quantum system associated with an active QCL period.

The Heisenberg-Langevin equation of motion for an operator $\hat{A}_{\mu}(t)$ reads as [86]–[88], [241]

$$\partial_t \hat{A}_{\mu}(t) = -\mathrm{i}\hbar^{-1} [\hat{A}_{\mu}(t), \hat{H}_{\mathrm{s}}(t)] + \hat{D}_{\mu}(t) + \hat{F}_{\mu}(t) = \hat{M}_{\mu}(t) + \hat{F}_{\mu}(t) \,. \tag{4.3}$$

Here, the drift operator $\hat{D}_{\mu}(t)$ and fluctuation operator $\hat{F}_{\mu}(t)$ account for the influence of the reservoirs on the system. $[\cdot, \cdot]$ denotes the commutator $[\hat{X}, \hat{Y}] = \hat{X}\hat{Y} - \hat{Y}\hat{X}$. For the drift operator \hat{D}_{μ} we can under the Markovian approximation write [87], [88]

$$\hat{D}_{\mu} = -\sum_{i,j} \delta(\omega_i, -\omega_j) \left\{ [\hat{A}_{\mu}, \hat{Q}_i] \hat{Q}_j w_{ij}^+ - \hat{Q}_j [\hat{A}_{\mu}, \hat{Q}_i] w_{ji}^- \right\}, \tag{4.4}$$

where w^{\pm} are the reservoir spectral densities and \hat{Q}_i is a function of system operators. For a detailed description and derivation of this theory together with the calculation examples for specific operators \hat{A}_{μ} , we refer to [88] and [87].

The reservoir average of the fluctuation operator vanishes, $\langle \hat{F}_{\mu}^{\dagger} \rangle_{R} = \langle \hat{F}_{\mu} \rangle_{R} = 0$. The diffusion coefficient for a Markovian system is defined as

$$2\langle \hat{D}_{\mu\nu}(t)\rangle_{R}\delta(t-t') = \langle \hat{F}_{\mu}(t)\hat{F}_{\nu}(t')\rangle_{R}, \qquad (4.5)$$

and can be calculated by applying the fluctuation-dissipation theorem. Here, the δ -function indicates the very short memory period of the reservoirs. The *generalized Einstein relation* for the calculation of the diffusion coefficient is given by [86], [88], [321]

$$2\langle \hat{D}_{\mu\nu}(t)\rangle_{R} = \partial_{t}\langle \hat{A}_{\mu}(t)\hat{A}_{\nu}(t)\rangle_{R} - \langle \hat{M}_{\mu}(t)\hat{A}_{\nu}(t)\rangle_{R} - \langle \hat{A}_{\mu}(t)\hat{M}_{\nu}(t)\rangle_{R}. \tag{4.6}$$

From Eq. (4.3) together with Eqs. (4.1) and (4.4) the quantum Langevin equations for the three-level QCL quantum system can be derived. Therefore, we introduce the electron population operators $\hat{\sigma}_{ii} = |i\rangle\langle i|$ and the coherence operators $\hat{\sigma}_{ij} = |i\rangle\langle j|$. The term $\hat{\sigma}_{32}\hat{a}^{\dagger}$ describes the creation of a photon accompanied by an electron transition from the lower to the higher lying energy level and $\hat{\sigma}_{23}\hat{a}$ the annihilation of a photon accompanied by an electron transition from the higher to the lower lying energy level. At this point we drop these counter-rotating energy non-conserving terms in the interaction Hamiltonian \hat{H}_{I} as in the commonly used rotating wave approximation [86], [320]. This simplifies the following calculations of the noise terms. A more complete calculation should also include more than one mode of the optical field in the system Hamiltonian. However, these concessions do not affect the form of the specific noise terms which are ultimately used in our simulations. The corresponding equations of motion are given by

$$\partial_t \hat{a}(t) = -i\omega_0 \hat{a}(t) - \frac{\kappa}{2} \hat{a}(t) - g\hat{\sigma}_{23} + \hat{F}_a(t), \qquad (4.7a)$$

$$\partial_t \hat{\sigma}_{23}(t) = -\frac{\mathrm{i}}{\hbar} \Delta_{32} \hat{\sigma}_{23}(t) - \gamma_{23} \hat{\sigma}_{23}(t) + \mathrm{i}\Omega_{1'3} \hat{\sigma}_{21'}(t) + \mathrm{i}g(\hat{\sigma}_{33}(t) - \hat{\sigma}_{22}(t))\hat{a}(t) + \hat{F}_{23}(t), \qquad (4.7b)$$

$$\partial_t \hat{\sigma}_{31'}(t) = -\frac{\mathrm{i}}{\hbar} \Delta_{1'3} \hat{\sigma}_{31'}(t) - \gamma_{1'3} \hat{\sigma}_{31'}(t) + \mathrm{i} \Omega_{1'3} (\hat{\sigma}_{33}(t) - \hat{\sigma}_{1'1'}(t)) + \mathrm{i} g \hat{\sigma}_{21'}(t) \hat{a}^{\dagger}(t) + \hat{F}_{31'}(t), \qquad (4.7c)$$

$$\partial_t \hat{\sigma}_{21'}(t) = -\frac{\mathrm{i}}{\hbar} \Delta_{1'2} \hat{\sigma}_{21'}(t) - \gamma_{1'2} \hat{\sigma}_{21'}(t) + \mathrm{i} \Omega_{1'3} \hat{\sigma}_{23}(t) + \mathrm{i} g \hat{\sigma}_{31'}(t) \hat{a}(t) + \hat{F}_{21'}(t), \qquad (4.7d)$$

$$\partial_t \hat{\sigma}_{33}(t) = -\frac{1}{\tau_3} \hat{\sigma}_{33}(t) + r_{32} \hat{\sigma}_{22}(t) + r_{31'} \hat{\sigma}_{1'1'}(t) + ig \left[\hat{a}^{\dagger}(t) \hat{\sigma}_{23}(t) - \hat{a}(t) \hat{\sigma}_{23}^{\dagger}(t) \right]$$

$$-i\Omega_{1'3}(\hat{\sigma}_{31'}^{\dagger}(t) - \hat{\sigma}_{31'}(t)) + \hat{F}_{33}(t), \qquad (4.7e)$$

$$\partial_t \hat{\sigma}_{22}(t) = r_{23} \hat{\sigma}_{33}(t) - \frac{1}{\tau_2} \hat{\sigma}_{22}(t) + r_{21'} \hat{\sigma}_{1'1'}(t) + ig \left[\hat{a}(t) \hat{\sigma}_{23}^{\dagger}(t) - \hat{a}^{\dagger}(t) \hat{\sigma}_{23}(t) \right] + \hat{F}_{22}(t), \tag{4.7f}$$

$$\partial_{t}\hat{\sigma}_{1'1'}(t) = r_{1'3}\hat{\sigma}_{33}(t) + r_{1'2}\hat{\sigma}_{22}(t) - \frac{1}{\tau_{1'}}\hat{\sigma}_{1'1'}(t) - i\Omega_{1'3}\left[\hat{\sigma}_{31'}(t) - \hat{\sigma}_{31'}^{\dagger}(t)\right] + \hat{F}_{1'1'}(t), \qquad (4.7g)$$

where κ is the cavity decay rate, Δ_{ij} denotes the energy separation between levels $|i\rangle$ and $|j\rangle$, $\tau_i^{-1} = \sum_{i \neq j} r_{ji}$ is the inverse population lifetime, $r_{ij,i \neq j}$ represents the scattering rate from level j to i and γ_{ij} is the dephasing

rate, which can be calculated using Eq. (3.29). In QCLs, the pure dephasing rate $\gamma_{ij,p}$ mainly consists of elastic scattering contributions due to impurity and interface roughness [35]. The equivalent equations for $\hat{a}^{\dagger}(t)$, $\hat{\sigma}_{32}(t)$, $\hat{\sigma}_{1'3}(t)$ and $\hat{\sigma}_{1'2}(t)$ are given by the Hermitian conjugates of Eqs. (4.7)(a)-(d).

Using Eqs. (4.5) and (4.6), we can calculate the second-order correlation function relevant for the polarization operator as

$$\langle \hat{F}_{23}^{\dagger}(t)\hat{F}_{23}(t')\rangle_{R} = \left[\partial_{t}\langle \hat{\sigma}_{33}(t)\rangle_{R} - \langle \hat{M}_{23}^{\dagger}(t)\hat{\sigma}_{23}(t)\rangle_{R} - \langle \hat{\sigma}_{23}^{\dagger}(t)\hat{M}_{23}(t)\rangle_{R}\right]\delta(t-t')$$

$$= \left[\left\langle -\frac{1}{\tau_{3}}\hat{\sigma}_{33}(t) + r_{32}\hat{\sigma}_{22}(t) + r_{31'}\hat{\sigma}_{1'1'}(t) + ig\left[\hat{a}^{\dagger}(t)\hat{\sigma}_{23}(t) - \hat{a}(t)\hat{\sigma}_{23}^{\dagger}(t)\right]\right]$$

$$- i\Omega_{1'3}\left[\hat{\sigma}_{31'}^{\dagger}(t) - \hat{\sigma}_{31'}(t)\right]\right\rangle_{R} - \left\langle \left\{\frac{i}{\hbar}\Delta_{32}\hat{\sigma}_{23}^{\dagger}(t) - \gamma_{23}\hat{\sigma}_{23}^{\dagger}(t) - ig\left[\hat{\sigma}_{33}(t) - \hat{\sigma}_{22}(t)\right]\hat{a}^{\dagger}(t)\right\}$$

$$- i\Omega_{1'3}\hat{\sigma}_{1'2}(t)\right\}\hat{\sigma}_{23}(t)\right\rangle_{R} - \left\langle \hat{\sigma}_{23}^{\dagger}(t)\right\{-\frac{i}{\hbar}\Delta_{32}\hat{\sigma}_{23}(t) - \gamma_{23}\hat{\sigma}_{23}(t) + ig\left[\hat{\sigma}_{33}(t) - \hat{\sigma}_{22}(t)\right]\hat{a}(t)$$

$$+ i\Omega_{1'3}\hat{\sigma}_{21'}(t)\right\}\right\rangle_{R}\left[\delta(t-t')\right]$$

$$= \left[\left(2\gamma_{23} - \frac{1}{\tau_{3}}\right)\langle \hat{\sigma}_{33}(t)\rangle_{R} + r_{32}\langle \hat{\sigma}_{22}(t)\rangle_{R} + r_{31'}\langle \hat{\sigma}_{1'1'}(t)\rangle_{R}\right]\delta(t-t').$$

$$(4.8)$$

Here, we take into account the orthogonality of the levels $\langle i|j\rangle=\delta_{ij}$ and obtain

$$\hat{\sigma}_{23}^{\dagger}\hat{\sigma}_{23} = (|3\rangle\langle 2|2\rangle\langle 3|) = (|3\rangle\langle 3|) = \hat{\sigma}_{33}. \tag{4.9}$$

We use the same procedure to determine the other non-vanishing second-order correlation functions [87], [88]

$$\langle \hat{F}_a^{\dagger}(t)\hat{F}_a(t')\rangle_{\mathbf{R}} = \kappa n_{\text{th}}(\omega_0)\delta(t-t'), \qquad (4.10a)$$

$$\langle \hat{F}_a(t)\hat{F}_a^{\dagger}(t')\rangle_{\mathbf{R}} = \kappa(n_{\text{th}}(\omega_0) + 1)\delta(t - t'), \qquad (4.10b)$$

$$\langle \hat{F}_{23}(t)\hat{F}_{23}^{\dagger}(t')\rangle_{R} = \left[r_{23}\langle \hat{\sigma}_{33}(t)\rangle_{R} + \left(2\gamma_{23} - \frac{1}{\tau_{2}}\right)\langle \hat{\sigma}_{22}(t)\rangle_{R} + r_{21'}\langle \hat{\sigma}_{1'1'}(t)\rangle_{R}\right]\delta(t - t'), \qquad (4.10c)$$

$$\langle \hat{F}_{31'}^{\dagger}(t)\hat{F}_{31'}(t')\rangle_{R} = \left[r_{1'3}\langle \hat{\sigma}_{33}(t)\rangle_{R} + r_{1'2}\langle \hat{\sigma}_{22}(t)\rangle_{R} + \left(2\gamma_{1'3} - \frac{1}{\tau_{1'}}\right)\langle \hat{\sigma}_{1'1'}(t)\rangle_{R}\right]\delta(t - t'), \qquad (4.10d)$$

$$\langle \hat{F}_{31'}(t) \hat{F}_{31'}^{\dagger}(t') \rangle_{\mathbf{R}} = \left[\left(2\gamma_{1'3} - \frac{1}{\tau_3} \right) \langle \hat{\sigma}_{33}(t) \rangle_{\mathbf{R}} + r_{32} \langle \hat{\sigma}_{22}(t) \rangle_{\mathbf{R}} + r_{31'} \hat{\sigma}_{1'1'}(t) \right] \delta(t - t') , \qquad (4.10e)$$

$$\langle \hat{F}_{21'}^{\dagger}(t)\hat{F}_{21'}(t')\rangle_{R} = \left[r_{1'3}\langle \hat{\sigma}_{33}(t)\rangle_{R} + r_{1'2}\langle \hat{\sigma}_{22}(t)\rangle_{R} + \left(2\gamma_{1'2} - \frac{1}{\tau_{1'}}\right)\langle \hat{\sigma}_{1'1'}(t)\rangle_{R}\right]\delta(t - t'), \qquad (4.10f)$$

$$\langle \hat{F}_{21'}(t)\hat{F}_{21'}^{\dagger}(t')\rangle_{R} = \left[r_{23}\langle \hat{\sigma}_{33}(t)\rangle_{R} + \left(2\gamma_{1'2} - \frac{1}{\tau_{2}}\right)\langle \hat{\sigma}_{22}(t)\rangle_{R} + r_{21'}\langle \hat{\sigma}_{1'1'}(t)\rangle_{R}\right]\delta(t - t'), \qquad (4.10g)$$

$$\langle \hat{F}_{33}(t)\hat{F}_{33}(t')\rangle_{R} = \left[\frac{1}{\tau_{3}}\langle \hat{\sigma}_{33}(t)\rangle_{R} + r_{32}\langle \hat{\sigma}_{22}(t)\rangle_{R} + r_{31'}\langle \hat{\sigma}_{1'1'}(t)\rangle_{R}\right]\delta(t - t'), \qquad (4.10h)$$

$$\langle \hat{F}_{22}(t)\hat{F}_{22}(t')\rangle_{R} = \left[r_{23}\langle \hat{\sigma}_{33}(t)\rangle_{R} + \frac{1}{\tau_{2}}\langle \hat{\sigma}_{22}(t)\rangle_{R} + r_{21'}\langle \hat{\sigma}_{1'1'}(t)\rangle_{R}\right]\delta(t - t'), \qquad (4.10i)$$

$$\langle \hat{F}_{1'1'}(t)\hat{F}_{1'1'}(t')\rangle_{R} = \left[r_{1'3}\langle \hat{\sigma}_{33}(t)\rangle_{R} + r_{1'2}\langle \hat{\sigma}_{22}(t)\rangle_{R} + \frac{1}{\tau_{1'}}\langle \hat{\sigma}_{1'1'}(t)\rangle_{R} \right] \delta(t - t'). \tag{4.10j}$$

Here, $n_{\text{th}}(\omega_0) = \left[\exp\left(\frac{\hbar\omega_0}{k_{\text{B}}T}\right) - 1\right]^{-1}$ is the number of thermal photons in the lasing mode at temperature T.

4.2 The C-Number Langevin Equations

In order to derive the stochastic noise terms for the semiclassical Maxwell-density matrix equations, the operator Langevin equations have to be converted into the associated c-number Langevin equations.

The quantum Langevin equation for the operator $\hat{A}_{\mu}(t)$ in chosen order is given by

$$\partial_t \hat{A}_{\mu}(t) = -i\hbar^{-1} [\hat{A}_{\mu}(t), \hat{H}_{s}(t)]^c + \hat{D}_{\mu}^c(t) + \hat{F}_{\mu}^c(t), \qquad (4.11)$$

where we make use of the commutation relation $\hat{A}^{\dagger}_{\mu}\hat{A}_{\nu}=\hat{A}_{\nu}\hat{A}^{\dagger}_{\mu}-[\hat{A}_{\nu},\hat{A}^{\dagger}_{\mu}]$ to bring the equation into the chosen order. We use the superscript c to highlight that we have put the operators in chosen order. To explain this formulation in more detail, we use the fluctuation operator $\hat{F}_{\mu}(t)$ as an example, but the following description holds for the other operators in the same way. For a chosen order $\hat{A}_{1},\ldots,\hat{A}_{\mu}$, we can write

$$\hat{F}_{\mu} = \hat{F}_{\mu}^{c}(\hat{A}_{1}, \dots, \hat{A}_{\mu}), \tag{4.12}$$

where the fluctuation operator \hat{F}_{μ}^{c} in the chosen order is, of course, equal to the fluctuation operator \hat{F}_{μ} in the original order. The associated c-number fluctuation term $F_{\mu}^{c}(A_{1},...,A_{\mu})$ is obtained using c-numbers A_{ν} . By defining a linear chosen ordering operator \hat{C} we can further indicate [87], [322]

$$\hat{F}_{\mu}^{c}(\hat{A}_{1},...,\hat{A}_{\mu}) = \hat{C}(F_{\mu}^{c}(A_{1},...,A_{\mu})), \qquad (4.13)$$

where the operator \hat{C} has the function of replacing each A_{ν} by the corresponding operator \hat{A}_{ν} and bringing all terms into chosen order.

If we now convert the quantum Langevin equation into the equivalent c-number Langevin equation, we may write

$$\partial_t A_{\mu}(t) = L_{\mu}(t) + D_{\mu}(t) + F_{\mu}^{c}(t) = M_{\mu}(t) + F_{\mu}^{c}(t), \qquad (4.14)$$

with $L_{\mu}(t)$ being the coherent term corresponding to the commutation of $\hat{A}_{\mu}(t)$ with the system Hamiltonian \hat{H}_s , and $D_{\mu}(t)$ denoting the drift term. Furthermore, by the use of Eq. (4.14) we obtain the c-number equation

$$\partial_{t} \left[A_{\mu}(t) A_{\nu}(t) \right] = A_{\mu}(t) \partial_{t} A_{\nu}(t) + A_{\nu}(t) \partial_{t} A_{\mu}(t)$$

$$= A_{\mu}(t) M_{\nu}(t) + A_{\nu}(t) M_{\mu}(t) + A_{\mu}(t) F_{\nu}^{c}(t) + A_{\nu}(t) F_{\mu}^{c}(t) .$$

$$(4.15)$$

In analogy to the reservoir average in the operator case, we may write the c-number equation

$$\partial_t \langle A_{\mu}(t) A_{\nu}(t) \rangle_{\mathbf{R}} = \langle A_{\mu}(t) M_{\nu}(t) \rangle_{\mathbf{R}} + \langle A_{\nu}(t) M_{\mu}(t) \rangle_{\mathbf{R}} + 2 \langle D_{\mu\nu}(t) \rangle_{\mathbf{R}}, \tag{4.16}$$

where we can make use of the following relation under the Markovian approximation [86], [87]

$$2\langle D_{\mu\nu}(t)\rangle_{\mathbf{R}} = \langle A_{\mu}(t)F_{\nu}^{\mathbf{c}}(t) + A_{\nu}(t)F_{\mu}^{\mathbf{c}}(t)\rangle_{\mathbf{R}}. \tag{4.17}$$

The diffusion coefficients in the c-number Langevin equations may differ from the ones in the quantum Langevin equations, as the c-numbers commute, whereas the operators do not. By requiring the equivalence of Eq. (4.16) and Eq. (4.6) in both c-number and quantum Langevin theory, it can be shown that in general

$$2\langle \hat{D}_{\mu\nu}(t)\rangle_{\mathbf{R}} \neq 2\langle \hat{C}(D_{\mu\nu}(t))\rangle_{\mathbf{R}}. \tag{4.18}$$

By taking our chosen ordered operator representation of the system operators \hat{a}^{\dagger} , $\hat{\sigma}_{23}^{\dagger}$, $\hat{\sigma}_{31'}^{\dagger}$, $\hat{\sigma}_{21'}^{\dagger}$, $\hat{\sigma}_{33}$, $\hat{\sigma}_{22}$, $\hat{\sigma}_{1'1'}$, $\hat{\sigma}_{21'}$, $\hat{\sigma}_{23}$, \hat{a} , we obtain the corresponding c-numbers a^* , σ_{23}^* , $\sigma_{31'}^*$, $\sigma_{21'}^*$, σ_{33} , σ_{22} , $\sigma_{1'1'}$, $\sigma_{21'}$, $\sigma_{31'}$, σ_{23} , a.

As an example, we provide a detailed derivation of the diffusion coefficient $D_{3333}(t)$. Here, we prove the difference in diffusion coefficients, which arises through the transition from operator to c-number Langevin equations. By the use of Eqs. (4.6) and (4.7)(e), we obtain

$$\partial_{t}\langle\hat{\sigma}_{33}(t)\hat{\sigma}_{33}(t)\rangle_{R} = -\frac{2}{\tau_{3}}\langle\hat{\sigma}_{33}(t)\hat{\sigma}_{33}(t)\rangle_{R} + r_{32}\left[\underline{\langle\hat{\sigma}_{22}(t)\hat{\sigma}_{33}(t)\rangle_{R}} + \langle\hat{\sigma}_{33}(t)\hat{\sigma}_{22}(t)\rangle_{R}\right] + r_{31'}\left[\underline{\langle\hat{\sigma}_{1'1'}(t)\hat{\sigma}_{33}(t)\rangle_{R}} + \langle\hat{\sigma}_{33}(t)\hat{\sigma}_{1'1'}(t)\rangle_{R}\right] + ig\left[\underline{\langle\hat{a}^{\dagger}(t)\hat{\sigma}_{23}(t)\hat{\sigma}_{33}(t)\rangle_{R}} - \langle\hat{a}(t)\hat{\sigma}_{23}^{\dagger}(t)\hat{\sigma}_{33}(t)\rangle_{R} - \langle\hat{a}(t)\hat{\sigma}_{33}(t)\rangle_{R}\right] - i\Omega_{1'3}\left[\langle\hat{\sigma}_{31'}^{\dagger}(t)\hat{\sigma}_{33}(t)\rangle_{R} - \underline{\langle\hat{\sigma}_{31'}(t)\hat{\sigma}_{33}(t)\rangle_{R}} - \underline{\langle\hat{\sigma}_{31'}(t)\hat{\sigma}_{33}(t)\rangle_{R}} - \langle\hat{\sigma}_{33}(t)\hat{\sigma}_{31'}(t)\rangle_{R}\right] + 2\langle\hat{D}_{3333}(t)\rangle_{R}}.$$

$$(4.19)$$

Here, the terms that are underlined in red are not in the chosen order. The commutation relations are used to bring these terms into chosen order, and by exploiting the level orthogonality similarly to Eq. (4.9) we derive

$$[\hat{\sigma}_{22}(t), \hat{\sigma}_{33}(t)] = \hat{\sigma}_{22}(t)\hat{\sigma}_{33}(t) - \hat{\sigma}_{33}(t)\hat{\sigma}_{22}(t) = 0, \tag{4.20a}$$

$$[\hat{\sigma}_{23}(t), \hat{\sigma}_{33}(t)] = \hat{\sigma}_{23}(t),$$
 (4.20b)

$$[\hat{\sigma}_{33}(t), \hat{\sigma}_{23}^{\dagger}(t)] = \hat{\sigma}_{23}^{\dagger}(t),$$
 (4.20c)

$$[\hat{\sigma}_{31'}(t), \hat{\sigma}_{33}(t)] = -\hat{\sigma}_{31'}(t), \tag{4.20d}$$

$$[\hat{\sigma}_{33}(t), \hat{\sigma}_{31}^{\dagger}(t)] = -\hat{\sigma}_{31}^{\dagger}(t). \tag{4.20e}$$

With this, we can restructure Eq. (4.19) as follows:

$$\partial_{t}\langle\hat{\sigma}_{33}(t)\hat{\sigma}_{33}(t)\rangle_{R} = -\frac{2}{\tau_{3}}\langle\hat{\sigma}_{33}(t)\hat{\sigma}_{33}(t)\rangle_{R} + 2r_{32}\langle\hat{\sigma}_{33}(t)\hat{\sigma}_{22}(t)\rangle_{R} + 2r_{31'}\langle\hat{\sigma}_{33}(t)\hat{\sigma}_{1'1'}(t)\rangle_{R}$$

$$+2ig\left[\langle\hat{a}^{\dagger}(t)\hat{\sigma}_{33}(t)\hat{\sigma}_{23}(t)\rangle_{R} - \langle\hat{a}(t)\hat{\sigma}_{23}^{\dagger}(t)\hat{\sigma}_{33}(t)\rangle_{R}\right] - 2i\Omega_{1'3}\left[\langle\hat{\sigma}_{31'}^{\dagger}(t)\hat{\sigma}_{33}(t)\rangle_{R}$$

$$-\langle\hat{\sigma}_{33}(t)\hat{\sigma}_{31'}(t)\rangle_{R}\right] + 2\langle\hat{D}_{3333}(t)\rangle_{R} + ig\left[\langle\hat{a}^{\dagger}(t)\hat{\sigma}_{23}(t)\rangle_{R} - \langle\hat{a}(t)\hat{\sigma}_{23}^{\dagger}(t)\rangle_{R}\right]$$

$$+i\Omega_{1'3}\left[\langle\hat{\sigma}_{31'}^{\dagger}(t)\rangle_{R} - \langle\hat{\sigma}_{31'}(t)\rangle_{R}\right].$$

$$(4.21)$$

Here, the additional terms resulting from the operator ordering are underlined in green. With the use of Eqs. (4.14) and (4.15) we can derive the corresponding c-number equation

$$\partial_{t} \langle \sigma_{33}(t) \sigma_{33}(t) \rangle_{R} = -\frac{2}{\tau_{3}} \langle \sigma_{33}(t) \sigma_{33}(t) \rangle_{R} + 2r_{32} \langle \sigma_{33}(t) \sigma_{22}(t) \rangle_{R} + 2r_{31'} \langle \sigma_{33}(t) \sigma_{1'1'}(t) \rangle_{R}$$

$$+ 2ig \left[\langle a^{*}(t) \sigma_{33}(t) \sigma_{23}(t) \rangle_{R} - \langle a(t) \sigma_{23}^{*}(t) \sigma_{33}(t) \rangle_{R} \right] - 2i\Omega_{1'3} \left[\langle \sigma_{31'}^{*}(t) \sigma_{33}(t) \rangle_{R}$$

$$- \langle \sigma_{33}(t) \sigma_{31'}(t) \rangle_{R} \right] + 2\langle D_{3333}(t) \rangle_{R} .$$

$$(4.22)$$

If we now require the equivalence of the left-hand sides of Eqs. (4.21) and (4.22), we end up with the diffusion coefficient

$$\langle F_{33}(t)F_{33}(t')\rangle_{\mathbf{R}} = \left\{ \frac{1}{\tau_{3}} \langle \sigma_{33}(t)\rangle_{\mathbf{R}} + r_{32} \langle \sigma_{22}(t)\rangle_{\mathbf{R}} + r_{31'} \langle \sigma_{1'1'}(t)\rangle_{\mathbf{R}} + ig \left[\langle a^{*}(t)\sigma_{23}(t)\rangle_{\mathbf{R}} - \langle a(t)\sigma_{23}^{*}(t)\rangle_{\mathbf{R}} \right] + i\Omega_{1'3} \left[\langle \sigma_{31'}^{*}(t)\rangle_{\mathbf{R}} - \langle \sigma_{31'}(t)\rangle_{\mathbf{R}} \right] \right\} \delta(t - t'),$$

We further derive the c-number second-order moments for the remaining populations σ_{22} and $\sigma_{1'1'}$, which result in differing terms compared to the operator case:

$$\langle F_{22}(t)F_{22}(t')\rangle_{\mathbf{R}} = \left\{ r_{23}\langle \sigma_{33}(t)\rangle_{\mathbf{R}} + \frac{1}{\tau_2}\langle \sigma_{22}(t)\rangle_{\mathbf{R}} + r_{21'}\langle \sigma_{1'1'}(t)\rangle_{\mathbf{R}} + ig\left[\langle a^*(t)\sigma_{23}(t)\rangle_{\mathbf{R}} - \langle a(t)\sigma_{23}^*(t)\rangle_{\mathbf{R}}\right] \right\}$$

$$\delta(t - t'), \qquad (4.23a)$$

$$\langle F_{1'1'}(t)F_{1'1'}(t')\rangle_{R} = \left\{ r_{1'3}\langle \sigma_{33}(t)\rangle_{R} + r_{1'2}\langle \sigma_{22}(t)\rangle_{R} + \frac{1}{\tau_{1'}}\langle \sigma_{1'1'}(t)\rangle_{R} + i\Omega_{1'3} \left[\langle \sigma_{31'}^{*}(t)\rangle_{R} - \langle \sigma_{31'}(t)\rangle_{R} \right] \right\} \delta(t - t') . \tag{4.23b}$$

Additionally, we obtain diffusion coefficients absent in the quantum Langevin theory, e.g.

$$\langle F_{23}(t)F_{23}(t')\rangle_{\mathbf{R}} = 2\mathrm{i}g\langle a(t)\sigma_{23}(t)\rangle_{\mathbf{R}}\delta(t-t'), \qquad (4.24a)$$

$$\langle F_{31'}(t)F_{31'}(t')\rangle_{R} = -2i\Omega_{1'3}\langle \sigma_{31'}(t)\rangle_{R}\delta(t-t').$$
 (4.24b)

The complete diffusion matrix D(A,t) including all relevant cross-correlation terms of the three-level QCL system with the c-number vector $A = \begin{bmatrix} a^*, a, \sigma_{23}^*, \sigma_{31'}^*, \sigma_{21'}^*, \sigma_{33}, \sigma_{22}, \sigma_{1'1'}, \sigma_{21'}, \sigma_{31'}, \sigma_{23} \end{bmatrix}^T$ is given by

In literature ([323], [324]) it has been shown that a set of Ito stochastic differential equations (SDEs) can be derived for the given c-number vector and can serve as an efficient basis for numerical simulations. The equivalent Ito SDEs to the Langevin theory are given by

$$\partial_t \mathbf{A}(t) = \mathbf{M}(t) + \mathbf{F}(t) = \mathbf{M}(t) + \mathbf{B}(\mathbf{A}, t) \cdot \boldsymbol{\xi}(t), \qquad (4.26)$$

where $\xi(t)$ is a vector with real, independent Gaussian random numbers. Here, a semi-definite and symmetric diffusion matrix D(A, t) is required, which can then be factorized into the form [89], [323], [325]

$$\mathbf{D}(\mathbf{A},t) = \mathbf{B}(\mathbf{A},t)\mathbf{B}^{\mathrm{T}}(\mathbf{A},t), \qquad (4.27)$$

where the derived noise matrix B(A, t) is not necessarily symmetric.

To calculate the full noise matrix B(A,t) for the three-level QCL system, we can divide the diffusion matrix D(A,t) into four different submatrices, where a correlation between the corresponding terms is identified. The given subvector A_{ν} as well as the submatrices $B_{\nu}(A_{\nu},t)$ and $D_{\nu}(A_{\nu},t)$ are illustrated in Table 4.1. Here, we include correlations between three states by taking into account a tunneling transition followed by an optical transition. This leads to a substantial extension of the initially derived quantum theory of propagation of nonclassical radiation in a two-level system [89] and is of essential importance for the description of quantum fluctuations in THz QCL systems, where electron transport across thick barriers is mediated by tunneling between closely aligned energy levels. A detailed symbolic derivation of the noise submatrices $B_{\nu}(A_{\nu},t)$ and the resulting noise matrix B(A,t) for the three-level QCL system can be found in the GitHub project mbsolve [58].

By calculating the operator expectation value in the Schrödinger picture, we can demonstrate that the cnumbers representing the quantum system can be replaced by the density matrix elements ρ_{23} , $\rho_{31'}$, $\rho_{21'}$, ρ_{33} , ρ_{22} , $\rho_{1'1'}$, $\rho_{1'2}$, $\rho_{1'2}$, $\rho_{1'3}$, ρ_{32} . The expectation value can be written as

$$\langle \hat{\sigma}_{ij} \rangle = \text{Tr}\{|i\rangle\langle j|\hat{\rho}(t)\} = \text{Tr}\left\{|i\rangle\langle j|\sum_{i',i'}\rho_{j'i'}(t)|j'\rangle\langle i'|\right\} = \rho_{ji}(t). \tag{4.28}$$

Furthermore, we can write the interaction Hamiltonian \hat{H}_1 of the quantum system and the optical field as

$$\hat{H}_{I} = -\hat{d}_{z}\hat{E}_{z} = -d_{z,23}\hat{E}_{z}(\hat{\sigma}_{32} + \hat{\sigma}_{23}), \qquad (4.29)$$

where the electrical field operator \hat{E}_z is defined as

$$\hat{E}_z = \sqrt{\frac{\omega_0}{2\hbar\epsilon_r\epsilon_0 V_p}} (\hat{a}^\dagger + \hat{a}) e_z. \tag{4.30}$$

For devices in which the intraband transitions between quantized states occur within the conduction band, e.g., the QCL quantum well heterostructure, only the dipole matrix element d_z for the polarization in growth direction z is nonzero and relevant.

4.3 Generalized Maxwell-Density Matrix Langevin Equations in 1D

In the following, we derive the generalized Maxwell-density matrix Langevin equations with additional microscopic fluctuation terms and characterize the influence of spontaneous emission noise on the optical field evolution. For the description of the coherent carrier dynamics and the incoherent relaxation processes, as well as the interaction with the classical optical field, the generalized full-wave Maxwell-density matrix equations constitute a compact semiclassical model. By combining it with the Langevin approach, the microscopic noise characteristics can be fully taken into account. Here, the carrier dynamics in a SCL system are described in the density matrix formulation using the Lindblad equation

$$\partial_t \hat{\rho} = -i\hbar^{-1} [\hat{H}_0 + \Delta \hat{V}_{tb} + \hat{H}_I, \hat{\rho}] + \mathcal{D}(\hat{\rho}) + \mathcal{F}(\hat{\rho}), \qquad (4.31)$$

Table 4.1 Division of the diffusion matrix into submatrices $D_{\nu}(A_{\nu},t)$ and the corresponding c-number subvectors A_{ν} and noise submatrices $B_{\nu}(A_{\nu},t)$. In order to preserve the physical properties of the quantum system description, we have to interpret noise matrices $B_{\nu}(A_{\nu},t)$ differently for occupation and coherence terms. The differing matrix expressions for the coherence terms are highlighted here in red. Reprinted from J. Popp *et al.*, "Modeling of fluctuations in dynamical optoelectronic device simulations within a Maxwell-density matrix Langevin approach" [59] (CC BY 4.0).

subvector A_{ν}	submatrix $\boldsymbol{B}_{\nu}(\boldsymbol{A}_{\nu},t)$	submatrix $\boldsymbol{D}_{\nu}(\boldsymbol{A}_{\nu},t)$
$\begin{bmatrix} \sigma_{23}^* \\ \sigma_{33} \\ \sigma_{22} \\ \sigma_{23} \end{bmatrix}, \begin{bmatrix} \sigma_{31'}^* \\ \sigma_{33} \\ \sigma_{1'1'} \\ \sigma_{31'} \end{bmatrix}, \begin{bmatrix} \sigma_{21'}^* \\ \sigma_{22} \\ \sigma_{1'1'} \\ \sigma_{21'} \end{bmatrix}, \begin{bmatrix} \sigma_{21'}^* \\ \sigma_{33} \\ \sigma_{22} \\ \sigma_{1'1'} \\ \sigma_{23} \end{bmatrix}, \begin{bmatrix} \sigma_{31'}^* \\ \sigma_{33} \\ \sigma_{22} \\ \sigma_{31'} \end{bmatrix}, \begin{bmatrix} \sigma_{21'}^* \\ \sigma_{33} \\ \sigma_{22} \\ \sigma_{21'} \end{bmatrix}$	$\begin{bmatrix} a & -ia \\ -b & -ic \\ b & ic \\ a^* & ia^* \end{bmatrix}$	$\begin{bmatrix} 0 & -ab - ac & ab + ac & 2 a ^2 \\ -ab - ac & b^2 - c^2 & -b^2 + c^2 & -a^*b + a^*c \\ ab + ac & -b^2 + c^2 & b^2 - c^2 & a^*b - a^*c \\ 2 a ^2 & -a^*b + a^*c & a^*b - a^*c & 0 \end{bmatrix}$
$\begin{bmatrix} \sigma_{33} \\ \sigma_{22} \end{bmatrix}, \begin{bmatrix} \sigma_{33} \\ \sigma_{1'1'} \end{bmatrix}, \begin{bmatrix} \sigma_{22} \\ \sigma_{1'1'} \end{bmatrix}$ $\begin{bmatrix} \sigma_{23}^* \\ \sigma_{23} \\ \sigma_{23} \end{bmatrix}, \begin{bmatrix} \sigma_{31'}^* \\ \sigma_{31'} \end{bmatrix}$	$\begin{bmatrix} a \\ -a \end{bmatrix}, \begin{bmatrix} a \\ a^* \end{bmatrix}$	$\begin{bmatrix} a^2 & -a^2 \\ -a^2 & a^2 \end{bmatrix}, \begin{bmatrix} a^2 & a ^2 \\ a ^2 & (a^*)^2 \end{bmatrix}$
$\begin{bmatrix} \sigma_{23}^* \\ \sigma_{31'}^* \\ \sigma_{31'} \\ \sigma_{23} \end{bmatrix}, \begin{bmatrix} \sigma_{23}^* \\ \sigma_{21'}^* \\ \sigma_{21'} \\ \sigma_{23} \end{bmatrix}, \begin{bmatrix} \sigma_{23}^* \\ \sigma_{21'}^* \\ \sigma_{23}^* \end{bmatrix}$	$\begin{bmatrix} a & ia \\ b & -ib \\ c & ic \\ a^* & -ia^* \end{bmatrix}$	$\begin{bmatrix} 0 & 2ab & 0 & 2 a ^2 \\ 2ab & 0 & 2bc & 0 \\ 0 & 2bc & 0 & 2a^*c \\ 2 a ^2 & 0 & 2a^*c & 0 \end{bmatrix}$
$\begin{bmatrix} \sigma_{23}^* \\ \sigma_{23} \end{bmatrix}, \begin{bmatrix} \sigma_{31'}^* \\ \sigma_{31'} \end{bmatrix}, \begin{bmatrix} \sigma_{21'}^* \\ \sigma_{21'} \end{bmatrix}$	$\begin{bmatrix} a & ia \\ a & -ia \end{bmatrix}$	$\begin{bmatrix} 0 & 2a^2 \\ 2a^2 & 0 \end{bmatrix}$

which is coupled to Maxwell's equations in one dimension

$$\partial_t E_z = \varepsilon^{-1} \left(-\sigma E_z - \partial_t P_{z,\text{class}} - \Gamma \partial_t P_{z,\text{om}} + \partial_x H_v \right), \tag{4.32a}$$

$$\partial_t H_y = \mu^{-1} \partial_x E_z \,, \tag{4.32b}$$

where $\mathcal{D}(\hat{\rho})$ is the dissipation superoperator, $\mathcal{F}(\hat{\rho})$ is an additional Langevin fluctuation superoperator and the other operators have their usual meanings. The permittivity is given by the product $\varepsilon = \varepsilon_0 \varepsilon_r$, σ is the material conductivity, μ is the permeability, and the confinement factor $\Gamma \in [0,1]$ gives the spatial overlap of the transverse optical field mode with the quantum system. As we focus in this work on optoelectronic devices with invariant transverse field distribution, the reduction to a one-dimensional model for the optical propagation in the waveguide is justified [47]. The Lindblad equation is the general form of a time-local and Markovian linear master equation for a quantum system, described by its completely positive trace-preserving density matrix, interacting with an environment. Obviously, the conventional Bloch equations, corresponding to a two-level system, describe the interaction of the laser levels with the optical field E_z and constitute a special case of the Lindblad equation given in Eq. (4.31). The interaction with the environment is here modeled by scattering and dephasing rates, r_{ij} and γ_{ij} . Further levels can be considered in Eq. (4.31), and additional effects such as tunneling are included in the Hamiltonian. Moreover, quantum fluctuations are considered in the model given by Eq. (4.31) by adding a suitable Langevin fluctuation superoperator \mathcal{F} . Maxwell's equations capture the optical propagation through the waveguide resonator, where the coupling with the quantum system is described by the macroscopic polarization $P_{z,qm}$ arising from the contributions of the dipole matrix elements. The expectation value of the dipole moment operator \hat{d}_z is calculated by averaging over a large ensemble of quantum systems within an adequate volume V_p around the position z, and we can write for the macroscopic polarization

$$P_{z,\text{qm}} = n_{3D} \operatorname{Tr} \{ \hat{d}_z \hat{\rho} \} = n_{3D} (d_{z,23} \rho_{32} + d_{z,32} \rho_{23}) = n_{3D} d_{z,23} (\rho_{32} + \rho_{23}), \tag{4.33}$$

where n_{3D} is the carrier number density. The two classical contributions, $P_{z,\text{class}} = \epsilon_0 \chi E_z$ and σE_z , account for the polarization caused by bulk and waveguide dispersion as well as the material losses [326].

Finally, the update equations of the density matrix elements for the QCL laser system depicted in Fig. 4.1 can be written as

$$\partial_t \rho_{32}(t) = -\frac{\mathrm{i}}{\hbar} \Delta_{32} \rho_{32}(t) - \gamma_{23} \rho_{32}(t) + \mathrm{i}\Omega_{1'3} \rho_{1'2}(t) + \frac{\mathrm{i}}{\hbar} d_{z,23} E_z [\rho_{33}(t) - \rho_{22}(t)] + F_{23}(t), \qquad (4.34a)$$

$$\partial_t \rho_{1'3}(t) = -\frac{\mathrm{i}}{\hbar} \Delta_{1'3} \rho_{1'3}(t) - \gamma_{1'3} \rho_{1'3}(t) + \mathrm{i} \Omega_{1'3} [\rho_{33}(t) - \rho_{1'1'}(t)] + \frac{\mathrm{i}}{\hbar} d_{z,23} E_z \rho_{1'2}(t) + F_{31'}(t), \qquad (4.34b)$$

$$\partial_t \rho_{1'2}(t) = -\frac{\mathrm{i}}{\hbar} \Delta_{1'2} \rho_{1'2}(t) - \gamma_{1'2} \rho_{1'2}(t) + \mathrm{i} \Omega_{1'3} \rho_{32}(t) + \frac{\mathrm{i}}{\hbar} d_{z,23} E_z \rho_{1'3}(t) + F_{21'}(t), \qquad (4.34c)$$

$$\partial_{t}\rho_{33}(t) = -\frac{1}{\tau_{3}}\rho_{33}(t) + r_{32}\rho_{22}(t) + r_{31'}\rho_{1'1'}(t) - 2\hbar^{-1}d_{z,23}E_{z}\mathfrak{Im}\{\rho_{32}(t)\} - 2\Omega_{1'3}\mathfrak{Im}\{\rho_{1'3}(t)\} + F_{33}(t),$$

$$(4.34d)$$

$$\partial_t \rho_{22}(t) = r_{23}\rho_{33}(t) - \frac{1}{\tau_2}\rho_{22}(t) + r_{21'}\rho_{1'1'}(t) + 2\hbar^{-1}d_{z,23}E_z \mathfrak{Im}\{\rho_{32}(t)\} + F_{22}(t), \qquad (4.34e)$$

$$\partial_t \rho_{1'1'}(t) = r_{1'3} \rho_{33}(t) + r_{1'2} \rho_{22}(t) - \frac{1}{\tau_{1'}} \rho_{1'1'}(t) + 2\Omega_{1'3} \mathfrak{Im} \{ \rho_{1'3}(t) \} + F_{1'1'}(t) . \tag{4.34f}$$

Via the macroscopic polarization $P_{z,qm}$, the quantum fluctuations added to the coherence term of Eq. (4.34a) have an influence on the evolution of the classical optical field. The quantum-mechanical fluctuation terms for the three-level QCL quantum system are derived within the framework of the Langevin theory. In this work, we have calculated the full diffusion matrix resulting from the c-number Langevin equations. Exploiting the positive semi-definiteness of the diffusion matrix, one can show that there exists a set of Ito stochastic differential equations equivalent to the Langevin equations. We can factorize the diffusion matrix to obtain a noise matrix that can be directly integrated into the Maxwell-density matrix approach for numerical modeling of fluctuations in dynamical optoelectronic devices. With a suitable choice of the noise matrix, one can guarantee a completely positive trace-preserving update map for long-term simulations. For the three-level QCL system, the fluctuation

terms will fully account for the influence of the reservoirs and the properties of the nonlinear coupling between QCL system and optical field, including the incoherent tunneling transition, and can be represented as follows:

$$\begin{split} F_{23}(t) &= \xi_{11}(t)\sqrt{v_{32}} + \xi_{14}(t)\sqrt{v_{12}} - \xi_{24}(t)\sqrt{2id_{z,23}E_z(t)}\rho_{32}(t) - \xi_{31}^*(t)\frac{id_{z,23}E_z(t)}{2} + \xi_{32}^*(t)\frac{id_{z,23}E_z(t)}{2} \\ &+ \xi_{33}^*(t)\sqrt{\frac{\gamma_{12} - \gamma_{123} + \gamma_{23}}{2}} + \xi_{41}^*(t)\left[\frac{\gamma_{123} - \gamma_{12} - \gamma_{23}}{2} + \frac{r_{32}\rho_{22}(t)}{2} + \frac{2\gamma_{23} - r_{123} - r_{23}}{2}\rho_{33}(t) - \frac{d^2_{z,23}E_z(t)^2}{2} - r_{12} - r_{22} + d_{z,23}E_z(t)|\rho_{32}(t)\right]^{1/2}, \end{split} \tag{4.35a} \\ &- \frac{d^2_{z,23}E_z(t)^2}{2} - r_{12} - r_{22} + d_{z,23}E_z(t)|\rho_{32}(t)| \int_{-2}^{1/2} + \frac{r_{32}\rho_{22}(t)}{2} + \frac{2\gamma_{23} - r_{123} - r_{23}}{2}\rho_{33}(t) \\ &+ \xi_{32}^*(t)\left[\frac{2\gamma_{13} - \gamma_{12} - \gamma_{23}}{2}\rho_{11}(t)\sqrt{t_{12}} + \xi_{13}(t)\rho_{12}(t) + \frac{r_{12}}{2}\rho_{22}(t) - |\rho_{31}(t)|^2 + \frac{r_{12}}{2}\rho_{33}(t) - d^2_{z,23}E_z(t)^2 - r_{123}}{2} - r_{23} + \Omega_{31}|\rho_{31}(t)\right]^{1/2}, \end{split} \tag{4.35b} \\ &F_{21'}(t) = \xi_{13}(t)\sqrt{r_{12}} + \xi_{16}(t)\sqrt{r_{22}} + \xi_{32}(t)\rho_{12}(t) + \xi_{33}^*(t)\sqrt{\frac{\gamma_{12} - \gamma_{12} + \gamma_{23}}{2}}\rho_{12}(t) \\ &+ \xi_{43}^*(t)\left[\frac{2\gamma_{12} - \gamma_{12} - \gamma_{22}}{2}\rho_{31}(t)\right]^2\right]^{1/2}, \end{split} \tag{4.35c} \\ &F_{33}(t) = -\xi_{11}^*(t)\frac{\sqrt{r_{23}\rho_{23}\rho_{23}}(t)}{2} + \xi_{16}(t)\sqrt{r_{23}\rho_{23}\rho_{23}(t)} + \xi_{12}^*(t)\frac{\sqrt{r_{13}\rho_{13}}(t)}{2} + \xi_{12}(t)\frac{\sqrt{r_{13}\rho_{13}}(t)}{2} \\ &+ \xi_{13}^*(t)\frac{\sqrt{r_{23}\rho_{23}\rho_{23}}(t)}{2} + \xi_{13}(t)\left[\frac{\sqrt{r_{23}\rho_{23}}\rho_{33}(t)}{2} + \xi_{12}^*(t)\frac{\sqrt{r_{13}\rho_{13}}(t)}{2} + \xi_{12}(t)\frac{\sqrt{r_{13}\rho_{23}}(t)}{2} \\ &+ \xi_{13}^*(t)\frac{\sqrt{r_{23}\rho_{23}}(t)}{2} + \xi_{13}(t)\frac{\sqrt{r_{23}\rho_{23}}(t)}{2} + \xi_{13}(t)\frac{\sqrt{r_{13}\rho_{13}}(t)}{2} + \xi_{12}(t)\frac{\sqrt{r_{13}\rho_{13}}(t)}{2} \\ &- \xi_{16}(t)\frac{\sqrt{r_{23}\rho_{23}}(t)}{2} + \xi_{21}(t)\left[-(r_{23} + 1)|\rho_{12}(t)|^2 + r_{23}[\rho_{33}(t) - |\rho_{13}(t)|^2] + r_{31}[\rho_{12}(t)} \\ &+ r_{13}[\rho_{33}(t) - |\rho_{13}(t)|^2]\right]^{1/2}, \end{split} \tag{4.35d} \\ &F_{22}(t) = \xi_{11}^*(t)\frac{\sqrt{r_{12}\rho_{23}}(t)}{2} + \xi_{16}(t)\frac{\sqrt{r_{12}\rho_{23}}(t)}{2} + \xi_{15}(t)\frac{\sqrt{r_{12}\rho_{23}}(t)}{2} + \xi_{15}(t)\frac{\sqrt{r_{12}\rho_{23}}(t)}{2} \\ &+ \xi_{15}(t)\frac{\sqrt{r_{12}\rho_{23}}(t)}{2} + \xi_{16}(t)\frac{\sqrt{r_{12}\rho_{23}}(t)}{2} - \xi_{15}(t)\frac{\sqrt{r_{12}\rho_{23}}(t)}{2} \\ &+ \xi_{15}(t)\frac{\sqrt{r_{12}\rho_{23}}(t)}{2} + \xi_{16}(t)\frac{\sqrt{r_{12}\rho_{23}$$

$$F_{1'2}(t) = \xi_{13}^*(t)\sqrt{r_{1'2}} + \xi_{16}^*(t)\sqrt{r_{32}} + \xi_{32}^*(t)\rho_{21'}(t) + \xi_{33}(t)\sqrt{\frac{\gamma_{1'2} - \gamma_{1'3} + \gamma_{23}}{2}}\rho_{1'3}(t) + \xi_{43}(t) \left[\frac{r_{1'2}}{2}\rho_{22}(t) + \frac{2\gamma_{1'3} - \gamma_{1'2} - \gamma_{23}}{2}\rho_{1'1'}(t) - |\rho_{21'}(t)|^2 + \frac{r_{1'3}}{2}\rho_{33}(t) - r_{1'2} - r_{32} - \frac{\gamma_{1'3} - \gamma_{1'2} - \gamma_{23}}{2} \right]$$

$$\times |\rho_{31'}(t)|^2 \Big]^{1/2}, \qquad (4.35g)$$

$$F_{1'3}(t) = \xi_{12}^*(t)\sqrt{r_{1'3}} + \xi_{15a}^*(t)\sqrt{r_{23}} + \xi_{15b}^*(t)id_{z,23}E_z(t) + \xi_{25}(t)\sqrt{2i\Omega_{31'}\rho_{31'}(t)} + \xi_{31}^*(t)\rho_{31'}(t) + \xi_{42}(t) \left[\frac{r_{1'2}}{2}\rho_{22}(t) + \frac{2\gamma_{1'3} - \gamma_{1'2} - \gamma_{23}}{2}\rho_{1'1'}(t) - |\rho_{31'}(t)|^2 + \frac{r_{1'3}}{2}\rho_{33}(t) - d_{z,23}^2E_z(t)^2 - r_{1'3} - r_{23} + \Omega_{3'1}|\rho_{31'}(t)|\right]^{1/2}, \qquad (4.35h)$$

$$F_{32}(t) = \xi_{11}^*(t)\sqrt{r_{32}} + \xi_{14}^*(t)\sqrt{r_{1'2}} + \xi_{24}(t)\sqrt{-2id_{z,23}E_z(t)\rho_{23}(t)} + \xi_{31}(t)\frac{id_{z,23}E_z(t)}{2} - \xi_{32}(t)\frac{id_{z,23}E_z(t)}{2} + \xi_{33}(t)\sqrt{\frac{\gamma_{1'2} - \gamma_{1'3} + \gamma_{23}}{2}} + \xi_{41}(t)\left[\frac{\gamma_{1'3} - \gamma_{1'2} - \gamma_{23}}{2} + \frac{r_{32}\rho_{22}(t)}{2} + \frac{2\gamma_{23} - r_{1'3} - r_{23}}{2}\rho_{33}(t) - \frac{d_{z,23}^2E_z(t)^2}{2} - r_{1'2} - r_{32} + d_{z,23}E_z(t)|\rho_{32}(t)|\right]^{1/2}. \qquad (4.35i)$$

Here, the terms ξ_{11} , ξ_{12} , ξ_{13} , ξ_{14} , ξ_{15a} , ξ_{15b} , ξ_{16} , ξ_{31} , ξ_{32} , ξ_{33} , ξ_{41} , ξ_{42} , ξ_{43} are complex, while ξ_{21} , ξ_{22} , ξ_{23} , ξ_{24} , ξ_{25} are real.

For the reduction to a two-level system, we obtain similar noise terms as derived by Drummond and Raymer [89]. However, unlike Drummond and Raymer we can assure the preservation of the physical properties of the density matrix, i.e., positive definiteness and unit trace. This is accomplished by a suitable choice of the submatrices $B_{\nu}(A_{\nu}, t)$ depicted in Table 4.1.

4.4 Summary

In this chapter, we have described the quantum Langevin approach for a three-level quantum system. Here, the non-classical operator description is used for the derivation of the Heisenberg-Langevin equations. Based on the generalized Einstein relation the diffusion coefficients can be calculated. The presented approach is an extension of the well-known two-level quantum theory by Drummond and Raymer [89], where we additionally take into account incoherent tunneling injection into the upper laser level. The quantum Langevin equations are then converted into the associated c-number Langevin equations. It is shown that the diffusion coefficients in the c-number Langevin equations differ from those in the quantum Langevin equations. The c-numbers commute, while the operators do not. The complete diffusion matrix including all relevant cross-correlation terms of the three-level QCL system is calculated. On the basis of Ito-SDEs, we have derived the complete noise matrix for the three-level QCL system.

We combine the c-number Langevin equations with the Maxwell-density matrix equations to account for microscopic fluctuations accompanying electronic transport and spontaneous emission in the dynamical simulations of light-matter interaction in multilevel quantum optoelectronic systems, such as QCLs and QD lasers. Within the generalized Maxwell-density matrix Langevin equations we can ensure the preservation of the physical properties of the density matrix, i.e., positive definiteness and unit trace. The derived noise terms are included in our open-source simulation tool *mbsolve*. Our modeling approach based on the generalized Maxwell-density matrix Langevin equations shows great potential for the theoretical investigation of intermodal intensity correlations in photonic devices and the development of low-noise integrated light emitters, also with regard to the generation of non-classical light.

5 An Open-Source Solver for the Maxwell-Density Matrix Langevin Equations

The Maxwell-density matrix equations are commonly treated in the so-called rotating-wave/slowly varying amplitude approximation, generally used to reduce the numerical load associated with the fast field oscillations [43], [47]. This is only valid for relatively narrowband (and not too strong) optical fields. However, QCLs offer the potential for generating spectra extending over a full octave and beyond [108]. None of the available open-source platforms are suitable for our purposes, mostly because they employ the rotating-wave approximation. For this reason, the Computational Photonics group has developed the open-source project *mbsolve* in recent years. It enables numerically extensive simulations of multilevel systems based on the full-wave Maxwell-density matrix equations [58], [72]. An important point in this work was the extension of the codebase towards the Maxwell-density matrix Langevin equations, so that we can account for vacuum fluctuations due to spontaneous emission and fluctuations related to electronic transport [44], [233], [251].

In detail, the development of the codebase has been based on various principles. Here, the generalized Lindblad equation (Eq. (4.31)) instead of the usual, quite restrictive two-level Bloch equation model is used. Furthermore, numerical methods have been developed that preserve physical properties, such as the complete positivity and trace preservation of the density matrix [47], [328]. This is especially important in the context of long-term simulations, as required for frequency comb modeling. A computational speedup is obtained by using parallelization techniques [329]. Our scientific software package *mbsolve* is developed following sustainable software engineering strategies and includes all common and essential best software engineering practices [329], [330]. It is based on C++ for performance reasons and features an easy-to-use Python interface facilitating the setup and active quantum system of the low-dimensional optoelectronic structures. The modular architecture of the *mbsolve* project, as shown in Fig. 5.1, provides the required flexibility in the numerical treatment of the Maxwell-density matrix (Langevin) equation system to efficiently model the spatio-temporal dynamics in active photonic devices. The extensions of the *mbsolve* simulation library carried out in this work with the corresponding components are highlighted in dark blue. For a detailed package description, including the remaining modules, the reader is referred to [72] and [331]. The central part of the software is the objectoriented mbsolve-lib base library, providing a framework for defining a simulation setup and the infrastructure to add solver and writer components. Importantly, mbsolve supports different numerical methods for solving the Lindblad equation [328], [331], as well as different parallelization techniques, e.g., OpenMP for shared memory systems.

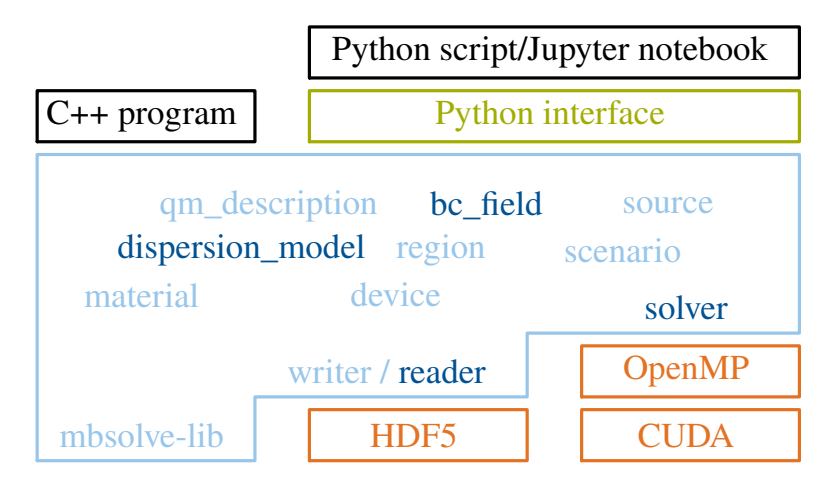


Figure 5.1 Overview of the *mbsolve* project. Modified from M. Riesch, The QCL Stock Image Project [327] (CC BY 4.0).

This chapter is organized as follows: In Section 5.1, an overview of the mbsolve-lib base library is given. We will review existing numerical methods for the Maxwell-density matrix (Langevin) equations and introduce the new implementations in *mbsolve*, e.g., the calculation of the fluctuations terms, the truncation of the optical field at the simulation boundaries or the treatment of chromatic waveguide dispersion. Another new function for restarting the simulation is also described. Subsequently, the corresponding code changes with regard to the numerical treatment of the Maxwell-density matrix Langevin equations are presented in Section 5.2. Therefore, we introduce the auxiliary differential equation (ADE) finite-difference time-domain method for the truncation of lossy and dispersive media and the update algorithm for the density matrix equation including the propagation of the fluctuations. An overview of the new generalized updating equations for lossy and dispersive materials including the absorbing boundary conditions is given in Section 5.3 and the simulation main loop is explained. Finally, we conclude with a short summary.

5.1 Implementations and Extensions of mbsolve

Different methods exist in literature to solve the density matrix equation. We will give here a short overview of the existing methods and characterize their properties with respect to physical accuracy and numerical performance. In [332] and [333] the implicit Crank-Nicolson (CN) scheme refined by the predictor-corrector (PC) technique was used to solve the Lindblad equation. Furthermore, implementations based on matrix exponentials (ME) [334]–[338] and the Runge-Kutta (RK) method [339]–[341] have been presented. The main criterion for the evaluation of the master equation is the preservation of the physical properties of the density matrix, e.g., positive definiteness and trace preservation. In recent years, the above techniques have been verified [328], [335], [342], and only the ME methods can provide a fully positive, trace-preserving update map. A detailed comparison of the different methods can be found in [331]. Within the current version of the open-source *mbsolve* project, we provide the two most promising density matrix algorithms based on the matrix exponential approach. The class algo_lindblad_reg_cayley implements the operator splitting method by Bidégaray [335], [343]. In the second implementation algo_lindblad_cvr_rodr, we consider the density matrix in the coherence vector representation [344], in which the density matrix is transformed into a real-valued, non-redundant vector. Here, the matrix exponential calculations are conducted using Rodrigues' formula [331]. The two methods complement each other well in terms of accuracy and reasonable performance. While the first one shows a good overall performance, the latter one is especially suited for two- and three-level systems problems in terms of numerical efficiency. We further extended our code base considering vacuum fluctuations due to spontaneous emission and fluctuations associated with electronic transport [44], [233], [251]. Therefore, we have added a new density matrix algorithm class to account for fluctuations accompanying the electronic transport and vacuum fluctuations. The density matrix algorithm class algo_lindblad_reg_cayley_qnoise is based on the aforementioned operator splitting method. In addition to the class method **propagate dissipation** for the dissipation update step, the **propagate_fluctuation** method for updating the fluctuations is specified here.

In the context of Maxwell-density matrix equations mainly two numerical methods out of many are used to solve Maxwell's equations, namely the pseudo-spectral time-domain (PSTD) and the finite difference time-domain (FDTD) method. The PSTD method, which has been used in related works [334], [336], calculates the spatial derivatives using the fast Fourier transform (FFT) in space. Therefore, the numerical dispersion can be minimized and the spatial discretization requirements can be significantly reduced, provided that the Nyquist-Shannon theorem is satisfied. A spatial discretization size $\lambda/10$ has been used in literature [334], with λ denoting the smallest occurring wavelength. Major drawbacks of this method are the potentially expensive calls for the FFT and the complex implementations of e.g., absorbing boundary conditions (ABCs). In the context of Maxwell-density matrix equations, the FDTD method is mostly used [47], [251], [332], [333], [335], [349], [343], [345]–[348], as it has a great advantage in terms of simplicity. The approximation of the spatial and temporal derivatives by central differences makes the implementation quite easy and the integration of ABCs or source terms straightforward. However, a finer spatial discretization is required to reduce the numerical dispersion, resulting in an increased numerical workload. Spatial discretization sizes between $\lambda/20$ and $\lambda/200$ have been found adequate [47], [332], [335], [349], [350]. A template class **solver_cpu_fdtd** is implemented in *mbsolve*

targeting CPU based shared memory systems. Here we can simply add the above-mentioned density matrix algorithms as template arguments and compile specific solver objects, e.g., solver_cpu_reg_cayley_qnoise with the corresponding algorithm algo_lindblad_reg_cayley_qnoise for updating the density matrix. We need to provide the template argument at compile time, which significantly increases the time required for compilation but provides an efficient approach at runtime. Furthermore, an advanced FDTD implementation is available, which takes advantage of redundant calculations of the field values to reduce the synchronization overhead during runtime [351], [352]. The template class solver_cpu_fdtd_red with the suffix red implements this communication-reducing approach and can be combined with various density matrix algorithms in a similar way as with solver_cpu_fdtd.

A major challenge in simulating optical devices in open radiation problems is the truncation of the FDTD lattice [353]. One idea to solve this is to use a highly absorbing, reflectionless layer at the outer boundary of the spatial FDTD grid. Berenger therefore introduced the perfectly matched layers (PMLs) as a non-physical absorber in 1994 [354]. His approach is based on the so-called field-splitting method, where the field components are split into two orthogonal components resulting in modified Maxwell's equations. In addition, Fang et al. developed a general PML method for lossy materials by extending the original PML approach [355], [356]. A uniaxial anisotropic PML (UPML) absorber was presented by Gedney [357], where the mathematical model of field-splitting is replaced by a more physical model based on the Maxwellian formulation. In a later publication, he extended the approach to the absorption of fields in lossy and dispersive materials [358]. Wang et al. used both the unsplit and field-splitting methods for truncating a gain medium in a semiconductor Maxwell-Bloch framework [359]. To improve the absorbing characteristics of open radiation simulations in *mbsolve*, a modified PML model is introduced [360]. Parasitic reflection errors at the boundary arising from an impedance mismatch due to the interaction with the internal quantum system can be suppressed by expanding the active QCL gain medium into the PML region. We further have developed partially reflecting layer (PRL) boundary conditions [361], which model the reflectance R at the facet of e.g., THz DFG-QCL frequency comb devices correctly without decreasing the simulation performance by adding surrounding layers at the active gain medium facets [90]. It is important to emphasize here the necessity of PRLs for correct light outcoupling (R < 1) at the facet. In a DFG OFC QCL setup, for example, a spatially averaged loss would impose an unrealistically strong attenuation on the DFB mode, which counteracts the optical feedback mechanism. Single-mode operation would be suppressed, and DFG mixing and THz comb generation would not be feasible. These boundary conditions are based on the modified PMLs [360]. Unlike in PML absorbing boundaries, we here introduce a predefined impedance mismatch at the interface of the active region and the PRL. The facet reflectance R is adjusted by the relative permeability of the artificial boundary material, i.e.,

$$\mu_{\rm r,PRL} = \mu_{\rm r} \cdot \left(\frac{1 \pm \sqrt{R}}{1 \mp \sqrt{R}}\right)^2,$$
 (5.1)

where μ_r is the relative permeability of the material at the truncation facet. In the mbsolve-lib base library, the abstract base class **bc_field** together with different subclasses for the truncation of the active waveguide medium are specified. In addition to the UPML and PRL boundary conditions, perfectly magnetic conductors (PMCs), perfectly electric conductors (PECs), Mur and periodic boundary conditions are implemented. The device class holds a map as a property, which contains key-value pairs for the **left** and **right** boundary conditions. The default boundary conditions for both facets are initialized as PMCs but can be changed using the method **set_bc_field**. Within the **solver_cpu_fdtd** class the update algorithms in the boundaries are selected at runtime with respect to the defined device properties. A class **algo_bc_field_fdtd** is responsible for the correct simulation updates in the boundaries. The underlying properties for modeling the physical components within the boundary layer are combined in an artificial material, which is composed in relation to the adjacent material of the simulation setup and the boundary properties. The class function **set_artificial_mat_bc** is called within the initialization process of the **solver_cpu_fdtd** class.

Furthermore, we have extended the equations of the optical field towards a multi-polarization term, where the bulk and waveguide dispersion are taken into account. A new class **dispersion_model** is introduced, which includes all necessary properties of the modeled dispersion. There are various material dispersion models available in FDTD to adequately model the frequency-dependent characteristics of dispersive media, from

the three important generic classes (Debye relaxation, Lorentzian resonance and Drude model for metals) to more complex ones, such as quadratic complex rational function (QCRF) [353], [362]. The complex-valued, frequency-domain susceptibility function $\chi(\omega)$ can in general be described by a combination of multiple dispersion models. For example, the optical and conductive properties of doped III-V semiconductors, which are controlled by free carrier absorption, lattice vibration and background permittivity, can be adequately described in the mid-IR and THz range by a Drude-Lorentz function [363]. The different susceptibility functions are stored in the material class, where the **dispersion_model** vector can be filled using the function **add_susceptibility**. To capture the complex dispersion model within the class **solver_cpu_fdtd**, the FDTD update steps have been modified.

The simulation results are provided by the writer class, which can generally be extended to process any file format. Here, we provide a writer hdf5 class, which utilizes the Hierarchical Data Format (HDF) highperformance software library and file format. The HDF5 format is used by many institutions in the industrial sector, e.g., in aerospace or silicon manufacturing, and computational science, e.g., in computational fluid dynamics or astronomy [364]. Application programming interfaces (APIs) for different programming languages such as C/C++ or Fortran 90 are officially supported and third-party bindings for various other programming languages, e.g., Python and Matlab, are available. The HDF5 data model is specified by a hierarchical structure with two main entities: groups and datasets. An HDF5 file consists of a root group, which contains other groups or links to objects in other files. Each group in turn can hold other groups or datasets. In general, the handling is quite similar to that of the UNIX filesystem, where objects can be addressed by their absolute path. A dataset contains the raw data and is described by additional HDF5 objects, e.g., datatypes, dataspaces, properties and attributes. As the HDF5 library only provides a low-level C/C++ interface, we decided to use the modern C++14 wrapper Highfive [365]. The header-only library supports standard template library (STL) containers/classes such as vector or string, as well as types from Eigen, Boost::UBLAS, Boost::Multi-array and Xtensor. C++ templating is used for automatic type mapping, which increases programmer productivity and reduces coding bugs. For most of our use cases, we can employ the integrated H5Easy interface, which simplifies the reading/writing of data sets and attributes thanks to a minimalistic syntax. In order to improve the reproducibility of future simulation results, we reworked the data concept of the write method. The simulation meta-informations are stored in a group setup, which is divided into two datasets: scenario and device. This data concept enables uncomplicated recording of all important simulation parameters for better traceability.

We further have introduced a new class **reader** which, in combination with some modifications in the class **writer**, enables the simulation to be resumed. In order to restart a simulation from the last run, all simulation data including the field and density matrix values at the last discretized timestep of a simulation run are saved in an object of class **sim_data**. The method **autosave** added to the abstract class **writer** is intended to save the simulation data in a file. An implementation of this method is provided for the **writer_hdf5** class. It should be mentioned here that Highfive can handle the complex datatype of the STL, which is important for storing the off-diagonal entries of the density matrix. The abstract **reader** class features the two functions **read_field** for the field values and **read_density** for the density matrix entries. In Listing 5.1, the autosave and reload of the simulation data are demonstrated. We have included the autosave/restart mechanism as an example in the Python script for the investigation of self-induced transparency (SIT) in two-level systems. The application example that reproduces the pioneering work of Ziolkowski *et al.* [332] can be found on GitHub, cf. tools/python/ziolkowski1995.py in the *mbsolve* repository [58].

Listing 5.1 Code snippet of a Python script that can be used to restart the *mbsolve* simulation.

```
# import mbsolve libraries
import mbsolve.lib as mb
import mbsolve.solvercpu
import mbsolve.writerhdf5
import mbsolve.readerhdf5

# Restart with initialization from autosaved simulation data
# Please choose the right autosave file to restart simulation
read = mb.reader.create_instance("hdf5")
rho_init = read.read_density(filename_autosave)
ic_d = mb.ic_density_autosave(rho_init)
```

5.2 Numerical Treatment of the Maxwell-Density Matrix Langevin Equations

As discussed above, different features such as ABCs or the modeling of fluctuations are integrated into the *mbsolve* framework. The corresponding code changes lead to an increased complexity in the numerical update scheme. In the following, we will discuss the numerical treatment of the Maxwell-density matrix Langevin equations in more detail. Firstly, the ADE finite-difference time-domain method for the truncation of lossy and dispersive media is presented. Secondly, the new density matrix algorithm class **algo_lindblad_reg_cayley_qnoise** is described. Finally, an overview of the new generalized updating equations for lossy and dispersive materials including the absorbing boundary conditions is given.

5.2.1 ADE-FDTD Method for Maxwell's Equations

The optical field propagation in photonic devices can be described with the help of Ampere's law (Eq. (4.32)(a)) and Faraday's law (Eq. (4.32)(b)). Based on the FDTD method, a discretization of the variables, e.g., the electric field E_z and magnetic field H_y , is carried out. In order to derive the update equations for the PML medium, we utilize the ADE techniques. For PML ABCs, the ADE-FDTD implementation can be performed by considering the constitutive relation between electric flux density D_z , electric field E_z and polarization field P_z . In the time domain, we thus obtain

$$\partial_t D_z = \varepsilon_0 \varepsilon_r \partial_t E_z + \sigma E_z + \partial_t P_{z,qm} + \partial_t P_{z,class}. \tag{5.2}$$

Here, $\partial_t P_{z,\text{class}} = \sum_i \partial_t P_{z,\text{class}}^i$ describes the multi-polarization term accounting for bulk and waveguide dispersion, where i is the number of individual dispersion models [353]. By taking into account the constitutive parameter $s_x = 1 + \frac{\sigma_x}{i\omega \varepsilon_0}$ for the attenuation of the field values within the PML, the time evolution equation for the electric flux density is given by

$$\partial_t D_z = \partial_x H_y - \frac{\sigma_x}{\varepsilon_0} D_z \,. \tag{5.3}$$

Furthermore, the time evolution equation of the magnetic field can be written as

$$\partial_t H_y = \mu^{-1} \partial_x E_z - \frac{\sigma_x}{\epsilon_0} H_y \,, \tag{5.4}$$

with the permeability $\mu = \mu_0 \mu_r$.

In order to reduce the parasitic reflection errors from the PML layers, the conductivity σ_x in the PML layers is gradually increased along the propagation direction. Therefore, the conductivity is varied using a smooth polynomial with depth x in the PML layer [353], [357]

$$\sigma_x(x) = (x/d)^m \sigma_{x,\text{max}}. \tag{5.5}$$

The optimal choice for $\sigma_{x,\text{max}}$ is given by [353], [358]

$$\sigma_{x,\text{opt}} = \frac{0.8(m+1)}{\eta_0 \Delta_x \sqrt{\varepsilon_{\text{r.eff}} \mu_{\text{r.eff}}}},$$
(5.6)

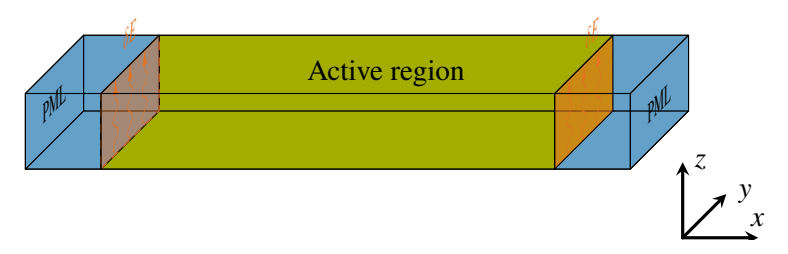


Figure 5.2 Schematic of a SCL gain medium setup truncated with two PML boundaries at the facets. The thermal radiation sources are placed next to the PML-cavity interface and are highlighted by orange arrows.

where η_0 is the free-space wave impedance, Δ_x is the lattice-cell dimension, and $\varepsilon_{r,eff}$ and $\mu_{r,eff}$ are constants representing the effective relative permittivity and permeability, respectively. The values of $\varepsilon_{r,eff}$ and $\mu_{r,eff}$ should be chosen either to be mean values of the physical parameters or the values at the wavenumber of the fundamental mode in the waveguide [353]. Here it is important to take into account the macroscopic polarization of the quantum system in the PML in order to reduce the reflection error at the interface layer between the absorbing boundary and the main simulation region.

In addition, we use a numerical model presented in [253] to simulate the thermal noise in open cavities due to the output coupling with the FDTD method. The PML boundaries are interpreted here as blackbodies, which ideally absorb all incident light. To keep the system in thermal equilibrium, the blackbody has to radiate into the cavity through the facets. This blackbody radiation acts as noise to the intracavity optical field. To model this, soft sources must be added at the PML-cavity interfaces. A schematic of the numerical treatment of the blackbody radiation within the FDTD calculations is illustrated in Fig. 5.2. The spectral properties of these noise sources are derived from blackbody theory. The temporal correlation function for the source electric field δE is thus obtained as

$$\langle \delta E(t_1) \delta E(t_2) \rangle = \frac{\delta_{\text{th}}^2}{2\pi} \int_{-\infty}^{\infty} D_n(|\omega|, T) \exp(i\omega(t_2 - t_1)) d\omega, \qquad (5.7)$$

where $\delta_{\rm th}$ is the rms amplitude of the noise field and $\int_{-\infty}^{\infty} D_n(|\omega|,T)d\omega = 2\pi$ yields the normalized energy density of the blackbody radiation. The electric field value δE of the thermal noise source at timestep t_j is calculated by

$$\delta_{th}E(t_j) = \frac{\delta}{\sqrt{\tau_{sim}}} \sum_{l=-M}^{M-1} (M_l + iN_l) D_n^{1/2}(|\omega_l|, T) \exp(i\omega_l t_j)$$
(5.8)

with 2M being the number of timesteps, τ_{sim} the simulation time and $\omega_l = 2\pi l/\tau_{\text{sim}}$. The independent Gaussian random numbers M_l and N_l with zero mean and a variance of one have the symmetry properties $M_l = M_{-l}$ and $N_l = -N_{-l}$. A detailed derivation of the thermal noise terms can be found in [253]. In *mbsolve*, a source class **thermal_noise** is provided, which implements the calculation of the electric field values δE in the function **calc_value**. We further have included a Python test script for the application given in [253], which can be found on GitHub, cf. tools/python/andreasen2008.py. The code snippet with the definition of the two noise sources at the boundaries is illustrated in Listing 5.2. An in-depth examination of thermal noise sources is beyond the scope of this thesis and has to be conducted in future work.

Listing 5.2 Code snippet of the Python script tools/python/andreasen2008.py to add the thermal noise sources to the simulation scenario.

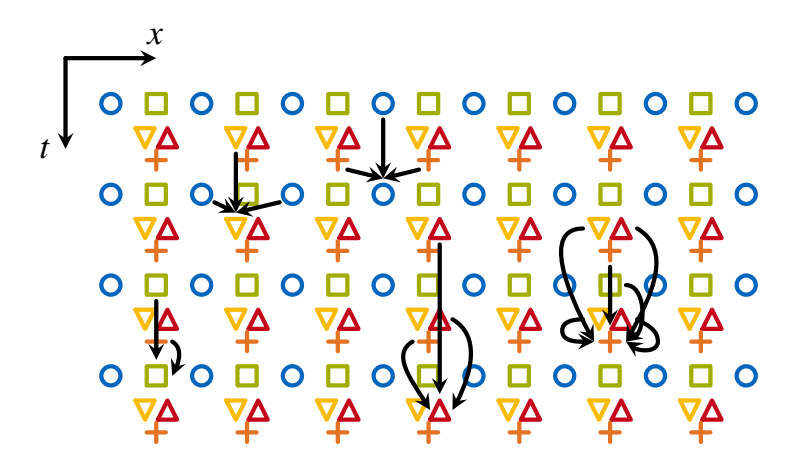


Figure 5.3 The standard Yee grid of the ADE-FDTD method combined with the discretization of the density matrix with respect to time and space. Electric and magnetic fields are denoted with orange crosses and blue circles, respectively. Electric flux density and polarization are represented by yellow and red (mirrored) triangles, respectively. The density matrix discretization is marked using green squares. The arrows indicate the data dependencies during the update of five quantities. Modified from M. Riesch *et al.*, "Numerical simulation of the quantum cascade laser dynamics on parallel architectures" [352] (CC BY 4.0).

We can now turn to the numerical treatment of the propagation equations (5.2) - (5.4) and start with the discretization of the variables therein. Here, the spatial index m and discretization size Δx as well as the temporal index n and discretization size Δt are used. The continuous field variables, e.g., the electric field $E_z(x,t)$, are then approximated at discrete grid points in space and time $E_z^{m,n} = E_z(m\Delta z, n\Delta t)$. Here, the central differences are used to solve the spatial and temporal derivatives with second-order accuracy. In the ADE-FDTD approach, the Yee grid is the central element in order to calculate the central differences. As depicted in Fig. 5.3, the discretization points are staggered by half of the respective step size [366]. Based on this, the differential equations (5.2) - (5.4) can be transformed into the difference equations

$$\frac{D_z^{m,n+1} - D_z^{m,n}}{\Delta t} = \varepsilon_0 \varepsilon_r \frac{E_z^{m,n+1} - E_z^{m,n}}{\Delta t} + \sigma \frac{E_z^{m,n+1} + E_z^{m,n}}{2} + \partial_t P_{z,qm}^{m,n+1/2} + \sum_i \frac{P_{z,class}^{i,(m,n+1)} - P_{z,class}^{i,(m,n)}}{\Delta t}, \quad (5.9)$$

$$\frac{E_z^{m+1,n} - E_z^{m,n}}{\Delta x} = \mu \frac{H_y^{m+1/2,n+1/2} - H_y^{m+1/2,n-1/2}}{\Delta t} + \frac{\mu \sigma_x^{m+1/2}}{\epsilon_0} \frac{H_y^{m+1/2,n+1/2} + H_y^{m+1/2,n-1/2}}{2}$$
(5.10)

and

$$\frac{H_y^{m+1/2,n+1/2} - H_y^{m-1/2,n+1/2}}{\Delta x} = \frac{D_z^{m,n+1} - D_z^{m,n}}{\Delta t} + \frac{\sigma_x^m}{\epsilon_0} \frac{D_z^{m,n+1} + D_z^{m,n}}{2}.$$
 (5.11)

To ensure the stability of the ADE-FDTD method, the Courant-Friedrichs-Lewy condition must be fulfilled, which is defined as

$$\Delta t < \frac{n}{c} \Delta x \,. \tag{5.12}$$

Here, $c/n = (\mu \varepsilon)^{-1/2}$ is the speed of light in the material under consideration. A simulation setup can consist of multiple materials with varying refractive indices n_i . The minimum time interval Δt must be selected taking into account the Courant-Friedrichs-Lewy condition. This corresponds to the material with the highest speed of light c/n_{\min} , which is inversely proportional to the minimum refractive index n_{\min} . We obtain the modified condition

$$\Delta t = C \frac{n_{\min}}{c} \Delta x, \ C < 1, \tag{5.13}$$

where the Courant number C is introduced [353]. While the treatment of the derivatives and the integration of the conductivities σ_x , σ is straightforward, the classical polarization term $P_{z,\text{class}}^{(m,n+1)}$ has to be discussed in

more detail here. As outlined above, various models for the characterization of dispersive media exist. For the definition of the dispersive ADE-FDTD formulation, we focus here on Lorentz media characterized by a frequency-dependent relative dielectric constant consisting of complex-conjugate pole pairs, written as

$$\varepsilon_{\rm r}(\omega) = \varepsilon_{\rm r,\infty} + \chi(\omega) = \varepsilon_{\rm r,\infty} + \frac{\Delta \epsilon \omega_0^2}{\omega_0^2 + 2j\omega\delta - \omega^2}$$
 (5.14)

Here, $\chi(\omega)$ is the material susceptibility and $\Delta \varepsilon = \varepsilon_{r,s} - \varepsilon_{r,\infty}$ is the difference of the static relative permittivity $\varepsilon_{r,s}$ and the relative permittivity at infinite frequency $\varepsilon_{r,\infty}$. The other two parameters correspond to the resonant frequency ω_0 and a damping constant δ . The absorption of light leads to resonant phonon excitation at ω_0 in the material [363].

To derive the update equation of the polarization term, the auxiliary expression $P_{z,\text{class}} = \varepsilon_0 \chi(\omega) E_z$ is used. With Eq. (5.14), the discretization of the inverse Fourier transform is given by

$$\omega_0^2 P_{z,\text{Lorentz}}^{m,n} + 2\delta \frac{P_{z,\text{Lorentz}}^{m,n+1} - P_{z,\text{Lorentz}}^{m,n-1}}{2\Delta t} + \frac{P_{z,\text{Lorentz}}^{m,n+1} - 2P_{z,\text{Lorentz}}^{m,n} + P_{z,\text{Lorentz}}^{m,n-1}}{\Delta t^2} = \epsilon_0 \Delta \epsilon \omega_0^2 E_z^{m,n}. \tag{5.15}$$

5.2.2 Numerical Treatment of the Master Equation

The macroscopic polarization $P_{z,qm}$ and the evolution of the density matrix are the remaining components to be discussed. Here, we start with the discretization of the macroscopic polarization $P_{z,qm}$ by taking into account the interaction of the optical field and the quantum system. The contributions of the dipole moment to the polarization are calculated as

$$\partial_{t} P_{z,\text{qm}} = n_{3D} \operatorname{Tr} \{ \hat{d}_{z} \partial_{t} \hat{\rho} \} = n_{3D} \operatorname{Tr} \{ -i\hbar^{-1} \hat{d}_{z} [\hat{H}_{0} + \Delta \hat{V}_{\text{tb}} - \hat{d}_{z} E_{z}, \hat{\rho}] + \hat{d}_{z} \mathcal{D}(\hat{\rho}) + \hat{d}_{z} \mathcal{F}(\hat{\rho}) \}$$

$$= n_{3D} \operatorname{Tr} \{ -i\hbar^{-1} \hat{d}_{z} [\hat{H}_{0} + \Delta \hat{V}_{\text{tb}}, \hat{\rho}] + \hat{d}_{z} \mathcal{D}(\hat{\rho}) + \hat{d}_{z} \mathcal{F}(\hat{\rho}) \},$$
(5.16)

where we make use of the master equation for the density matrix (Eq. (4.31)). Further, the commutator property

$$[\hat{H}_0 + \Delta \hat{V}_{tb} - \hat{d}_z E_z, \hat{\rho}] = [\hat{H}_0 + \Delta \hat{V}_{tb}, \hat{\rho}] - [\hat{d}_z E_z, \hat{\rho}]$$
(5.17)

and the properties (cyclic property and linearity) of the trace operation are utilized, leading to the relation

$$\operatorname{Tr}\left\{\hat{d}_{z}\left[\hat{d}_{z}E_{z},\hat{\rho}\right]\right\} = E_{z}\operatorname{Tr}\left\{\hat{d}_{z}\hat{d}_{z}\hat{\rho}\right\} - E_{z}\operatorname{Tr}\left\{\hat{d}_{z}\hat{\rho}\hat{d}_{z}\right\} = 0. \tag{5.18}$$

The discretized equation is then given by

$$\partial_z P_{z,\text{om}}^{m,n+1/2} = n_{3D} \operatorname{Tr} \left\{ -i\hbar^{-1} \hat{d}_z \left[\hat{H}_0 + \Delta \hat{V}_{\text{tb}}, \hat{\rho}^{m,n+1/2} \right] + \hat{d}_z \mathcal{D}(\hat{\rho}^{m,n+1/2}) + \hat{d}_z \mathcal{F}(\hat{\rho}^{m,n+1/2}) \right\}. \tag{5.19}$$

Here, the density matrix is discretized at the same temporal gridpoints as the magnetic field, which is referred to as weak coupling (depicted in Fig. 5.3). In contrast, one speaks of a strong coupling, if the density matrix is sampled at the same temporal discretization points as the electric field. In general, both approaches are stable, however, methods using weak coupling tend to be simpler and computationally more efficient as the density matrix and electric field can be updated alternately with explicit update equations [335].

Using the ME method, the update step of the density matrix can be written as

$$\hat{\rho}^{m,n+1/2} = \exp\left[\left(\mathcal{L}^{m,n-1/2} + \mathcal{D}\right)\Delta t\right] \hat{\rho}^{m,n-1/2} = \mathcal{V}^{m,n-1/2} \hat{\rho}^{m,n-1/2}, \tag{5.20}$$

where $\mathcal{L}(\hat{\rho}) = -i\hbar^{-1}[\hat{H}_0 + \Delta\hat{V}_{tb} + \hat{H}_I, \hat{\rho}]$ is the Liouville superoperator and $\mathcal{V}^{m,n-1/2}$ represents the update superoperator. The Liouville superoperator is assumed to be time-independent during an update step, which is appropriate in the scope of Maxwell-density matrix simulations with the ADE-FDTD method. In this expression, we neglect the fluctuation superoperator \mathcal{F} , for which the update step is treated separately and will be described below. Whether an exact form of the matrix exponential can be found, depends on the representation. In the Liouville space, for example, an analytical ME expression exists and the update of the density matrix in vector

form is straightforward. For a density matrix of size $N \times N$, we need to perform exponential calculations of $N^2 \times N^2$ matrices in Liouville space. This leads to $O(N^6)$ operations per update, which makes it rather impractical for quantum structures with a large number of states N.

In order to reduce the numerical effort for the evaluation of the matrix exponential function, we will not use the direct calculation and concentrate here on an approximation based on the symmetric Strang operator splitting technique [367]. Here, the density matrix is in regular representation and the superoperator \mathcal{V} is given by

$$\mathcal{V}^{m,n} \approx \exp(\mathcal{D}\Delta t/2) \exp(\mathcal{L}^{m,n}\Delta t) \exp(\mathcal{D}\Delta t/2), \tag{5.21}$$

where the right-hand side of the master equation (Eq. (4.31)) is divided into two parts, the Liouvillian \mathcal{L} and dissipation superoperator \mathcal{D} , respectively. The operator splitting method results in a product of matrix exponentials and thus retains the CPTP map. However, it generates an additional error of order $O(\Delta t^2)$. The solution of the exponential function with the Liouvillian reads

$$\exp(\mathcal{L}^{m,n}\Delta t)\hat{\rho} = \exp\left[i\hbar^{-1}(\hat{H}_0 + \Delta\hat{V}_{tb} + \hat{H}_I)^{m,n}\Delta t\right]\hat{\rho}\exp\left[-i\hbar^{-1}(\hat{H}_0 + \Delta\hat{V}_{tb} + \hat{H}_I)^{m,n}\Delta t\right]. \tag{5.22}$$

The update step is dominated by the exponential matrix calculation with a complexity of $O(N^3)$, and has to be executed for each time step due to the time dependence of the electric field. In order to further reduce the numerical cost, we approximate the matrix exponential operation by

$$\exp\left[i\hbar^{-1}(\hat{H}_{0} + \Delta\hat{V}_{tb} + \hat{H}_{I})^{m,n}\Delta t\right] \approx \left[\hat{I} - i\hbar^{-1}(\hat{H}_{0} + \Delta\hat{V}_{tb} + \hat{H}_{I})^{m,n}\Delta t/2\right]^{-1} \times \left[\hat{I} + i\hbar^{-1}(\hat{H}_{0} + \Delta\hat{V}_{tb} + \hat{H}_{I})^{m,n}\Delta t/2\right].$$
(5.23)

This approximation is known as the Cayley transformation and guarantees unitarity [368]. The additional numerical error is acceptable, as the density matrix properties are preserved and a reduced complexity $O(N^{\approx 2.37})$ is obtained for the multiplication of $N \times N$ matrices. In *mbsolve*, the Eigen library is used for linear algebra [369]. Here, the matrix operations can be further optimized by applying suitable algorithms.

In the following, we will divide the dissipation superoperator into two parts, where population and coherence terms are processed independently. By taking into account Eq. (3.29), the time derivatives of the coherence terms ($i \neq j$) are given by

$$\partial \rho_{ij} = -\gamma_{ij}\rho_{ij} \,. \tag{5.24}$$

The elementwise update step is thus derived as

$$\rho_{ij}^{m,n+1/2} = \exp(-\gamma_{ij}\Delta t)\rho_{ij}^{m,n-1/2}.$$
(5.25)

The derivative of the population terms can be written in matrix-vector form

$$\partial_{t} \begin{bmatrix} \rho_{11} \\ \rho_{22} \\ \vdots \\ \rho_{NN} \end{bmatrix} = \begin{bmatrix} -\tau_{1}^{-1} & r_{12} & \dots & r_{1N} \\ r_{21} & -\tau_{2}^{-1} & \dots & r_{2N} \\ \vdots & \vdots & \ddots & \vdots \\ r_{N1} & r_{N2} & \dots & -\tau_{N}^{-1} \end{bmatrix} \begin{bmatrix} \rho_{11} \\ \rho_{22} \\ \vdots \\ \rho_{NN} \end{bmatrix},$$
(5.26)

If we use the vector representation $\operatorname{diag}(\hat{\rho})$ for the main diagonal of the density matrix and the transition rate matrix Q, we can express the update step as

$$\operatorname{diag}(\hat{\rho})^{m,n+1/2} = \exp(\boldsymbol{Q}\Delta t)\operatorname{diag}(\hat{\rho})^{m,n-1/2}.$$
(5.27)

It is assumed here that the dissipation operator is time-independent so that the matrix operations can be calculated in advance. The method **propagate_dissipation** only needs to perform the update step based on the equations (5.25) and (5.27).

The density algorithm class **algo_lindblad_reg_cayley_qnoise** contains the method **propagate_fluctuation**, which calculates the fluctuations for an update step by adding the product of the fluctuation superoperator and the time interval $(\Delta t \cdot \mathcal{F}(\rho))$ to the updated density matrix $\rho^{n+1/2}$. In Chapter 4, the implementation of c-number

stochastic noise terms for the modeling of fluctuations within the *mbsolve* simulation tool is derived. Here, we have investigated an active QCL gain medium in lasing operation above threshold. In the simulations, we have to find the balance between numerical efficiency and modeling accuracy. Most of the fluctuation terms in Eqs. (4.35)(a)-(i) arise from the operator ordering when reducing the operator equations to c-number Langevin equations. As it was proven in literature [233], [239], these terms are negligible in the lasing regime above threshold with strong optical fields in the laser cavity. The fluctuation terms for a *N*-level system featuring diagonal elements F_{ii} and off-diagonal elements $F_{ij} = F_{ji}^{\dagger}$ can thus be significantly reduced for the numerical treatment and are described by

$$F_{ii}^{j} = -F_{jj}^{i} = \xi_{1,ij} \sqrt{\frac{r_{ji}\rho_{ii} + r_{ij}\rho_{jj}}{N_{\text{cell}}}},$$
(5.28a)

$$F_{ii} = \sum_{j \neq i} F_{ii}^j, \tag{5.28b}$$

$$F_{ij} = \left(\xi_{2,ij} + i\xi_{3,ij}\right) \sqrt{\frac{-\tau_j^{-1}\rho_{jj} + \sum_{n\neq j} r_{jn}\rho_{nn} + 2\gamma_{ij}\rho_{jj}}{2N_{\text{cell}}}},$$
for $i > j$, (5.28c)

where N_{cell} is the number of carriers in one grid cell. The $\xi_{2,ij}$, $\xi_{2,ij}$ and $\xi_{3,ij}$ are real Gaussian random numbers and fulfill the correlation function

$$\langle \xi_{k,ij}(t)|\xi_{l,mn}(t')\rangle = \delta_{kl}\delta_{im}\delta_{jn}\delta(t-t'). \tag{5.29}$$

For future applications, in which a more detailed fluctuation treatment would be beneficial, it might be necessary to extend our numerical model by additional noise terms derived in the previous chapter. However, additional Gaussian random numbers have to be drawn, which is at the expense of computing efficiency.

To optimize the random number generation process, we make use of the header-only C++ library EigenRand in *mbsolve* [370]. The library provides vectorized random number engines and vectorized random distribution generators and supports Eigen classes such as matrices and arrays. In contrast to the standard Eigen random functions, a speedup of $5 \sim 10$ times can be achieved. The code snippet in Listing 5.3 is used in the method **propagate_fluctuations** to generate the random numbers for the fluctuation update described in the equations 5.28 (a)-(c). Here, we use a vectorized version of the Mersenne Twister algorithm as a random number generator (Eigen::Rand::Vmt19937_64).

Listing 5.3 Code snippet of the C++ method **propagate_fluctuations** to generate a Matrix with $3 \times N(N-1)/2$ Gaussian random numbers. The Eigen matrix object is used for the fluctuation update in the density algorithm class **algo_lindblad_reg_cayley_qnoise**.

```
/* random number generator*/
Eigen::MatrixXd v{3, num_lvl * (num_lvl - 1) / 2};
v = Eigen::Rand::normalLike(v, generator);
```

Furthermore, we have implemented a class **ic_density_random_2lvl**, which represents random initial conditions for the common Maxwell-Bloch two-level system. As the dipole moment operators σ_{12} , σ_{21} and the atomic operators σ_{11} , σ_{22} do not commute, we have to take into account a non-vanishing initial stochastic value for the polarization term following the uncertainty principle [233], [371]. The tipping angle θ is obtained by drawing a random number from a Gaussian distribution with a standard deviation $\sigma = 2N_{\text{cell}}^{-1/2}$ and the angle ϕ in xy-plane is obtained by drawing a random number from a uniform distribution [251].

5.3 Parallel Implementation of the ADE-FDTD Method

The update equations for the truncation of the optical fields with partially or fully absorbing boundary layers are derived from Eqs. (5.9)- (5.11), where we have applied the centered differencing scheme. The equations are given in implicit form and have to be rearranged. The update equation for the electric field element is written as

$$E_{z}^{m,n+1} = aE_{z}^{m,n} - b\partial_{t}P_{z,\text{qm}}^{m,n+1/2} + b\Delta t_{\text{inv}} \sum_{i} \left(P_{z,\text{class}}^{i,(m,n)} - V_{z}^{i,(m,n)}\right) + c\Delta x_{\text{inv}} \left(H_{y}^{m+1/2,n+1/2} - H_{y}^{m-1/2,n+1/2}\right) + dD_{z}^{m,n},$$
(5.30)

with the coefficients

$$a = \frac{1 - \Delta t (2\epsilon_0 \epsilon_\infty)^{-1} \sigma}{1 + \Delta t (2\epsilon_0 \epsilon_\infty)^{-1} \sigma}, \qquad b = \frac{\Delta t (\epsilon_0 \epsilon_\infty)^{-1}}{1 + \Delta t (2\epsilon_0 \epsilon_\infty)^{-1} \sigma}, \qquad \Delta t_{\text{inv}} = \frac{1}{\Delta t},$$

$$c = \frac{1}{1 + \Delta t (2\epsilon_0)^{-1} \sigma_x} b, \qquad \Delta x_{\text{inv}} = \frac{1}{\Delta x}, \qquad d = -\frac{(\epsilon_0)^{-1} \sigma_x}{1 + \Delta t (2\epsilon_0)^{-1} \sigma_x} b.$$

The non-physical quantity V_z^i will be introduced below in the context of the numerical treatment of the classical polarization terms $P_{z,\text{class}}^i$. The update equation for the magnetic field is given by

$$H_y^{m+1/2,n+1/2} = kH_y^{m+1/2,n-1/2} + l'\left(E_z^{m+1,n} - E_z^{m,n}\right),\tag{5.31}$$

and the update equation of the electric flux density is written as

$$D_z^{m,n+1} = kD_z^{m,n} + l\left(H_y^{m+1/2,n+1/2} - H_y^{m-1/2,n+1/2}\right). \tag{5.32}$$

The coefficients are given by

$$k = \frac{1 - \Delta t (2\epsilon_0)^{-1} \sigma_x}{1 + \Delta t (2\epsilon_0)^{-1} \sigma_x}, \qquad l' = \mu^{-1} l = \frac{1}{\mu \Delta x} \frac{\Delta t}{1 + \Delta t (2\epsilon_0)^{-1} \sigma_x}.$$

Within one material, the coefficients are constant or vary gradually within the boundary layer and thus can be precalculated to improve the numerical efficiency. The spatial gridpoints N_x are a prerequisite in *mbsolve* and are specified as a property of the **scenario** class. The spatial discretization $\Delta x = L/(N_x - 1)$ can be calculated with the help of the total length L of the simulation domain, corresponding to the waveguide length. For each boundary layer the number of gridpoints $N_{\rm BL}$ has to be specified individually. Here, one has to find the balance between numerical accuracy and efficiency. The temporal discretization size Δt is calculated with Eq. (5.13), where a Courant number C = 0.5 is set as default value and was adapted from several studies in literature [47], [332]. If another value for the Courant number seems to be more appropriate for certain simulation scenarios, e.g., a superfluorescence setup [233], the value can be set within the simulation scenario using the member function **set_courant_number**. With the simulation endtime $t_{\rm e}$ the number of temporal gridpoints is derived. In order to obtain an integer number $N_{\rm t}$, we have to use the ceiling function, which leads to a small reduction in the simulation endtime. The helper functions **init_fdtd_simulation** and **get_fdtd_constants** are implemented for the initialization of discretization sizes, numbers of gridpoints, and the calculations of the ADE-FDTD coefficients, respectively. The **algo_bc_field_fdtd** class provides a method **get_fdtd_constants_bc**, which returns the corresponding coefficients in the boundary layer.

For the inclusion of the chromatic background dispersion present in the waveguide materials, we have introduced an auxiliary expression based on the complex-valued, frequency-domain susceptibility function $\chi(\omega)$. As illustrated in Eq. (5.15) for the Lorentzian dispersion model, the storage of the full classical polarization vector at two independent timesteps is required for the numerical update step. Here, we introduce the two non-physical quantities V_z^i and W_z^i to streamline the update step and make it more efficient. The resulting update equations are given by

$$P_{z,\text{class}}^{i,(m,n+1)} = V_z^{i,(m,n)}, (5.33)$$

$$V_z^{i,(m,n+1)} = e_i E_z^{m,n+1} + f_i P_{z,\text{class}}^{i,(m,n+1)} - W_z^{i,(m,n)},$$
(5.34)

$$W_z^{i,(m,n+1)} = g_i P_{z,\text{class}}^{i,(m,n+1)}. (5.35)$$

For the Lorentz model, we obtain the coefficients

$$e = \frac{\Delta t^2 \epsilon_0 \Delta \epsilon \omega_0^2}{1 + \Delta t \delta}, \qquad f = \frac{2 - \omega_0^2 \Delta t^2}{1 + \Delta t \delta}, \qquad g = \frac{1 - \Delta t \delta}{1 + \Delta t \delta}. \tag{5.36}$$

In addition, we introduce here the coefficients of the Drude model for the modeling of highly doped semiconductor materials, written as

$$e = \frac{2\Delta t^2 \epsilon_0 \omega_0^2}{2 + \gamma_p \Delta t}, \qquad f = \frac{4}{2 + \gamma_p \Delta t}, \qquad g = \frac{2 - \gamma_p \Delta t}{2 + \gamma \Delta t}, \tag{5.37}$$

where γ_p is the inverse of the pole relaxation time.

When analyzing Eqs. (5.30)- (5.35), we find that all individual variables can be updated in parallel, but synchronization steps between the quantities are necessary. This also applies to the density matrix updates, which do not depend on their spatial neighbors. The increased number of equations in the ADE-FDTD formulation results in a more complex update procedure than with the standard FDTD method. The implementations of the main loop are shown schematically in Algorithm 1. Here, the abstract functions update_h, update_v, **update_e**, and **update_d** represent together with the simpler expressions for p_{class} , w the update equations (5.30)- (5.35). Furthermore, the functions **update d** and **calc p qm** refer to the update of the density matrix and the calculation of the polarization term in Eq. (5.19), which are both provided by the specific algorithm for the density matrix Langevin equation. A larger block of the simulation main loop contains the quantity updates within the boundary layers. Regardless of the selected boundary conditions, the endpoints have to be updated individually using the methods update_h_bc_end and update_e_bc_end of the class algo_bc_field_fdtd. In Algorithm 1, we have divided the electric field update into two parts, where the main update procedure is summarized in update_e, and the addition of the electric flux density is dealt with in a separate step. If we take a closer look at the coefficient d in equation (5.30), we will notice that it only has non-zero values within the boundary layer, where $\sigma_x \neq 0$. We therefore only need to update the electric flux density within the boundary layer, as it is not needed as an input value for updating quantities other than the electric field. The classical polarization and the related quantities v and w are stored in a two-dimensional vector to account for multiple susceptibilities (num_suscept ≥ 1). As their name suggests, the functions sync and record_results are responsible for synchronizing all computing units and recording the desired simulation results.

By adding OpenMP directives (e.g. #pragma omp parallel for) to the serial code, the loops over m in Algorithm 1 can be distributed over multiple threads. In principle, the procedure is simple, as the compiler handles complicated tasks such as synchronization and thread creation. In order to further optimize the parallelization of the task, further details have to be taken into account. Our implementations serve as an extension of the work in [331], where the necessary steps for the optimization of parallel code including memory allocation and thread pinning are discussed. The parallel efficiency of the implementations was measured [329], [352] and the analysis shows good performance.

5.4 Summary

For the simulation of broadband frequency comb operation or ultrashort pulse generation in active SCL devices, full-wave Maxwell-density matrix approaches could be advantageous over models relying on the RWA. For such full-wave simulations, we have developed an open-source solver in recent years. In addition, we have integrated fluctuations from the quantum Langevin theory, which arise from the interactions of the optical field and the quantum system with their reservoirs. An overview of the existing *mbsolve* toolbox is given here and further extensions, e.g., the truncation of the optical field at the simulation boundaries or the treatment of chromatic waveguide dispersion, are presented.

We have provided a brief overview of existing numerical methods for the density matrix equations and evaluated them with respect to their numerical performance and long-term stability. The latter criterion is

Algorithm 1 Simulation main loop – advanced ADE-FDTD version.

```
for n = 0 to n_{\text{max}} do
  for m = 1 to m_{\text{max}} do
      h[m] \leftarrow \text{update\_h}(e[m], e[m-1])
      dm[m] \leftarrow update\_dm(e[m])
      p_{qm}[m] \leftarrow \text{calc}_{p_{qm}}(dm[m])
      for i = 0 to num_suscept do
         p_class[m][i] \leftarrow v[m][i]
         v[m][i] \leftarrow \text{update\_v}(e[m], p\_\text{class}[m][i], w[m][i])
         w[m][i] \leftarrow g[i] * p\_class[m][i]
      end for
  end for
  for all algo_bc_f ∈ algo_bc_field do
      algo_bc_f :: update_h_bc_end(e, h)
  end for
  sync()
  for m = 0 to m_{\text{max}} - 1 do
      e[m] \leftarrow \text{update\_e}(h[m+1], h[m], p\_qm[m])
      for i = 0 to num_suscept do
         e[m] \leftarrow \text{update\_e}(p\_\text{class}[m][i], v[m][i])
      end for
  end for
  sync()
  for all algo_bc_f ∈ algo_bc_field do
      algo_bc_f :: update_e_bc_end(e, d, p_{class}, v, w)
      m_{\text{bc start}} \leftarrow \text{algo\_bc\_f} :: \text{get\_ind\_boundary\_start}()
      m_{bc\_stop} \leftarrow algo\_bc\_f :: get\_ind\_boundary\_stop()
      for m = m_{bc\_start} to m_{bc\_stop} do
         e[m] \leftarrow e[m] - d[m]
         d[m] \leftarrow \text{update\_d}(h[m+1], h[m])
      end for
  end for
  sync()
  record_results()
```

end for

strongly linked to the preservation of the physical properties of the density matrix, e.g., positive definiteness and trace preservation. Two density matrix algorithms based on the matrix exponential approach are implemented in *mbsolve*, as they have proven to be the most promising for our purposes. For the numerical treatment of Maxwell's equations, two suitable candidates exist, which are evaluated in terms of implementation complexity and numerical accuracy. Here, the finite-difference time-domain method is used, as it offers advantages in terms of simplicity. We further have focused on the simulation of optical devices in open radiation problems. Therefore, an overview of existing absorbing boundary conditions for the truncation of the FDTD grid is provided. An uniaxial anisotropic perfectly matched layer absorber proves to be a suitable choice for the *mbsolve* toolbox. The implemented UPML model is thereby refined by taking into account an additional impedance mismatch arising from the internal quantum system. From the UPML boundary condition, we have derived a partially reflective layer boundary condition by implementing an impedance mismatch at the interface. The integration of those and other existing BCs into *mbsolve* is then described. Furthermore, we have presented a model for the numerical treatment of waveguide dispersion and introduced a new reader class to resume simulation scenarios.

The numerical treatment of the Maxwell-density matrix Langevin equation is also described. Firstly, the evolution of the optical field in lossy and dispersive media is treated numerically within the framework of the auxiliary differential equation FDTD method. Two auxiliary expressions are defined here, which use the electric flux density for the attenuation of the electric field in the boundary layer and the classical polarization terms for treating the bulk and waveguide dispersion. The resulting four differential equations are then converted into difference equations. Secondly, the evolution of the density matrix equation and the discretization of the macroscopic polarization are described. In addition, the implementation of c-number stochastic noise terms for the modeling of fluctuations within the *mbsolve* simulation tool is discussed. Finally, we have given a brief overview of the new generalized update equations and explained the simulation main loop in more detail.

6 Verification of the Simulation Framework for the Maxwell-Density Matrix Langevin Equations

For the numerical validation of the code extensions presented in Chapter 5, we use an active gain medium based on a well-studied THz quantum cascade laser design [14], [55] and an incoherent two-level system, which is used for modeling the transition from superfluorescence to amplified spontaneous emission [233], [372], [373]. First, we will give a short description of the active THz OCL gain medium and introduce the simulation setup in Section 6.1. The THz QCL simulation setup is then used to analyze the reflection error of the implemented PML absorbing boundary conditions. To avoid detrimental reflection errors at the boundary of the simulation domain, the adapted PML model takes into account impedance mismatch effects arising from the internal quantum system. Improved absorbing characteristics for the truncation of active gain media in our Maxwell-density matrix simulation approach can be demonstrated. Further simulations are executed to characterize the influence of group velocity dispersion on the formation of THz frequency combs. Chromatic dispersion is known to be one of the main degradation mechanisms of THz frequency combs and has been added to the *mbsolve* simulation tool. The implementation using the Lorentz model is applied to the investigated QCL frequency comb setup. The reported results are in good agreement with the experimental data. Especially, the need for dispersion compensation is confirmed to be crucial for the generation of terahertz frequency combs in the given QCL setup. Secondly, the superfluorescence setup in a two-level configuration is presented in Section 6.2 to test the Maxwell-density matrix Langevin approach [233], [373]. Here, it is important to account for the fluctuations arising from the quantum system. With this, we can reproduce the transition from SF to amplified spontaneous emission accompanying the decrease of dephasing times, as demonstrated in the experiment. Finally, the chapter is concluded by a short summary of the numerical validation of the extended dynamical simulation tool mbsolve.

6.1 Time-Domain Modeling of Terahertz Quantum Cascade Lasers

In order to analyze the code base extensions of *mbsolve*, we decide to use a well-studied THz QCL frequency comb device based on a resonant LO phonon depopulation active region [14], [55]. An experimental laser setup with this QCL design integrated into a dispersion compensating waveguide has been shown to produce stable frequency comb emission at a center frequency of $f_c = 3.5$ THz. The coherent emission comprises a full comb spectrum of more than 70 equidistant longitudinal modes in free-running operation mode.

In order to execute time-domain simulations of the THz QCL structure, we have to provide a detailed simulation setup including eigenenergies, scattering, and dephasing rates of the quantum-mechanical system.

In Section 6.1, the gain analysis and reflection error results are partially reproduced with permission from J. Popp, L. Seitner, M. Haider, *et al.*, "Reducing the reflection error of PML absorbing boundary conditions within a generalized Maxwell-Bloch framework", in 2022 3rd URSI Atlantic and Asia Pacific Radio Science Meeting (AT-AP-RASC), 2022, pp. 1–4. DOI: 10.23919/AT-AP-RASC54737.2022.9814330.

The group velocity dispersion results are extracted from L. Seitner, J. Popp, M. Riesch, *et al.*, "Group velocity dispersion in terahertz frequency combs within a generalized Maxwell-Bloch framework", *J. Phys.: Conf. Ser.*, vol. 2090, no. 1, p. 012 082, 2021. DOI: 0.1088/1742-6596/2090/1/012082, an open access article published under the terms of the Creative Commons Attribution 3.0 International License, which permits unrestricted use, distribution, and reproduction in any medium, provided the original author and source are credited.

Section 6.2 is largely based on Section III A of J. Popp, J. Stowasser, M. A. Schreiber, *et al.*, "Modeling of fluctuations in dynamical optoelectronic device simulations within a Maxwell-density matrix Langevin approach", *APL Quantum*, vol. 1, no. 1, p. 016109, 2024. DOI: 10.1063/5.0183828, an open access article published under the terms of the Creative Commons Attribution 4.0 International License, which permits unrestricted use, distribution, and reproduction in any medium, provided the original author and source are credited.

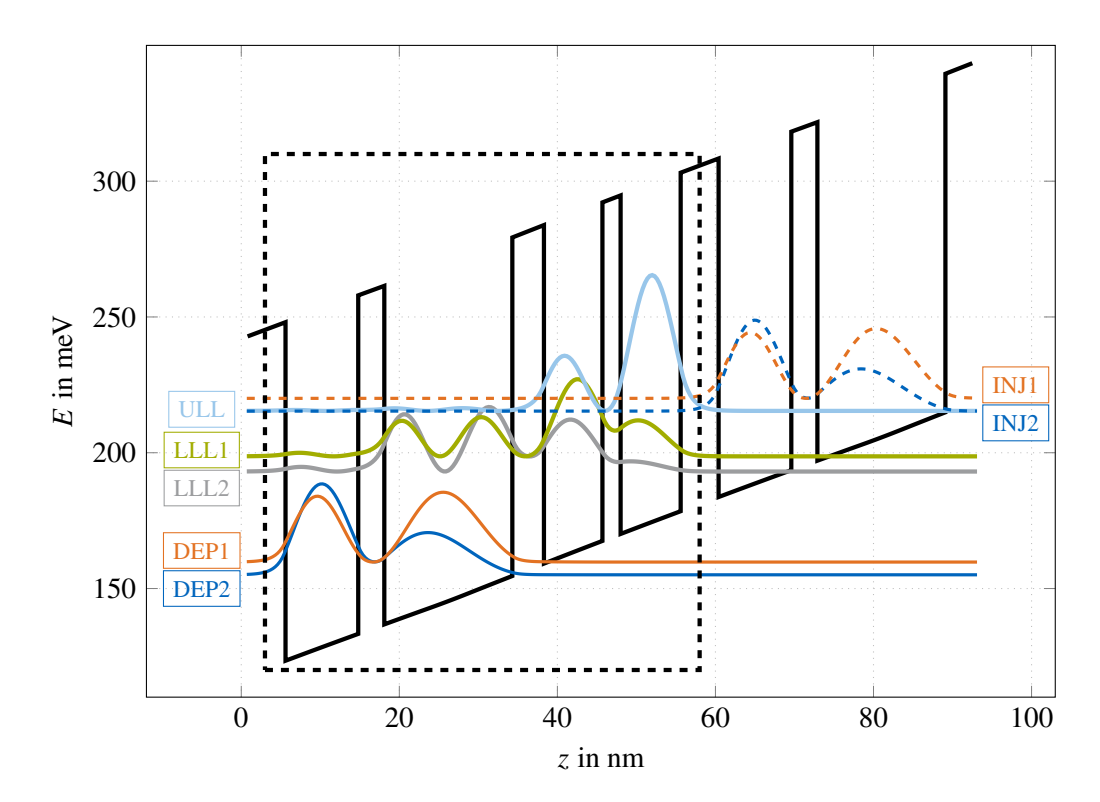


Figure 6.1 Calculated conduction band profile and probability densities of the investigated THz QCL structure [14], [55] at a bias field strength of 11 kV cm⁻¹. The dashed rectangle comprises a single QCL period. Here, the upper and lower laser levels together with the depopulation levels are represented by bold solid lines. The injection levels of the adjacent period are further shown by dashed lines. Adapted from J. Popp *et al.*, "Reducing the reflection error of PML absorbing boundary conditions within a generalized Maxwell-Bloch framework" [360].

Therefore, we have performed a detailed analysis of the active gain medium using the Schrödinger-Poisson solver for wavefunction calculations and the DM-EMC method for carrier transport simulations. In Fig. 6.1, the calculated wavefunctions at a bias field strength of $11\,\mathrm{kV}\,\mathrm{cm}^{-1}$ are illustrated. Here, we use the tight-binding states to adequately describe the physical properties within the active gain medium. Each period comprises five wavefunctions, which are labeled according to the assumed role. Furthermore, the two injection states $|\mathrm{INJ1}\rangle$ and $|\mathrm{INJ2}\rangle$ of the adjacent period are presented to highlight the carrier injection into the upper laser level $|\mathrm{ULL}\rangle$. Using the tight-binding approximation, we obtain for the two injection pairs the anticrossing energies $\hbar\Omega_{\mathrm{INJ1,ULL}}\approx 1.18\,\mathrm{meV}$ and $\hbar\Omega_{\mathrm{INJ2,ULL}}\approx 1.38\,\mathrm{meV}$, respectively. The anticrossing energies are comparably strong, however, the tunneling transition $\mathrm{INJ2} \to \mathrm{ULL}$ is more pronounced due to the strong resonance condition between level $|\mathrm{INJ2}\rangle$ and $|\mathrm{ULL1}\rangle$.

There exist two lower laser levels $|LLL1\rangle$ and $|LLL2\rangle$. In the literature [55], the dipole moment was analyzed for both optical transitions and it was found that the optical transition between $|ULL\rangle \rightarrow |LLL1\rangle$ is the most likely to occur. We, therefore, decided to only take into account one optical transition for the dynamical modeling and set a dipole moment of $4 \text{ nm} \times e$ for the optical transition $|ULL\rangle \rightarrow |LLL1\rangle$. Nevertheless, non-radiative transitions from $|ULL\rangle$ into $|LLL2\rangle$ remain possible and are modeled by including the corresponding scattering rate in the scattering matrix. The remaining two levels $|DEP1\rangle$ and $|DEP2\rangle$ are referred to as depopulation levels. Due to the periodicity of the QCL structure, the depopulation levels correspond to the injection levels of the next period. By applying periodic boundary conditions, we can summarize the aforementioned levels and add the scattering rates between the two lower laser levels and the injector levels of the next period. The simulation setup for the THz QCL consisting of an active period with five eigenstates is illustrated in Listing 6.1.

Listing 6.1 Code snippet of the Python script for the THz OFC QCL setup at a bias field strength of 11 kV cm⁻¹ given in [72].

Hamiltonian

```
energies = [4.065e-3 * mb.E0, 0, 0, -0.016 * mb.E0, -0.02087 * mb.E0]
off_diagonales = [0, -1.18e-3 * mb.E0, -1.38e-3 * mb.E0, 0, 0, 0, 0, 0]
                   0, 0, 0]
H = mb.qm_operator(energies, off_diagonales)
# dipole moment operator
dipoles = [0, 0, 0, 0, 0, -4e-9 * mb.E0, 0, 0, 0]
u = mb.qm_operator([ 0, 0, 0, 0, 0], dipoles)
# relaxation superoperator
# scattering rate matrix R
rates = [ [ 0, 0.4947e12, 0.0974e12, 0.8116e12, 1.0410e12 ],
           [ 0.8245e12, 0, 0.1358e12, 0.6621e12, 1.1240e12 ],
            0.0229e12, 0.0469e12, 0, 0.0794e12, 0.0357e12
            0.0047e12, 0.0029e12, 0.1252e12, 0, 0.2810e12
           [ 0.0049e12, 0.0049e12, 0.1101e12, 0.4949e12, 0 ] ]
# pure dephasing rates
deph_inj1_ull = 1 / 0.3e-15
deph_inj2_ull = 1 / 0.6e-12
deph_xxx_xxx = 1 / 1e-12
pure_deph = [0, deph_inj1_ull, deph_inj2_ull, deph_xxx_xxx,
             deph_xxx_xxx, deph_xxx_xxx, deph_xxx_xxx,
             deph_xxx_xxx, deph_xxx_xxx, deph_xxx_xxx ]
relax_sop = mb.qm_lindblad_relaxation(rates, pure_deph)
# initial density matrix
rho_init = mb.qm_operator([ 0, 0, 1, 0, 0 ])
# quantum-mechanical description
qm = mb.qm_description(5.6e21, H, u, relax_sop)
```

Based on the quantum-mechanical description in Listing 6.1, we can start with the time-domain simulations and characterize the optical properties of the THz-QCL. Therefore we investigate the design in a slab waveguide with a length of 5 mm. In the experiment, the spectral gain profile as well as the strength of the chromatic dispersion can be determined using the so-called THz time-domain spectroscopy (THz-TDS) technique [374]–[376]. In the simulation, we can extract the gain and dispersion characteristics of the QCL quantum system with the help of the corresponding pump-probe measurement. Here, we excite the system with a Gaussian field pulse $E_z(0,t) = A \exp[-(t-t_0)/\tau]^2 \sin(2\pi f_0 t)$ at the left facet of the setup and measure the amplified field at the position x = L = 4 mm. The pulse parameters are $A = 1 \times 10^{-3}$ V m⁻¹, $\tau = 0.707$ ps, $t_0 = 30$ ps, and $t_0 = 3.8$ THz. The following command for the Gaussian pulse source has to be added to the Python script for the simulation setup:

In the following, we will denote the electric field of the injected seed pulse as $E_{\rm in}(t)$ and the recorded electric field as $E_{\rm out}(t)$. We further obtain the Fourier transforms $E_{\rm in}(\omega)$ and $E_{\rm out}(\omega)$ with the angular frequency ω . The field amplitude of the seed pulse is set to a small value to obtain a linear response of the gain medium. The active gain medium can then be described by a complex refractive index $\underline{n}(\omega) = n(\omega) + \mathrm{i}\kappa(\omega)$. For the amplitude gain coefficient, we obtain $g(\omega) = -\kappa(\omega)\omega/c$, which can be calculated with the Fourier transforms of the recorded electric fields $E_{\rm in}(\omega)$ and $E_{\rm out}(\omega)$ by

$$g(\omega) = \frac{1}{L} \ln \left(\frac{|E_{\text{out}}(\omega)|}{|E_{\text{in}}(\omega)|} \right). \tag{6.1}$$

Here, we can exploit the dependence between seed and output field, which is given by $E_{\text{out}}(\omega) = E_{\text{in}}(\omega) \times \exp(i\omega \underline{n}L/c)$. The resulting spectral gain profile of the THz QCL gain medium is depicted as the blue line in Fig. 6.2. We observe two gain peaks at f = 3.63 THz and f = 4.13 THz and a peak gain value of $g_p = 19.7$ cm⁻¹.

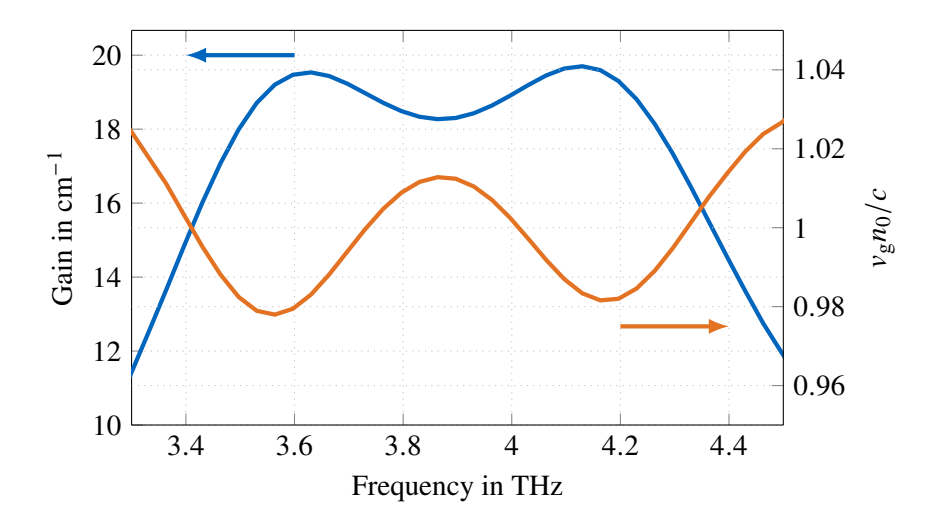


Figure 6.2 Simulated spectral gain profile (blue curve, left y-axis) together with the normalized group velocity $v_g n_{\text{eff}}/c$ (orange curve, right y-axis).

The two states $|\text{ULL}\rangle$ and $|\text{INJ2}\rangle$ form a doublet of states separated by approximately the anticrossing energy $2\hbar\Omega_{\text{INJ2,ULL}}$ and optically interact with the lower laser level $|\text{LLL1}\rangle$. The relative radiative coupling strength between the individual level pairs depends on the detuning from resonance. In literature, it was found [295] that below the resonant bias, the high-frequency lobe of the gain dominates the transition, whereas above resonance the low lobe does.

We further calculate the group velocity v_g by

$$v_{g}(\omega) = \left[\frac{\partial k(\omega)}{\partial \omega}\right]^{-1},\tag{6.2}$$

with the wavenumber $k(\omega) = n(\omega)\omega/c$. Fig. 6.2 shows the group velocity normalized to the central frequency's phase velocity $c/n_{\rm eff}$ (orange curve). The low- and high-frequency components in correspondence to the strong resonances at f=3.63 THz and f=4.13 THz are delayed with respect to each other. Therefore, the normalized group velocity approaches values of 0.978 and 0.982 for the low- and high-frequency gain peaks, respectively. The doubly peaked resonant nature of the transition causes dispersion in the cavity without taking into account bulk or waveguide dispersion. The influence of dispersion on the frequency comb generation will be discussed below, but first, we will analyze the behavior of the absorbing PML boundary conditions in terms of the influence of the quantum system on the absorption quality.

6.1.1 Reflection Error of PML Absorbing Boundary Conditions

We validate the numerical stability of our modified PML model by investigating the light propagation in the aforementioned THz QCL gain structure for two different simulation setups, as depicted in Fig. 6.3. Setup 1 consists of an active region of length 5 mm, which is terminated by a perfect magnetic conductor layer on the left and a 200 gridpoints long PML region on the right facet. Setup 2 has a simulation domain twice as long as in setup 1 and is terminated with a PMC boundary layer on both sides. To ensure that there are no reflections from the right boundary during the time-stepping span of interest, we use a sufficiently long waveguide in setup 2. The chromatic dispersion in the investigated THz structure arises not only from the quantum system but also from the background material and the waveguide itself. Here, we will neglect the chromatic dispersion introduced by the background system, as we are only interested in the interaction of the PML region with the quantum system. The propagation of the Gaussian pulse is schematically illustrated in setup 2 of Fig. 6.3. The light pulse is amplified due to the interaction with the quantum system, while the dispersion caused by the quantum system leads to a spatial distortion of the pulse. This behavior can be deduced from the aforementioned gain and dispersion analysis and is documented in different theoretical and experimental investigations [14], [55], [56]. We will discuss this in more detail below.

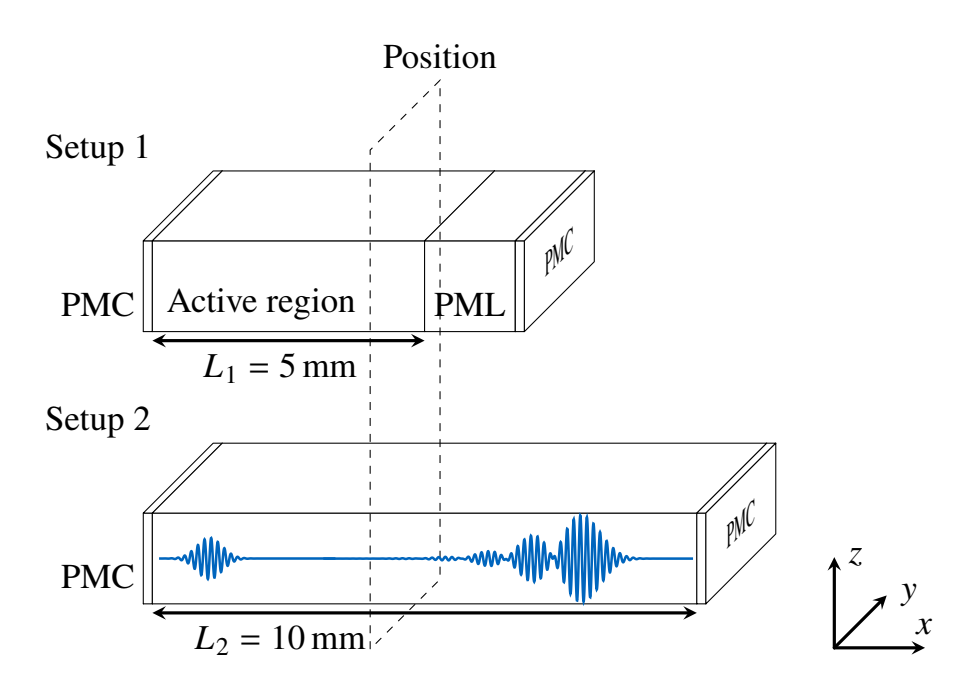


Figure 6.3 Illustration of the two different simulation setups under numerical investigation. Setup 1 describes a THz gain medium with length $L_1 = 5$ mm truncated with a PML boundary containing 200 gridpoints terminated by a PMC layer, setup 2 is based on the same material system with twice the length and two PMC layers at the facets. Here, the propagation of the Gaussian pulse is schematically demonstrated, resulting in an amplification and distortion of the initial pulse. Adapted from J. Popp *et al.*, "Reducing the reflection error of PML absorbing boundary conditions within a generalized Maxwell-Bloch framework" [360].

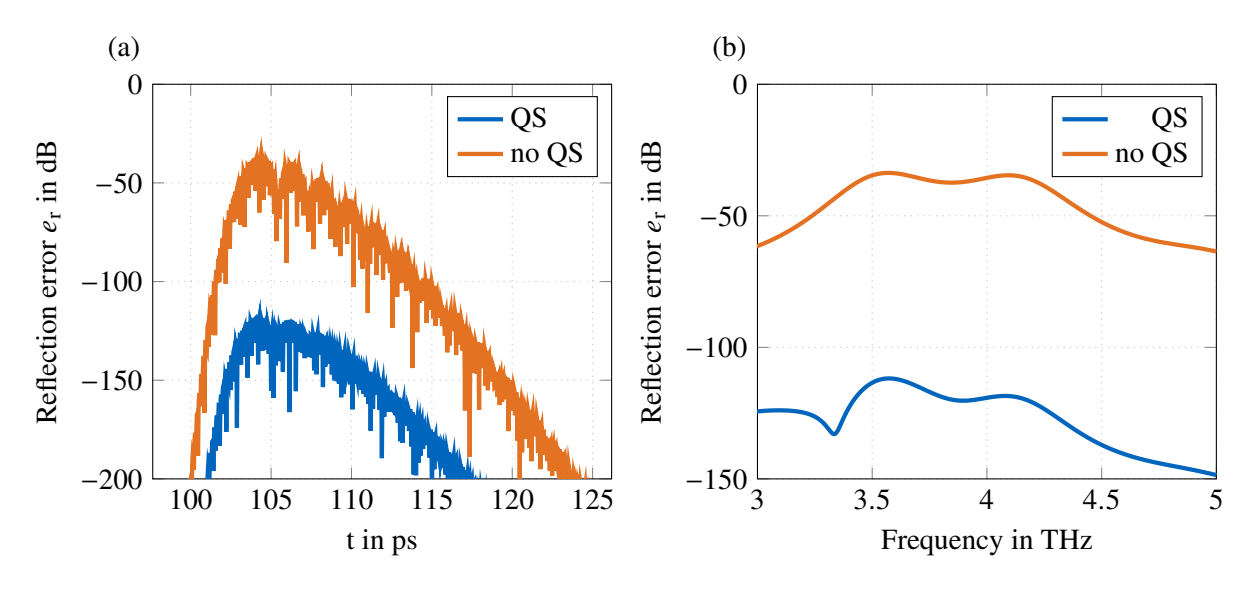


Figure 6.4 Reflection error for two PML configurations. The blue curve represents the reflection error including the macroscopic polarization of the QS in the PML region, whereas the orange curve represents the results obtained from the original PML formulation introduced by Gedney [357], [358]. (a) Time-domain analysis. Reprinted with permission from J. Popp *et al.*, "Reducing the reflection error of PML absorbing boundary conditions within a generalized Maxwell-Bloch framework" [360]. (b) Frequency-domain analysis.

For the PML characterization, we use the Gaussian pulse with the same parameters as introduced in the gain-dispersion analysis. We now quantify the reflection behavior at the PML boundary by introducing the reflection error e_r in time-domain, computed as

$$e_{\rm r}(t) = \left. \frac{|E_1(t) - E_2(t)|}{\max(|E_2(t)|)} \right|_{x=4\,\text{mm}},\tag{6.3}$$

with $E_1(t)$ being the reflected electric field in setup 1. The field $E_2(t)$ from setup 2 is used as reference value. Apart from the temporal behavior, we are also interested in the reflection error e_r in the frequency-domain, given by

 $e_{\rm r}(\omega) = \left| \frac{E_1(\omega) - E_2(\omega)}{E_2(\omega)} \right|_{x=4 \text{ mm}}.$ (6.4)

Here, we use the Fourier transforms of the recorded electric fields $E_1(\omega)$ and $E_2(\omega)$ for the error determination. As already pointed out, we include the quantum system of the active region in the adjacent PML region to obtain better impedance matching. The amplitude gain displayed in Fig. 6.2 now also acts on the outgoing electric field in the PML layer. The artificially introduced losses from Eq. (5.5) outperform the unintended amplification by far and the light gets efficiently absorbed in the PML region. In Fig. 6.4, we compare the results of our implementation to a similar PML region, where we omit the quantum system (QS) in the boundary. The results for the obtained reflection error in time-domain are illustrated in Fig. 6.4(a). If we do not take into account the QS within the PML layer, we obtain a maximum reflection error of $e_r \sim -36\,\mathrm{dB}$ arising from the corresponding impedance mismatch. By taking into account the QS in the PML layers, we obtain a reflection error e_r of less than $-118\,\mathrm{dB}$. For the frequency-domain, we obtain a similar behavior for the two PML configurations with respect to the undesired reflections. For the PML without QS a maximum reflection error of $e_r \sim -33\,\mathrm{dB}$ is obtained, while for the PML layer with QS a significantly reduced reflection error with a peak value of $e_r \sim -111\,\mathrm{dB}$ is present. In both cases, the spectrum of the reflection error indicates the two frequency lobes. This means that the reflected light has been amplified again on the way back to the detection point at 4 mm.

6.1.2 Group Velocity Dispersion in Terahertz Frequency Combs

To correctly simulate the QCL structure, we need to analyze the influence of chromatic dispersion on the coherent emission behavior. Therefore, we choose the parameters for the Lorentz dispersion model to match the GaAs bulk material. Using the values for the Reststrahlen region found in literature [363], [377], we define the Lorentz susceptibility as given in Listing 6.2 and add it to the active region material in the Python script for the QCL frequency comb simulation setup.

Listing 6.2 Code snippet of the Python script of the Lorentz dispersion model for n-doped gallium arsenide [326].

The phononic resonance frequency of the n-doped GaAs is approximately at 8 THz, so it is unfeasible to operate a laser at this frequency. However, for devices like our QCL frequency comb structure (≈ 4 THz) operating near this pole, the chromatic dispersion resulting from the varying relative permittivity can affect the laser performance and should be considered within the simulation. In Fig. 6.5 (a), the real and imaginary part of the

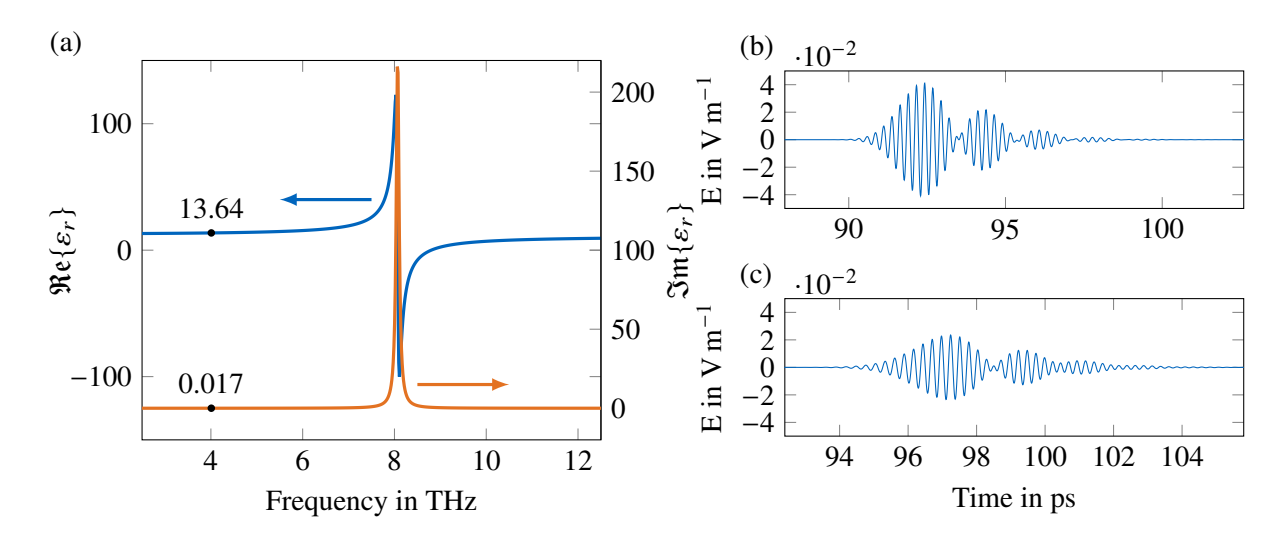


Figure 6.5 (a) Real and imaginary part of the permittivity for the Lorentz susceptibility model of the bulk material GaAs. The recorded Gaussian pulse at the second interface of the QCL waveguide is shown in (b) without the explicit dispersion model, and in (c) applying the model. Adopted from L. Seitner *et al.*, "Group velocity dispersion in terahertz frequency combs within a generalized Maxwell-Bloch framework" [326] (CC BY 3.0).

complex permittivity function is plotted, where the relative permittivity values for a frequency of 4 THz are highlighted. The real part of the relative permittivity has a value of about 13.64 with a positive slope at this frequency. This affects the group velocity dispersion and leads to different round trip times of the individual frequency modes in the laser resonator. The same pole near 8 THz can be identified in the imaginary part. The imaginary part of the function is responsible for additional losses. Therefore, field components with a frequency close to the pole experience a large attenuation. This also means that the total field strength inside the cavity is lower compared to the non-dispersive case, while the total power is distributed over a wider frequency range.

In order to analyze this in more detail, we will execute a pump-probe measurement with the previously introduced Gaussian pulse. We again use two different setups, one with and one without the Lorentzian susceptibility given in Listing 6.2. In Fig. 6.5 (b), no explicit group velocity dispersion within the bulk material is considered. The interaction of the optical field with the quantum system leads to an amplification of the pulse. In addition, the original pulse is broadened and distorted by the chromatic dispersion caused by the quantum system, as already stated. In Fig. 6.5 (c), the recorded pulse is illustrated by additionally taking into account the classical group velocity dispersion of the gain material. It can be seen that the broadening effect is even more pronounced. This is consistent with the above explanation of a longer round trip time and increased damping. The pulse in Fig. 6.5 (c) arrives at the second interface about 5 ps later, which is due to the increased real part of the permittivity. The amplified field strength in the case of an additional dispersion is lower due to the attenuation caused by the imaginary part of the relative permittivity.

Summarizing these results, it is found that there are two contributions to the total dispersion: one part is caused by the interaction of the optical field with the quantum system and the other part by the classical material dispersion. Experimental results show that a special dispersion grating can be used in such a way that both contributions roughly balance each other out. This results in improved laser performance [14]. Here, we do not model this complex grating and instead investigate the effect of the classical material dispersion of bulk GaAs on the frequency comb generation. Therefore, the electric field is randomly initialized with a mean value of zero and a standard deviation of approximately $5 \times 10^{-16} \,\mathrm{V}\,\mathrm{m}^{-1}$ at each grid point within the cavity. For the quantum system, we assume an almost perfect population inversion at the beginning in order to amplify the light-matter interaction. The system then propagates for 60 ns, i.e., about 500 roundtrips of the optical field in the cavity. The electric field strength at the interface of the cavity is recorded for further data analysis.

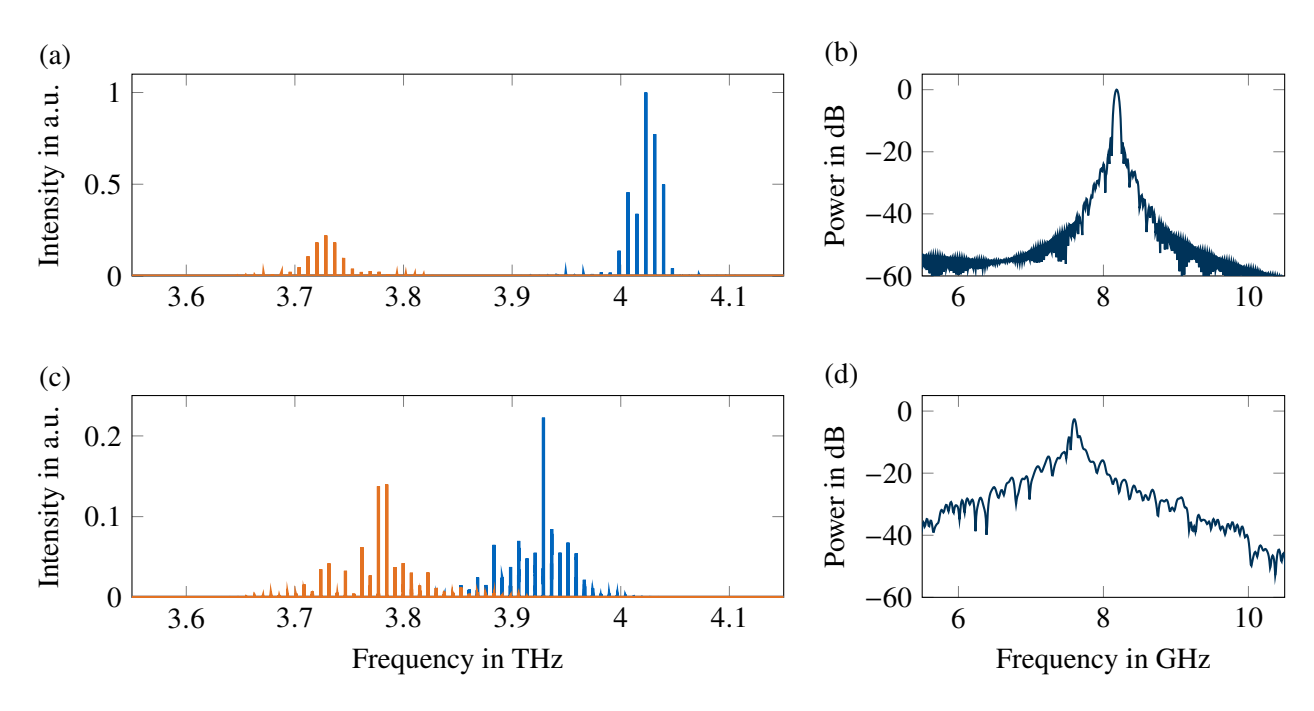


Figure 6.6 Simulation results of the THz frequency comb and the RF beatnote. Without background and waveguide GVD, there are two clear and distinct lobes of an OFC (a) and a sharp beat (b). When this type of GVD is included, the frequency comb broadens and loses intensity (c). The beatnote becomes more distorted (d). Reprinted from L. Seitner *et al.*, "Group velocity dispersion in terahertz frequency combs within a generalized Maxwell-Bloch framework" [326] (CC BY 3.0).

Frequency domain results

The laser enters a stable operating state after around 250 cycles. The recorded field data from this point can be Fourier-transformed to obtain the output spectrum of the laser. The resulting frequency comb spectra are shown in Fig. 6.6, for the "non-dispersive" case (a) and (b), and for the dispersive case (c) and (d). Firstly, we will analyze the case in which only the dispersion due to the quantum system is present. Fig. 6.6(a) clearly shows that two distinct frequency lobes have formed. The one at lower frequencies, displayed in orange color, has a center frequency of about 3.72 THz and the higher frequency lobe, plotted in blue color, is formed around 4.02 THz. The different colors are used to get an overview of the different modes when viewing the results over time. To divide the spectrum, we apply a bandpass filter to each of the lobes. In this normalized linear intensity diagram, about 20 different comb modes can be counted, whereby those of the higher frequency lobe clearly dominate. On a logarithmic scale, even up to 70 modes can be detected in the frequency range under consideration. This result agrees well with the results of the same structure simulated with the RWA [55], where chromatic dispersion due to the quantum system was also taken into account. Furthermore, the RF beatnote of the field is presented in Fig. 6.6 (b). At 8.1 GHz a distinct peak can be identified, which quickly drops to -20 dB and for more distant frequencies even to less than $-50\,\mathrm{dB}$. The different field modes mainly move at a similar group velocity. However, the frequency resolution is here limited by the Fourier transform to about 16 MHz. A more detailed investigation of the beatnote would require a much longer simulation time with our full-wave approach and would go beyond the scope of these investigations.

Let us now compare the results presented with the case in which the dispersion of bulk solids and waveguides is also included. Fig. 6.6 (c) clearly shows that both lobes have a reduced intensity and a broadened spectrum. For better comparison, the intensities in the graph are normalized to the highest intensity mode of the non-dispersive comb. We find that the number of identified modes increases, while the power is more equally distributed. The integration over all modes provides approximately the same total power in both the non-dispersive and the dispersive case. We see that material dispersion creates additional modes that carry some energy of the previous modes. The system behavior becomes more irregular and the efficient generation of the desired comb spectrum is impaired. This is also confirmed by the RF beatnote shown in Fig. 6.6 (d). Compared to the case without waveguide dispersion, more power is distributed to side modes, which have different round-trip frequencies.

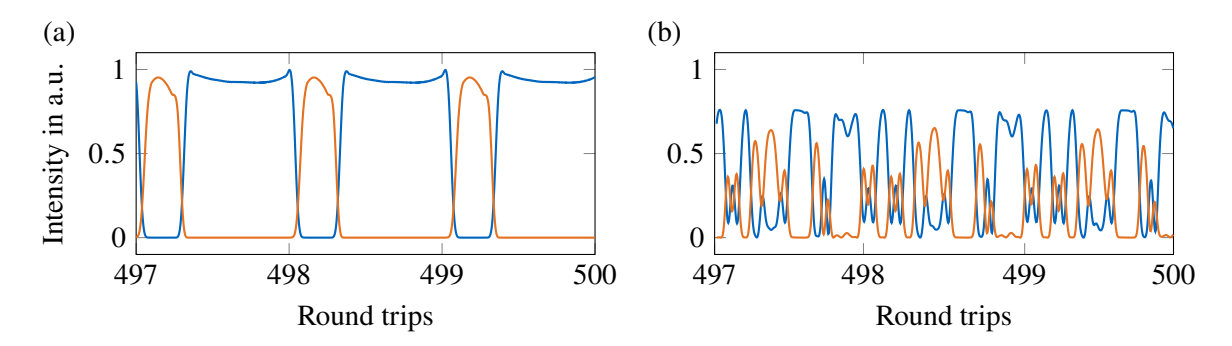


Figure 6.7 Electric field envelope at the interface of the laser cavity for the last three simulated round trips. In the absence of bulk and waveguide dispersion (a) a clear temporal separation between the higher and lower frequency lobe is visible. By inclusion of this kind of chromatic dispersion (b) the field is distributed to more modes with less intensity and the clear temporal separation is lifted. Reprinted from L. Seitner *et al.*, "Group velocity dispersion in terahertz frequency combs within a generalized Maxwell-Bloch framework" [326] (CC BY 3.0).

The most prominent peak is almost -3 dB weaker than in Fig. 6.6 (b). The shift in the center frequency below 8 GHz results from the increased permittivity due to the pole in the spectral function and the associated longer round trip time.

Time-domain results

In addition to the spectral results, it is also worth taking a brief look at the time-resolved fields. In Fig. 6.7, two plots are depicted in which the field envelopes are displayed. The indicated time covers the last three round trips, and the fields refer to (a) the dispersion-free case and (b) the case with dispersive waveguide material. The division into an orange and a blue part for the lower and higher frequency contributions can again be recognized in these diagrams. In Fig. 6.7 (a), a clear differentiation of the field into a higher and a lower frequency lobe can be detected. The blue lobe dominates the temporal behavior and corresponds to the greater intensity of the higher frequency lobe in Fig. 6.6 (a). Both components alternate in time. This has already been observed both experimentally and in simulations and has been called "temporal hole burning" [55], [378]. It is assumed that the reason for this behavior lies in the strong anticrossing of the injector quantum states. For the dispersive case depicted in Fig. 6.7 (b), a lower intensity and strong distortions of the envelopes can be observed. Here, we also normalize the field to the highest intensity in the non-dispersive case. It turns out that even in the presence of many parasitic modes, the periodicity and the exchange of field components or "temporal hole burning", is still present. The explicitly included dispersion model does not directly affect the quantum system, but only influences the propagating field in the cavity.

Nevertheless, these results indicate that the dispersion of the waveguide is detrimental to stable frequency comb operation. Therefore, we can support the assumption that a dispersion compensation grating in the waveguide is required for stable THz frequency comb operation [14].

6.2 Superfluorescence and Amplified Spontaneous Emission

The derived Maxwell-density matrix Langevin approach is tested using a SF setup in a two-level configuration [233], [373]. This setup describes the spontaneous build-up of a macroscopic coherent dipole moment in an initially inverted system, resulting in a collective emission of a superfluorescent pulse. This behavior can be reproduced numerically within our *mbsolve* framework by simulating an ensemble of excited ions and using a dephasing time $T_2 = 100 \,\mathrm{ps}$. All other parameters required for the simulation are taken from [233]. There, an excited state's lifetime $T_1 = 76 \,\mathrm{ns}$, carrier number density $n_{3D} = 8.53 \times 10^{19} \,\mathrm{m}^{-3}$, carrier number per cell $N_{\text{cell}} = 3 \times 10^4$, transition frequency $f = 477 \,\mathrm{THz}$, dipole length $d = 6.875 \times 10^{-2} \,\mathrm{nm}$ and equilibrium inversion $w_0 = -1$ are specified. We further investigate a device with length $L = 7 \,\mathrm{mm}$ using a grid discretization $\Delta x = 70 \,\mathrm{nm}$.

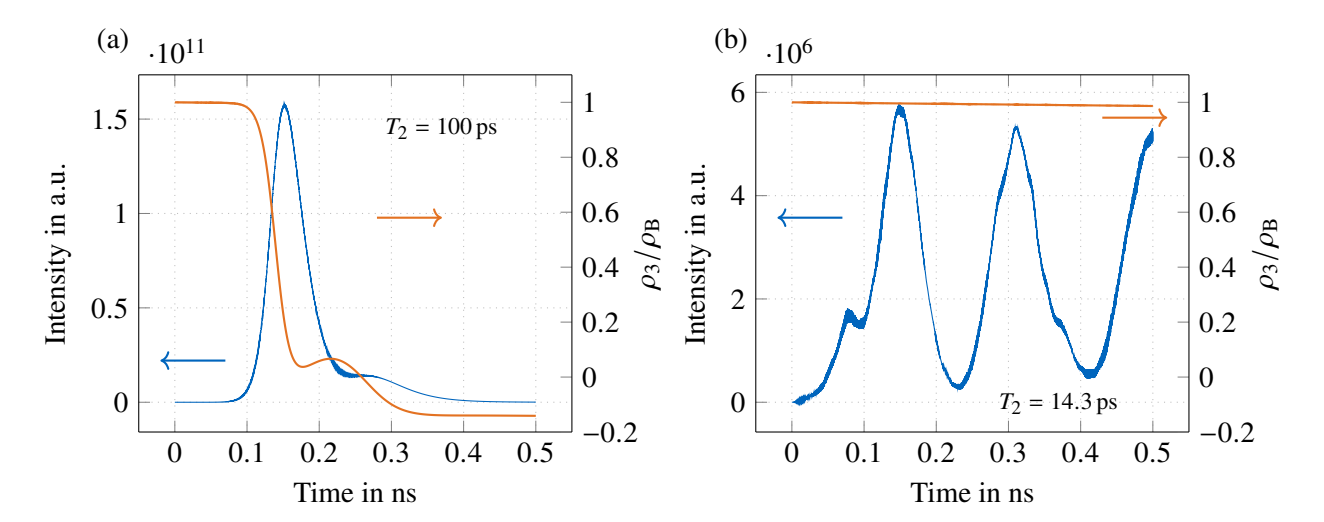


Figure 6.8 Simulation results for a superfluorescence test setup [233] in an initially inverted two-level system using the Maxwell-density matrix Langevin equations. (a) Cooperative emission characteristic of superfluorescence for the dephasing time $T_2 = 100 \,\mathrm{ps}$. (b) Amplified spontaneous emission pulse for the dephasing time $T_2 = 14.3 \,\mathrm{ps}$. Reprinted from J. Popp *et al.*, "Modeling of fluctuations in dynamical optoelectronic device simulations within a Maxwell-density matrix Langevin approach" [59] (CC BY 4.0).

The simulated SF pulse is illustrated in Fig. 6.8(a), and compares well with previous numerical and experimental findings [233], [372], [373]. By increasing the collisional dephasing rate within the system, the SF pulse is significantly disturbed and gets broadened until the spontaneous build-up of the coherent dipole moment is prevented. For a dephasing time $T_2 = 14.3$ ps below the critical point, the SF pulse is replaced by ASE. The increased noise amplitude accompanying the smaller dephasing time is crucial for the modeling of ASE, which cannot be reproduced otherwise. The ASE simulation results are presented in Fig. 6.8(b).

Furthermore, the degree of decoherence is studied using the quantity ρ_3/ρ_B , where $\rho_B = \sqrt{\rho_1^2 + \rho_2^2 + \rho_3^2}$ is the length of the Bloch vector. When the dephasing time T_2 is high (Fig. 6.8(a)), the population inversion ρ_3 is quickly depleted through the spontaneous buildup of the macroscopic dipole moment and the SF emission, which clearly surpasses the decay of ρ_1 and ρ_2 and results in a rapid drop of ρ_3/ρ_B . In the second case (Fig. 6.8(b)) we have used a smaller dephasing time T_2 , which prevents the macroscopic dipole moment build-up and limits the radiative decay. This decoherence state indicates a very slow decay of ρ_3/ρ_B , which stays close to one.

6.3 Summary

The extensions to the *mbsolve* simulation library are verified in this chapter using different simulation setups. Firstly, we have applied the ADE-FDTD implementations to a THz QCL gain medium and have conducted a comprehensive study of the optical quantum system, including the characterization of gain and intrinsic dispersion. The THz-QCL setup is then used to study the advanced PML absorbing boundary conditions, demonstrating effective attenuation of the outward propagating fields. Here, the integration of the quantum gain system into the PML region assures an improved outcoupling of the optical field, and a significantly reduced reflection error as compared to previous PML models can be achieved.

We further have used the simulation setup to analyze the influence of chromatic dispersion on optical frequency comb formation in THz QCLs. The results show a degradation of frequency comb formation in the presence of group velocity dispersion, which is consistent with experiments and current literature. The extension of our simulation approach towards the modeling of chromatic dispersion can be used for accurate performance predictions of quantum-optical devices. In particular, this makes it possible to design the chromatic dispersion based on the bulk material and the waveguide geometry in such a way that it compensates for other dispersion mechanisms, e.g., by choosing a waveguide design with an integrated grating.

Finally, we have proved the validity of our derived Maxwell-density matrix Langevin approach for modeling the fluctuations accompanying electronic transport and spontaneous emission in the dynamical simulations of light-matter interaction in multilevel optoelectronic quantum systems. Therefore, we have used a superfluorescence setup, proving the validity of our implementation by an excellent agreement with previous experimental and theoretical results. Detailed simulations of noise properties are required for the development of low-noise optoelectronic quantum sources, which will receive more and more attention in the context of exploring and utilizing nonlinear and nonclassical properties.

7 Simulation and Optimization of Photovoltaic Quantum Cascade Detectors

Intersubband photodetectors are a suitable choice for the detection of light in the mid-IR and THz regimes. They are categorized into two main classes based on their working principle: photoconductive quantum well-infrared photodetectors and photovoltaic quantum cascade detectors. Here, we focus on QCDs, which operate at zero bias and thus exhibit superior noise behavior due to the absence of dark current noise [130]. Together with quantum cascade lasers, they are suitable for integration in on-chip applications such as gas sensors. Lattice matched QCDs are based on the material system In_{0.53}Ga_{0.47}As/In_{0.52}Al_{0.48}As with a conduction band offset of 520 meV. The detection wavelengths for lattice-matched QCDs are thus limited to values well above 4 µm. However, short wavelength QCDs based on strain-compensated material systems, e.g., In_{0.61}Ga_{0.39}As/In_{0.45}Al_{0.55}As [379], can be fabricated. A CBO of 610 meV is determined for this material system using the model solid state theory [94], [271].

We present simulation results of QCDs in the mid-infrared and THz regime. For this purpose, we use the modeling approach presented in Chapter 3, which is based on a rate equation model for the calculation of the extraction efficiency and a Kirchhoff resistance network for noise modeling. The scattering rates are extracted here from the ensemble Monte Carlo transport approach. Firstly, we investigate two devices, which are based on an InGaAs/InAlAs material system lattice matched to the InP substrate [124], [126], [130], [380]. We further present simulation results of a strain-compensated QCD detecting at 4 µm [124], [379]. Finally, a THz design, which consists of a GaAs/AlGaAs-based superlattice structure on a semi-insulating GaAs substrate, is analyzed [281]. The detection wavelength for this QCD is 84 µm.

A Bayesian optimization algorithm in combination with a scattering-based simulation approach is used for the optimization of quantum cascade detectors. The appropriate surrogate model of Bayesian optimization is based on Gaussian process regression, which can handle noisy offsets on the objective function evaluations inherent in ensemble Monte Carlo simulations. Here, we focus on the optimization of a matured mid-infrared QCD design detecting at $4.7\,\mu m$. For optimization, we choose as the figure of merit the specific detectivity, which gives us a measure for the signal-to-noise ratio. The trade-off between high extraction efficiency and low detector conductance is important for good detection performance. We search for the perfect layer composition and vary the thicknesses of different cascade layers. A simulation temperature of $300\,\mathrm{K}$ is chosen due to the high-temperature requirements, which are of interest for low-cost and mobile on-chip sensor applications. Our optimization strategy yields an improvement of specific detectivity by a factor of $\sim 2-3$ at room temperature using two different parameter sets. Furthermore, we investigate the sensitivity of our approach to fabrication tolerances, showing the robustness of the optimized designs against growth fluctuations under fabrication conditions.

Section 7.1 is largely based on Section IV of C. Jirauschek, J. Popp, M. Haider, *et al.*, "Ensemble Monte Carlo modeling of quantum cascade detectors", *J. Appl. Phys.*, vol. 130, no. 20, p. 203 103, 2021. DOI: 10.1063/5.0065540, an open access article published under the terms of the Creative Commons Attribution 4.0 International License, which permits unrestricted use, distribution, and reproduction in any medium, provided the original author and source are credited. I was in the lead in conceptualizing and writing of Section IV [5].

In Section 7.1, the simulation results for the QCD design N1037 are partially reproduced with permission from J. Popp, M. Haider, M. Franckié, *et al.*, "Monte Carlo modeling of a short wavelength strain compensated quantum cascade detector", in *2021 Conference on Lasers and Electro-Optics Europe & European Quantum Electronics Conference (CLEO/Europe-EQEC)*, 2021, pp. 1–1. DOI: 10.1109/CLEO/Europe-EQEC52157.2021.9542111 | 978-1-6654-1876-8 /21/\$31.00 © 2021 EU.

Section 7.2 is largely based on Section 5 of J. Popp, M. Haider, M. Franckié, *et al.*, "Bayesian optimization of quantum cascade detectors", *Opt. Quant. Electron.*, vol. 53, no. 5, p. 287, 2021. DOI: 10.1007/s11082-021-02885-0, an open access article published under the terms of the Creative Commons Attribution 4.0 International License, which permits unrestricted use, distribution, and reproduction in any medium, provided the original author and source are credited.

The Chapter is organized as follows: In Section 7.1, the EMC-based modeling approach for photovoltaic QCD operation is validated against experimental results of mid-infrared and THz QCD designs. For the presented THz QCD, we provide a comparison with NEGF results contributed by Martin Franckié from the Quantum Optoelectronics group at the ETH Zurich. In addition, we investigate a short-wavelength QCD, which is based on a strain-compensated InGaAs/InAlAs material system. In Section 7.2, results of the Bayesian optimization of a QCD using two different parameter sets are depicted. Here, we focus on the well-established mid-IR QCD design N1022 with a detection wavelength of 4.7 µm, and discuss the obtained results of improved spectral detectivity. The last section of this chapter summarizes the simulation and optimization results of the present work and provides a brief outlook on future applications.

7.1 Ensemble Monte Carlo Results of Quantum Cascade Detectors

In the following, we present the simulation results of QCDs in the mid-infrared and terahertz regime. The three simulated devices detecting in the mid-infrared region have their absorption maxima at wavelengths of 4 μm, 4.7 μm and 7.5 μm, respectively. Two devices are based on a lattice-matched InGaAs/InAlAs material system, and a third device for detecting short wavelengths is based on a strain-compensated InGaAs/InAlAs material system [124], [126], [130], [379], [380]. The terahertz structure consists of a GaAs/AlGaAs-based superlattice structure on a semi-insulating GaAs substrate and exhibits a detection wavelength of 84 μm [281].

7.1.1 Mid-Infrared Quantum Cascade Detectors

The investigated devices in the mid-infrared range have the sample identifier names N1021 (7.6 μ m), N1022 (4.7 μ m) and N1037 (4 μ m). The active region of the two lattice-matched designs consists of 30 periods and the strain-compensated N1037 design uses 10 repetitions of the active period. In this configuration, a 45° wedge geometry mesa-structure with a double-pass waveguide is considered for the simulation. The facet transmittance is assumed to be 70 %. Further information about these designs, along with experimental data used for comparison purposes in this work, can be found in the literature, where also details on the measurements are given [124], [126], [130], [379], [380].

The strongly delocalized Bloch-type wavefunction solutions of the Schrödinger equation for perfectly periodic potentials are not adequate for describing carrier transport in realistic QCD structures, since any amount of disorder due to, e.g., growth irregularities and impurities, leads to the formation of localized states [381], [382]. In addition, scattering-induced dephasing suppresses multiple-tunneling processes, and thus also contributes to a localization of states [383], [384]. Hence, we restrict the spatial simulation window in our Schrödinger-Poisson solver such that wavefunction solutions extending over multiple periods are avoided. The resulting conduction band profile and energy eigenstates are shown in Fig. 7.1 for the QCD N1021. The lattice constant of InGaAs at room temperature is 0.587 nm, and the thinnest well of the structure has a width of 2.8 nm. Interface roughness is included in our carrier transport simulations using typical values of 0.1 nm for the average root-mean-square roughness height and 10 nm for the in-plane correlation length. Absorption takes place in the active well of each period between the ground level g and the two closely spaced absorption levels a₁ and a₂. As explained in Section 3.2, the weighted average for the extraction efficiency p_e of the transitions $g \to a_1$ and $g \to a_2$ is calculated using Eq. (3.25). Both absorption levels extend over two wells and give rise to resonant tunneling transport through the thick barrier between the active well and the subsequent well. Transport through the cascade is mediated by LO phonon-assisted scattering and to a lesser extent by interface roughness scattering. Efficient extraction is achieved by arranging the energy spacing between two consecutive states close to the LO phonon energy of 32 meV in In_{0.53}Ga_{0.47}As. More specifically, the quantum well structure is engineered to optimize detectivity, which involves a trade-off between close to unity extraction efficiency p_e and high detector resistance $R_{\rm d}$. For the design N1021, the extractor states are localized in their respective wells. Since in this case, the overlap between adjacent states mainly results from the wavefunction leakage into the thick barrier regions, the corresponding scattering rates tend to be considerably lower than in QCLs, which typically feature thinner barriers and more delocalized wavefunctions.

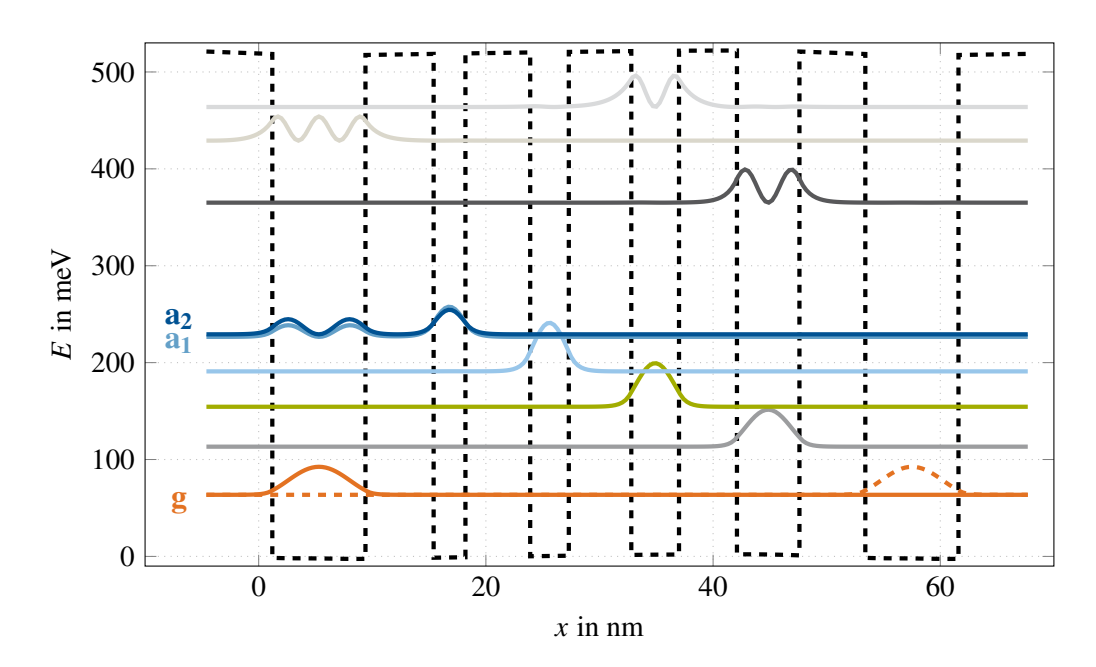


Figure 7.1 Calculated conduction band profile and probability densities of the investigated mid-infrared QCD structure N1021 detecting at 7.6 μ m [130], [380]. Starting from the leftmost well, the layer sequence (in nm) of one period with barriers in boldface and n-doped layers (3×10^{17} cm⁻³) underlined is 8.2/6.0/2.8/5.7/3.4/5.5/4.2/5.1/5.5/5.8. Space charge effects are included by self-consistently solving the Schrödinger and Poisson equation. The electron densities in the states are modeled accounting for thermal equilibrium under zero external bias and no incident light for a lattice temperature of 300 K. Reprinted from C. Jirauschek *et al.*, "Ensemble Monte Carlo modeling of quantum cascade detectors" [42] (CC BY 4.0).

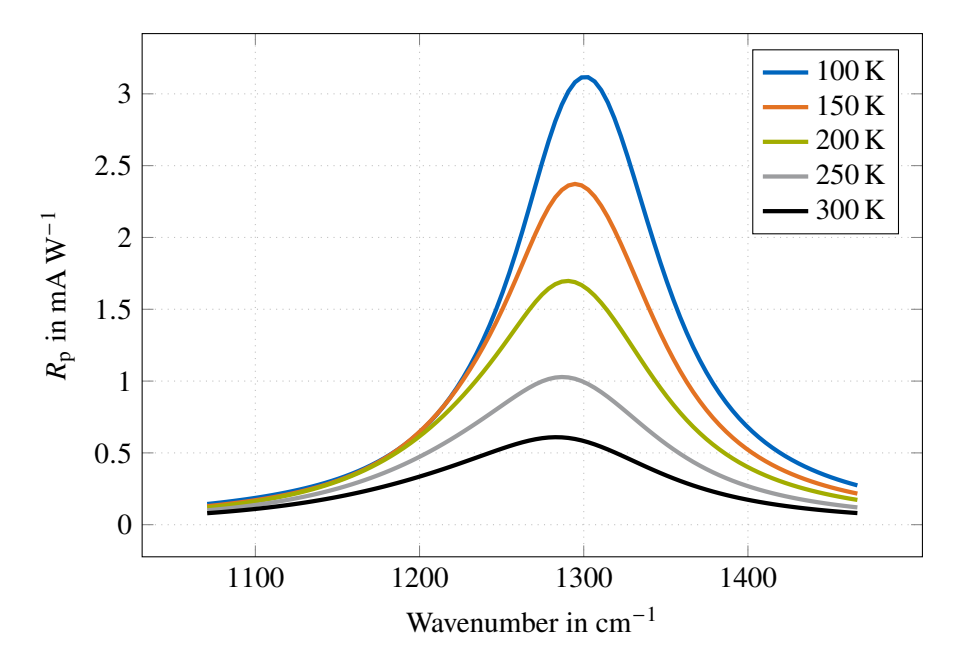


Figure 7.2 Simulated responsivity R_p of the QCD structure N1021 as a function of wavenumber in the temperature range 100 K to 300 K. Reprinted from C. Jirauschek *et al.*, "Ensemble Monte Carlo modeling of quantum cascade detectors" [42] (CC BY 4.0).

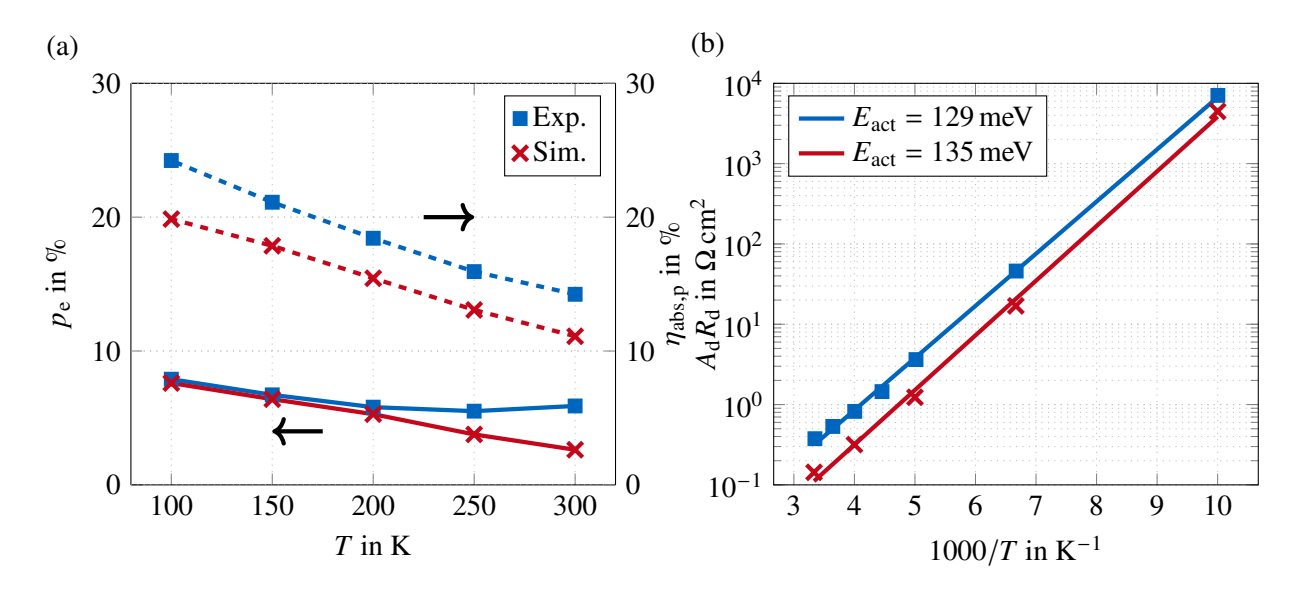


Figure 7.3 Comparison of simulated (x marks) and experimental (squares) results for the detector structure N1021. (a) Extraction efficiency p_e (solid lines) and peak absorption $\eta_{abs,p}$ (dashed lines) as a function of temperature T. (b) Detector resistance-area product A_dR_d as a function of the inverse temperature T^{-1} . The lines represent the Arrhenius plots with calculated activation energies E_{act} . Reprinted from C. Jirauschek *et al.*, "Ensemble Monte Carlo modeling of quantum cascade detectors" [42] (CC BY 4.0).

The simulated responsivity spectrum for the detector structure N1021 is depicted in Fig. 7.2. At 300 K, we obtain a peak responsivity of $0.61\,\text{mA}\,\text{W}^{-1}$, in comparison to a measured value of $1.69\,\text{mA}\,\text{W}^{-1}$. For lower temperatures, the simulated and measured responsivities show considerably better agreement. The simulated peak responsivity increases to $3.1\,\text{mA}\,\text{W}^{-1}$ for $100\,\text{K}$, as compared to a measured value of $3.8\,\text{mA}\,\text{W}^{-1}$. At a temperature of $300\,\text{K}$ the simulated peak detection wavelength is $7.8\,\mu\text{m}$ in comparison to $7.62\,\mu\text{m}$ in the experiment. This slight blueshift of the experimental detection energy was also recognized in the design process [126] and is attributed to process uncertainties in the fabrication, which can lead to thickness variations of the active QW. The observed redshift with increasing operation temperature, which is attributed to nonparabolicity and band filling, is replicated in the simulations by the inclusion of energy-dependent effective subband masses.

To validate our detector model, we evaluate the simulation results for the extraction efficiency $p_{\rm e}$, power absorption efficiency $\eta_{\rm abs}$ and device resistance $R_{\rm d}$, and compare them with the experimentally measured values. Results are illustrated in Fig. 7.3 for 100 K to 300 K.

The power absorption efficiency in Fig. 7.3(a) decreases linearly from 20 % at 100 K to 11 % at 300 K for the simulated results and is ~3 \% smaller than in experiment. Due to broadening effects and reduced population of the ground level g with rising temperatures, the absorption efficiency and thus the responsivity get reduced. For decreasing temperature, a shift of the probability density maximum of state a_1 to the right thinner QW and of state a_2 to the left active QW occurs due to the change in band bending associated with space charge effects. The peak absorption of the transition $g \rightarrow a_2$ thus increases significantly and becomes the dominating absorption transition. The responsivity depends furthermore on the extraction efficiency p_e , which is also displayed in Fig. 7.3(a). Over the plotted range, the simulated p_e decreases linearly with increasing temperature, whereas the experimental values saturate to $p_{\rm e,300\,K} = 5.9\,\%$ for temperatures above 200 K. Evaluation of the simulated scattering rates shows that LO phonon emission is the dominant mechanism for relaxation from the two absorption levels a_1 , a_2 to the ground level g. Extraction to the cascade is dominated by interface roughness and LO phonon scattering. Furthermore, the calculation of the individual extraction efficiencies in one period exhibits that backscattering in the extraction cascade affects significantly the behavior of p_e over temperature. Backscattering by LO phonon absorption degrades due to the thermal reduction of the phonon occupation for low temperatures. By reducing the temperature, backscattering in the extraction cascade gets suppressed, which results in an efficient charge extraction to the ground state of the adjacent period [29]. Lastly, the device

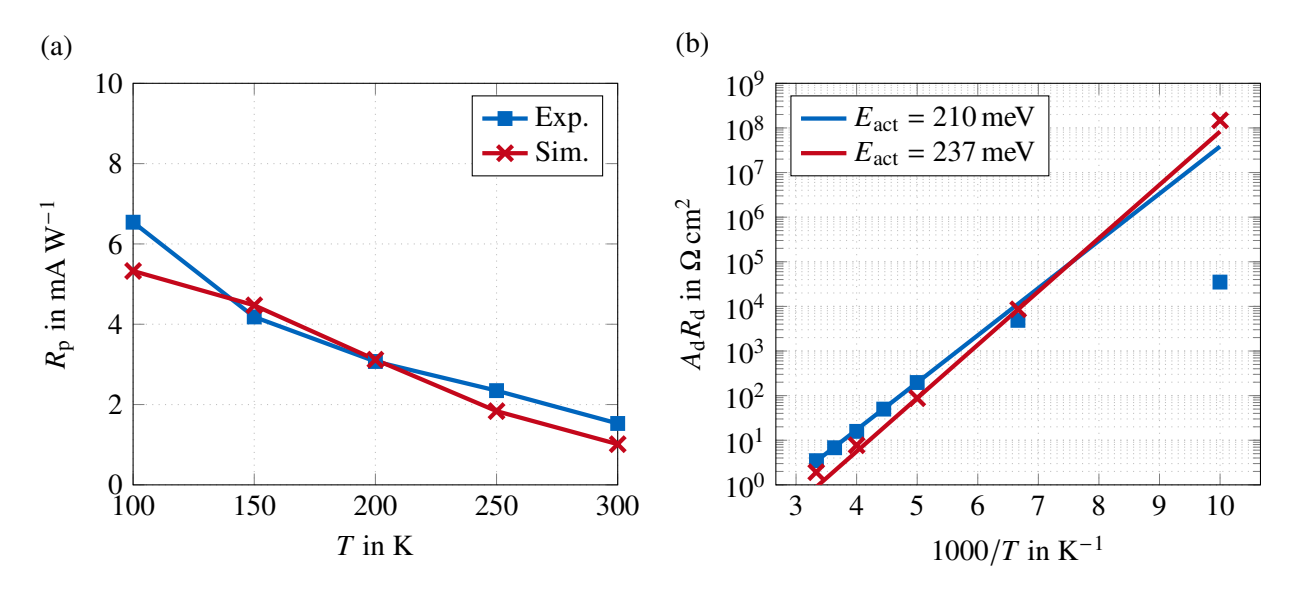


Figure 7.4 Comparison of simulated (x marks) and experimental (squares) results for the predefined figures of merit of the detector structure N1022. (a) Peak responsivity R_p as a function of temperature T. (b) Detector resistance-area product A_dR_d as a function of the inverse temperature T^{-1} . The lines represent the Arrhenius plots with calculated activation energies E_{act} . Reprinted from C. Jirauschek *et al.*, "Ensemble Monte Carlo modeling of quantum cascade detectors" [42] (CC BY 4.0).

resistance R_d is presented in Fig. 7.3(b). Experimentally, the device resistance R_d was determined from dark current measurements at zero bias. In the temperature range 100 K to 300 K the exponential behavior of the detector resistance is replicated. The calculated activation energy of $E_{act} = 133$ meV is in good agreement with the experimentally obtained value of $E_{act} = 129$ meV. The close correspondence of the experimentally obtained resistance values with the simulated ones confirms the validity of the resistance model presented in Section 3.2 for the investigated temperature range.

The second mid-infrared detector N1022 exhibits a similar layer composition as N1021. Here, the thickness of the active well is reduced from 82 Å (N1021) to 51 Å, and the cascade is extended by three extractor levels. The structure modifications result in a higher detecting energy of 268 meV. The peak responsivity R_p and detector resistance-area product A_dR_d for the temperature range 100 K to 300 K are presented in Fig. 7.4(a) and 7.4(b), respectively. The simulated peak responsivity R_p decreases from 5.3 mA W⁻¹ at 100 K to 1.0 mA W⁻¹ at 300 K similar to the experimental data. At 300 K, the values $p_e = 17.2\%$ and $\eta_{abs} = 4.63\%$ are obtained from the simulated scattering rates, which is in good agreement with the experimentally obtained values of $p_e = 12.5\%$ and $\eta_{abs} = 9\%$ at room temperature. As illustrated in Fig. 7.4(b), the device resistance shows the Arrhenius plot behavior. The high-temperature activation energy of $E_{act} = 237$ meV calculated from the simulated detector resistance values compares well with the experimentally obtained value of $E_{act} = 210$ meV. Below 150 K, the experimental values for the resistance-area product deviate from the Arrhenius plot slope and exhibit a flattening trend, which cannot be replicated in the simulation. This behavior is ascribed in literature to the presence of parasitic parallel resistance, generated e.g., by defects or surface currents [28].

For the investigated mid-infrared QCD structure N1037, the calculated wavefunctions and conduction band profile from the Schrödinger-Poisson solver are given in Fig. 7.5. Here, the nonparabolicity and the effects of strain on (parallel and perpendicular) effective mass and bandgap energy are taken into account [29], [265]. The normalized responsivity spectra are depicted in Fig. 7.6(a) for temperatures of 100 K to 300 K. The experimentally documented broadening of the absorption spectra attributed to thermal band filling can also be observed in the simulation. However, the redshift with increasing temperature is not as pronounced as experimentally measured and has to be investigated in further simulations. At 150 K, we obtain a simulated peak responsivity of 13.9 mA W⁻¹, which is slightly higher than the measured value of 10.7 mA W⁻¹. The Johnson noise limited detectivity of QCDs is modeled by a noise-equivalent resistance network replicating the intersubband transitions in the active region. In Fig. 7.6(b), the simulation results together with the

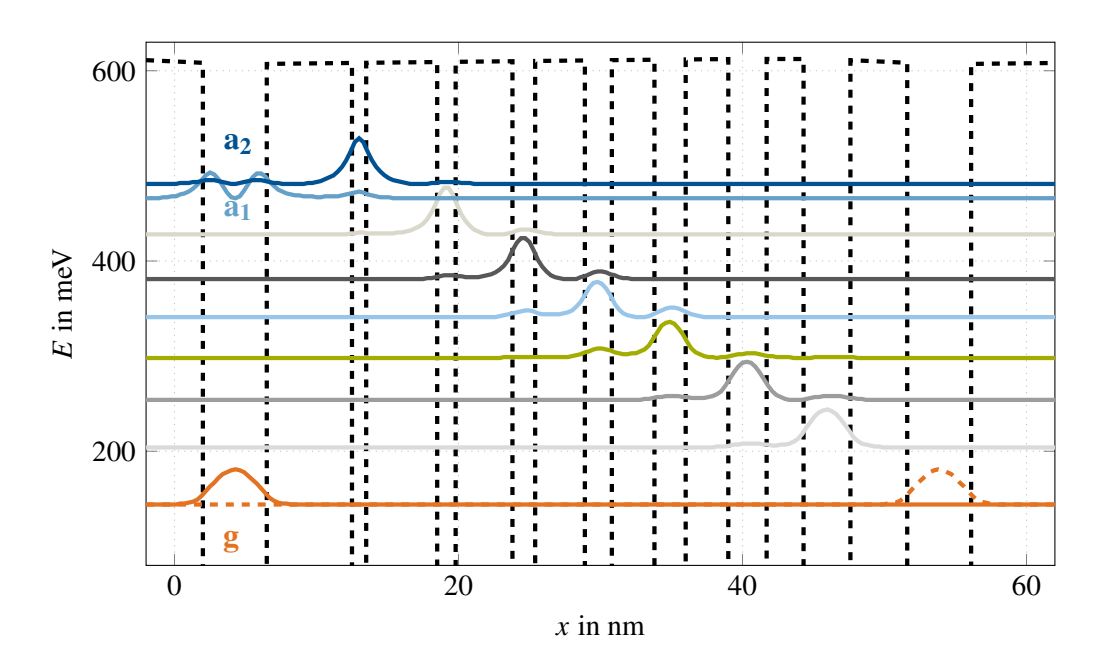


Figure 7.5 Calculated conduction band profile and probability densities of the investigated mid-infrared QCD structure N1037 detecting at $4 \, \mu m$ [124], [379]. Starting from the leftmost well, the layer sequence (in nm) of one period with barriers in boldface and n-doped layers $(1 \times 10^{18} \, \text{cm}^{-3})$ underlined is 4.5/6.0/1.0/5.0/1.3/4.0/1.6/3.5/1.9/3.0/2.2/3.0/2.7/2.6/3.3/4.0. Space charge effects are included by self-consistently solving the Schrödinger and Poisson equation. The electron densities in the states are modeled accounting for thermal equilibrium under zero external bias and no incident light for a lattice temperature of 300 K. Reprinted with permission from J. Popp *et al.*, "Monte Carlo Modeling of a Short Wavelength Strain Compensated Quantum Cascade Detector" [385] | 978-1-6654-1876-8 /21/\$31.00 © 2021 EU.

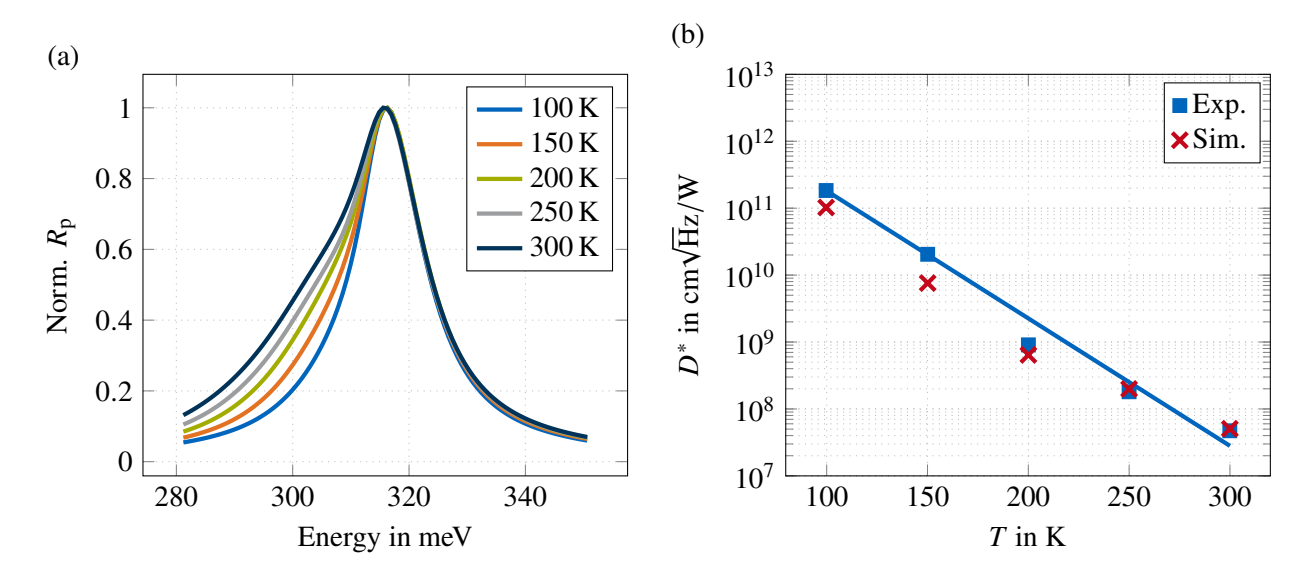


Figure 7.6 (a) Normalized simulated responsivity R_p of the QCD structure N1037 as a function of energy in the temperature range 100 K to 300 K. (b) Simulated (x marks) and experimentally measured (squares) specific detectivity as a function of temperature T. Adopted with permission from J. Popp *et al.*, "Monte Carlo Modeling of a Short Wavelength Strain Compensated Quantum Cascade Detector" [385] | 978-1-6654-1876-8 /21/\$31.00 © 2021 EU.

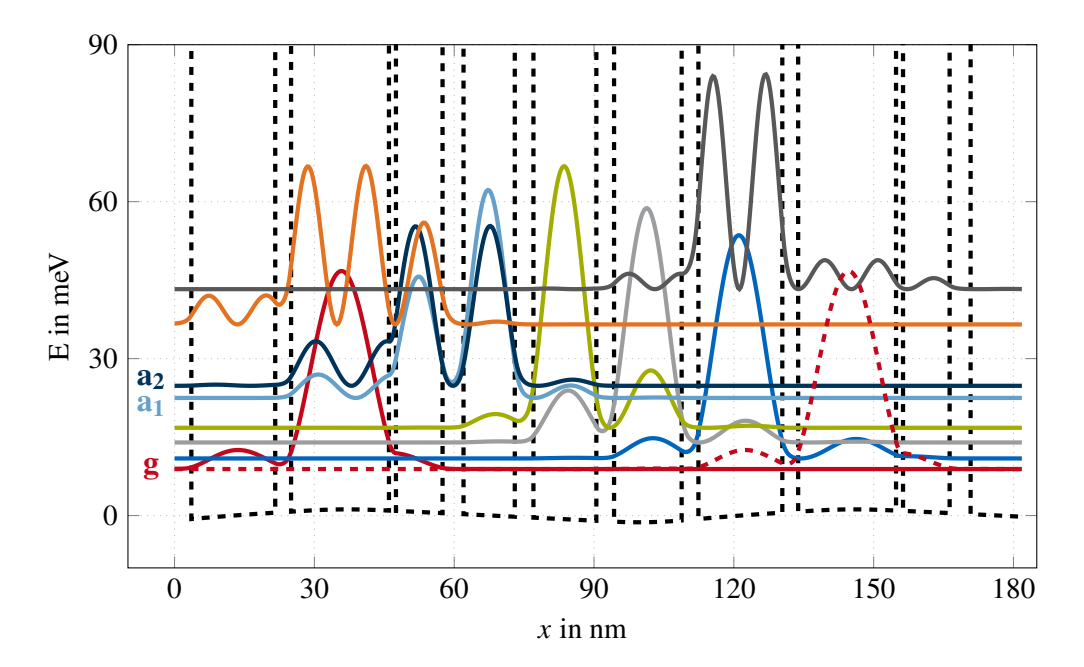


Figure 7.7 Calculated conduction band profile and probability densities of the investigated terahertz QCD structure detecting at $84\,\mu\text{m}$ for a lattice temperature of $10\,\text{K}$. Starting from the leftmost well, the layer sequence (in nm) of one period with barriers in boldface and n-doped layers ($6\times10^{15}\,\text{cm}^{-3}$) underlined is 18.0/3.4/21.0/1.5/10.0/4.5/11.0/4.0/13.5/3.8/14.5/3.6. Reprinted from C. Jirauschek *et al.*, "Ensemble Monte Carlo modeling of quantum cascade detectors" [42] (CC BY 4.0).

experimentally measured values in the temperature range $100\,\mathrm{K}$ to $300\,\mathrm{K}$ are illustrated. Here, the exponential behavior of the Johnson noise-limited detectivity is replicated. The simulated detectivity of $5.06\times10^7\,\mathrm{cm}\sqrt{\mathrm{Hz}}/\mathrm{W}$ at $300\,\mathrm{K}$ compares well with the experimental value of $4.9\times10^7\,\mathrm{cm}\sqrt{\mathrm{Hz}}/\mathrm{W}$.

7.1.2 Terahertz Quantum Cascade Detector

Furthermore, our approach has been applied to a GaAs/AlGaAs-based terahertz QCD operating at a wavelength of around $84 \,\mu m$ [281]. Here, we assume again a 45° double-pass waveguide mesa configuration with a transmittance at the air/GaAs interface of $70 \,\%$.

In Fig. 7.7, the conduction band diagram and energy eigenstates obtained with a Schrödinger-Poisson solver for a lattice temperature of 10 K are shown. Here, we choose a conduction band offset of 135 meV for the calculation of the wavefunctions. The thinnest barrier has a width of 1.5 nm, which is approximately three lattice constants (0.565 nm for GaAs). Figure 7.8 displays the simulated and measured spectral responsivity at a temperature of 10 K, showing good agreement. Our simulation yields a peak responsivity of 10.6 mA W⁻¹ at $109\,\mathrm{cm}^{-1}$, which compares well with the experimental value of $8.6\,\mathrm{mA}\,\mathrm{W}^{-1}$ at $119\,\mathrm{cm}^{-1}$. The simulated extraction efficiency of $p_e = 0.36$ is in reasonable agreement with the experimental estimate of $p_e \approx 0.5$, which was obtained under idealized assumptions [281]. For the two relevant transitions $g \to a_1$ and $g \to a_2$ absorption efficiencies of $2.4\,\%$ and $3.8\,\%$ are obtained from the simulation, which agrees reasonably well with the estimate of $3\,\%$ for both transitions, inferred from the calculated dipole matrix elements [281]. However, the experimentally measured absorption values were below $2\,\%$, which was in part attributed to trapping of electrons by impurities [281]. In addition to experimental uncertainties, certain effects may be relevant that are not considered in the simulation, in part because their quantitative influence is not well known. For example, the measured photocurrent, and therefore the derived responsivity, depends on the extraction from the device contacts, which are not included in the model.

Furthermore, we have compared the EMC results with simulation results obtained by Martin Franckié from the Quantum Optoelectronics group at ETH Zurich using a non-equilibrium Green's function approach [34], [386], [387]. Here, the responsivity is calculated by simulating the photocurrent under irradiation. This model has been developed for simulating QCLs under operating conditions, where small (several A/cm²) uncertainties

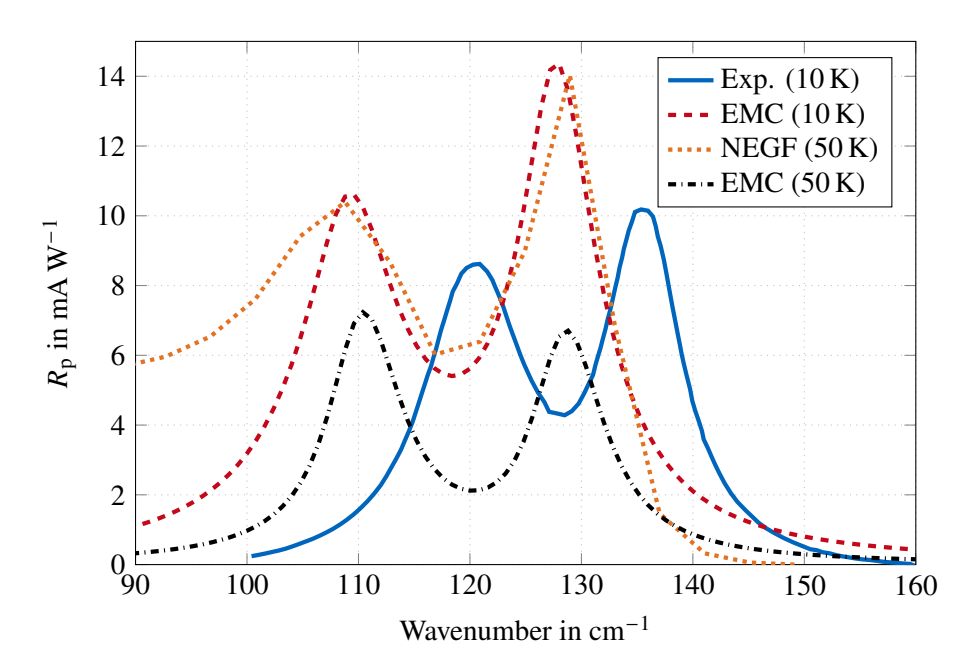


Figure 7.8 Responsivity spectrum R_p as a function of wavenumber for the 3.5 THz QCD structure at a temperature of 10 K, as obtained from the simulation and extracted from experimental photocurrent measurements. Furthermore, a comparison between EMC and NEGF simulation results is shown for 50 K. Reprinted from C. Jirauschek *et al.*, "Ensemble Monte Carlo modeling of quantum cascade detectors" [42] (CC BY 4.0).

in the current density due to the limited number of periods and basis states considered are acceptable. However, the dark currents and photocurrents in QCDs are on a similar order of magnitude as this uncertainty. Therefore, we have subtracted from the photocurrent a constant offset defined as the photocurrent at a high frequency (160 cm $^{-1}$) where the simulated absorption is close to zero. The obtained responsivity spectra of both the EMC and NEGF simulations for a lattice temperature of 50 K are illustrated in Fig. 7.8. The two responsivity peaks of $10.4 \,\mathrm{mA} \,\mathrm{W}^{-1}$ at $109 \,\mathrm{cm}^{-1}$ and $14.6 \,\mathrm{mA} \,\mathrm{W}^{-1}$ at $129 \,\mathrm{cm}^{-1}$ from the NEGF simulations are in good agreement with the EMC results of $7.2 \,\mathrm{mA} \,\mathrm{W}^{-1}$ at $110 \,\mathrm{cm}^{-1}$ and $6.7 \,\mathrm{mA} \,\mathrm{W}^{-1}$ at $129 \,\mathrm{cm}^{-1}$. Notably, both the EMC and NEGF spectra are red-shifted with respect to the measured one. The depolarization shift, not considered in our simulations, is estimated to be $\sim 0.1 \,\mathrm{meV}$ [388], and is thus too small to account for the discrepancy. Another explanation might be that similar fabrication uncertainties as described for the mid-infrared designs lead to slightly higher measured peak absorption energies. In general, the peak responsivity decreases with increasing temperature due to the thermal activation of electrons and the resulting occupation of higher-lying states. According to the EMC simulations, this results for an increase from $10 \,\mathrm{K}$ to $50 \,\mathrm{K}$ in a peak responsivity reduction of $32.1 \,\%$ at $109 \,\mathrm{cm}^{-1}$ and $53.5 \,\%$ at $129 \,\mathrm{cm}^{-1}$, respectively.

Fig. 7.9 shows the simulated current-voltage characteristics of the terahertz QCD without illumination. The simulated results of the NEGF and EMC models are compared to the experimentally measured values for the three temperatures 50 K, 100 K and 150 K. As mentioned above, the currents in QCDs are significantly smaller than in QCLs, which makes the dark current simulation of such terahertz QCD devices with NEGF and EMC at small biases rather unpractical. In fact, the NEGF simulations only converged for certain bias points and only showed robust results at 50 K when electron-electron interaction was included [287]. As illustrated in Fig. 7.9, the experimentally measured dark currents for applied biases below 0.2 V cannot be reproduced by both simulation approaches. This problem becomes even more manifest for temperatures of 50 K and below, resulting in even smaller dark current densities. For higher biases, both simulation models can replicate the measured current-voltage characteristics.

From the experimentally measured dark current at $50\,\mathrm{mV}$ [281], we estimate a zero-bias resistance-area product $R_\mathrm{d}A_\mathrm{d}=300\,\Omega\,\mathrm{cm}^2$ at $10\,\mathrm{K}$ under the assumption that this bias is already in the linear regime. The simulated resistance-area products of $R_\mathrm{d}A_\mathrm{d}=3\,\Omega\,\mathrm{cm}^2$ (EMC) and $R_\mathrm{d}A_\mathrm{d}=1\,\Omega\,\mathrm{cm}^2$ (NEGF) are two orders of magnitude smaller. For temperatures below $20\,\mathrm{K}$, the dark current is expected to be dominated by a temperature-independent contribution based on direct tunneling processes [281]. This effect is not included in the EMC

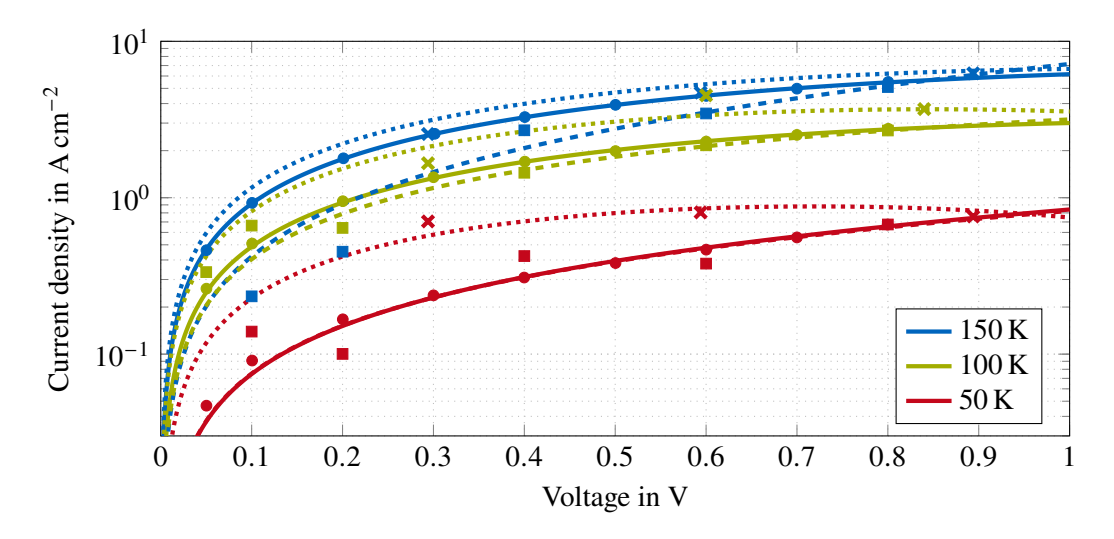


Figure 7.9 The measured current-voltage characteristics of the THz detector design (dots) is compared to results obtained from EMC (squares) and NEGF including electron-electron scattering (crosses) simulations for 50 K, 100 K and 150 K. Fits to the experimental results (solid lines) as well as to the simulation results for EMC (dashed lines) and NEGF (dotted lines) are included using a polynomial function of second degree. Reprinted from C. Jirauschek *et al.*, "Ensemble Monte Carlo modeling of quantum cascade detectors" [42] (CC BY 4.0).

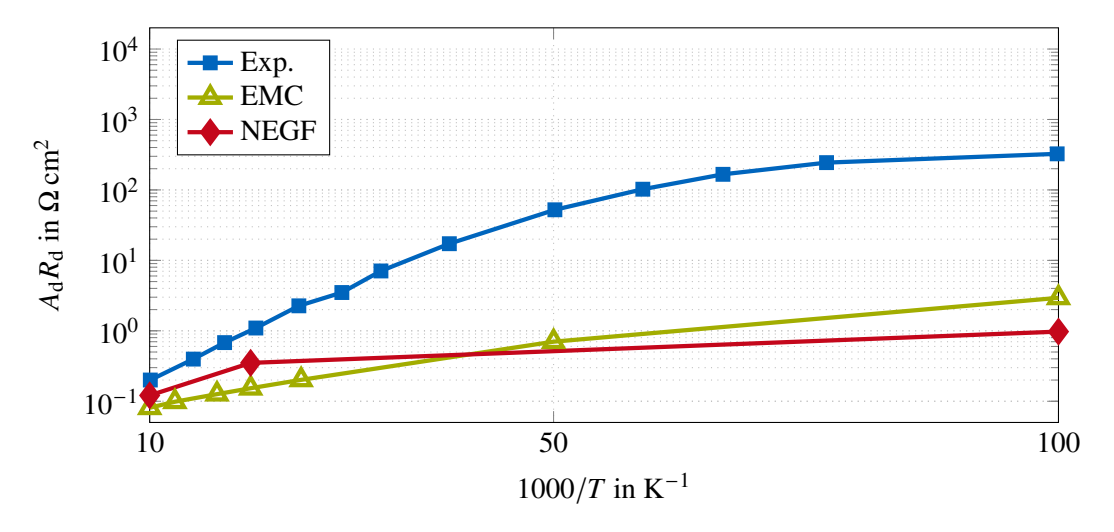


Figure 7.10 Detector resistance-area product A_dR_d as a function of the inverse temperature T^{-1} , as obtained from EMC and NEGF simulations and extracted from experimental dark current measurements. Reprinted from C. Jirauschek *et al.*, "Ensemble Monte Carlo modeling of quantum cascade detectors" [42] (CC BY 4.0).

approach but fully accounted for in the NEGF simulations, thus it does not explain the observed discrepancy between theory and experiment. In Fig. 7.10, the temperature-dependent resistance-area product R_dA_d extracted from the measured current-voltage characteristics and obtained with EMC and NEGF is displayed logarithmically as a function of the inverse temperature T^{-1} .

A simulated specific detectivity $D^* = 1.05 \times 10^9 \, \mathrm{cm} \sqrt{\mathrm{Hz}} / \mathrm{W}$ is calculated from the EMC scattering rates at 10 K. By substituting the experimentally measured responsivity $R_p = 8.6 \, \mathrm{mA} \, \mathrm{W}^{-1}$ and resistance-area product into Eq. (3.26), we obtain a specific detectivity $D^* = 6.6 \times 10^9 \, \mathrm{cm} \, \sqrt{\mathrm{Hz}} / \mathrm{W}$ at 10 K. Experimentally, the specific detectivity was measured using a QCL with an emitting wavelength of 87 $\mu \mathrm{m}$ [280] to estimate the noise equivalent power (NEP) of the THz QCD. With the measured NEP = 7 nW a specific detectivity of $5 \times 10^7 \, \mathrm{cm} \, \sqrt{\mathrm{Hz}} / \mathrm{W}$ at 10 K was obtained [281], which is two orders of magnitude smaller than the value obtained from the dark current measurement. As it was pointed out above, the dominant noise mechanism for temperatures below 20 K is not temperature dependent, and thus the simulated detectivity based on our Kirchhoff's resistance model, taking into account Johnson noise as the main noise mechanism, cannot replicate the experimentally measured specific detectivities. The resulting discrepancy between the measured specific detectivity and the one deduced from the dark current measurements implies a second noise source appearing in the photocurrent measurements, e.g., additional blackbody radiation entering through the cryostat window of the measurement setup.

7.2 Bayesian Optimization of Quantum Cascade Detectors

In this section, we present a Bayesian optimization of a QCD device using our monacoQC framework. The device N1022 detects at a wavelength of 4.7 µm and is based on the lattice-matched material system $In_{0.53}Ga_{0.47}As/In_{0.52}Al_{0.48}As$ grown on an InP substrate [126]. The conduction band profile and the calculated wavefunctions are illustrated in Fig. 7.11(a) for the operation temperature 300 K. The QCD structure consists of multiple periods comprising a doped active quantum well (QW) and an adjacent extraction cascade of QWs with varying thicknesses. Photo-excitation occurs between the ground level g and the two degenerate absorption levels a_1 , a_2 in the active QW, followed by the extraction through the staircase of subbands via longitudinal optical phonon-assisted tunneling to the ground state of the adjacent period.

The structure N1022 was validated both with our scattering rate model and the EMC approach and the experimentally measured results compare well with the simulated ones [126]. Here, we investigated the specific detectivity D^* , the responsivity R_p , extraction efficiency p_e and resistance R_d in the temperature range 100 K to 300 K. At 300 K, we obtain a specific detectivity $D^*_{\text{Matlab}} = 1.36 \times 10^7$ Jones and $D^*_{\text{EMC}} = 1.09 \times 10^7$ Jones, respectively. The simulation values show good agreement with measured values of $D^*_{\text{exp.}} \sim 2 \times 10^7$ Jones [126].

The aim of this work is to improve the signal-to-noise ratio of the mid-IR QCD N1022 for the elevated temperature regime. Therefore, we decided to concentrate on the layer sequence $[w_1b_1w_2b_2]$ indicated in Fig. 7.11(a). To reduce the optimization complexity, the sequence was divided into two subsystems with each parameter set consisting of three consecutive layers. Furthermore, we can analyze the impact of the changes in individual layer width on device parameters and thus have more flexibility in the selection of the best layer composition.

For the BO, we chose a step width of 0.1 Å and a testing interval dW \in [-2 Å, 2 Å] added to the nominal layer width of each considered layer. As an evaluation method, we used the Matlab function calc-scatt. We performed the BOs with 2000 evaluations using multiple cores to get enough training data for a GP, which is used to analyze the optimization results. The conduction band profile and wavefunctions of the most successful scheme in each subset are illustrated in Fig. 7.11(b), (c). The optimization scheme is based on the parameter set 1, changing the layer sequence $[b_1w_2b_2]$ shown in Fig. 7.11(b), and parameter set 2 by changing the layer sequence $[w_1b_1w_2]$ depicted in Fig. 7.11(c). In the following, the results of both optimization runs are explained in detail. In the concluding discussion, we compare both setups and justify the model accuracy and emerging challenges regarding fabrication tolerances.

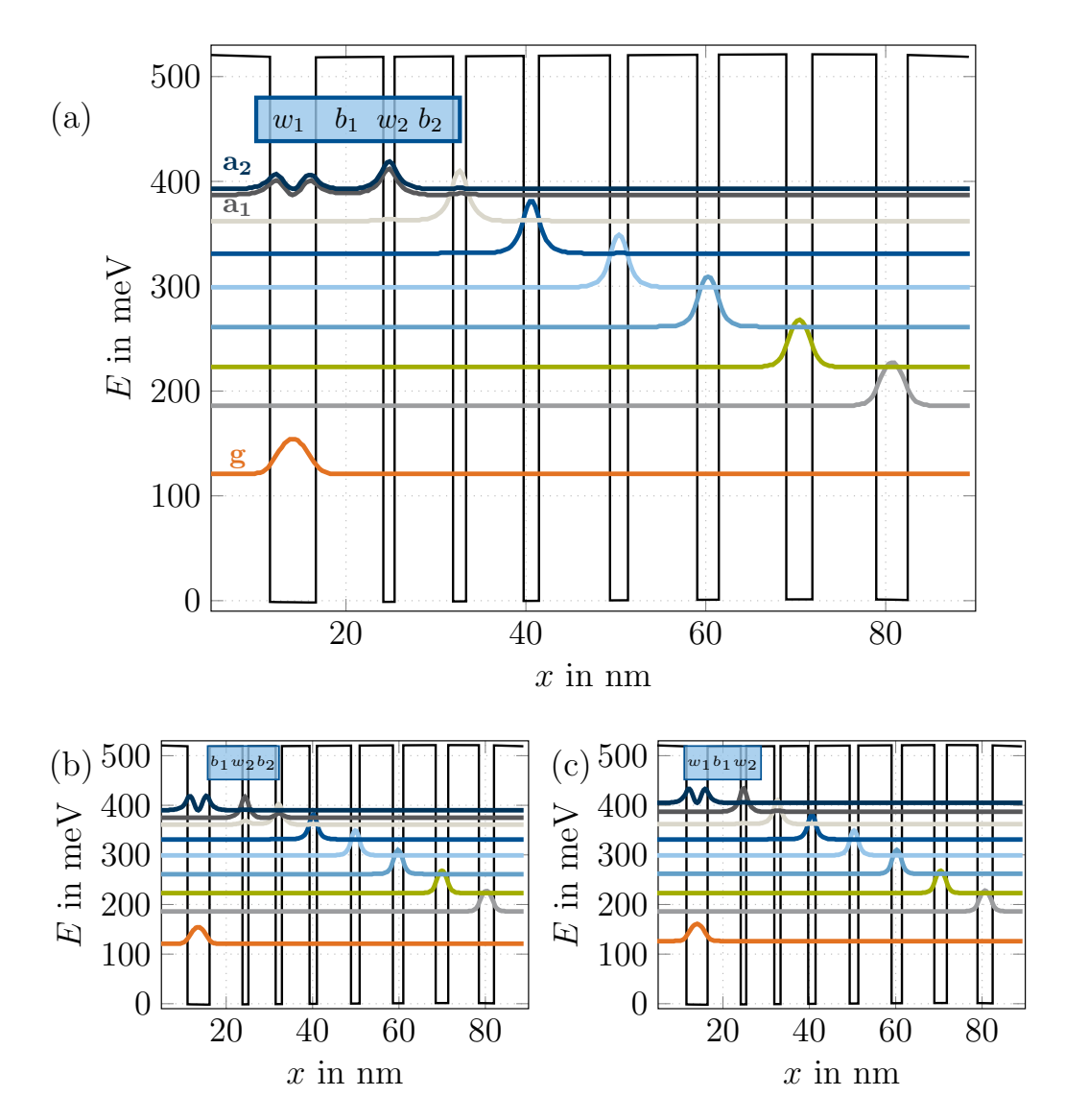


Figure 7.11 Calculated conduction band profile and probability densities of (a) the investigated mid-IR QCD structure N1022 [126] and the two optimized structures (b) r1_1 and (c) r2_1. The N1022 layer sequence of one period with InAlAs barrier layers in boldface and n-doped layers $(4 \times 10^{17} \, \text{cm}^{-3})$ underlined is $6.8/\underline{5.1}/7.5/1.25/6.5/1.45/6.4/1.7/7.9/2/7.7/2.4/7.5/2.9/7.1/3.5$. The labeled layers $[w_1b_1w_2b_2]$ in (a) are the investigated parameters for the optimization of the nominal structure N1022. The two optimization schemes (b) $[b_1w_2b_2]$ and (c) $[w_1b_1w_2]$ are illustrated by blue boxes, respectively. Reprinted from J. Popp *et al.*, "Bayesian optimization of quantum cascade detectors" [24] (CC BY 4.0).

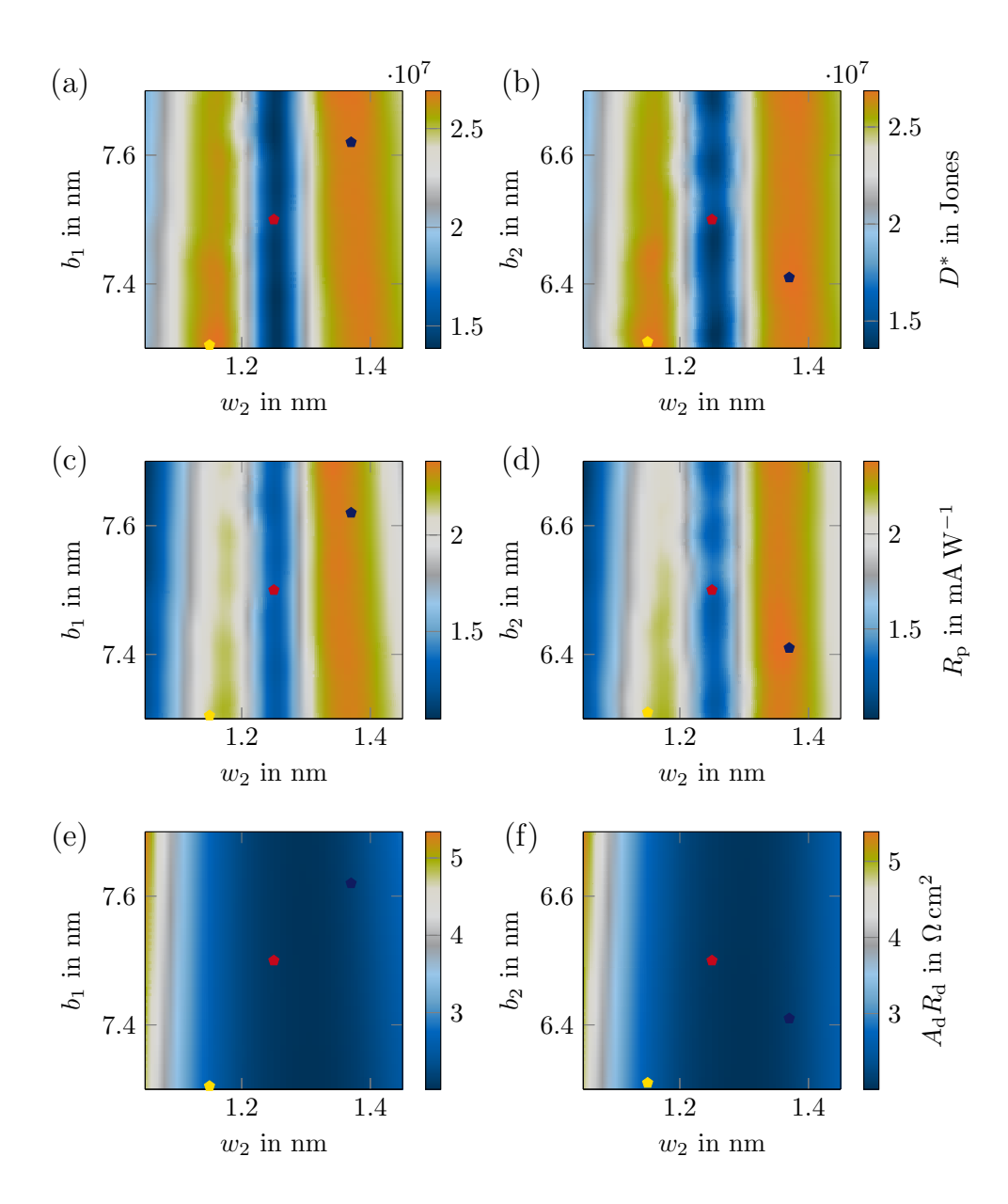


Figure 7.12 Dependence of specific detectivity D^* (a), (b), peak responsivity R_p (c), (d) and resistance-area product A_dR_d (e), (f) on pairs of parameters, starting from the nominal structure N1022 and using the BO results of parameter set 1 with layer sequence $[b_1w_2b_2]$. The red, yellow and blue pentagons indicate the layer sequence of the nominal design N1022 and the optimized structures r1_2 and r1_1, respectively. The labels are defined in Fig. 7.11. Reprinted from J. Popp *et al.*, "Bayesian optimization of quantum cascade detectors" [24] (CC BY 4.0).

7.2.1 Parameter Set 1

The parameter set 1 consists of the three layers $[b_1w_2b_2]$ next to the active well. With the layer sequence, we intend to increase the absorption efficiency η_{abs} , while keeping Johnson noise low and the extraction efficiency p_e high. The detection wavelength should only be slightly affected by the optimization, since the active well layer and thus the absorbing transition are not directly changed. The optimized structure r1_1, illustrated in Fig. 7.11(b), exhibits a change of the investigated layer sequence by [1.2 Å, 1.2 Å, -0.9 Å]. The simulation results of this structure are given in Table 7.1. We obtain an improvement of the simulated detectivity $D_{\text{opt.}}^* = 2.73 \times 10^7$ Jones by factor ~ 2 . As illustrated in Fig. 7.11(b), the change in layer composition results in a displacement of the two absorption levels. Here, the absorption maximum is shifted to the higher lying absorption level a_2 , whereas the lower lying absorption level a_1 acts then mainly as an extraction level. In this context, the oscillator strength between the ground level a_2 and the absorbing level a_2 is increased significantly. In summary, the peak responsivity is increased by 100 % and accounts for the great improvement of the specific detectivity.

Table 7.1 Layer sequence with barrier layers in boldface, peak wavelength λ_p , extraction efficiency p_e , peak responsivity R_p , resistance-area product A_dR_d and specific detectivity D^* of the nominal structure N1022 and the optimized structures.

ID	layer sequence	λ_{p}	p_{e}	$R_{ m p}$	$A_{\rm d}R_{\rm d}$	D^*
	$[w_1b_1w_2b_2] \text{ (nm)}$	(µm)	(%)	$(mA W^{-1})$	(Ωcm^2)	$(\cdot 10^7 \text{Jones})$
N1022	5.1/ 7.5 /1.25/ 6.5	4.77	19.14	1.22	2.07	1.37
r1_1	5.1/ 7.62 /1.37/ 6.41	4.72	17.10	2.41	2.11	2.73
r1_2	5.1/ 7.3 /1.15/ 6.31	4.71	14.45	2.19	2.56	2.73
r2_1	4.9/ 7.67 /1.27/ 6.5	4.57	24.34	3.03	2.32	3.58
r2_2*	4.8/7.57/1.23/6.5	4.50	28.18	3.32	2.50	4.07

To analyze the obtained optimization results in more detail, we used a GP, trained with the simulation results of the BO run. Using GP regression, we can predict the changes in specific detectivity D^* with variation of the given layer sequence. In Fig. 7.12, the dependence of the specific detectivity D^* , peak responsivity R_p and resistance area product $A_{\rm d}R_{\rm d}$ on pairs of layer thicknesses in the parameter set is shown. The position of the nominal structure N1022 is marked by a red pentagon. The specific detectivity D^* is influenced mostly by the well width w_2 , as depicted in Figs. 7.12(a), (b). Here, we obtain a maximum at the well width of $w_2 = 11.5 \text{ Å}$ and $w_2 = 13.5 \text{ Å}$, respectively. The impact of barrier widths b_1 and b_2 on the specific detectivity D^* is rather small. For characterization, we can divide the specific detectivity D^* into two parts: the responsivity, depending on the absorption and extraction efficiency, as a measure for the signal strength, and the detector resistance accounting for the current noise sensitivity. The optimized structure r1_1, representing the group of optimized structures at maximum $w_2 = 13.5 \,\text{Å}$, exhibits a significantly improved peak responsivity due to the increased absorption efficiency. The structure r1_2 given in Table 7.1 belongs to the other group with maximum $w_2 = 11.5 \,\text{Å}$. Here, both the area resistance product A_dR_d as well as the peak responsivity R_p are increased [Figs. 7.12(c)-(f)]. An increased resistance at the cost of reduced extraction efficiency leads to smaller responsivity values, which explains the difference between both maxima in Figs. 7.12(c), (d). In summary, both optimized structures listed in Table 7.1 exhibit similar signal-to-noise behavior and an absorption wavelength of $\sim 4.7 \,\mu m$, which is close to the absorption wavelength of the nominal structure N1022. Structure r1_1 seems to be more robust with respect to fluctuations in layer width w_2 than structures r1_2 (Figs. 7.12 (a), (b)). As the first design r1_1 offers better signal strength and the second design r1_2 favors low noise behavior, one can choose the best-suited design for different applications.

7.2.2 Parameter Set 2

The parameter set 2 consists of the three layers $[w_1b_1w_2]$ starting with the active well w_1 . Here, we are also interested in the influence of the layer width of the active well w_1 on the device performance. In order to keep the absorption frequency shift small, we introduce a new figure of merit

$$f(x) = D^*(x) \times \left(1 - \frac{|f_0 - f_{p,\text{opt.}}(x)|}{f_0}\right),\tag{7.1}$$

where the specific detectivity D^* is multiplied by a weighting factor including the peak absorption frequency f_0 of the nominal structure N1022 and the peak absorption frequency of the sampled structure $f_{p,opt.}$. The value x represents the parameter set consisting of the layer sequence $[w_1b_1w_2]$.

For the optimized design r2_1, a specific detectivity $D^* = 3.58 \times 10^7$ Jones is achieved, which implies even better results in absolute values as in BO run 1. The wavelength of 4.57 µm for the optimized design r2_1 is slightly smaller than in BO run 1. Due to the change of well width $w_1 = 49 \,\text{Å}$, both the ground level g and the absorption level a_2 are shifted to higher energy values. The change in energy of absorption level a_2 exceeds that of the ground level g, which results in a lower absorption wavelength. For all investigated structures, the transition rate from the absorption level a_2 to level a_1 , as well as to the next extraction level, is dominated by interface roughness scattering. In the case of structure r2_1 we observe an increased scattering from $a_2 \rightarrow a_1$ combined with an attenuated extraction from a_1 to the next extraction level. By comparison of Fig. 7.11(b) and Fig. 7.11(c), one identifies an increased energy gap between level a_1 and the next extraction level of structure r2_1, which implies a shift of the dominating scattering mechanism from interface roughness to longitudinal optical phonon emission. The extraction efficiency $p_e = 24.34 \%$ and the resistance-area product $A_d R_d = 2.32 \,\Omega$ cm² can thus simultaneously be increased, which results in superior signal-to-noise behavior.

In Fig. 7.13 the specific detectivity D^* , peak responsivity R_p and wavelength λ_p are shown for variation of pairs of parameters starting with the nominal structure values. Here, we see again a small dependence of the merit function on the layer width of barrier b_1 . As explained before, the decrease of well width w_1 results in a significant increase of the specific detectivity D^* at the expense of a detection wavelength shift. For thicker well widths w_1 , the opposite effect is observed. As illustrated in Figs. 7.13(b), (d) and (f), a strong correlation between the well widths w_1 and w_2 arises. Here, a balanced choice of these two layer widths is necessary for the optimization.

The optimization went to the edge of the parameter range for well width w_1 (Figs. 7.13(a), (c)). Therefore, we decided to extend the optimization range and did a third BO run starting from the optimized structure r2_1. By further decreasing the well width $w_1 = 4.8 \text{ Å}$, the optimized structure r2_2* with a specific detectivity $D^* = 4.07 \times 10^7$ Jones can be found. The simulation parameters of structure r2_2* are detailed in Table 7.1. By shrinking the well width w_1 , the specific detectivity can be substantially enhanced at the expense of an undesired wavelength shift.

7.2.3 Discussion

In this work, we focused on two different parameter sets for the Bayesian optimization of the detector design N1022 [126], [130]. The parameter set 1 with layer sequence $[b_1w_2b_2]$ ensures a stable optimization of the specific detectivity without fluctuations or drifts in the detection wavelength. As a consequence of BO run 1, we identify the influence of barrier width variations $(b_1 \text{ and } b_2)$ on the simulated device parameter to be rather small. The second parameter set includes the active well w_1 of the QCD. Here, we use specific detectivity multiplied with a weighting factor as the new figure of merit to ensure a rather stable detection wavelength. The transitions from absorption level a_2 to the following extractor levels are mainly based on interface roughness. By changing the well widths w_1 and w_2 , we can improve the extraction from level a_2 to a_1 and increase the energy gap from level a_1 to the next extraction level, which induces a transition of the dominating scattering mechanism from IF to LO phonon scattering. Here, the reduced scattering leads to an increased detector resistance. Furthermore, we can improve the absorption efficiency of all optimized structures due to the increased oscillator strength of $g \rightarrow a_2$. The important simulation parameters of the optimized structures are listed in Table 7.1, and

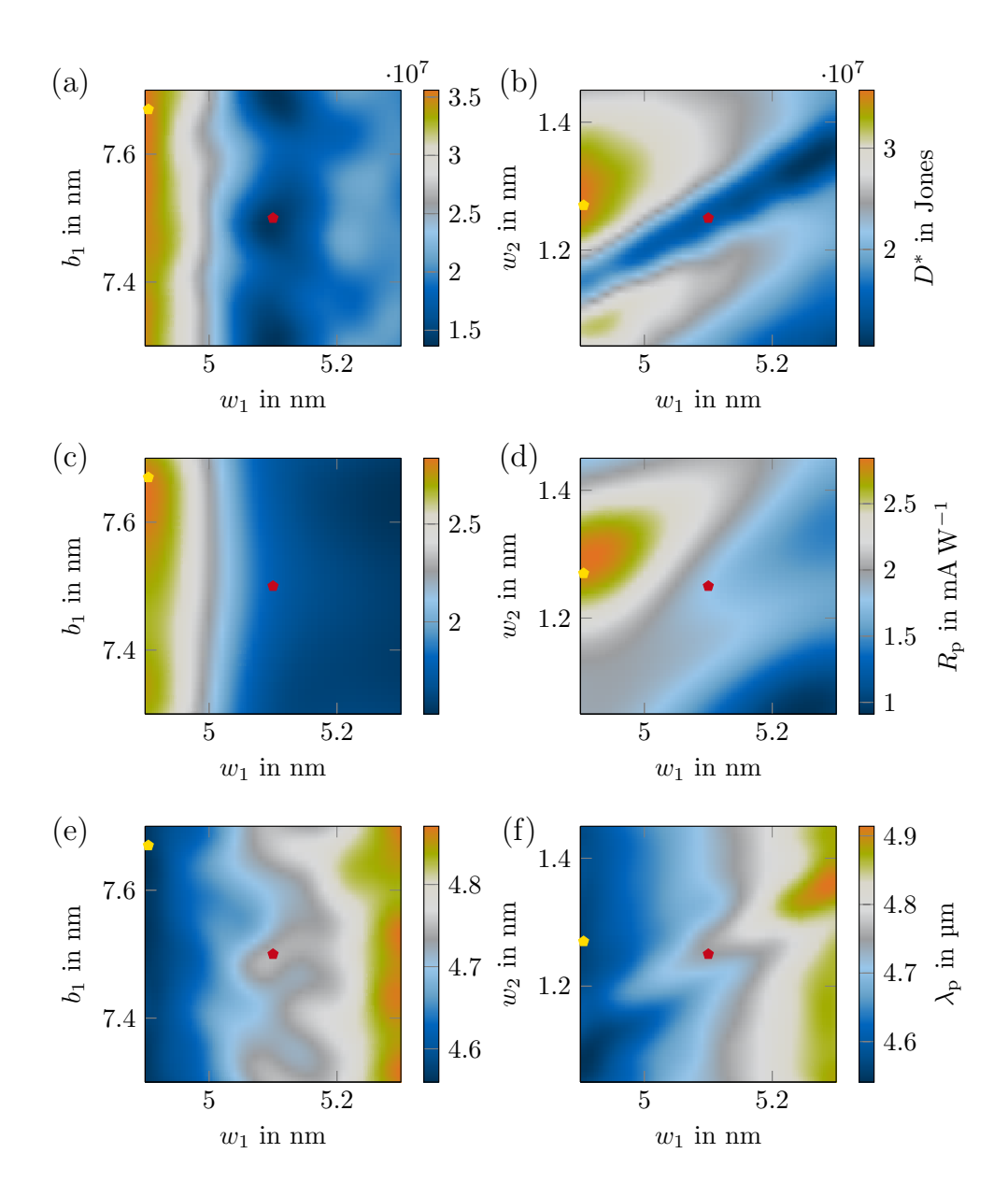


Figure 7.13 Dependence of specific detectivity D^* (a), (b), peak responsivity R_p (c), (d) and resistance-area product A_dR_d (e), (f) on pairs of parameters, starting from the nominal structure N1022 and using the BO results of parameter set 2 with layer sequence $[w_1b_1w_2]$. The red and orange pentagons indicate the layer sequence of the nominal design N1022 and the optimized structure r2_1. The labels are defined in Fig. 7.11. Reprinted from J. Popp *et al.*, "Bayesian optimization of quantum cascade detectors" [24] (CC BY 4.0).

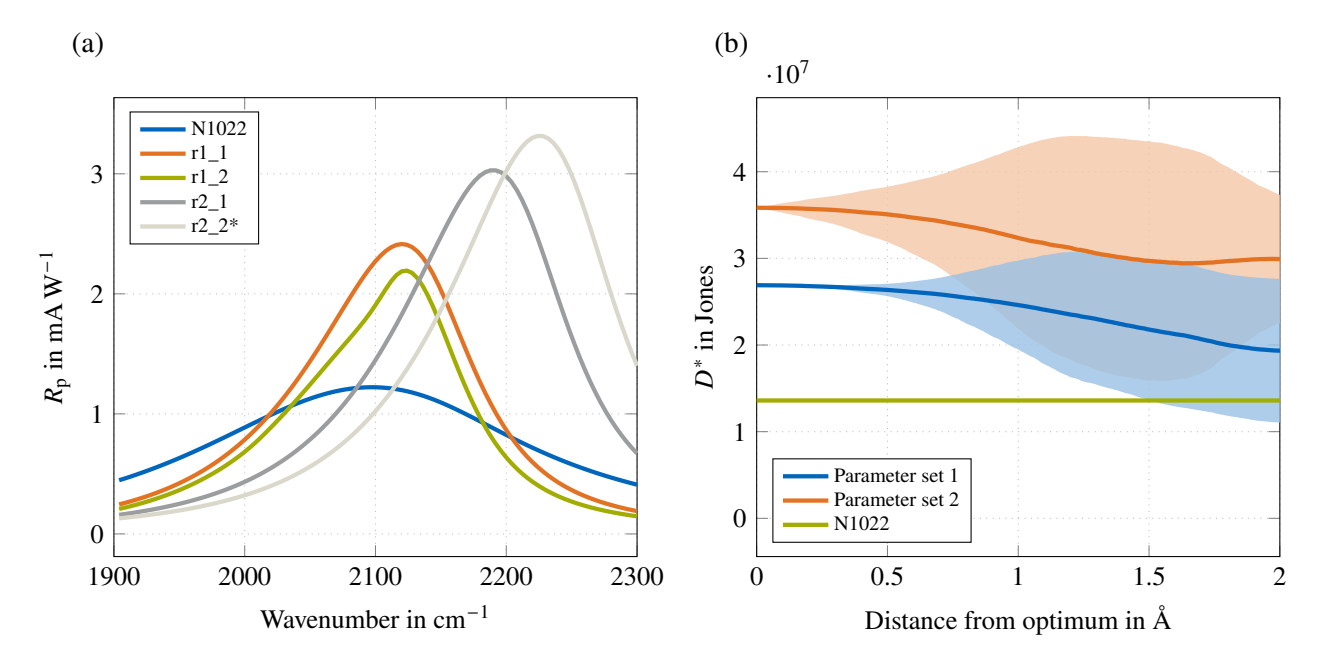


Figure 7.14 (a) Simulated responsivity R_p of the nominal QCD structure N1022 and the optimized structures as a function of wavenumber at 300 K. (b) Sensitivity on the specific detectivity D^* over distance from the optimum of parameter set 1 (blue) and 2 (orange). The lines exhibit the mean specific detectivity and the shaded areas represent the 95% prediction interval obtained by samples from the trained GP. Reprinted from J. Popp *et al.*, "Bayesian optimization of quantum cascade detectors" [24] (CC BY 4.0).

the responsivity spectra of the different structures together with the nominal structure N1022 are displayed in Fig. 7.14(a).

As mentioned before, the influence of specific layer widths on the wavefunctions and thus the detector behavior can vary significantly. Therefore, we decided to use smaller parameter sets, such that we could analyze correlations and sensitivities between layer widths and device parameters in more detail. The optimized structures of parameter set 2 imply better results than parameter set 1 in terms of signal-to-noise ratio. On the other hand, if a specific detection wavelength is crucial, one should concentrate more on parameter set 1. The defined goals of an optimization run are thus strongly dependent on the given constraints and thus the choice of the right input parameters is important.

In this BO, we used the scattering model based on Fermi's golden rule, which does not consider e-e scattering. EMC simulations including e-e scattering exhibit similar results for the mid-infrared detector N1022, which confirms the validity of our optimization. For simulations of terahertz structures in the low-temperature regime, e-e scattering becomes more important and has to be considered [41].

Furthermore, we investigated the sensitivity of our optimization results on variations in the parameter set [22]. These variations can arise through growth fluctuations in the fabrication. Starting from the optimal structure of each parameter set, a GP was trained to predict changes in the specific detectivity with respect to fluctuations in the well and barrier widths of the investigated layer sequence. By sampling ~ 500000 points, we can visualize the sensitivity of our model by plotting the predicted specific detectivity D^* over distance from the optimal structure r1_1 and r2_1, respectively. Here, the distance is the radius of a hypersphere in the three-dimensional parameter space. The results are illustrated in Fig. 7.14(b) and show the variation of specific detectivity D^* when diverging from the optimal values to a distance of 2 Å. Within a radius of 1 Å the variations of both structures are small, which ensures robustness against fluctuations. Even for longer distances up to 2 Å, both structures promise better results than obtained with the nominal structure N1022. As reported in the literature, small deviations of the period thickness in the range of 1 % to 2 % can be accomplished with the modern molecular-beam-epitaxy technology [21], [180], [389]. Applying this to the layer sequence $[w_1b_1w_2]$, possible deviations in the range -1.4 Å to 1.4 Å for this layer sequence can occur during the device growth. Within this tolerance, our optimization results are still reasonable, and the designs r2_1 and r1_1 show promising alternatives to the nominal design N1022.

7.3 Summary

We have presented simulation results for photovoltaic QCD operation in the mid-infrared and THz regime using an EMC-based modeling approach. The comparison with experimental data yields good agreement for both mid-infrared and terahertz QCD designs. For the modeling of the short-wavelength design based on a strain-compensated material system, we have calculated the material parameters including strain effects. The results are in good agreement with the experiment. Furthermore, the EMC results of the investigated terahertz structure are compared to NEGF simulations, yielding good agreement. Notably, for low temperatures the simulated zero-bias resistance of this structure is much lower than the value extracted from the experiment. Due to its accuracy, versatility and relative numerical efficiency, the presented simulation approach is well-suited for the systematic optimization of QCD structures.

Therefore, we have combined it with the Bayesian optimization algorithm and used the QCD design N1022 as a test setup. The approach exhibits precise and robust optimization results. Investigating two different parameter sets, the specific detectivity D^* of the nominal structure can be improved by a factor of $\sim 2-3$. The oscillator strength between ground level g and absorption level a_2 leads to a significantly increased absorption efficiency η_{abs} , thus resulting in peak responsivities 2-3 times higher than for the nominal structure N1022. Using a GP trained with the simulation results of the BO runs, we can make assumptions about the sensitivity of the optimized designs regarding fabrication tolerances. The optimized structures of both parameter sets appear to be quite robust against growth layer variations. For this optimization approach, we have used a scattering model based on Fermi's golden rule. For further optimizations, we will also use the self-consistent EMC model for the evaluation of QCD figures of merit, and compare them with the scattering rate approach used in this work.

For the design and optimization of on-chip applications in environmental sensing based on quantum cascade devices, this approach could be useful, e.g., for temperature optimization. It further enables the investigation of the robustness of a design against manufacturing tolerances by stochastic sampling of points in the design parameter space.

8 Multi-Domain Modeling of Free-Running Frequency Comb Formation in Quantum Cascade Lasers

Optical frequency comb emission in quantum cascade lasers is highly attractive for applications in metrology and sensing. Here, the large third-order nonlinearity $\chi^{(3)}$ present in QCLs leads to broadband FWM processes, that trigger mode proliferation. Recently, coherent OFC mode-locking in a novel operation regime with large intermodal spacing was demonstrated in QCLs. These self-starting harmonic frequency combs show highly phase-stable operation and promise interesting perspectives toward optical or even quantum communication. Aiming for a full understanding of the physical mechanisms behind the HFC generation and harmonic ordering, a detailed theoretical characterization of the QCL gain medium is required. Here, we present a numerical study of coherent OFC emission in QCLs based on our self-consistent multi-domain modeling approach. Our theoretical characterization is divided into stationary carrier transport simulations, based on the ensemble Monte Carlo method, and dynamical simulations of the light-matter interaction, based on multilevel Maxwell-density matrix equations. We investigate the influence of the chosen eigenstate basis on the gain spectrum and present self-consistent simulation results of stable HFC operation in a double metal terahertz QCL. In our simulations, the studied QCL gain medium shows self-starting harmonic mode-locking for different bias and waveguide configurations, resulting in a mode spacing of up to twelve times the cavity round trip frequency. Furthermore, we characterize the spectral time evolution of the coherent HFC formation process, yielding the spontaneous build-up of a dense multimode state which is gradually transferred into a broad and clear harmonic OFC state. Finally, we also analyze the noise contributions to the comb characteristics using the Langevin extensions.

Gas sensors based on THz OFC QCL sources show great potential for mobile applications. Unfortunately, direct THz quantum cascade laser frequency comb generation is currently not achievable at room temperature. However, THz comb generation based on intracavity difference frequency generation in mid-infrared QCLs is a promising alternative. Here, DFG in the active region of a dual-wavelength mid-IR QCL is considered for the generation of THz radiation. The mixing process and thus THz generation requires a high second-order intersubband nonlinear susceptibility in the QCL active region, and can be obtained by targeted quantum engineering. The associated nonlinear effects are included in the Hamiltonian of our Maxwell-density matrix simulation approach. Notably, such simulations require a full-wave Maxwell-density matrix solver which does not employ the common rotating wave approximation, as a broadband optical field extending from the THz to the mid-IR region is investigated. Our modeling approach and the obtained simulation results for two THz DFG-QCL comb setups are validated against experimental data, showing reasonable agreement. Furthermore, we obtain a locked frequency-modulated comb state for the mid-IR and THz regimes.

Section 8.1 is largely based on Section III of J. Popp, L. Seitner, F. Naunheimer, *et al.*, "Multi-domain modeling of free-running harmonic frequency comb formation in terahertz quantum cascade lasers", *IEEE Photonics J.*, vol. 16, no. 2, p. 0600711, 2024. DOI: 10.1109/JPHOT.2024.3370189, an open access article published under the terms of the Creative Commons Attribution 4.0 International License, which permits unrestricted use, distribution, and reproduction in any medium, provided the original author and source are credited.

The noise characteristics presented in Subsection 8.1.3 are reproduced from Section III B of J. Popp, J. Stowasser, M. A. Schreiber, *et al.*, "Modeling of fluctuations in dynamical optoelectronic device simulations within a Maxwell-density matrix Langevin approach", *APL Quantum*, vol. 1, no. 1, p. 016 109, 2024. DOI: 10.1063/5.0183828, an open access article published under the terms of the Creative Commons Attribution 4.0 International License, which permits unrestricted use, distribution, and reproduction in any medium, provided the original author and source are credited.

Section 8.2 is largely based on Section III of J. Popp, L. Seitner, M. A. Schreiber, *et al.*, "Modeling of self-starting harmonic mode-locking in THz quantum cascade lasers", in *Infrared Terahertz Quantum Workshop (ITQW 2023)*, Jun. 2023, an open access article published under the terms of the Creative Commons Attribution 4.0 International License, which permits unrestricted use, distribution, and reproduction in any medium, provided the original author and source are credited.

The chapter is structured as follows: In Section 8.1, simulation results for self-starting harmonic mode-locking in a THz QCL are presented. Since several theoretical analyses of QCL gain media have shown that the chosen wavefunction basis has a significant influence on the gain properties, we first analyze the influence of the eigenstate basis on the laser output state. The influence of the basis set on the gain characteristics and the harmonic mode-locking behavior is discussed here. Additionally, we illustrate frequency-resolved results of the unsaturated gain profile, obtained by pump-probe dynamical simulations, and long-term simulations of the four quantum well QCL in harmonic comb operation. We investigate the influence of the applied bias and the waveguide geometry on the harmonic ordering and characterize the spectral time evolution of the self-starting harmonic mode-locking mechanism. Furthermore, we discuss the effects of noise contributions on the THz HFC characteristics. Section 8.2 presents simulation results of intracavity terahertz comb difference frequency generation in mid-infrared quantum cascade lasers. Firstly, we present stationary charge carrier transport simulations of the given structures based on the EMC method and compare them with the corresponding experimental data. Secondly, dynamic simulations of the light-matter interaction using the open-source Maxwell-density matrix simulation tool *mbsolve* are provided. The chapter concludes with a short summary.

8.1 Self-Starting Harmonic Mode-Locking in Terahertz Quantum Cascade Lasers

In the following, we present simulation results for a self-starting THz HFC QCL setup [73], [181]. The device consists of a four quantum well active region, which is embedded in a double-metal waveguide featuring high facet reflectance. A schematic of the THz HFC QCL setup is illustrated in Fig. 1.4. As described above, we investigate the influence of the chosen eigenstates basis on the gain spectrum and present self-consistent simulation results of stable HFC operation with a mode spacing of $4 \times f_{rt}$. Furthermore, we investigate the influence of the applied bias and waveguide geometry on the harmonic ordering. Finally, we characterize the spectral time evolution of the self-starting harmonic mode-locking mechanism.

8.1.1 Influence of Wavefunction Basis Sets on the Coherent Operation in THz HFC QCLs

For an adequate optical and electrical description of the THz QCL active gain medium, we take into account five wavefunctions in one active period. The QCL system is investigated using extended and localized wavefunction configurations within the SP solver. Electron injection into the upper laser level is governed by resonant tunneling from the injector state of the adjacent period [blue rectangle in Fig. 2.7(b)] and can be appropriately described within the tight-binding model [35], [36]. Additionally, we take into account further coherences arising from closely aligned energetic levels by applying an EZ-transformation [184]. Here, eigenstates separated by an energy of less than 5 meV are summarized within a multiplet of states. These subsets of eigenstates are diagonalized with respect to the dipole moment operator [184]. A transformed triplet of states within the investigated THz QCL configuration is schematically illustrated in Fig. 2.7(c) by an orange rectangle. For the characterization of the full dynamical range extending from single-mode operation to fundamental and harmonic comb states, carrier transport simulations over an extended bias range have been conducted for the two configurations, respectively. In the following, we analyze the unsaturated gain behavior of the four quantum well QCL gain medium.

In Fig. 8.1, the peak gain and center frequency for the bias range 40 mV/period to 60 mV/period are illustrated. We can identify two operating regimes. In the lower bias range < 51 mV/period, both the peak gain and center frequency for the localized states tend towards higher values compared to the extended states. Due to the strong localization of ULL and LLL in space, the transition exhibits a smaller lifetime broadening for the optical transition, resulting in narrower gain curves with increased peak values. The center frequency is also higher, as the EZ-transformation shifts the eigenenergies of the triplet of wavefunctions [LLL, depopulation level 1 (DP1), and 2 (DP2)] towards a collective energy level, which is below the LLL eigenenergy of the extended states. In the second bias interval > 51 mV/period, the peak gain value for the extended states collapses, while the optical frequency continues to increase successively. The wavefunctions depicted in Fig. 2.7 are obtained for an applied bias of 50 mV/period, which is close to the intersection of the two intervals. The energy position of the two

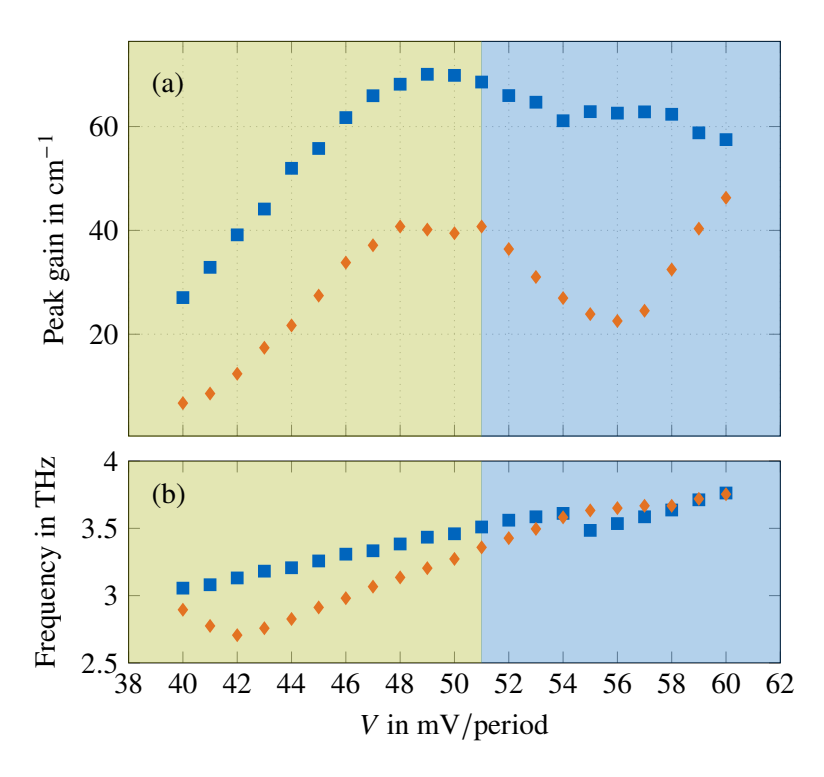


Figure 8.1 Monte Carlo simulation results of the THz QCL gain medium using extended (orange diamonds) and localized states (blue squares). Simulated unsaturated peak gain values (a) and center frequencies (b) are shown as a function of the applied bias *V*. The bias window is divided into two operating regimes, which are highlighted by shades of green and blue. The specific characteristics of the different configurations within the two regimes are explained in the text. Reprinted from J. Popp *et al.*, "Multi-domain modeling of free-running harmonic frequency comb formation in terahertz quantum cascade lasers" [178] (CC BY 4.0).

wavefunctions INJ and LLL at the injection barrier becomes crucial within the second interval [green rectangle in Fig. 2.7(a)]. By increasing the bias, the anticrossing energy gap is gradually reduced until the crossing point of eigenenergies is reached. This crossing process for the extended states is accompanied by a wavefunction extension for the INJ and ULL levels across the injection barrier. The increasing impurity dephasing rate due to the ionized donors in the injection well results in a broadened gain curve with a reduced peak value. In contrast, we have a strong spatial localization of these wavefunctions in the localized states configuration as illustrated in Fig. 2.7(c) (blue rectangle), leaving the gain characteristics unaffected by artificial broadening mechanisms. At 55 mV/period, we identify a small frequency drop for the localized states configuration, as the energy gap between the lower laser level LLL and the depopulation level DP1 exceeds 5 meV and the EZ-transformation for this subset of wavefunctions is no longer conducted. The wavefunctions of the LLL have a similar shape in both configurations. Besides, the peak gain value in the extended states configuration gradually grows for increasing bias values, as the two wavefunctions INJ and ULL separate again in energy. The presented carrier-transport results are publicly available and can be found in the *monacoQC* GitHub repository [254].

From the stationary carrier transport simulation results, we can extract the quantum-mechanical description of the QCL active gain medium and use it as input for the dynamical Maxwell-DM solver. To specify the influence of the tunneling transition INJ \rightarrow ULL on the spectral gain profile, we perform a dynamical gain analysis within the Maxwell-DM framework. As incoherent tunneling is absent in the extended state basis, but this is the major injection mechanism to the ULL in the diagonal transition design, we do not consider this configuration in the following dynamical simulations. For the modeling of the gain characteristics within the *mbsolve* framework, we seed a weak Gaussian pulse on the left facet and record the electric field at the middle of the 4 mm waveguide to measure the light amplification within the active gain medium [55], [360]. A linear field loss term $\alpha_0 = 6.5 \, \text{cm}^{-1}$ extracted from COMSOL simulations for a copper-copper (Cu-Cu) double-metal waveguide [73] is included in the simulation setup and has to be taken into account for the interpretation of the dynamical simulation results. The obtained unsaturated gain spectrum is depicted in Fig. 8.2 for the localized

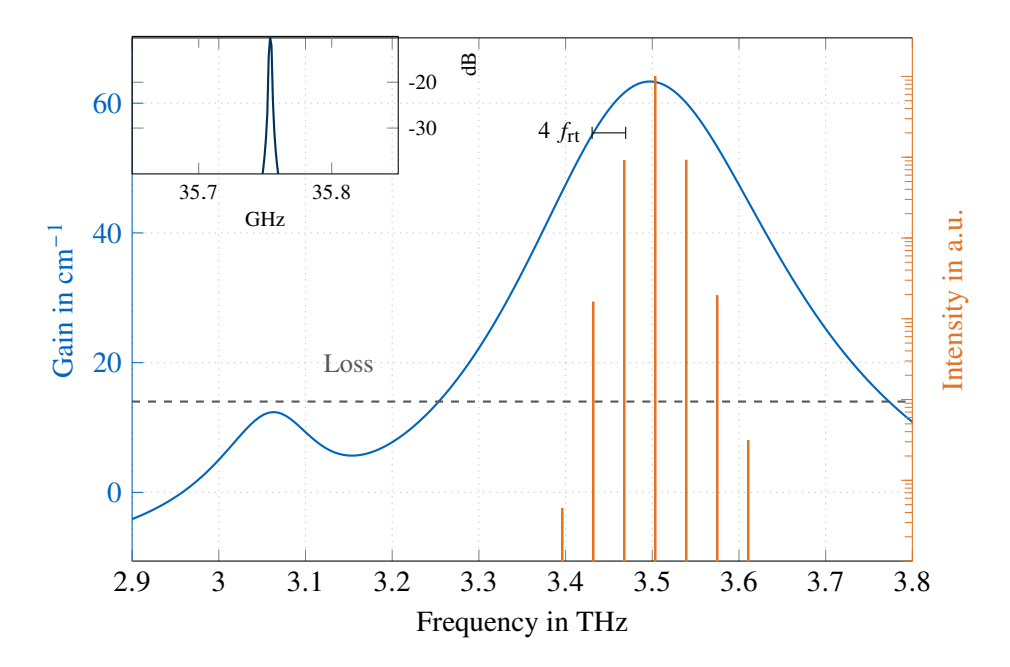


Figure 8.2 Spectrum of the Maxwell-DM simulation setup at a bias of $V = 50 \,\text{mV/period}$. The individual comb lines follow well the unsaturated gain curve, proving the validity of the self-consistent multi-domain simulation approach. Inset: Zoom on the radiofrequency beatnote with a numerical frequency resolution of 1 MHz. Reprinted from J. Popp *et al.*, "Multi-domain modeling of free-running harmonic frequency comb formation in terahertz quantum cascade lasers" [178] (CC BY 4.0).

states configuration. We obtain a strong gain lobe for the optical transition accompanied by a weak side gain lobe at the lower frequency, which results from the incorporation of the tunneling transition INJ \rightarrow ULL in the system Hamiltonian.

In recent years, the linewidth enhancement factor has become an important parameter for the description of QCL dynamics [51], [70]. It gives a measure for the coupling between amplitude and phase fluctuations in semiconductor lasers with fast gain dynamics and was initially introduced in the linewidth theory of semiconductor lasers, going beyond the Schalow-Townes limit [390]. Microscopic models of varying complexity, e.g., based on EMC [391] and NEGF [392] simulation approaches, were used to calculate the LEF factor in QCLs. In our full-wave Maxwell-DM equations, the LEF factor is introduced by the gain asymmetry resulting from the tunnel coupling between the INJ and ULL states, while assuming that other contributions, e.g., due to nonparabolicity, play a secondary role in this THz QCL. To extract the LEF, we carry out pump-probe simulations with a Gaussian pulse as seed, where we iteratively increase the pulse power until the gain clamping condition is reached. The LEF, also known as α -factor, can be computed at the center frequency ω_c using

$$\alpha = \frac{\partial_I \Re \{\chi(\omega_c)\}}{\partial_I \Im \{\chi(\omega_c)\}}.$$
(8.1)

Here, $\chi(\omega)$ is the complex susceptibility of the QCL gain medium. By slightly changing the pulse power in the dynamical simulations, we can calculate a LEF in the QCL design. An α -factor of ~ -0.1 is obtained for a bias of 50 mV period⁻¹. This is in good agreement with experimental and theoretical findings [52], [176], [392]–[395].

Furthermore, we conduct long-term simulations with an end time of $t_{\rm e}=1\,000\,{\rm ns}$ to characterize the particular mode-locking behavior. We obtain harmonic comb emission with a mode spacing of $4\times f_{\rm rt}$, located around the center of the gain maximum, determined by the pump-probe simulations. The intensity spectrum is depicted in Fig. 8.2, illustrating HFC emission with seven clear and narrow comb lines. The appearance of the associated harmonic beatnote, and the absence of the fundamental beatnote and its intermediate harmonic beatnotes, prove the purity of the harmonic state. A linewidth substantially below the numerical frequency resolution of 1 MHz is detected in the inset at 35.7 GHz of Fig. 8.2.

8.1.2 Analysis of Harmonic Mode-Locking Regimes in THz QCL Waveguides

In this section, we proceed with dynamical simulations using the QCL system based on the localized states configuration. From the simulation results in Fig. 8.2, we find that the contribution of the gain lobe caused by injection tunneling to the HFC mode proliferation is negligible. This is reflected in the small magnitude of the α -factor, as discussed above. Furthermore, all HFC modes lie within the gain lobe arising from the optical transition between ULL and LLL. Therefore, we omit the Rabi energies corresponding to injection tunneling in the quantum-mechanical description and include additional scattering rates for the carrier injection. In the following, we present a HFC analysis of different bias values and waveguide geometries. Furthermore, we analyze the temporal evolution of the HFC modes.

Applied Bias

Initially, we set the facet reflectance to 0.5, which arises from the high impedance mismatch in double-metal waveguides [55], [73], [396]. Here, the facet reflectance can vary between R = 0.5 - 0.9 depending on the waveguide dimensions relative to the wavelength [6], [396]. The chosen reflectance value is thus at the lower limit. Various strategies for reducing the waveguide loss and attenuating the lasing of higher-order transverse modes in THz QCL setups are discussed in the literature [118]. Harmonic comb emission in THz QCLs was recently demonstrated by the use of a low loss Cu-Cu waveguide [73]. In contrast to gold-gold waveguides, where the HFC gradually builds up from a single mode, the HFC in Cu-Cu waveguides emerges spontaneously and alternates over the operating bias range with fundamental comb and high-noise states. The lower waveguide loss in Cu-Cu waveguides leads to a wider dynamic range and increased intracavity fields. The latter becomes important for the FWM processes, which are proportional to the cube of the electric field intensity. Harmonic comb states at bias points far above the laser threshold are detected. We conduct simulations for different bias values within the operation regime presented in Section 8.1.1 and obtain HFC emission spectra of varying harmonic orders. The distinct coherent comb regimes for three representative bias points are illustrated in Fig. 8.3. At smaller bias values of around 48 mV/period we obtain a dense/fundamental comb [Fig. 8.3(a) top]. A clear beatnote at 9.05 GHz is detected. The radiofrequency spectrum is shown in Fig 8.3(b) top, also containing higher beatnotes arising from the beating of wider-spaced modes. A regular field pattern consisting of a periodically repeating waveform at each roundtrip is retrieved, where a snippet of two roundtrips is depicted in Fig. 8.3(c) top. In recent years, the spectral and time domain properties of free-running THz QCLs have been extensively investigated both theoretically [50], [52], [55], [119], [120] and experimentally [110], [111], [114], [116], [118]. Self-starting OFC emission in THz QCLs is characterized by a simultaneous frequencyand amplitude-modulated signal. In the upper panel of Fig. 8.3(c), parts of the electric field profile exhibit a flat behavior, which can be explained by the help of the time-varying instantaneous frequency profile, also illustrated in Fig. 8.3(c). In the first time interval of ~ 20 ps, the electric field is governed by a single frequency mode, which acts as the dominant one in the intensity spectrum in Fig. 8.3(a). By applying a higher bias of 50 mV/period a harmonic comb with a mode spacing of $4 \times f_{rt} \approx 36.12$ GHz is obtained [see Fig. 8.3(a) middle], similar to the HFC results in Section 8.1.1. The associated RF spectrum is presented in Fig. 8.3(b) middle. In the time domain, a periodic waveform with four repetitions per roundtrip is visible [Fig. 8.3(c) middle]. As expected, the corresponding instantaneous frequency features the same periodicity as the amplitude. On closer inspection, it is clearly visible that only the strongest modes within a $\sim 10\,\mathrm{dB}$ power range of the optical spectrum contribute significantly to the temporal behavior of the instantaneous frequency. The quasilinear chirp is in good agreement with recently published experimental results for THz QCL OFCs [116], [118]. By further increasing the bias towards regimes of decreasing unsaturated gain values, the separation of the locked modes reduces again [see Fig. 8.3(a) bottom]. At a bias value of 54 mV/period a beatnote at the second harmonic roundtrip frequency of 17.83 GHz is detected [see Fig. 8.3(b) bottom]. The harmonic time signal repeats twice per roundtrip and is together with the instantaneous frequency shown in Fig 8.3(c) bottom. Here, the linear chirp trend is even more pronounced as for the HFC of the fourth order. By increasing the bias further, we obtain a noisier state, which however reveals tendencies towards higher-order harmonics. The system is then apparently not stable enough to evolve into a clear HFC state.

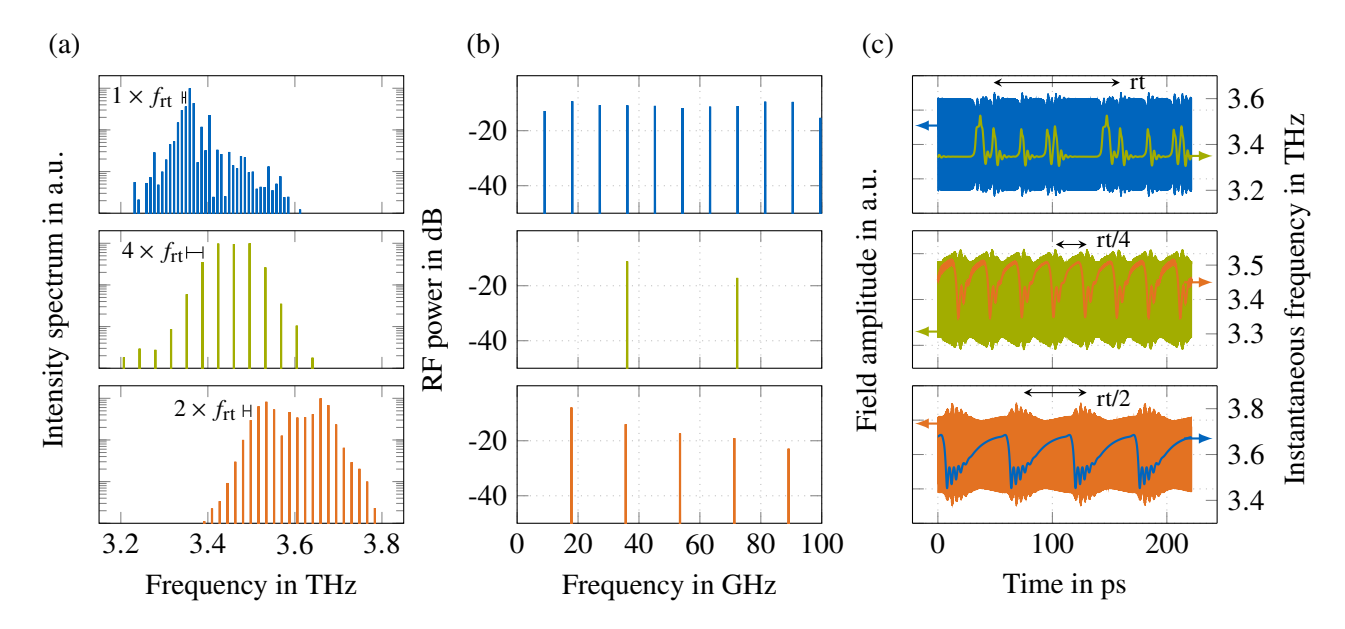


Figure 8.3 Comparison of three coherent regimes in a 4 mm long THz QCL device with a metal-metal waveguide at 80 K [73]. Results of a fundamental frequency comb (top panel, 48 mV/period), harmonic combs of $4 \times f_{rt}$ (middle panel, 50 mV/period) and with a mode spacing of $2 \times f_{rt}$ (bottom panel, 54 mV/period) are presented. (a) Intensity spectra of the optical radiation for the three regimes exhibiting clear mode spacings. (b) RF spectra with beatnotes at the fundamental (9.05 GHz), fourth harmonic (36.12 GHz), and second harmonic (17.83 GHz) roundtrip frequency f_{rt} , respectively. (c) Time-resolved electric field amplitudes and calculated instantaneous frequency from the Hilbert transform of the simulated electric field. Arrows indicate the individual waveform period for the three regimes. Reprinted from J. Popp *et al.*, "Multidomain modeling of free-running harmonic frequency comb formation in terahertz quantum cascade lasers" [178] (CC BY 4.0).

The obtained results are in good agreement with experimental findings [73], [170], where OFC states of varying order are retrieved and the transition from a dense state to a harmonic comb state and back for bias sweeping in a given interval is documented. Furthermore, we can reproduce the bias-dependent alternation between different comb states, as it is documented for Cu-Cu waveguides [73]. Obviously, a change in bias results in a change of center frequency and gain shape, and also the dynamical properties of the quantum system, e.g., the level lifetimes and dephasing rates, vary with the bias. It is worthwhile mentioning that in our simulations only one optical transition is considered. This implies that self-starting harmonic mode-locking can also emerge without the assistance of an asymmetric gain profile, which has been interpreted in earlier theoretical approaches to be essential [73].

Waveguide Geometries

In the experimental studies, the THz HFC QCL setup was characterized for different waveguide configurations with variations in the cavity length and width [73]. In order to emulate the changed impedance mismatch for different waveguide widths in our simulations, we vary the facet reflectance R for the THz HFC QCL setup at an applied bias of 50 mV/period. In addition to the results of Fig. 8.3, we present simulation results for facet reflectances of 0.32 and 0.8, which represent a single-plasmon and a second double-metal waveguide with different geometries, respectively. For the reflectance of 0.32, a HFC emission spectrum with a mode repetition rate of $3 \times f_{rt}$ is obtained [see Fig. 8.4(a)]. Interestingly, two twin lobes around the center frequency evolve. A similar shape of the optical spectrum can be derived from experiments in which a HFC state with a mode spacing of $5 \times f_{rt}$ is obtained at a drive current of 800 mA [73]. In Fig. 8.4(b), the emission spectrum for a reflectance of 0.8 is presented, revealing a HFC state with eighth harmonic order. The changed intracavity dynamics appear to have an emphasized effect on the harmonic mode ordering. For increased reflectance values, we obtain higher intracavity fields, affecting both the FWM processes and the spatial hole burning, i.e., the arising spatial gain modulation in a linear cavity with standing waves. For a noisy operating regime with tendencies towards

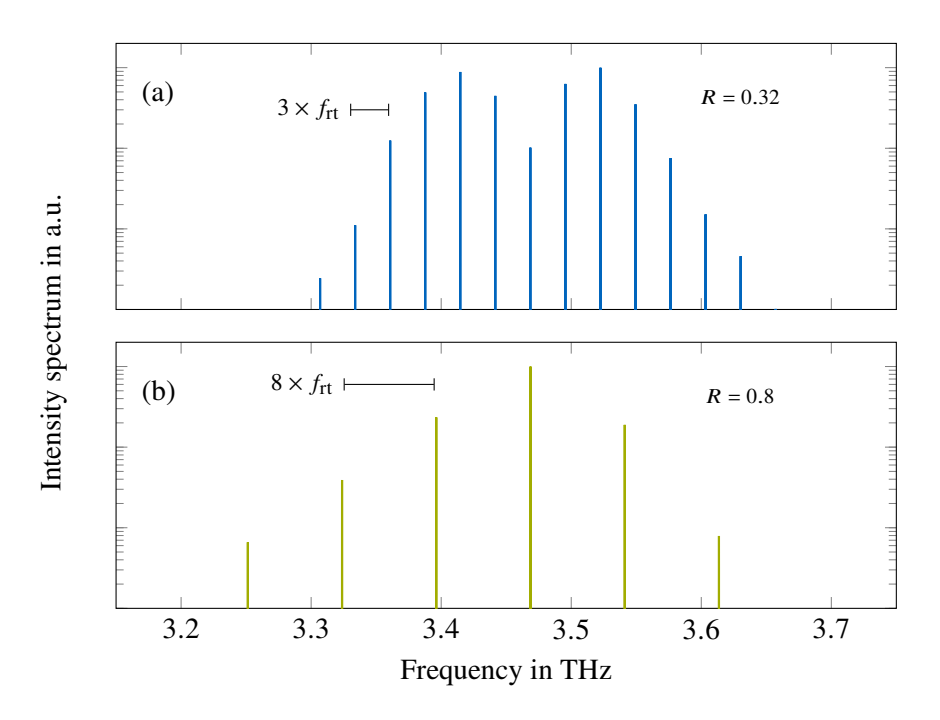


Figure 8.4 Intensity spectra of two harmonic states in a THz QCL at an applied bias of 50 mV/period and a temperature of 80 K. Simulation results for a facet reflectance of 0.32 (a) and 0.8 (b) are presented. Reprinted from J. Popp *et al.*, "Multi-domain modeling of free-running harmonic frequency comb formation in terahertz quantum cascade lasers" [178] (CC BY 4.0).

higher-order harmonics, an increase of the field strength within the cavity could result in a stabilization to a coherent state. We therefore execute a simulation of the THz QCL at a bias voltage of 55 mV per period and facet reflectance of 0.8. A stable HFC with a mode spacing of $12 \times f_{rt}$ is retrieved. It is obvious that the free-running THz QCL system is very sensitive to the different environmental parameters, highly affecting the dynamic behavior of the quantum system and thus the optical output.

Spectral Time Evolution

To gain an intuitive understanding of the spectral time evolution of the harmonic mode-locking in the THz HFC QCL setup, we investigate the OFC dynamics in the first 50 ns of the Maxwell-DM simulations. Here, we present simulation results for the three QCL configurations with facet reflectances of 0.32, 0.5 and 0.8 (see Fig. 8.5). The optical field within the THz QCL cavity is triggered by spontaneous emission events and starts from dense multimode lasing. From that, it evolves into the HFC state. The temporal characteristics of the three configurations are similar, whereby small deviations are evident. In Fig. 8.5(a), the HFC formation for the QCL setup with a reflectance of 0.32 is illustrated. Here, a strong center mode only changes weakly, while the energy of the emerging harmonic sidemodes increases gradually. The transition from the dense multimode state to a broad and clear HFC state with a mode repetition rate of $3 \times f_{\rm rt}$ is clearly recognizable. In the QCL configuration with a facet reflectance of 0.5, we observe a more inert behavior during the HFC generation [see Fig. 8.5(b)]. The sub-comb lines with a mode spacing of $1 \times f_{rt}$ from the strong harmonic pump modes only slowly fade out over time. This operation regime corresponds to the middle panel of Fig. 8.3(a), where we identify three strong central modes with similar intensity. In contrast, the two configurations with R = 0.32 and R = 0.8 (Figs. 8.4, and 8.5(a), (c), respectively), do not show similarly strong modes at the center frequency. Either the center mode is rather weak, with two stronger side lobes or the center mode is strong, with a strong decay of intensity in the side modes.

The QCL gain medium features a large third-order nonlinearity $\chi^{(3)}$ [12], [15], which leads in combination with SHB to a broadband FWM process and strong mode proliferation. In the case of harmonic mode-locking, the interaction of strong harmonic pump modes reduces the gain in their close spectral environment and thus acts as parametric suppression of adjacent sidemodes [81]. In addition, a parametric enhancement of widely

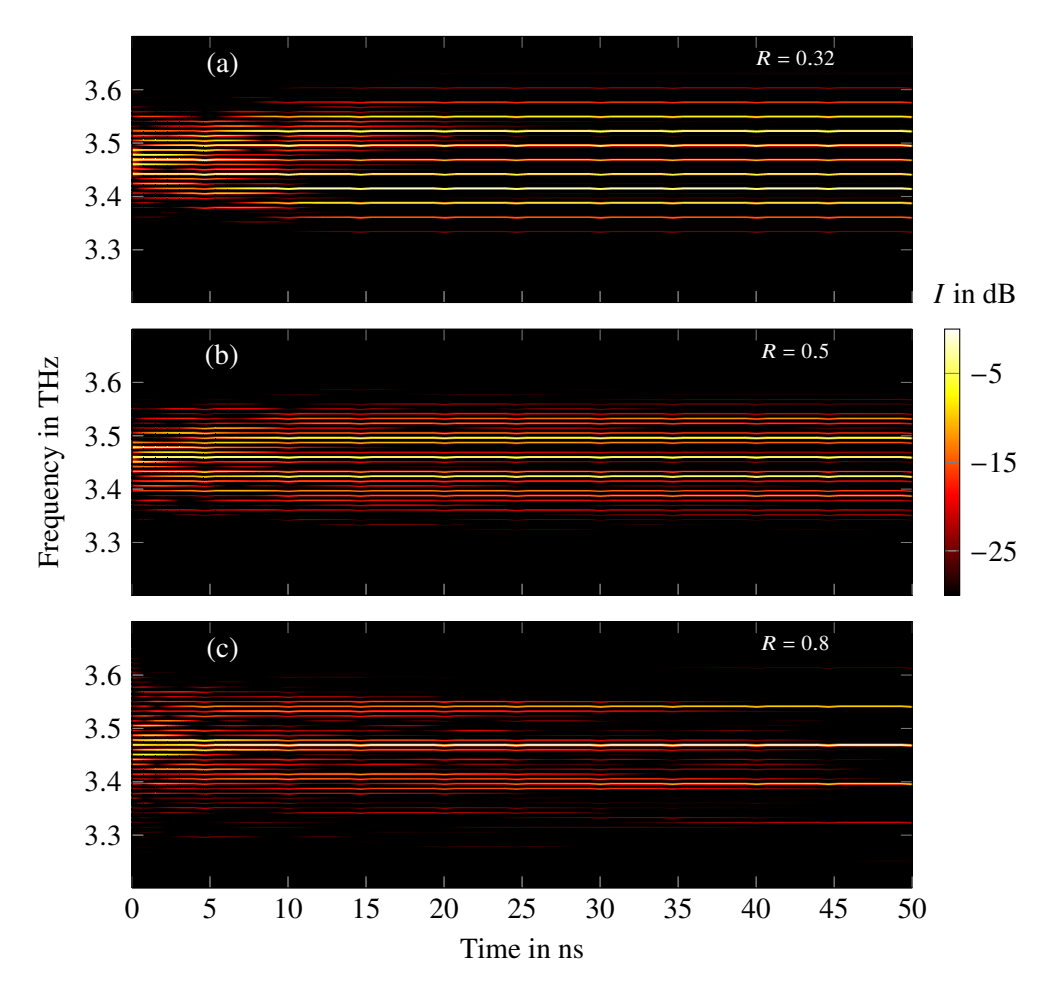


Figure 8.5 Time evolution of the spectral intensity *I* for self-starting harmonic mode-locking in three THz HFC QCL waveguide configurations at an applied bias of 50 mV/period and a temperature of 80 K. Simulation results for a facet reflectance of 0.32 (a), 0.5 (b) and 0.8 (c) are presented. Reprinted from J. Popp *et al.*, "Multi-domain modeling of free-running harmonic frequency comb formation in terahertz quantum cascade lasers" [178] (CC BY 4.0).

detuned modes is present and can clearly be observed in Fig. 8.5(c), showing the spectral time evolution of the HFC with eighth harmonic order for the QCL setup with a facet reflectance of 0.8. During the temporal evolution of the HFC, the adjacent sidemodes still get populated by degenerate FWM processes [55]. As long as the parametric suppression is too weak, the sidemodes can survive and no clear harmonic state evolves. In the case of the HFC state with the three dominant modes being equally strong and neighboring [see Fig. 8.3 second row and Fig. 8.5(b)], the parametric suppression competes with the seeding of the sidemodes, which results in a more inert behavior. A supplementary movie in [178] shows the evolution of the twelfth-order HFC state at a bias of 55 mV/period and for a reflectance value of 0.8. Here the above-mentioned dynamics in the initial phase of HFC evolution can be clearly seen.

8.1.3 Noise Characteristics in THz QCL Harmonic Frequency Comb Emission

Concerning the experimental investigation of intensity correlations in QCLs [83], we aim to characterize the noise properties of the self-starting THz QCL HFC setup. The charge carrier transport in the active gain medium at a bias of 50 kV/period is analyzed using our in-house Monaco framework. For an appropriate description of the physical properties, we consider five wavefunctions in the active quantum well heterostructure. Furthermore, one incoherent tunneling transition from the injector state into the upper laser level and one optical transition are specified for the quantum-mechanical description of the QCL system in the dynamical simulation. The Python script **forrer_2021_50mVperperiod.py** with the simulation setup to start the *mbsolve* simulation is given in Listing A.1 of Appendix A.1.1 and is furthermore included in the GitHub repository [58]. Here, all

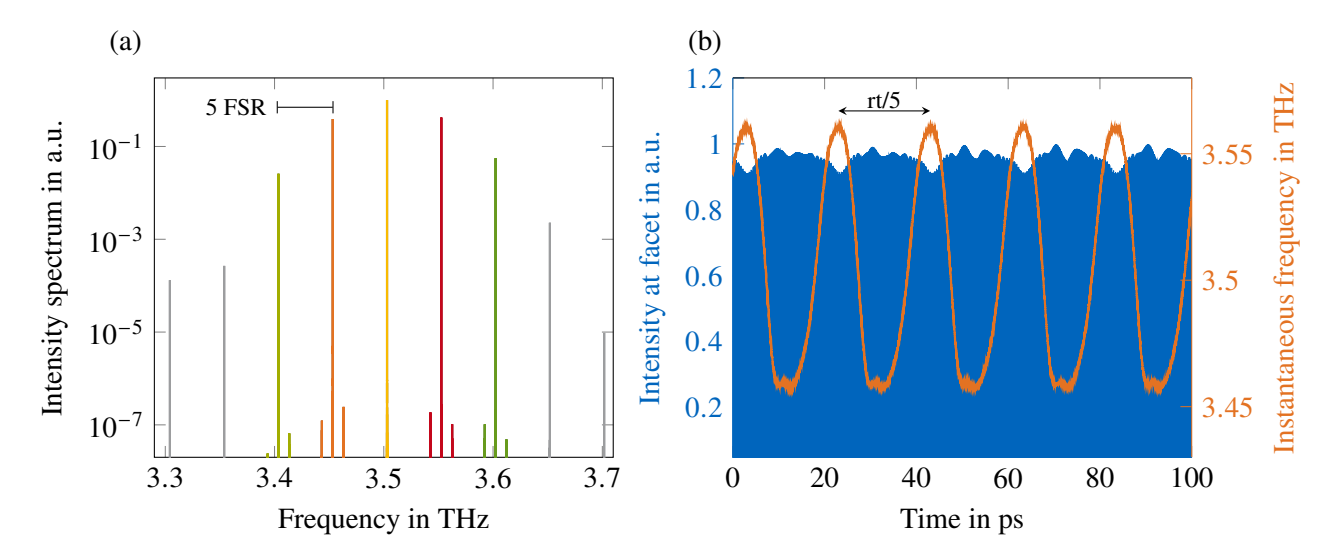


Figure 8.6 Maxwell-density matrix Langevin simulation results of HFC emission with a mode spacing of 5 FSR in a 4 mm long THz QCL device with a metal-metal waveguide at 80 K and for $V = 50 \,\mathrm{mV/period}$. (a) Intensity spectra of the optical radiation at the facet. (b) Simulated instantaneous intensity at the facet and calculated instantaneous frequency from the Hilbert transform of the simulated electric field over a single roundtrip time (rt). Reprinted from J. Popp *et al.*, "Modeling of fluctuations in dynamical optoelectronic device simulations within a Maxwell-density matrix Langevin approach" [59] (CC BY 4.0).

input parameters for the full description of the quantum system are extracted from self-consistent DM-EMC simulations.

In the following, we present simulation results for a 4 mm long double-metal THz QCL with a free spectral range (FSR) of 9.94 GHz. The intensity spectrum of the THz HFC at 3.5 THz with a mode spacing of 5 FSR is illustrated in Fig. 8.6(a). The THz QCL emits a broadband HFC with a cavity repetition rate of 49.7 GHz. We here obtain a slightly different emission behavior as compared to the simulation results without noise presented in Section 8.1.1. The reflectivity here is increased to R = 0.64, which results in an increase of the mode spacing by 1 FSR. In Fig. 8.6(b), the temporal evolution of the intensity at the facet and the calculated instantaneous frequency are depicted. We can identify a regular field pattern, which shows a periodic repetition with five times the roundtrip time. Here, only the three strongest modes are involved in the temporal evolution of the instantaneous frequency, as their intensities are of similar magnitude and contribute most to the overall comb emission power.

To specify the degree of coherence of the obtained HFC and for comparison with the experimental findings, we investigate the RF spectrum using an observation time window of 2 μ s. The obtained simulation results are shown in Fig. 8.7(a), and the clear appearance of the harmonic beatnote proves the purity of the harmonic state. The linewidth is substantially below the numerical frequency resolution of 500 kHz, which is confirmed by the zoom on the extremely narrow harmonic beatnote in the inset of Fig. 8.7(a). In addition, we can identify sub-beatnotes, which arise due to the beating of the center mode with the sub-comb lines. These sub-comb lines are generated by FWM processes, where the strong harmonic sidemodes act as pump modes and generate weak sidebands with a frequency spacing of 1 FSR from the corresponding pump modes. As can be seen in Fig. 8.6(a), the intensities of the sub-modes are at least \sim 5 orders of magnitude smaller than those of the pump modes.

To further analyze the noise characteristics of the THz QCL HFC setup, we calculate the relative intensity noise (RIN) for the total output power and for the power of the five harmonic comb lines contributing most to the HFC emission. Here, the RIN spectrum can be calculated by

$$RIN_{i}(f) = \lim_{T \to \infty} \frac{1}{T} \frac{\left| \int_{0}^{T} [P_{i}(t) - \langle P_{i}(t) \rangle] e^{-i2\pi f t} dt \right|^{2}}{\langle P_{i}(t) \rangle^{2}}, \tag{8.2}$$

where P_i is either the power of a specific mode i or the total power P_{all} . By numerically filtering the electric field at the facet $E_{\text{facet}}(t)$ using a filter with a 3 dB bandwidth of 20 GHz, we can extract the temporal electric

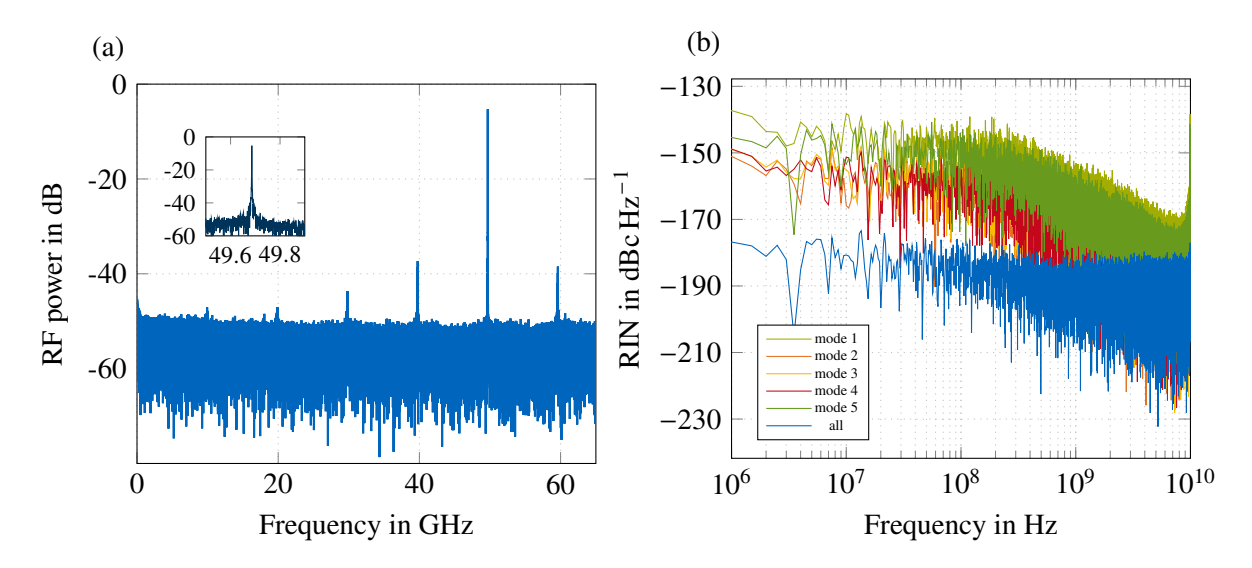


Figure 8.7 (a) Simulated RF spectrum of the THz QCL HFC setup with a clear beatnote signal at 49.7 GHz. Inset, zoom on the harmonic beatnote, indicating a narrow linewidth below the numerical frequency resolution (500 kHz). (b) Calculated RIN spectra associated with the total power $P_{\rm all}$ (blue) and the modal power P_i of each of the five harmonic modes contributing most to the HFC emission. The colors of the individual RIN spectra correspond to those of the individual comb lines in Fig. 8.6(a). Reprinted from J. Popp *et al.*, "Modeling of fluctuations in dynamical optoelectronic device simulations within a Maxwell-density matrix Langevin approach" [59] (CC BY 4.0).

field components $E_i(t)$ of the individual modes. The RIN results are depicted in Fig. 8.7(b) for the total power $P_{\rm all}$ and the power of the five central harmonic modes P_i with indices $i=1\ldots 5$. The total power RIN is around $-180\,{\rm dBc\,Hz^{-1}}$, while for the three central harmonic modes having a similar power a RIN around $-155\,{\rm dBc\,Hz^{-1}}$ is calculated. For the remaining two weaker modes 1 and 5 a higher RIN is obtained. This is in very good agreement with the experimental findings of a three-mode mid-IR HFC QCL setup [83]. For increasing power, the RIN of the sidemodes decreases to that of the central mode, while sidebands closer to threshold exhibit a noisier behavior. Furthermore, we identify an overlapping RIN for sidemodes featuring a comparable power level, which indicates a comparable noise level. A similar result could be retrieved from the mid-IR HFC RIN measurements [83].

8.1.4 Discussion

With our multi-domain simulation approach, we can replicate the experimental results for stable self-starting HFC generation of higher orders in THz QCLs. Furthermore, we provide a detailed analysis of the active gain medium and investigate the influence of the applied bias and waveguide geometries on the HFC formation. Harmonic states of different orders are retrieved for the different configurations and the experimentally documented behavior of alternating fundamental and harmonic comb states over the operating bias range is replicated in the simulations. To better categorize the results, we give a brief overview of existing simulation results of HFC emission in QCLs based on the MB equation system and compare them with our approach. Furthermore, we discuss ideas for the next steps to shed light on the physical origins of harmonic mode coupling in QCLs.

Numerical simulation results of QCL harmonic comb generation using a three-level Maxwell-density matrix model were presented in [75]. For the generation of HFCs of varying order, the simulation was seeded with an electric field consisting of a weak central mode and very weak sidemodes at higher orders of the intermodal spacing. Here, they could demonstrate, that the harmonic states are sustained after switching off the electric field seeding and can describe the typical QCL dynamics when interacting with a strong coherent laser field. The seeded HFC states were found to be only stable for a few thousand roundtrips, however, degrading to dense/fundamental states in the long run. More recently, simulation results of fundamental and harmonic comb generation in QCLs embedded in a Fabry-Perot cavity were published based on the ESMB equation approach [50], [52]. An extensive study on dense and harmonic regimes was provided and experimental

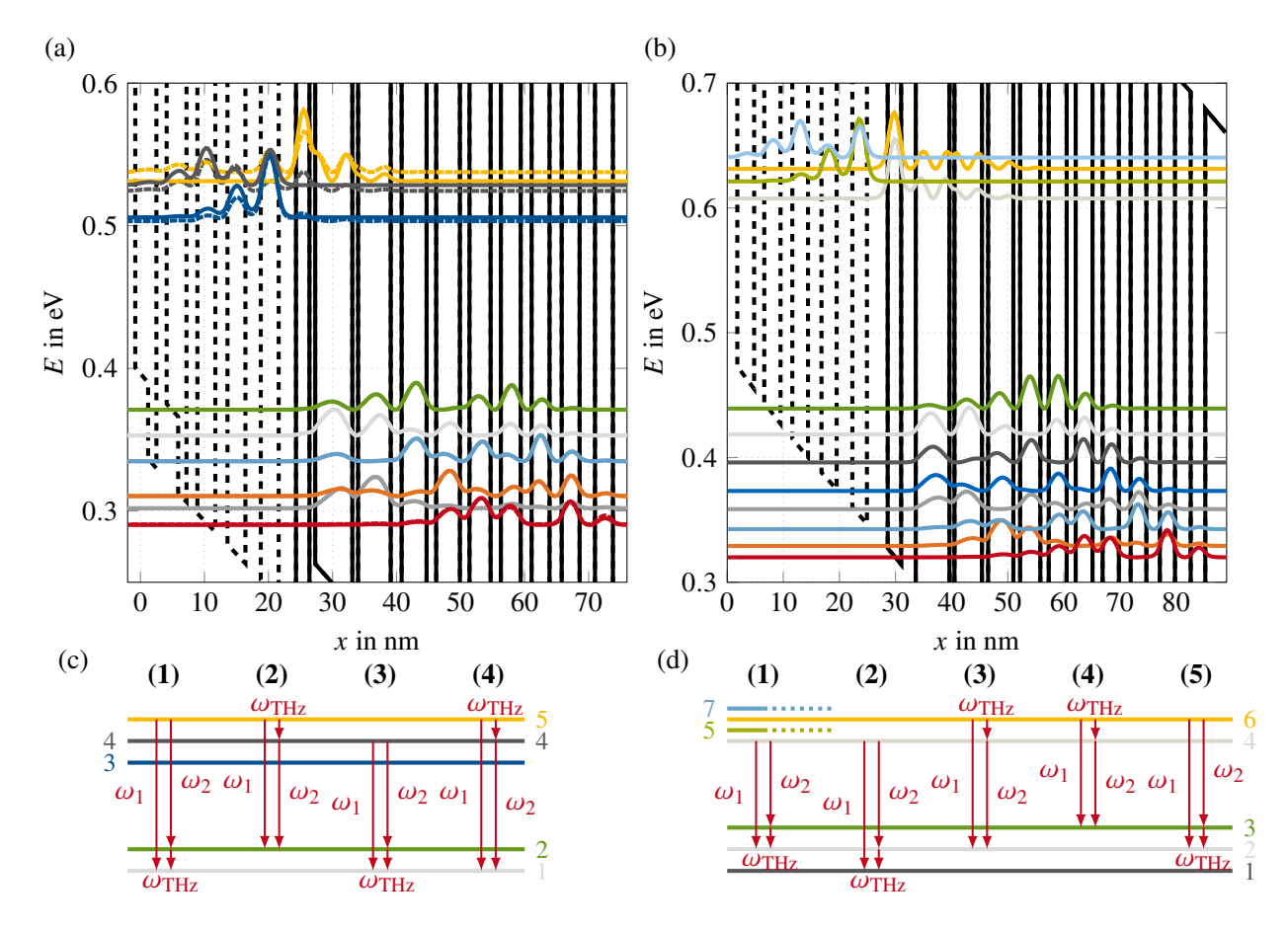
features such as the simultaneous amplitude and frequency modulation behavior could be reproduced. However, self-starting HFC operation could only be demonstrated in second-order using the ESMB equations.

The simulation approaches used in the aforementioned publications for the simulation of self-starting HFC generation in QCLs are based on the common rotating wave/slowly varying envelope approximation, generally used to reduce the numerical effort associated with the fast field oscillations [43], [47]. Optical interference effects such as SHB in Fabry-Perot resonators significantly influence the QCL dynamics and are taken into account by an inversion grating [47], [54], [67], [68], [70], [122], [159]. Further extensions towards third-order polarization grating were proposed and considered in studies of Risken-Nummedal-Graham-Haken instabilities in OCLs [69]. The ESMB equations additionally include a non-zero LEF to account for certain semiconductor specifics, such as asymmetric gain and dispersion profiles. Within our multi-domain simulation approach, we utilize the full-wave Maxwell-DM equations and thus intrinsically account for all required effects of selfstarting HFC formation, e.g., higher-order polarization and population gratings, nonlinearities and off-resonant dynamics. We have extended this approach by the inclusion of stochastic noise terms derived from the quantum Langevin equations to characterize the noise properties of the THz QCL HFC setup. The simulation results show good agreement with the experimental results. In fact, this realistic spontaneous emission noise is not amplified to macroscopic distortions but is intrinsically kept at low values. Therefore, the intermodal beatnote is still observed to be extremely narrow (below the numerical frequency resolution limit of ≈ 1 MHz), indicating a high purity of the observed comb states. Higher-order nonlinearities and grating terms were omitted in earlier HFC simulations employing the RWA, as their importance for HFC formation was considered negligible. Due to the complexity of our simulation approach, it is not possible to abstract the model. The higher-order grating terms and nonlinearities, which we will refer to as beyond-RWA effects, appear to have an essential influence on self-starting HFC formation in QCLs. To provide insights into the governing mechanisms of self-starting harmonic mode-locking, the crucial beyond-RWA effects have to be identified and characterized using simplified models. Possibly, the adiabatic elimination of specific terms may provide additional insights. This approach has already been used for the prediction of purely frequency-modulated combs in mid-IR QCLs [70] or recently for the description of passive single-pulse mode-locking in THz QCLs with distributed saturable absorbers [67].

Our numerical approach also shows great potential for the modeling of harmonic comb operation in mid-IR QCLs. The full-wave framework to model THz OFCs created by difference frequency generation in mid-IR QCLs is presented in the next section, showing good agreement with experimental data [90]. Numerically reproducing the entire optical spectrum spanning from the THz to mid-IR regime, is only possible by considering full-wave Maxwell-DM simulations. Broadband mid-IR HFC spectra with large intermodal spacing up to 26 times the free spectral range of the laser cavity were experimentally demonstrated [79], [171], pushing towards the intrinsic bandwidth limitations of MB models invoking the RWA. For such scenarios, our here-discussed approach might not only be applicable, but even necessary.

8.2 Intracavity Terahertz Comb Difference Frequency Generation by Mid-Infrared Quantum Cascade Lasers

In the following, we present simulation results for two different THz DFG-QCL setups. One setup consists of a single-phonon resonance depopulation (SPR-depopulation) structure [192], whereas the other setup is based on a dual-upper state active region [193]. The conduction band profile together with the probability densities of the wavefunctions for both QCL setups are illustrated in Fig. 8.8. For a complete characterization of the electrical and optical properties we divide this section into two parts: Firstly, we present stationary charge carrier transport simulations of the given structures based on the EMC method [29] and compare them with the corresponding experimental data [192], [193], [397]. Secondly, dynamic simulations of the light-matter interaction using the open-source Maxwell-density matrix simulation tool *mbsolve* are provided. Here, we can reproduce the experimentally obtained results and demonstrate THz frequency comb generation in DFG-based QCLs by self-consistent modeling [205], [206].



8.8 Investigated profiles probability densities conduction band and of the modeled THz DFG-OCL structures. Single-phonon resonance depopulation based (a) scheme on strain-balanced $In_{0.37}Al_{0.63}As/In_{0.65}Ga_{0.35}As/In_{0.53}Ga_{0.47}As$ material system latat a of temperature [192]. The layer sequence (in of 293 K nm) one period is **2.7**/2.1/**0.9**/3.2/2.6/**0.9**/3.0/2.1/**1.7**/2.4/1.5/**1.5**/2.0/1.3/**1.6**/1.8/1.3/**1.7**/2.8/**1.9**/2.8/**2.4**/2.8, well layers with $In_{0.53}Ga_{0.47}As$ are highlighted in italic, for the underlined layers a doping density of $1.7 \times 10^{17} \, \text{cm}^{-3}$ (n-type) is assigned, and the applied bias is 50 kV cm⁻¹. Here, tight-binding (solid lines) and extended states (dashed (b) Bandstructure of the dual-upper state active region based on a strain-compensated lines) are illustrated. In_{0.6}Ga_{0.4}As/In_{0.44}Al_{0.56}As material system at a lattice temperature of 78 K [193]. The layer sequence (in nm) of one period is 3.7/2.4/2.6/6.0/0.9/4.9/1.1/4.5/1.2/3.6/1.5/3.2/1.6/3.0/1.8/2.9/2.1/2.8/2.4/2.7/2.8/2.6, barriers are in boldface, and n-doped layers (Si, 1×10^{17} cm⁻³) are underlined. The applied bias is here 56 kV cm⁻¹. (c) Schematic description of the DFG processes in the single-phonon resonance depopulation structure (Fig. 8.8(a)). (d) Schematic description of the DFG processes in the dual-upper state active region (Fig. 8.8(b)). Reprinted from J. Popp et al., "Self-consistent simulations of intracavity terahertz comb difference frequency generation by mid-infrared quantum cascade lasers" [90] (CC BY 4.0).

8.2.1 Stationary Carrier Transport Simulations

To classify the efficiency of the nonlinear mixing process and the potential for broadband THz comb emission, we investigate the gain spectrum in the mid-IR regions and characterize the strength of the nonlinearity in the active gain region. Here, the optical gain is calculated with Eq. (3.28) and the second-order nonlinear susceptibility $\chi^{(2)}$ with Eq. (3.30).

Single-Phonon Resonance Depopulation Structure

The modeled THz DFG-QCL design consists of a SPR-depopulation structure emitting at $\lambda \sim 7.8 \,\mu m$ and is based on strain-balanced InGaAs/InAlAs; experimental data can be found in [192], [205]. At the operation temperature of 293 K, a CBO of 740 meV was specified in literature [192], and is used in this work for the calculation of the wavefunctions. Here, we investigate the THz DFG-QCL device for two potential approaches, as is illustrated in Fig. 8.8(a). On the one hand, we use a tight-binding potential $V_{\rm tb}$ for the calculation of nine wavefunctions per period giving rise to one upper laser level and three lower laser levels. The injection of charge carriers into the upper laser level is modeled here by resonant tunneling from two injector states of the adjacent period. The calculated coupling strengths of the two narrowest anticrossed pairs of tunneling states are $2\hbar\Omega_{45} = 14 \text{ meV}$ and $2\hbar\Omega_{35} = 17.8 \text{ meV}$, which is in good agreement with the coupling strength $2\hbar\Omega = 16.5$ meV determined in the experimental paper [192]. Notably, the tunneling transitions fully contribute to the DFG process in the dynamic Maxwell-density matrix simulations. However, no predictions about their contributions to the second-order nonlinear susceptibility can be made within the tight-binding approach, as the dipole moments d_{45} , d_{35} are insignificantly small due to the strong localization of the states to the left and right of the injection barrier. It is important to take into account also the extended state approach for the characterization of the nonlinear susceptibility since it was proposed in the experimental paper [192] that the injector levels can have a substantial impact on the DFG process. With the actual potential V we can determine the extended states. One of the injector states in the tight-binding approach now acts as an additional upper laser level. The lower laser levels as well as the depopulation miniband for the actual potential V do not change significantly in position and probability densities in comparison to the corresponding tight-binding levels. For the carrier transport simulations of the SPR-depopulation QCL design an average interface roughness height $\Delta = 0.06$ nm is selected to obtain realistic simulation results [102]. With the interface parameter product $\Delta \Lambda \approx 1 \text{ nm}^2$, the experimental estimate for the InGaAs/InAlAs material system [398], [399], a correlation length $\Lambda = 16.67$ nm is calculated.

In Fig. 8.9(a), the normalized gain curve from the EMC simulation for tight-binding as well as extended states and the experimentally measured electroluminescence (EL) curve from [192] are illustrated. We obtain simulated linewidth values of $\sim 412\,\mathrm{cm^{-1}}$ and $\sim 442\,\mathrm{cm^{-1}}$ for tight-binding states and extended states, respectively. The experimentally measured linewidth of $\sim 380\,\mathrm{cm^{-1}}$ is slightly narrower, however, the EL measurement was performed at a higher bias compared to the simulation. The bias change gives rise to varying lasing channels, thus the dominant optical transition in the simulation is $5\to 1$, while in the EL setup, $4\to 2$ is the dominant optical transition. The applied QCL bias in this work is adjusted for efficient THz DFG-QCL comb generation and is derived from the P-I-V characterization given in [205]. In addition, we see a small blue shift of the simulated curves with respect to the measured spectrum, although calculated wavefunctions and eigenstates are in good agreement with the ones shown in [192] at the given bias of 65 kV cm⁻¹. Minor inaccuracies in the calculation of the simulation parameters, e.g., CBO, could arise with the natural limitation of our theoretical model. On the other hand, small deviations could also stem from process uncertainties during the fabrication, i.e., layer thickness variations, which we cannot account for in the simulation [400].

In Fig. 8.9(b), the level broadening γ_i and the relative level occupation ρ_{ii} in the relevant period are shown as a function of the subband energy. We obtain a similar thermalized behavior of relative level occupations in the lower lying levels for both approaches. Level 3 acts as an efficient injector to upper laser level 5 in the tight-binding approach, whereas in the extended state approach, it acts more like an electron trap. With the given average doping of the active region $\sim 2.1 \times 10^{22}$ m⁻³ [192] we obtain mean population inversion densities $\Delta N_{5,\text{ext}} \approx 1.9 \times 10^{21}$ m⁻³, $\Delta N_{5,\text{tb}} \approx 2.5 \times 10^{21}$ m⁻³, and $\Delta N_{4,\text{ext}} \approx 2.8 \times 10^{21}$ m⁻³ for extended and tight-binding states, respectively. The level broadenings of the lower laser levels are almost identical for extended

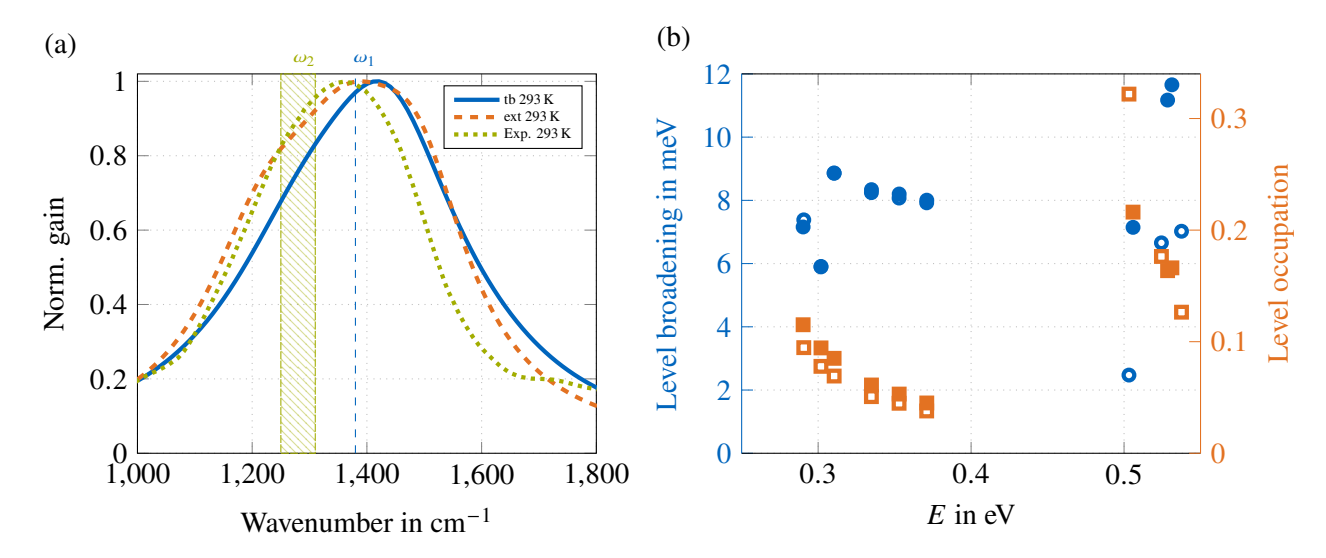


Figure 8.9 Simulation results of the SPR-depopulation design. (a) Normalized gain vs. wavenumber for simulated tight-binding (tb) (solid line) and extended (ext) states (dashed line), together with the measured EL curve (dotted line, from [192]). The spectral range of the FP comb at ω_2 and of the single DFB mode at ω_1 is indicated by the shaded area and dashed line, respectively. (b) Simulated level broadening γ_i (circles) and relative level occupation ρ_{ii} (squares) of the extended states (open marks) and tight-binding states (filled marks) for one QCL energy period as a function of the subband energy (see Fig. 8.8(a)). Reprinted from J. Popp *et al.*, "Self-consistent simulations of intracavity terahertz comb difference frequency generation by mid-infrared quantum cascade lasers" [90] (CC BY 4.0).

Table 8.1 Near-resonance DFG triplets of states and resulting second-order nonlinear susceptibility $\chi^{(2)}$ for the SPR-depopulation QCL active gain medium. All parameters are considered for extended states, except the triplet of state (1)', where the tight-binding solutions are presented. Listed are the resonance energy $\hbar\omega_{ij}$, pure dephasing energy $\gamma_{ij,p}$ (interface roughness contribution) in meV and transition dipole moments z_{ij} in nm for the mid-IR pump frequencies (ω_1 , ω_2) and the THz mode (ω_{THz}). Reprinted from J. Popp *et al.*, "Self-consistent simulations of intracavity terahertz comb difference frequency generation by mid-infrared quantum cascade lasers" [90] (CC BY 4.0).

	ω_1			ω_2			$\omega_{ ext{THz}}$		(2)
Triplet	$\hbar\omega_{ij}$	z_{ij}	$\gamma_{ij,p}$	$\hbar\omega_{ij}$	z_{ij}	$\gamma_{ij,\mathrm{p}}$	z_{ij}	$\gamma_{ij,\mathrm{p}}$	$\chi^{(2)}$ / nm V^{-1}
(1)	184.7	1.15	6.18(61%)	166.6	1.01	9.55(55%)	7.99	1.76(75 %)	-1.79 + i1.42
(1)'	178.3	-1.49	8.60(80%)	160.2	1.30	12.83(72%)	8.07	1.77(75%)	-4.99 + i3.38
(2)	166.6	1.01	9.55(55%)	153.5	5 -0.65	11.46(40%)	6.58	2.37(68 %)	-2.04 + i0.31
(3)	171.5	-0.75	8.28(42 %)				7.99	1.76(75%)	-1.55 + i1.25
(4)	184.7	1.15	7.57(50%)	171.5	-0.75	8.28(56%)	6.58	2.38(68 %)	-1.89 + i0.09

and tight-binding states, where we obtain the averaged values $\gamma_1 = 7.96 \,\mathrm{meV}$, $\gamma_2 = 8.14 \,\mathrm{meV}$. For the two upper laser levels in the tight-binding approach, the level broadenings $\gamma_4 = 11.17$ meV and $\gamma_5 = 11.66$ meV are extracted from the EMC simulations and are relatively high due to the tunneling contributions. In comparison, the corresponding level broadenings for the extended states are considerably smaller, with $\gamma_4 = 6.66 \,\mathrm{meV}$ and $\gamma_5 = 7.02 \,\mathrm{meV}$. In Fig. 8.8(c), the four triplets of states contributing most to the resonant second-order nonlinear susceptibility $\chi^{(2)}$ in the extended state configuration are illustrated. For the tight-binding approach, we investigate only a single triplet of states (1)', which corresponds to the extended states triplet (1) consisting of the states 5, 2 and 1. All additional parameters for the calculation of the second-order nonlinear susceptibility are summarized in Table 8.1. If we compare the pure dephasing energies for the two corresponding triplets (1) and (1), we identify shifts in the scattering contributions. The main mechanism accounting for the pure dephasing is interface roughness scattering, however, due to the extension of the upper laser levels for the actual potential V into the doping region, ionized impurity scattering plays a more important role in the extended state configuration. Taking this into account, we calculate the total dephasing energy for the mid-IR transitions of triplets (1) and (1)' and obtain $\Gamma_{52,ext.} = 17.02 \text{ meV}$, $\Gamma_{51,ext} = 13.72 \text{ meV}$, $\Gamma_{52,tb} = 22.66 \text{ meV}$, and $\Gamma_{51,tb} = 18.53$ meV. These values are in good agreement with values stated in literature [192], giving a transition linewidth of $\sim 15 \,\text{meV}$ to 20 meV. For the THz transition, total pure dephasing energies $\Gamma_{21,\text{ext}} = 9.76 \,\text{meV}$ and $\Gamma_{21,tb} = 9.88$ meV are calculated, respectively. As schematically indicated in Fig. 8.9(a), the mid-IR pump wavelengths (λ_1 , λ_2) are specified at the DFB mode $\lambda_{DFB} = 7.25 \,\mu m$ and at FP modes around $\lambda_{FP} \sim 7.81 \,\mu m$. The transition dipole moments and calculated susceptibilities $\chi^{(2)}$ for the five triplets are listed in Table 8.1. The four triplets in extended state configuration add up constructively, resulting in a total susceptibility value $|\chi^{(2)}| = 7.82 \,\mathrm{nm}\,\mathrm{V}^{-1}$. For the tight-binding triplet (1)' a total value $|\chi^{(2)}| = 6.03 \,\mathrm{nm}\,\mathrm{V}^{-1}$ is obtained. The values are somewhat smaller than the one given in [192] of $|\chi^{(2)}| = 20 \text{ nm V}^{-1}$. This is attributed to the fact that the given wavelengths λ_{DFB} and λ_{FP} could be inappropriate for the calculation of $|\chi^{(2)}|$ based on the simulation results, as we obtain a blue shift ($\sim 40 \, \mathrm{cm}^{-1}$) compared to the experimental data.

Dual-Upper State Active Region

The investigated QCL is based on a DAU active region with $\lambda \sim 6.8\,\mu\text{m}$ and consists of strain-compensated InGaAs/InAlAs layers; experimental data can be found in [82], [193], [397]. For the operation temperature of 78 K a CBO of 670 meV is calculated. As depicted in Fig. 8.8(b), the active gain medium constitutes 12 wavefunctions per period with two strongly anticrossed upper and multiple lower laser levels (miniband). Injection takes place via resonant tunneling from the electron states of the adjacent period. In the simulation, tunneling transitions from the lowest-lying injector level into the upper laser levels 4, 5 are found to be the strongest with coupling strengths of $2\hbar\Omega_{56} = 8.8\,\text{meV}$ and $2\hbar\Omega_{54} = 8.6\,\text{meV}$, respectively. Multiple lasing channels from the upper laser levels to the lower-lying miniband, featuring equal transition oscillator strengths, contribute to an extremely broad gain spectrum [397]. An improved device performance at room temperature compared to the BTC designs is obtained even without the need for heterogeneous cascades. In Fig. 8.10(a), the simulated and normalized gain curves for operating temperatures of 78 K and 300 K are depicted. Additionally, the measured EL spectrum from [397] for a mesa device in pulsed operation at a bias of 56.9 kV cm⁻¹ ($V = 13.7\,\text{V}$) and a temperature of 300 K is plotted. The simulated linewidth of $\sim 484\,\text{cm}^{-1}$ compares well with the experimentally measured linewidth of $\sim 490\,\text{cm}^{-1}$. The linewidth of DAU QCL designs is quite insensitive to bias variations due to similar spatial localization of the upper laser levels [397].

In Fig. 8.8(d), the five triplets of states contributing most to the resonant second-order nonlinear susceptibility $\chi^{(2)}$ are illustrated. All important microscopic quantities relevant for the determination of the optical nonlinearity can be extracted from the carrier transport simulations. In Fig. 8.10(b), the level broadening γ_i and the relative level occupation ρ_{ii} in the relevant period as a function of the subband energy are shown. For the relative occupations of the five levels contributing most to the optical gain and to the nonlinear mixing process, the simulation yields $\rho_{11} = 0.038$, $\rho_{22} = 0.036$, $\rho_{33} = 0.030$, $\rho_{44} = 0.202$, and $\rho_{66} = 0.094$. The mean population inversion density between upper laser levels 6, 4 and depleted miniband (3, 2, 1) is $\Delta N \approx 2.8 \times 10^{21} \,\mathrm{m}^{-3}$ and $\Delta N \approx 1 \times 10^{21} \,\mathrm{m}^{-3}$, respectively. Furthermore, level broadenings $\gamma_1 = 5.69 \,\mathrm{meV}$, $\gamma_2 = 4.58 \,\mathrm{meV}$, $\gamma_3 = 4.22 \,\mathrm{meV}$, and $\gamma_4 = 5.61 \,\mathrm{meV}$ are obtained. For the upper laser level 6, we obtain a relatively high level broadening $\gamma_6 = 11.65 \,\mathrm{meV}$ compared to the other levels, which is mainly due to increased interface roughness

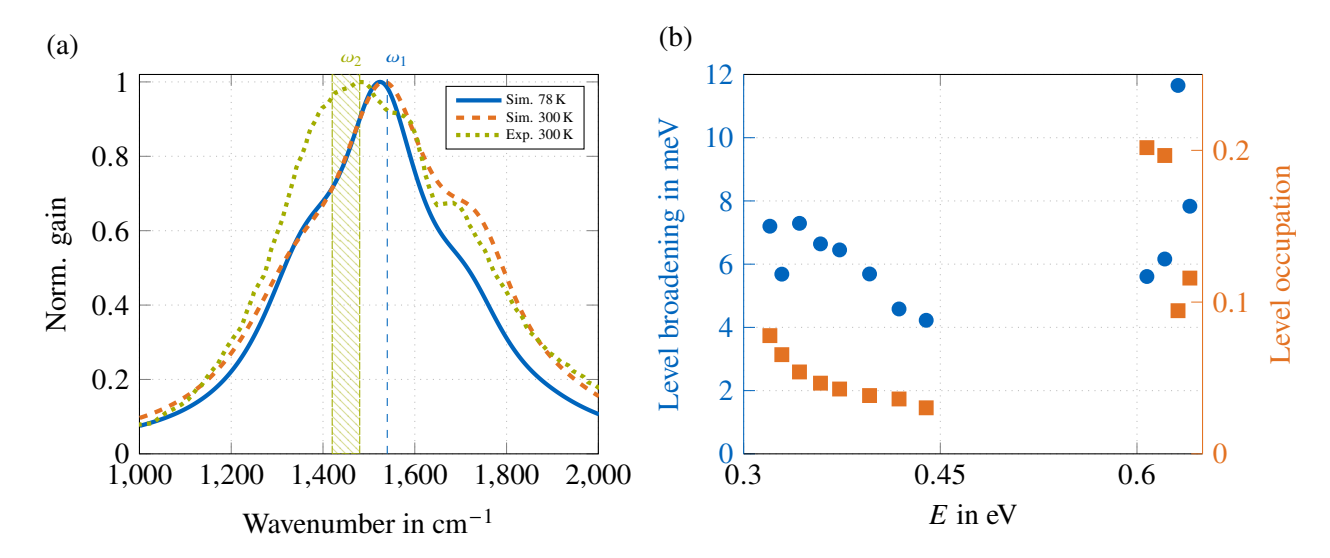


Figure 8.10 Simulation results of the DAU design. (a) Normalized gain as a function of wavenumber simulated at an operating temperature of 78 K (solid line) and 300 K (dashed line) together with the measured EL curve (dotted line, from [397]). The spectral ranges of the FP comb at ω_2 and single DFB mode at ω_1 are indicated by the shaded area and dashed line, respectively. (b) Simulated level broadening γ_i (circles) and relative level occupation ρ_{ii} (squares) for one QCL energy period as a function of the subband energy (see Fig. 8.8(b)). Reprinted from J. Popp *et al.*, "Self-consistent simulations of intracavity terahertz comb difference frequency generation by mid-infrared quantum cascade lasers" [90] (CC BY 4.0).

Table 8.2 Near-resonance DFG triplets of states and resulting second-order nonlinear susceptibility $\chi^{(2)}$ for the DAU QCL active gain medium. Resonance energy $\hbar\omega_{ij}$, pure dephasing energy $\gamma_{ij,p}$ (interface roughness contribution) in meV and transition dipole moments z_{ij} in nm for the mid-IR pump frequencies (ω_1, ω_2) and the THz mode (ω_{THz}). Reprinted from J. Popp *et al.*, "Self-consistent simulations of intracavity terahertz comb difference frequency generation by mid-infrared quantum cascade lasers" [90] (CC BY 4.0).

	ω_1			ω_2			$\omega_{ ext{THz}}$		(2)
Triplet	$\hbar\omega_{ij}$	z_{ij}	$\gamma_{ij,p}$	$\hbar\omega_{ij}$	z_{ij}	$\gamma_{ij,\mathrm{p}}$	$\overline{z_{ij}}$	$\gamma_{ij,\mathrm{p}}$	$\chi^{(2)}$ / nm V $^{-1}$
(1)	189	1.43	7.46(80%)	168.3	-1.17	9.83(68 %)	-6.99	0.58(31 %)	-1.92 + i6.51
(2)	211.5	-0.54	8.98(69 %)	189	1.43	7.46(80%)	-8.16	0.51(47%)	-0.97 + i1.59
(3)	212.8	1.15	5.84(82%)	109	1.43	7.40(80%)	-5.05	0.61(95%)	-1.50 + i0.84
(4)	192.1	-1.19	8.77(70%)	168.3	-1.17	9.83(68 %)	-3.03	0.01(93 %)	-0.24 + i1.71
(5)	212.8	1.15	6.17(61%)	192.1	-1.19	8.28(42%)	-6.99	2.37(68 %)	-0.44 + i0.90

scattering from the second upper laser level 4. For the carrier transport simulations of the DAU QCL design, we choose an average interface roughness height $\Delta = 0.1$ nm and a correlation length $\Lambda = 10$ nm.

According to Eq. (3.29) and the pure dephasing rates of Table 8.2, we calculate the total dephasing energies for the five mid-IR transitions to be in the range of 12.5 meV to 16.7 meV, resulting in slightly higher values compared to the experimental estimate of 12.5 meV given in [82], [200]. In literature, the additional linewidth broadening in strain-compensated DFG-QCLs is associated with the increased CBO and pronounced interface roughness [192], [398]. The contribution of interface roughness to the pure dephasing energy for the investigated triplets is illustrated in Table 8.2, yielding a significant impact for the mid-IR transitions. Taking also into account the reasonable match of simulated linewidth and experimental data, our simulated dephasing energies for the mid-IR regime appear to be reasonable. For the three investigated THz transitions, we obtain the total dephasing energy $\Gamma_{21} = 5.65$ meV, $\Gamma_{32} = 4.98$ meV, and $\Gamma_{64} = 9.24$ meV. The simulated THz values in the miniband compare well with the experimental assumption of 4 meV from [82], [200], except for the increased dephasing rate Γ_{64} arising from a larger level broadening γ_6 due to interface roughness. As it is schematically indicated in Fig. 8.10(a), the mid-IR pump wavelengths (λ_1, λ_2) are specified at the DFB mode $\lambda_{\rm DFB} = 6.5$ µm and at FP modes around $\lambda_{\rm FP} \sim 6.9$ µm. The transition dipole moments and calculated susceptibilities $\chi^{(2)}(\omega_{\rm THz} = \omega_{\rm DFB} - \omega_{\rm FP})$ for the five triplets are listed in Table 8.2. The five triplets contribute

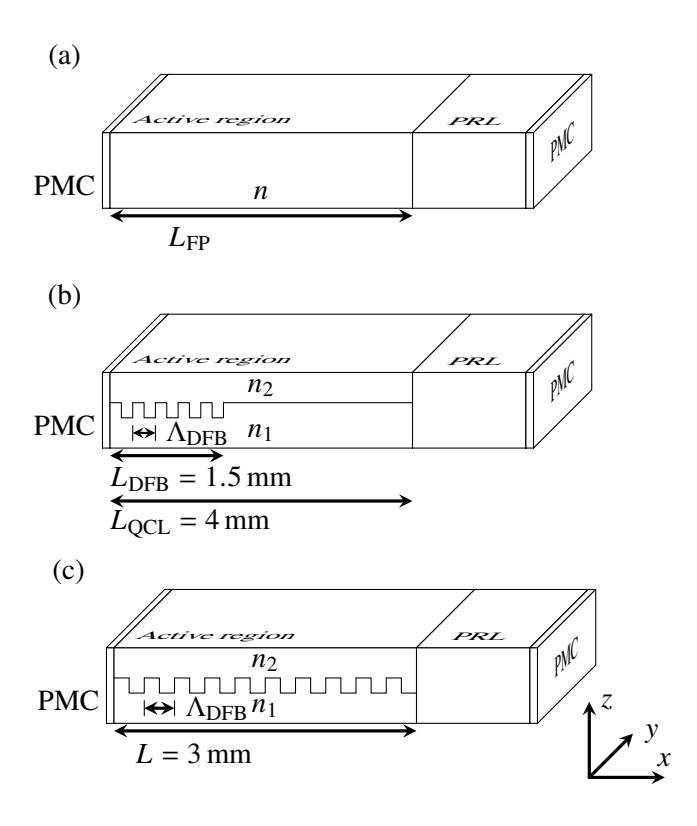


Figure 8.11 Simulation setups for the Maxwell-density matrix simulation of the two considered THz DFG-QCL frequency comb setups. (a) FP reference waveguide model. (b) Waveguide model of the SPR-depopulation QCL setup including a single-period DFB grating. (c) Waveguide model of the DAU QCL design including a single-period DFB grating. Reprinted from J. Popp *et al.*, "Self-consistent simulations of intracavity terahertz comb difference frequency generation by mid-infrared quantum cascade lasers" [90] (CC BY 4.0).

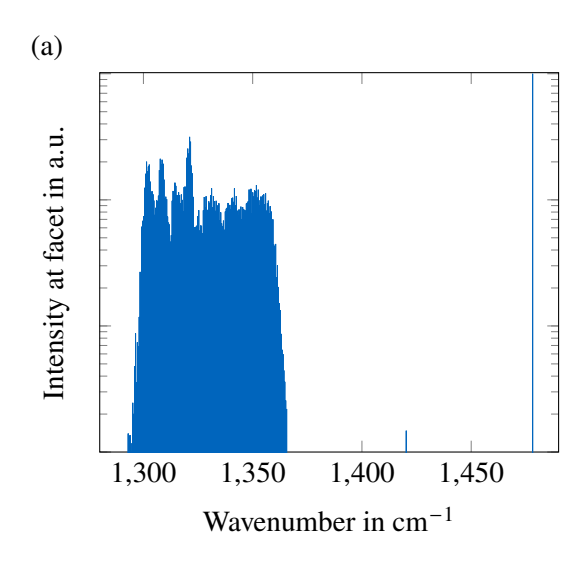
constructively, although the product of transition dipole moments for the triplets (3) and (4) differs from the others in sign. This results from the different DFG configuration of the triplets compared to (1), (2) and (5), which is shown schematically in Fig. 8.8(d). Summing up the individual contributions for the given frequency ω_{THz} , a total second-order nonlinear susceptibility value $|\chi^{(2)}| = 12.6 \,\mathrm{nm}\,\mathrm{V}^{-1}$ is obtained, which is slightly higher than the experimental estimate of $|\chi^{(2)}| = 7.8 \,\mathrm{nm}\,\mathrm{V}^{-1}$.

8.2.2 DFG-QCL Frequency Comb Simulations

In this section, we present dynamical simulation results of THz DFG-QCL frequency comb emission for the two different QCL setups. The description of the quantum-mechanical system is derived from the stationary carrier transport simulations. Furthermore, waveguide models for both QCL designs have to be specified and added to the simulation input script. Here, the investigated setups are based on integrated DFB gratings, defined in the experimental papers [205], [206]. The different DFB waveguide models are compared to the common FP waveguide model, as illustrated in Fig. 8.11. For the characterization of DFB gratings usually the coupling constant κ_{DFB} is used, which basically describes the field reflectance per unit length. In a first-order structure the period length is defined by $\Lambda_{\text{DFB}} = \lambda_{\text{B}}/2n_{\text{eff}}$ with the effective refractive index n_{eff} and the Bragg wavelength λ_{B} . It is assumed that the DFB wavelength $\lambda_{\text{DFB}} \approx \lambda_{\text{B}}$. We could derive from test simulations that the Bragg wavelength λ_{B} should be set roughly 0.1 μ m smaller than the desired DFB wavelength λ_{DFB} . The coupling constant κ_{DFB} of the DFB grating is defined within the coupled-mode theory and can be written as [401], [402]

$$\kappa_{\rm DFB} = \frac{\pi}{\lambda_{\rm DFB}} \frac{\Delta n}{2} \,, \tag{8.3}$$

where Δn is the modulation of the modal refractive index n_{eff} .



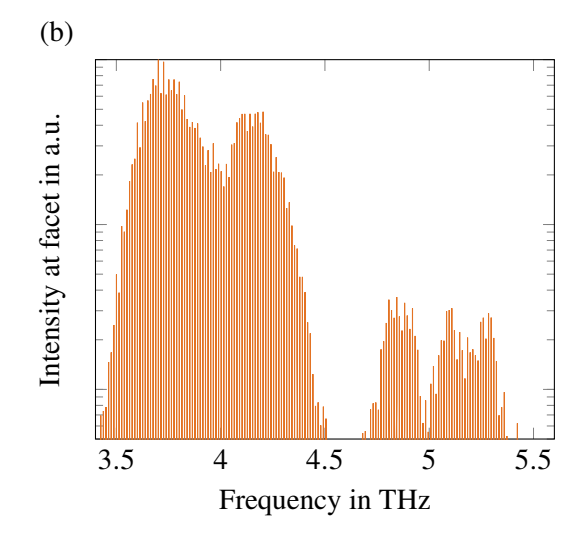


Figure 8.12 Simulated mid-IR (a) and THz (b) spectra of the DFG-QCL at a temperature of 293 K and an applied bias of 45 kV cm⁻¹. Experimental results are presented in [205]. Reprinted from J. Popp *et al.*, "Self-consistent simulations of intracavity terahertz comb difference frequency generation by mid-infrared quantum cascade lasers" [90] (CC BY 4.0).

Single-Phonon Resonance Depopulation Structure

For the dynamical simulation of the SPR-depopulation setup, we use the carrier transport simulation results obtained for the tight-binding potential at a bias of $45\,\mathrm{kV\,cm^{-1}}$. One tunneling pair is specified and the corresponding Rabi frequency Ω_{45} is added to the Hamiltonian. Two DFG triplets comprising one upper laser level and three lower laser levels are added. By taking into account these transitions for the dipole moment operator and the pure dephasing rates, we derive the complete quantum-mechanical description for the reduced SPR-depopulation structure.

Here, a 4 mm-long waveguide is patterned with a 1.5 mm DFB grating and terminated with an HR coated back facet. The single period DFB grating defined by e-beam lithography and dry etching is designed for single mode DFB lasing at $\lambda_{\text{DFB}} = 7.25 \,\mu\text{m}$, which is detuned by 80 cm⁻¹ from the FP comb emission frequency to minimize laser dispersion affected by the DFB structure. Due to the fact that the simulated gain curve is blue-shifted by roughly $\sim 40 \, \text{cm}^{-1}$ compared to the measured EL spectrum extracted from [192], we decided to choose a DFB frequency of $\lambda_{\text{DFB}} = 6.8 \, \mu\text{m}$ to retrieve the correct THz DFG frequency comb behavior. The DFB grating is defined by a period length $\Lambda_{\text{DFB}} = 1.15 \, \mu\text{m}$, and a coupling constant $\kappa_{\text{DFB}} = 35 \, \text{cm}^{-1}$ was estimated from the experimental subthreshold emission spectra. For our simulation, we set $\kappa_{\text{DFB,sim}} = 20 \, \text{cm}^{-1}$, as a simulative characterization of the DFB grating indicates this as best fit for a spectral separation of 3.5 cm⁻¹ from the DFB wavenumber. Furthermore, an effective refractive index $n_{\text{eff}} = 3$ with a modulation $\Delta n = 1.5 \times 10^{-2}$ is calculated. We use $N_x = 20000$ spatial gridpoints and set a simulation endtime of 50 ns, corresponding to ~ 600 roundtrips. The resulting Python script that starts a simulation in *mbsolve* is depicted in Appendix A.1.2 of the supplementary material. Here, a simulation time step of 1 ns takes approximately 45 minutes with a machine based on two AMD Epyc 7713 sockets with 64 cores each and 512 GB of RAM.

The obtained simulation results for the mid-IR spectrum and THz frequency comb of the SPR-depopulation setup are depicted in Fig. 8.12(a) and (b), respectively. Broadband FP frequency comb emission is obtained at a wavelength of around $\lambda_{FP} \sim 7.55\,\mu\text{m}$, which is slightly lower than the measured one at 7.81 μm and can be attributed to the blue-shifted gain in the simulation. By mixing the mid-IR FP comb with the DFB reference mode, a THz comb extending from 3.5 THz to 4.5 THz is generated. In comparison to the experimental data, which are presented in [205] and where the THz DFG frequency comb is located around 3 THz, a small blueshift is obtained. A smaller sidecomb extending from 4.7 THz to 5.5 THz is also visible, which is more than one order of magnitude smaller as compared to the main comb. Furthermore, we investigate the amplitude and phase dynamics of the field at the facet, both in the mid-IR and THz regimes.

As a reference, we simulate the SPR depopulation structure in a conventional Fabry-Perot waveguide, without considering dipole moments of THz transitions. Thus, we can validate if the well-studied hybrid

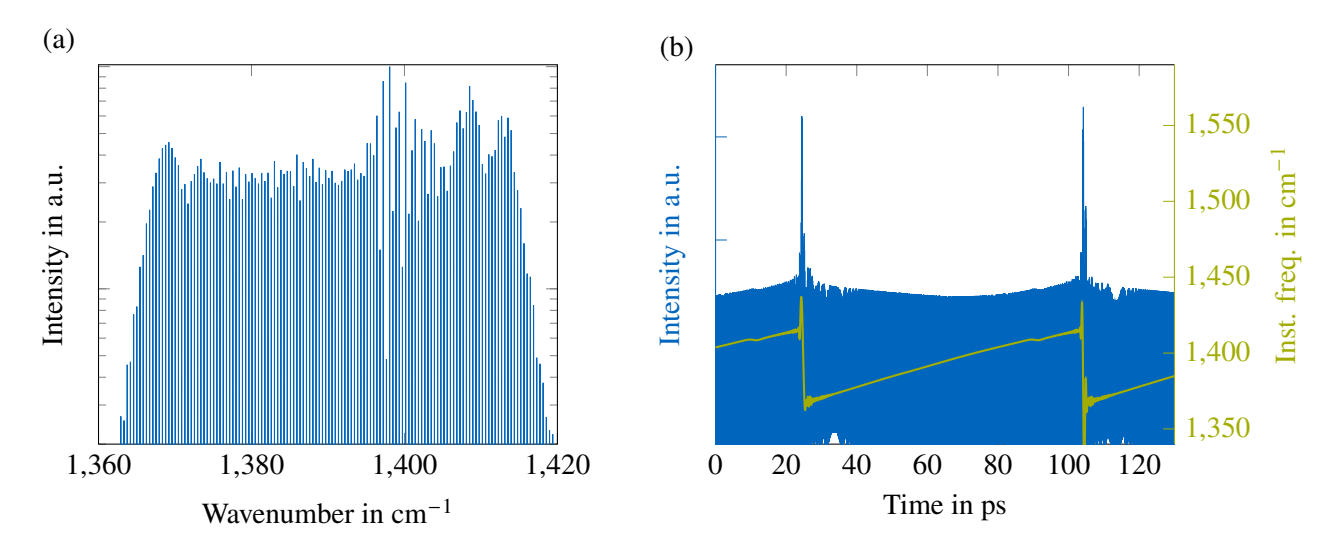


Figure 8.13 Simulation results of the QCL device in a FP waveguide and at a temperature of 293 K. The simulation parameters are determined in ensemble Monte Carlo simulations for a bias of 45 kV cm⁻¹. Experimental results are presented in [205]. (a) Simulated mid-IR intensity spectrum at the facet. (b) Simulated instantaneous intensity at the facet and calculated instantaneous frequency from the Hilbert transform of the simulated electric field. Reprinted from J. Popp *et al.*, "Self-consistent simulations of intracavity terahertz comb difference frequency generation by mid-infrared quantum cascade lasers" [90] (CC BY 4.0).

frequency/amplitude modulation properties of a mid-IR QCL frequency comb are present [115], [117]. The simulated spectrum and time trace of the intensity and instantaneous frequency are depicted in Fig. 8.13. In Fig. 8.13(a) a broad frequency comb, ranging from 1 360 cm⁻¹ to 1 420 cm⁻¹, can be observed, where most of the modes have comparable individual power. It can be identified clearly from Fig. 8.13(b), that a linear chirp in the instantaneous frequency is present. This result is comparable to the first experimental demonstration of such a chirp in [115], with intermodal phase measurements based on the SWIFTS technique. The calculated instantaneous frequency chirp extends from 1 360 cm⁻¹ to 1 420 cm⁻¹, covering the full intensity spectrum of the mid-IR FP frequency comb. Furthermore, the distinct AM state, with a very short characteristic time, is in good agreement with the experimental and theoretical findings [115], [119]. These discussed properties are strong indications of phase-locked FM comb operation. Notably, using our detailed multilevel simulation approach, we do not need to explicitly add a linewidth enhancement factor in order to obtain this type of comb, whereas for reduced models this has been reported to be necessary [70].

Besides this well-studied state, we analyze the temporal characteristic of the DFG-QCL setup within the DFB waveguide configuration shown in Fig. 8.11(b). The obtained results for the mid-IR and THz regimes are illustrated in Fig. 8.14(a) and (b), respectively. The temporal evolution of the instantaneous frequency in the mid-IR regime clearly shows linear behavior from 1 300 cm⁻¹ to 1 365 cm⁻¹, thus covering the whole FP frequency comb given in Fig. 8.12(a). Furthermore, the distinct AM state with a very short characteristic spike at the end of the periodic time signal is in good agreement with the experimental and theoretical findings [115], [119]. In comparison to the FP setup, we see a clear redshift of the mid-IR comb arising from the mode suppression introduced by the DFB grating. In the temporal dynamics of the mid-IR component, shown in Fig. 8.14(a), we identify numerous very fast intensity modulations, which are absent in mid-IR combs without DFB grating (compared to Fig. 8.13(b) and [110]). The reconstructed time trace of the THz signal is illustrated in Fig. 8.14(b). Here, a linear chirp over a considerable part of the roundtrip time is identified and extends from 3.5 THz to 4.5 THz, corresponding to the dominant lobe of the simulated THz spectrum in Fig. 8.12(b). The THz signal shows a mirrored characteristic as compared to the mid-IR signal, which illustrates the coupling arising from the DFG mixing.

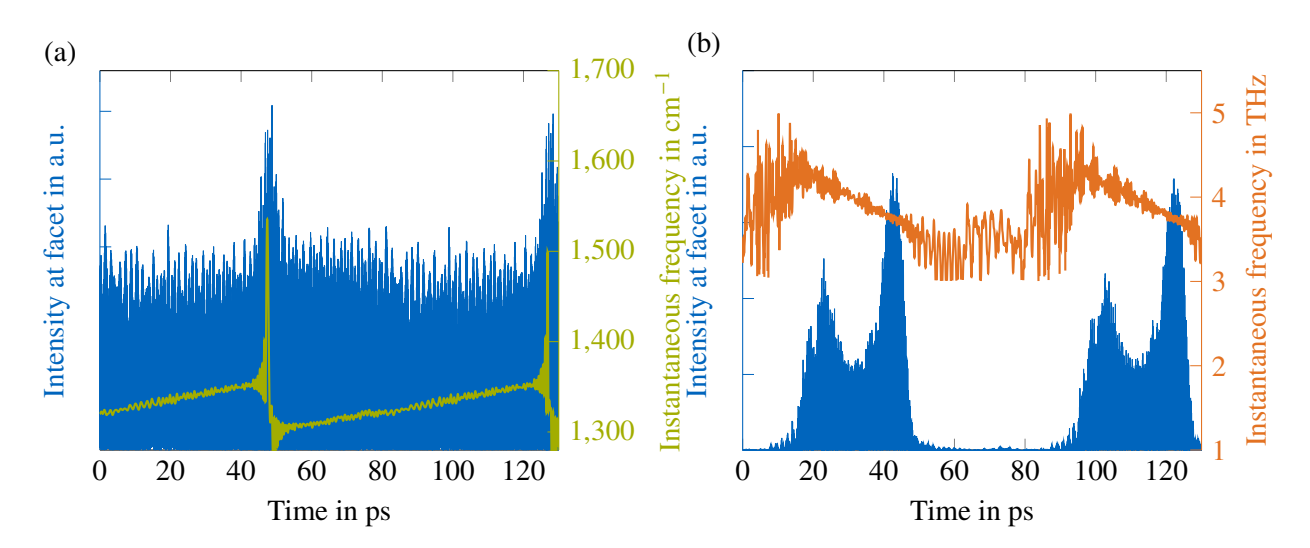


Figure 8.14 Simulation results of the DFG-QCL device at a temperature of 293 K. The simulation parameters are determined in EMC simulations for a bias of 45 kV cm⁻¹. Simulated instantaneous intensity at the facet and calculated instantaneous frequency from the Hilbert transform of the simulated electric field for the mid-IR FP components (a) and THz components (b). Reprinted from J. Popp *et al.*, "Self-consistent simulations of intracavity terahertz comb difference frequency generation by mid-infrared quantum cascade lasers" [90] (CC BY 4.0).

Dual-Upper State Active Region

In the carrier transport simulations, we have identified five main DFG triplets formed by different combinations of the two upper laser levels 6, 4 and three lower laser levels 3, 2, and 1, as illustrated in Fig. 8.8(d). The dipole moments of all mid-IR transitions (ω_1 , ω_2) and THz transitions are added to the dipole moment operator. Carrier injection is modeled by resonant tunneling, where four anticrossed tunneling pairs, formed by two injector states (7, 5) and two upper laser levels (6, 4), are included. The calculated anticrossing energies are added to the system Hamiltonian \hat{H}_s . For all quantum coherence terms considered in our Maxwell-density matrix model, we have to add the corresponding pure dephasing rates, while the level broadenings γ_i are directly calculated from the specified scattering rate matrix. Both terms are summarized in a relaxation superoperator class object and form together with the system Hamiltonian \hat{H}_s and dipole operator \hat{d} the quantum-mechanical description of the active region.

The QCL waveguide consists of a single-period DFB grating, which is defined by nanoimprint lithography. The first order grating period is $\Lambda_{\rm DFB}=1.04~\mu m$. To avoid the suppression of the broadband FP comb emission, the DFB mode has to be largely detuned from the gain maximum. Here, the single mode DFB wavelength is chosen to be $\lambda_{\rm DFB}=6.5~\mu m$ and FP frequency comb modes are generated around $\lambda_{\rm FP}=6.9~\mu m$. The coupling constant is estimated in [206] as $\kappa_{\rm DFB}\sim7~{\rm cm}^{-1}$. Based on that, we calculate an effective refractive index $n_{\rm eff}=3.08$ with a modulation $\Delta n=2.9\times10^{-2}$ for the DFB grating. An overlap factor $\Gamma=0.6$ and field losses $\alpha_0=3.2~{\rm cm}^{-1}$ are assumed for the two materials comprising the DFB grating period. The device with a cavity length $L=3~{\rm mm}$ is HR coated on the back facet and for the front facet we use PRL boundary conditions specified by the reflectance $R=|n_{\rm eff}-1|^2/|n_{\rm eff}+1|^2$. To assure an adequate spatial discretization, we specify the number of spatial gridpoints $N_x=15000$. The simulation endtime was set to 100 ns, which equals around ~1500 roundtrips. The simulation setup consisting of a device and a scenario is summarized in a Python script, which is depicted in Appendix A.1.3 and can be used to start a dynamical DFG-QCL simulation with the open-source tool *mbsolve*. For this quite complex and computationally demanding application, we use a machine based on two AMD Epyc 7713 sockets. Nevertheless, a simulation time of 1 ns takes approximately 45 minutes.

The obtained DFG-QCL simulation results are depicted in Fig. 8.15(a) for the mid-IR spectrum and in Fig. 8.15(b) for the THz frequency emission. We clearly identify a single DFB mode, which proves the validity of the implementation of the DFB grating in the *mbsolve* simulation framework.

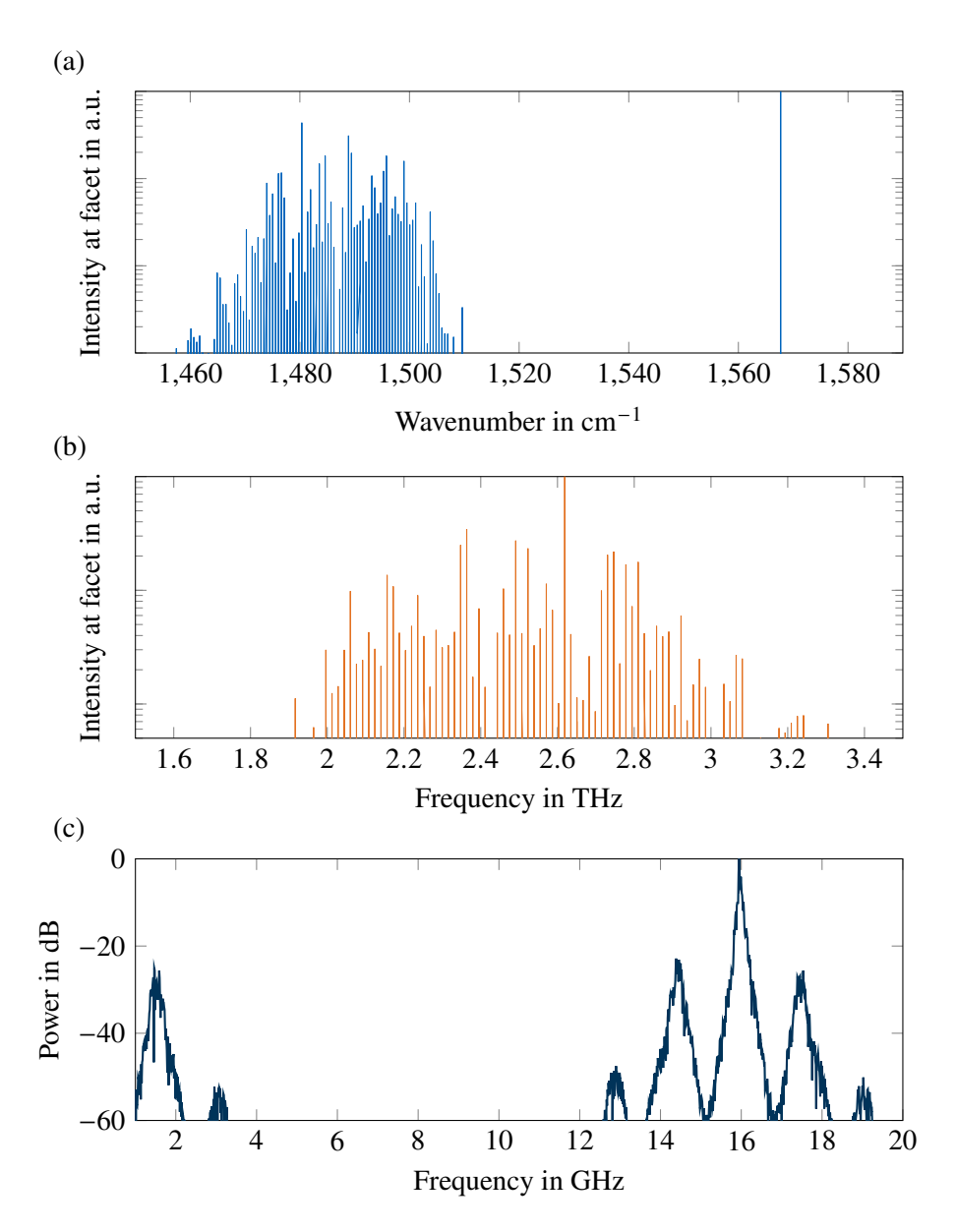
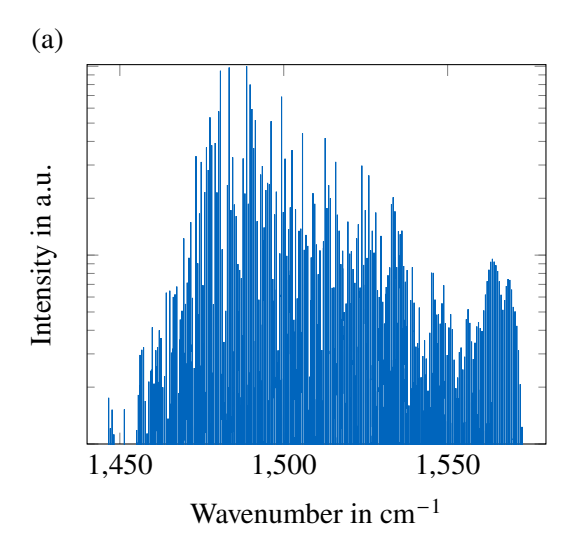


Figure 8.15 Simulated mid-IR (a), THz (b) spectra and RF beatnote (c) of the DFG-QCL at a temperature of 78 K and a bias of 56 kV cm⁻¹. Experimental results are presented in [206]. Reprinted from J. Popp *et al.*, "Self-consistent simulations of intracavity terahertz comb difference frequency generation by mid-infrared quantum cascade lasers" [90] (CC BY 4.0).



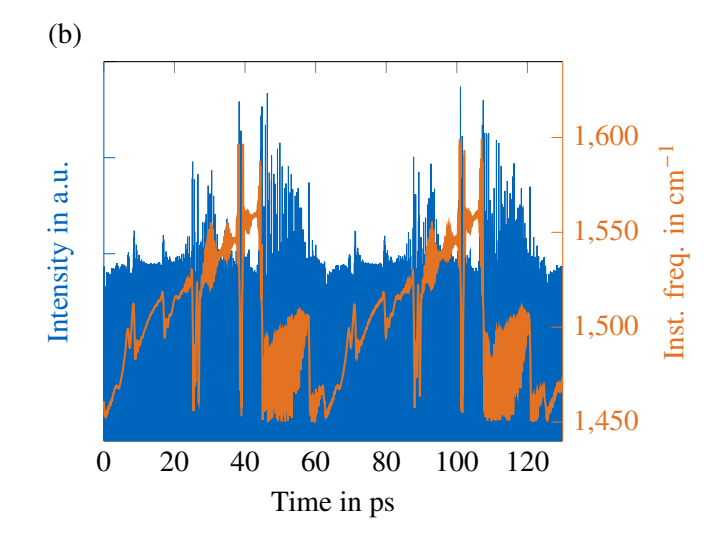


Figure 8.16 Simulation results of the QCL device in a FP waveguide and at a temperature of 78 K. The simulation parameters are determined in ensemble Monte Carlo simulations for a bias of 56 kV cm⁻¹. (a) Simulated mid-IR intensity spectrum at the facet. (b) Simulated instantaneous intensity at the facet and calculated instantaneous frequency from the Hilbert transform of the simulated electric field. Reprinted from J. Popp *et al.*, "Self-consistent simulations of intracavity terahertz comb difference frequency generation by mid-infrared quantum cascade lasers" [90] (CC BY 4.0).

As our simulated gain curve exhibits a slight blue shift in comparison to experimental results, also the simulated mid-IR FP spectrum is slightly shifted towards higher frequencies, relative to the measured spectrum in [206]. The simulated spectrum spans from $\sim 1\,460\,\mathrm{cm^{-1}}$ to $1\,510\,\mathrm{cm^{-1}}$, which is still in good agreement with the experimental bandwidth. To compensate for that we decided to also shift the DFB mode in the simulations towards a higher wavenumber of $1\,567\,\mathrm{cm^{-1}}$. The intracavity mixing between the mid-IR FP multimodes and single DFB mode leads to a downconversion to the THz spectrum extending from $1.9\,\mathrm{THz}$ to $3.3\,\mathrm{THz}$. The simulation results are in reasonable agreement with the experimentally measured ultra-broadband THz emission extending from $1.8\,\mathrm{THz}$ to $3.3\,\mathrm{THz}$, as reported in [206]. In the experiment, a relatively flat plateau at the gain peak was measured, which constitutes a relative gain variation of less than $5\,\%$ within the FP spectral range from $1\,420\,\mathrm{cm^{-1}}$ to $1\,480\,\mathrm{cm^{-1}}$. In contrast, a more distinct gain peak is obtained in the stationary carrier transport simulations. Here, a relative gain variation of $\sim 20\,\%$ in the aforementioned FP spectral range is calculated. The mid-IR FP bandwidth and in consequence the THz spectrum shows a more pronounced lobe for the dynamical simulation, resulting in less intense sidemodes.

Additionally, we analyze the RF beatnote of the electric field at the facet, depicted in Fig. 8.15(c). The main peak at 16 GHz corresponds to the inverse of the roundtrip time. Two additional beatnotes appear in the RF spectrum close to the main beatnote, at 14.5 GHz and 17.5 GHz, as well as higher-order sidebands. Therefore, a narrow beatnote spacing of 1.5 GHz is given, which can be explained by the formation of sub-combs. Similar behavior has been observed in [403], where the dynamics of comb formation in THz QCLs were investigated. The emergence of spectrally separated sub-combs was previously also detected in microresonator combs, where four-wave mixing processes induce mode proliferation [404]. The sidepeaks in the RF signal arise from the coexisting sub-combs in the cavity, which feature the same mode spacing but exhibit slightly different carrier offset frequencies. At the simulated bias point of 56 kV cm⁻¹ the DFG QCL device appears to not fully operate in the stable fundamental frequency comb regime in our simulations. It rather exhibits a state where the coexistence of different sub-combs hinders the build-up of a fundamental comb. In the time-trace of the intensity and instantaneous frequency this results in alternating frequency and amplitude modulated behavior, similar to the results in [115].

A more turbulent spectral and temporal intensity profile for both cases, i.e., with and without the presence of the DFB grating and active THz transitions, is observed. In Fig. 8.16(a) the mid-IR spectrum of the Fabry-Perot device is depicted, showing significant modal contributions from 1 450 cm⁻¹ to 1 575 cm⁻¹. However, single modes tend to have large and random intensity fluctuations, compared to the adjacent ones. For the overall

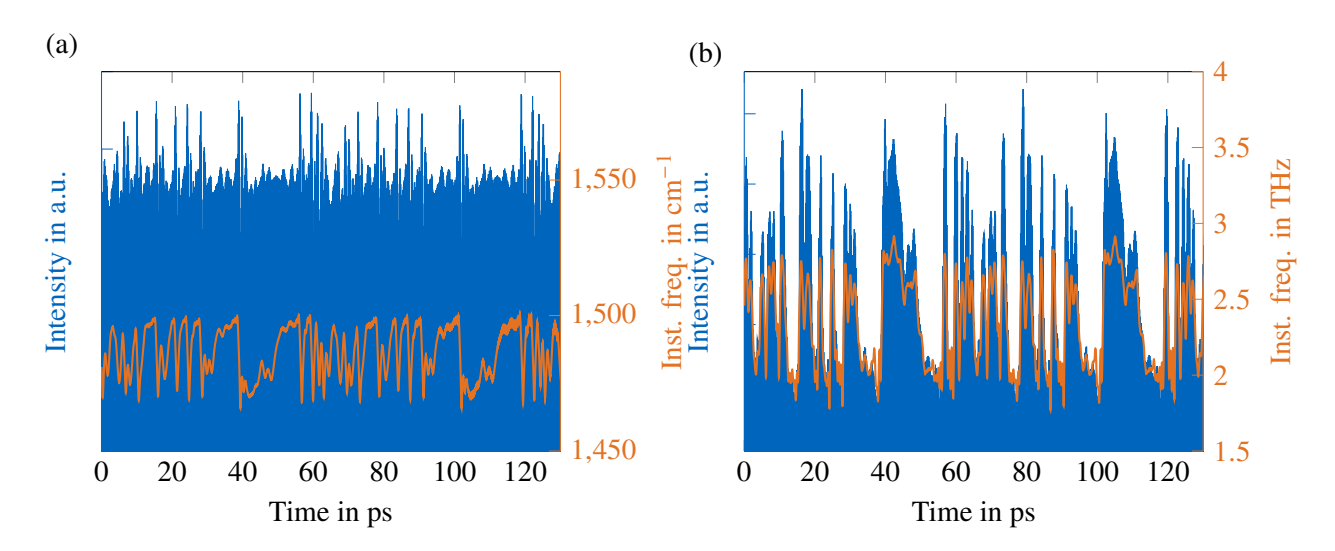


Figure 8.17 Simulation results of the DFG-QCL device at a temperature of 78 K. The simulation parameters are determined in ensemble Monte Carlo simulations for a bias of 56 kV cm⁻¹. Simulated instantaneous intensity at the facet and calculated instantaneous frequency from the Hilbert transform of the simulated electric field for the mid-IR FP components (a) and THz components (b). Reprinted from J. Popp *et al.*, "Self-consistent simulations of intracavity terahertz comb difference frequency generation by mid-infrared quantum cascade lasers" [90] (CC BY 4.0).

intensity time-trace in Fig. 8.16(b) this results in a rather irregular pattern. However, the instantaneous frequency reveals that a linear frequency chirp is still present, but is repeatedly interrupted by amplitude modulations. We assume that this behavior is a result of the interaction with the undesired sub-combs and should disappear at a differently chosen bias point.

In Fig. 8.17, the intensity and instantaneous frequency of two roundtrips are shown under the presence of the DFB grating and THz field, in Fig. 8.17(a) for the mid-IR component, and in Fig. 8.17(b) for the THz component. Now, the behavior appears to be even more irregular, in agreement with the results of the SPR structure. Nevertheless, in the mid-IR component, some intervals of a rather linearly modulated frequency can be observed, e.g. from 40 ps to 60 ps and from 100 ps to 120 ps. Interestingly, for these times the THz signal has a rather constant frequency and a strong amplitude modulation.

Even in this state, the emission of multimode THz radiation could be simulated and can unambiguously be assigned to the DFG process in a mid-IR QCL, necessitating the elaborate full-wave approach. In order to retrieve a complete understanding of the different dynamical regimes, including the fully locked DFG QCL comb state, a detailed study with an extended bias sweep would be required and will be addressed in future works.

8.3 Summary

Firstly, we have provided a substantial theoretical analysis of self-starting THz HFC emission in QCLs. The simulation results of harmonic combs featuring different orders are conducted using a self-consistent multidomain modeling approach, coupling a DM-EMC carrier transport simulation tool to a dynamical Maxwell-DM solver. The investigation of different basis states reveals their influence on the gain characteristics and the formation of HFC states in THz QCLs. By comparing extended to localized states in the here simulated QCL structure, we have identified an underestimation of the injection transition into the upper laser level in the extended configuration. The resulting small gain appears to be unsuitable for the formation of a HFC in this setup. In contrast, the more pronounced gain spectrum in the localized state basis with a dominant optical transition ULL \rightarrow LLL alleviates the formation of a dense FC comb, which evolves over time into a harmonic comb. Additionally, we have investigated the influence of the applied bias and waveguide geometry on the HFC formation and obtained different dynamical regimes with varying harmonic orders. We have characterized the spectral time evolution of the self-starting harmonic mode-locking mechanism, providing new insights into the

HFC creation process. We have also analyzed the noise properties of a coherent THz QCL HFC setup and obtained a good match with experimental findings [73], [83]. In the future, we aim to pin down the physical mechanisms enabling harmonic mode-locking by reducing the model complexity.

Secondly, we have presented THz DFG-QCL frequency comb simulation results. For the calculation of the important material parameters, e.g., CBO, we fully take into account important environmental influences such as strain and nonparabolicity effects. We have investigated the THz frequency comb formation by DFG in two OCL designs, consisting of a single-phonon resonance depopulation scheme and a dual-upper state active region, respectively. The experimentally obtained broad gain curve and calculated high second-order nonlinearity are closely reproduced by our stationary carrier transport simulations. Furthermore, we have performed dynamical full-wave simulations of THz frequency comb emission based on difference frequency generation for both setups, where the THz comb is obtained by nonlinear mixing of a largely detuned DFB mid-IR single mode and a mid-IR FP comb. All in all, the THz DFG-QCL comb results are in good agreement with the experimental measurements. For the SPR-depopulation QCL setup, we obtain a linear instantaneous frequency chirp at the investigated bias, in reasonable agreement with experimental findings. Furthermore, the obtained THz time trace follows the mid-IR signal and thus corroborates the concept of DFB downconversion from the mid-IR FP comb into a THz comb. In the dynamical simulations of the dual-upper state DFG QCL setup we have identified sidepeaks in the RF beatnote spectrum at the investigated bias, indicating the coexistence of sub-combs, which affect the modulation behavior of the fundamental comb. For both setups, the simulated mid-IR FP frequency comb is slightly shifted towards higher frequencies. Therefore, we have obtained a smaller frequency gap between the FP comb and DFB mode with respect to the experimental data, and the resulting THz frequency comb is somewhat red-shifted. We have retrieved broad THz spectra for both designs and reproduced the measured ultra-broadband THz emission in the DAU device. The reasonable agreement with experimental data shows that our simulation approach contains all the relevant effects. Thus, it constitutes a suitable tool for systematic design optimization of THz DFG-QCL comb structures, which can be speeded up by using a quantum system model with a reduced number of levels that includes all the optical and nonlinear effects responsible for the DFG description.

9 Conclusion and Outlook

In this work, we have dealt with the theoretical modeling and numerical simulation of intersubband quantum cascade devices. Therefore, we have focused on QCLs as optically coherent light sources and QCDs as their photovoltaic counterparts. In Chapter 1 the basic operating principles of both devices including nonlinear and nonclassical effects were discussed and the enormous potential for future applications in the fields of metrology, sensing and quantum technologies was outlined. In order to systematically improve the performance in terms of operating temperature, efficiency and spectral range a deep theoretical understanding of the physical mechanisms is required. Therefore, we implemented the object-oriented *monacoQC* framework for the development and improvement of optoelectronic QC devices [254], which was presented in Chapter 2. Special physical properties of semiconductors and environmental influences such as temperature, strain in the semiconductor lattice and nonparabolicity effects were here taken into account for the calculations of certain material parameters such as the energy band gap or the effective mass. In addition, the Schrödinger-Poisson solver library was described, which is integrated into the *monacoQC* framework and can be used for the design and engineering of quantized electron states in heterostructures with respect to e.g., their eigenenergy or shape. We further gave an overview of the Bayesian optimization tool, which is used in combination with a scattering-based simulation approach for the optimization of quantum cascade devices.

In Chapter 3, advanced self-consistent carrier models for quantum cascade devices were discussed and their potential for integration into the *monacoQC* framework was analyzed. More specifically, we focused on the in-house DM-EMC solver and a rate equation solver model. Firstly, the most important scattering mechanisms in the quantum well heterostructure were characterized and the corresponding scattering rates were calculated using Fermi's Golden Rule. With these scattering rates as input, the in-house DM-EMC solver for carrier transport simulations of QCLs was described in more detail. Since direct EMC modeling of photovoltaic QCDs is not feasible, a robust and compact approach based on a rate equation model and a Kirchhoff resistance network was introduced. By exploiting thermodynamic equilibrium relations, we derived expressions for the responsivity and specific detectivity. Different physical quantities such as absorption coefficient, extraction efficiency, and resistance for QCDs and gain profiles or the second-order nonlinear susceptibility in QCLs were calculated using the stationary simulation results. For dynamical simulations, a reduced quantum system description is required and can be composed using the presented **mbsolve_sim** module of the *monacoQC* framework.

A full-wave Maxwell-density matrix simulation tool including c-number stochastic noise terms was presented in Chapter 4. This is especially important for the simulation of spatiotemporal dynamics in active photonic devices, e.g., quantum cascade lasers. Here, the coherent light-matter interaction plays an important role in the generation of frequency combs and other nonlinear and nonclassical optical phenomena. Since the emergence of nonlinear and nonclassical features is directly linked to the noise properties, detailed simulations of the noise characteristics are required for the development of low-noise QCL sources. We calculated the stochastic noise terms of the quantum Langevin equations and derived the generalized description of the Maxwell-density matrix Langevin equations for a QCL laser system. For the calculation of drift and diffusion operators in the quantum Langevin theory, we considered the influence of various surrounding reservoirs on our laser system. The noise implementations in the *mbsolve* dynamic simulation framework are publicly available [58].

An overview of the complete open-source solver tool *mbsolve* was given in Chapter 5. Here, we evaluated numerical methods for the Maxwell-density matrix Langevin equations. Additionally, we reviewed the existing codebase and introduced new implementations, e.g., the truncation of the optical field at the simulation boundaries, the treatment of chromatic waveguide dispersion and the calculation of the fluctuations terms. The numerical treatment of the equation system with the auxiliary differential equation FDTD method for Maxwell's equations and the matrix exponential method for the density matrix were discussed in detail. We concluded with a brief overview of the new generalized update equations and explained the simulation main loop. The simulation framework and the code extensions were verified in Chapter 6. Therefore, we used an active gain

Monaco framework

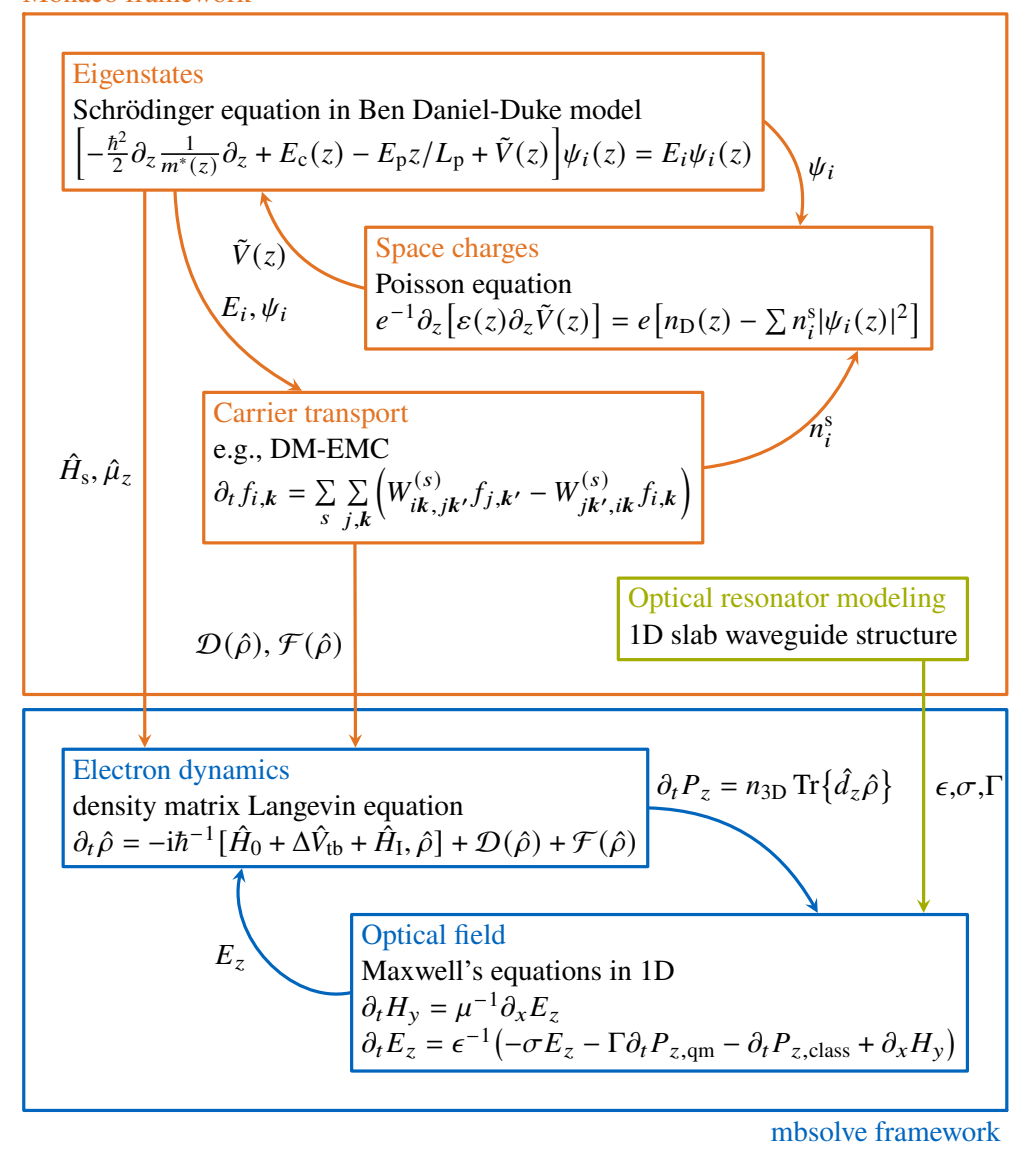


Figure 9.1 Schematic illustration of the multi-domain simulation approach for intersubband QC devices.

medium based on a well-studied THz quantum cascade laser design for OFC generation and an incoherent two-level system for superfluorescence. By taking into account impedance mismatch effects arising from the internal quantum system within our PML implementations, improved absorbing characteristics for the truncation of active gain media were obtained. Further simulations were executed to characterize the influence of group velocity dispersion on the formation of THz frequency combs. We validated our fluctuation implementation with a superfluorescence setup, where we could prove the validity of our implementation by an excellent agreement with previous experimental and theoretical results.

By combining both simulation tools (monacoQC and mbsolve), a multi-domain modeling approach is realized that can be used for fully time-dependent and self-consistent simulations of intersubband QC devices. A schematic illustration of this multi-domain simulation approach is depicted in Fig. 9.1. The monacoQC framework comprises a Schrödinger-Poisson solver for the calculation of the wavefunctions and eigenenergies in the QC conduction band heterostructure and the DM-EMC tool for the simulation of the stationary charge transport behavior, including the calculation of scattering rates, dephasing rates and occupations. The obtained simulations results are used as input parameters for the mbsolve simulation tool, to generate the active QC setup file consisting of e.g., the Hamiltonian, and the dipole matrix elements. Here, the electron dynamics are

described by the Lindblad equation, the optical field by the classical Maxwell's equations and the light-matter interaction is taken into account by the quantum-mechanical polarization $P_{z,qm}$.

The development of low-noise intersubband detectors, as required for the detection of non-classical features in the optical output of QCLs and especially in QCL-based frequency combs, was one important aspect of this work. With a view to future commercial applications, we concentrated on increasing the operating temperature in order to achieve operation at room temperature with moderate effort, e.g., through thermoelectric cooling. A reliable simulation approach that is self-consistent, i.e., that does not require empirical or fitting parameters as input, is essential for systematic design optimization. In Chapter 7, we first evaluated our simulation approach by applying it to QCD designs in the mid-infrared and terahertz range. We obtained good agreement with the experimental data. For the terahertz structure studied, the EMC results were also compared with NEGF simulations, yielding good agreement. However, the simulated zero-bias resistance of this structure is much lower than the experimentally determined value at low temperatures. Since the predominant noise mechanism for temperatures below 20 K is not temperature dependent, our Kirchhoff resistance model, which considers Johnson noise as the main noise mechanism, is not suitable for reproducing the experimental results for temperatures close to 0 K. Secondly, our Bayesian optimization approach within the *monacoOC* framework was tested using the mid-IR QCD design N1022. Our optimization strategy yields an improvement of specific detectivity by a factor of $\sim 2-3$ at room temperature using two different parameter sets. The oscillator strength between ground level g and absorption level a_2 leads to a significantly increased absorption efficiency η_{abs} . Furthermore, we investigated the sensitivity of our approach to fabrication tolerances, showing the robustness of the optimized designs against growth fluctuations under fabrication conditions. For this optimization approach, we used a scattering model based on Fermi's golden rule. For further optimizations, we will also use the self-consistent EMC model for the evaluation of QCD figures of merit, and compare them with the scattering rate approach used here.

In Chapter 8, we first provided a substantial theoretical analysis of self-starting THz HFC emission in QCLs. The simulation results of harmonic combs featuring different orders were conducted using the self-consistent multi-domain modeling approach. The investigation of different basis states reveals their influence on the gain characteristics and the formation of HFC states in THz QCLs. Additionally, we investigated the influence of the applied bias and waveguide geometry on the HFC formation and obtained different dynamical regimes with varying harmonic orders. We characterized the spectral time evolution of the self-starting harmonic mode-locking mechanism, providing new insights into the HFC creation process. We also analyzed the noise properties of a coherent THz QCL HFC setup and obtained good agreement with experimental results. Furthermore, simulation results of THz frequency comb emission in QCLs based on intracavity difference frequency generation using the self-consistent multi-domain simulation approach were presented in Chapter 8. We investigated the THz frequency comb formation by DFG in two QCL designs, consisting of a single-phonon resonance depopulation scheme and a dual-upper state active region, respectively. The experimentally obtained broad gain curve and calculated high second-order nonlinearity are closely reproduced by our stationary carrier transport simulations. Furthermore, we performed dynamical full-wave simulations of THz frequency comb emission based on difference frequency generation for both setups. All in all, the THz DFG-QCL comb results are in good agreement with the experimental measurements. The reasonable agreement with the experimental data shows that our simulation approach includes all relevant effects.

The Bayesian optimization algorithm in combination with the presented simulation approach proves to be an efficient tool for the optimization of QCDs. We therefore plan to use it for the design and optimization of QCDs assed on-chip applications for environmental sensing. In particular, the systematic design optimization of QCLs with respect to nonlinear and nonclassical optical effects will be very important. Our multi-domain simulation approach shows great potential for modeling harmonic THz comb operation at room temperature based on the DFG of a mid-IR QCL comb. Furthermore, the physical mechanisms that enable harmonic mode-locking could be analyzed by reducing the model complexity. Higher-order gratings and nonlinearities seem to have a significant impact on self-starting HFC formation in QCLs. To gain insight into the underlying mechanisms, the crucial nonlinear effects need to be identified. Possibly, the adiabatic elimination of specific terms within the Maxwell-density matrix equations may provide additional insights. It has already been used for the prediction of pure FM combs in mid-IR QCLs and for the description of passive single-pulse mode-locking in THz QCLs with

distributed saturable absorbers. Our modeling approach, which is based on the generalized Maxwell-density matrix Langevin equations, opens up great perspectives for the theoretical investigation of intermodal intensity correlations in photonic devices and the development of low-noise integrated light emitters. With respect to the generation of nonclassical light, the semiclassical model will serve as a starting point for the development and validation of fully quantum optical approaches.

A Appendix

A.1 Mbsolve Simulation Setups

Here, the Python scripts for setting up and running *mbsolve* simulations of the presented QCL setups are given. The scripts include all input parameters for the description of the quantum system and the simulation scenario. The quantum-mechanical description comprises the level occupations ρ_{ii} , the system Hamiltonian \hat{H}_s with eigenenergies E_i and anticrossing energies $\hbar\Omega_{ij}$, the dipole moment operator \hat{d}_z , the scattering rates r_{ij} and the dephasing rates γ_{ij} . For the one-dimensional dynamic Maxwell-density matrix simulations, the energy-resolved dephasing rates are simulated within the EMC approach and have to be averaged over the population inversions of the involved subbands.

A.1.1 Four Quantum Well Diagonal Transition Design

Listing A.1 Code snippet of the Python script for the THz HFC QCL setup in [73].

```
import mbsolve.lib as mb
import mbsolve.solvercpu
import mbsolve.writerhdf5
import mbsolve.readerhdf5
import math
import time
# Hamiltonian
energies = [ 0.0097 * mb.E0, 0.0082 * mb.E0, -0.0047 * mb.E0,
-0.0083 * mb.E0, -0.0097 * mb.E0 ]
off_diagonales = [ 0.0005 * mb.E0, 0, 0, 0, 0, 0, 0, 0, 0]
H = mb.qm_operator(energies, off_diagonales)
# dipole moment operator
off_dipoles = [ 0, -2.9500e-09 * mb.E0, 0, 0, 0, 0, 0, 0, 0]
diag\_dipoles = [ 0, 0, 0, 0, 0 ]
u = mb.qm_operator(diag_dipoles, off_dipoles)
# relaxation superoperator
# scattering rate matrix R
\texttt{rates} \ = \ [ \ [ \ 0 \,, \ 1.8815\,e + 09 \,, \ 2.1290\,e + 10 \,, \ 4.0984\,e + 09 \,, \ 5.6000\,e + 09 \ ] \,,
          [ 3.5006e+09, 0, 3.2437e+08, 2.2854e+10, 2.0029e+12 ],
          [ 6.5578e+10, 6.2829e+08, 0, 8.0333e+11, 6.1577e+09 ],
          [ 6.8416e+09, 3.6845e+08, 6.6107e+11, 0, 4.7378e+12
          [ 5.2192e+08, 6.7259e+10, 4.7554e+09, 4.7726e+12, 0 ] ]
# pure dephasing rates
pure_deph = [ 3.5857e+12, 9.3257e+11, 0, 0, 0, 0, 0, 0, 0]
relax_sop = mb.qm_lindblad_relaxation(rates, pure_deph)
# initial density matrix
rho_init = mb.qm_operator([ 0.3705, 0.4937, 0.0741, 0.0333, 0.0285])
h = 15e-6
w = 60e - 6
A = h * w
```

```
N = 6.35e21
N_x = 2000
l_{device} = 4e-3
d_x = l_{device} / N_x
f_noise = 1
N_cell = N * A * d_x * f_noise
qm = mb.qm_description(N, N_cell, H, u, relax_sop)
loss = 760
mat_ar = mb.material("AR_Forrer", qm, 12.96, 1, loss, 1.0)
mb.material.add_to_library(mat_ar)
dev = mb.device("51v1")
dev.add_region(mb.region("Active_region", mat_ar, 0.0, 1_device))
# Scenario
ic_d = mb.ic_density_const(rho_init)
ic_e = mb.ic_field_const(0.0)
sce = mb.scenario("hc_noise_forrer2021", N_x, 2200e-9, ic_d, ic_e, ic_e)
sce.add_record(mb.record("e1",0,4e-3))
# run solver
sol = mb.solver.create_instance("cpu-fdtd-5lvl-reg-cayley-qnoise", dev, sce)
print('Solver_' + sol.get_name() + '_started')
tic = time.time()
sol.run()
toc = time.time()
print('Solver_' + sol.get_name() + '_finished_in_' + str(toc - tic) + '_sec')
# write results
wri = mb.writer.create_instance("hdf5")
outfile = dev.get_name() + "_" + sce.get_name() + "." + wri.get_extension()
results = sol.get_results()
wri.write(outfile, sol.get_results(), dev, sce)
outfile_autosave = dev.get_name() + "_" + sce.get_name() + \
    "_autosave." + wri.get_extension()
sim_data = sol.get_sim_data()
wri.autosave(outfile_autosave, sim_data, dev, sce)
```

A.1.2 Single-Phonon Resonance Depopulation Structure

Listing A.2 Code snippet of the Python script for the THz DFG-QCL frequency comb setup in [205].

```
0, 0, -1.5024e-09 * mb.E0, 0, 0, -7.7231e-09 * mb.E0, 0, 0,
8.5270e-10 * mb.E0, 0, 0, 0, -9.6066e-09 * mb.E0, 0, 0, 0, 0, 0, 0, 0]
diag_dipoles = [ 0, 0, 0, 0, 0, 0, 0, 0]
u = mb.qm_operator(diag_dipoles, off_dipoles)
# relaxation superoperator
# scattering rate matrix R
\texttt{rates} \ = \ [ \ [ \ 0 \,, \ 6.3404 \, e + 12 \,, \ 8.2476 \, e + 11 \,, \ 9.8128 \, e + 11 \,, \ 3.0317 \, e + 11 \,, \ 1.0214 \, e + 12 \,, \ ]
2.2912e+12, 2.0735e+12, 2.5442e+12],
          1.7981e+12, 2.1488e+12, 3.2406e+12],
           [ \ 5.9908e+11 \, , \ 7.3614e+11 \, , \ 0 \, , \ 6.3595e+10 \, , \ 3.9869e+12 \, , \ 5.4609e+10 \, , \\
1.6018e+11, 1.0369e+11, 3.3741e+11 ],

[ 1.7823e+12, 1.7633e+12, 7.7225e+10, 0, 3.3881e+12, 7.5580e+11,

6.2112e+11, 9.0933e+11, 2.4700e+12 ],
          [8.5771e+11, 8.5734e+11, 4.3316e+12, 5.5535e+12, 0, 2.0688e+11,
            4.5472e+11, 1.2056e+12 ],
2.6087e+11,
          [ 3.5943e+11, 3.7340e+11, 1.0512e+11, 1.4468e+11, 2.5631e+10, 0, ]
2.4215e+12, 2.1533e+12, 8.8086e+11],
          [ 9.2614e+11, 6.5962e+11, 3.6980e+11, 1.4087e+11, 4.5674e+10,
3.0169e+12, 0, 2.8364e+12, 9.4669e+11],
          [1.0467e+12, 9.6775e+11, 2.2926e+11, 2.5742e+11, 8.5454e+10,
3.3164e+12, 3.6008e+12, 0, 1.6133e+12],
          [1.9550e+12, 2.2559e+12, 3.9631e+11, 1.0249e+12, 3.2138e+11,
2.0770e+12, 1.8605e+12, 2.5300e+12, 0 ] ]
# pure dephasing rates
0\,,\ 0\,,\ 1.4928\,e+13\,,\ 0\,,\ 0\,,\ 4.2425\,e+12\,,\ 0\,,\ 0\,,\ 1.7950\,e+13\,,\ 0\,,\ 0\,,\ 3.5116\,e+12\,,\ 0\,,
0, 0, 0, 0, 0, 0, 0]
relax_sop = mb.qm_lindblad_relaxation(rates, pure_deph)
# initial density matrix
rho_init = mb.qm_operator([ 0.1123, 0.1233, 0.1537, 0.1584, 0.2212, 0.0387,
0.0492, 0.0588, 0.0842])
n_D = 1.0747e + 22
# quantum-mechanical description
qm = mb.qm_description(n_D, H, u, relax_sop)
# DFB grating
# Period length in m
L_p = 1.15e-6
# Grating coupling in m^-1
kappa = 2000
# Effective refractive index
lambda_DFB = 6.7e-6 \# in m
n_{eff} = lambda_{DFB} / (2 * L_p)
# Length grating
L_g = 1.5e-3
# Amplitude variation refractive index grating.
delta_n = 2 * kappa * lambda_DFB / math.pi
# material 1
n_1 = n_eff - delta_n / 2
eps1 = pow(n_1, 2)
mat_DFB1 = mb.material("mat_DFB1", qm, eps1, 0.6, 60)
mb.material.add_to_library(mat_DFB1)
# material 2
n_2 = n_eff + delta_n / 2
eps2 = pow(n_2, 2)
```

```
mat_DFB2 = mb.material("mat_DFB2", qm, eps2, 0.6, 60)
mb.material.add_to_library(mat_DFB2)
# set up device with reflecting boundary conditions
dev = mb.device("lu2019")
## DFB setup
# Number of periods
num_period = math.ceil(L_g / L_p)
x1 = 0
x2 = L_p/2
for i in range(num_period):
    if i!=0:
        x1 = x1 + L_p/2
        x2 = x2 + L_p/2
    dev.add_region(mb.region("DFB_1", mat_DFB1, x1, x2))
    x1 = x1 + L_p/2
    x2 = x2 + L_p/2
    dev.add_region(mb.region("DFB_2", mat_DFB2, x1, x2))
# Length device
L = 4e-3
dev.add_region(mb.region("DFB_1", mat_DFB1, x2, L))
## FP setup
\# eps_eff = pow(n_eff, 2)
# mat_FP = mb.material("mat_FP", qm, eps_eff, 0.6, 60)
# mb.material.add_to_library(mat_FP)
# dev.add_region(mb.region("DFB 1", mat_FP, 0, L))
R = pow(n_eff - 1, 2) / pow(n_eff + 1, 2)
dev.set_bc_field(mb.bc_PMC(), mb.bc_field_reflectivity(R, 1, 400))
# scenario
ic_d = mb.ic_density_const(rho_init)
ic_e = mb.ic_field_random(0.0, 1.0, 1e-6)
ic_m = mb.ic_field_const(0.0)
sce = mb.scenario("Basic", 20000, 50e-9, ic_d, ic_e, ic_m)
sce.add_record(mb.record("e0", 0.0, 0.0))
sce.add_record(mb.record("e1", 0.0, L))
# run solver
sol = mb.solver.create_instance("cpu-fdtd-9lvl-reg-cayley", dev, sce)
sol.run()
# write results
wri = mb.writer.create_instance("hdf5")
outfile = dev.get_name() + "_" + sce.get_name() + "." + wri.get_extension()
results = sol.get_results()
wri.write(outfile, sol.get_results(), dev, sce)
```

A.1.3 Dual-Upper State Active Region

```
Listing A.3 Code snippet of the Python script for the THz DFG-QCL frequency comb setup in [206].
```

```
# import mbsolve libraries
    import mbsolve.lib as mb
    import mbsolve.solvercpu
    import mbsolve.writerhdf5
    import math
    import time
    # Hamiltonian
    energies = [ 0.1602 * mb.E0, 0.1511 * mb.E0, 0.1410 * mb.E0, 0.1274 * mb.E0,
    -0.0409 * mb.E0, -0.0617 * mb.E0, -0.0841 * mb.E0, -0.1070 * mb.E0,
     -0.1216 * mb.E0, -0.1376 * mb.E0, -0.1511 * mb.E0, -0.1602 * mb.E0 ]
    off_diagonales = [ 0.0033 * mb.E0, 0, 0.0044 * mb.E0, 0.0032 * mb.E0, 0,
    0, 0, 0, 0, 0, 0, 0, 0, 0, 0, 0, 0, 0]
    H = mb.qm_operator(energies, off_diagonales)
    # dipole moment operator
    off_dipoles = [0, 0, 0, 0, -5.0471e-09 * mb.E0, 0, 0, -1.1892e-09 * mb.E0,
    0, -1.1712e-09 * mb.E0, 0, 1.1508e-09 * mb.E0, 0, 1.4275e-09 * mb.E0,
    diag\_dipoles = [ 0, 0, 0, 0, 0, 0, 0, 0, 0, 0, 0]
    u = mb.qm_operator(diag_dipoles, off_dipoles)
    # scattering rate matrix R
    rates = [ \ [ \ 0 \ , \ 2.3650e + 10 \ , \ 3.3405e + 12 \ , \ 1.1677e + 10 \ , \ 1.0484e + 11 \ , \ 1.5182e + 11 \ , \ 1.0484e + 11 \ , \ 1.0484
    4.3028e+11, 8.0841e+11, 9.8779e+11, 2.0537e+12, 1.1839e+12, 3.1250e+12],
                           [ 2.8765e+10, 0, 4.2016e+10, 5.1157e+12, 3.7948e+10, 6.9304e+10,
    4.8488e+10, 7.3111e+10, 7.3028e+10, 5.9399e+10, 7.1742e+10, 1.4924e+11],
                           [ 6.8605e+12, 5.8135e+10, 0, 2.7775e+10, 2.6069e+10, 4.3583e+10, 
    7.8223e+10, 2.0511e+11, 3.1951e+11, 9.8743e+11, 8.2653e+11, 2.6700e+12],
                           9.1430\,e+10\,,\ 1.3380\,e+11\,,\ 1.2148\,e+11\,,\ 8.9938\,e+10\,,\ 8.2512\,e+10\,,\ 7.7550\,e+10\,\,]\,,
                           8.8725e+11, \ 4.9303e+11, \ 3.9650e+11, \ 2.8588e+11, \ 2.5934e+11, \ 1.7008e+11 \ ],
                           [ 3.4251e+10, 1.6395e+11, 7.0068e+09, 1.6352e+11, 1.8325e+12, 0,
    1.3278e + 12, \ 6.2432e + 11, \ 4.6777e + 11, \ 3.1556e + 11, \ 1.9244e + 11, \ 1.5394e + 11 \ ],
                            [ \ 1.0269\,e+11 \,, \ 1.0759\,e+11 \,, \ 1.3373\,e+10 \,, \ 1.1062\,e+11 \,, \ 1.2677\,e+12 \,, \\
    1.8340e+12, 0, 1.4766e+12, 8.3224e+11, 5.0183e+11, 3.9581e+11, 3.3313e+11],
                          9.8705\,e+11\,,\ 1.9423\,e+12\,,\ 0\,,\ 2.2626\,e+12\,,\ 8.9217\,e+11\,,\ 5.0611\,e+11\,,\ 4.1263\,e+11\ ]\,,
    [ 2.8656e+11, 1.5280e+11, 5.4202e+10, 1.3420e+11, 6.2519e+11, 7.6856e+11, 1.2494e+12, 2.6601e+12, 0, 1.5068e+12, 8.7770e+11, 4.8869e+11 ], [ 7.1796e+11, 9.4419e+10, 1.8298e+11, 6.4174e+10, 5.6404e+11, 6.1309e+11, 9.0199e+11, 1.5309e+12, 2.1689e+12, 0, 1.6595e+12, 1.4171e+12 ], [ 4.9164e+11, 1.2731e+11, 1.7519e+11, 7.3334e+10, 6.1918e+11,
    4.5092e+11, 8.3076e+11, 9.8865e+11, 1.5616e+12, 2.0487e+12, 0, 1.9082e+12],
                           [ 1.7408e+12, 1.8384e+11, 7.5227e+11, 6.9276e+10, 5.1718e+11,
    4.4865e+11, 8.8865e+11, 1.0070e+12, 1.0889e+12, 2.4328e+12, 2.6033e+12, 0 ] ]
# pure dephasing rates
pure\_deph = [ 1.1394e+13, 0, 1.8234e+13, 1.7919e+13, 9.2799e+11, 1.3005e+13, 9.2799e+11, 9.2799e+11,
0, 1.3491e+13, 0, 1.5143e+13, 0, 8.9466e+12, 0, 1.1436e+13, 8.7776e+11, 0, 0,
0, 0, 0]
relax_sop = mb.qm_lindblad_relaxation(rates, pure_deph)
```

```
# initial density matrix
rho_init = mb.qm_operator([ 0.1149, 0.0954, 0.1941, 0.2032, 0.0306, 0.0361,
0.0388, 0.0430, 0.0466, 0.0543, 0.0655, 0.0775])
# quantum-mechanical description
qm = mb.qm_description(1.6915e+22, H, u, relax_sop)
# DFB grating
# Period length in m
L_p = 1.04e-6
# Grating coupling in m^-1
kappa = 700
lambda_DFB = 6.3e-6 \# in m
# Effective refractive index
n_eff = lambda_DFB / (2 * L_p)
# Length device
L = 3e-3
# Amplitude variation refractive index grating.
delta_n = 2 * kappa * lambda_DFB / math.pi
# material 1
n_1 = n_eff - delta_n / 2
eps1 = pow(n_1, 2)
mat_DFB1 = mb.material("mat_DFB1", qm, eps1, 0.6, 320)
mb.material.add_to_library(mat_DFB1)
# material 2
n_2 = n_eff + delta_n / 2
eps2 = pow(n_2, 2)
mat_DFB2 = mb.material("mat_DFB2", qm, eps2, 0.6, 320)
mb.material.add_to_library(mat_DFB2)
# device
dev = mb.device("consolino2021")
# number of periods
num_period = math.ceil(L / L_p)
x1 = 0
x2 = L_p/2
for i in range(num_period):
    dev.add_region(mb.region("DFB_1", mat_DFB1, x1, x2))
    x1 = x1 + L_p/2
    x2 = x2 + L_p/2
    dev.add_region(mb.region("DFB_2", mat_DFB2, x1, x2))
    x1 = x1 + L_p/2
    x2 = x2 + L_p/2
R = pow(n_eff - 1, 2) / pow(n_eff + 1, 2)
dev.set_bc_field(mb.bc_PMC(), mb.bc_field_reflectivity(R, 1, 400))
# Scenario setup
ic_d = mb.ic_density_const(rho_init)
ic_e = mb.ic_field_random(0.0, 1.0, 1e-6)
ic_m = mb.ic_field_const(0.0)
sce = mb.scenario("Basic", 15000, 100e-9, ic_d, ic_e, ic_m)
sce.add_record(mb.record("e0", 0.0, 0))
sce.add_record(mb.record("e1", 0.0, L))
# run solver
sol = mb.solver.create_instance("cpu-fdtd-12lvl-reg-cayley", dev, sce)
sol.run()
# write results
```

```
wri = mb.writer.create_instance("hdf5")
outfile = dev.get_name() + "_" + sce.get_name() +"." + wri.get_extension()
results = sol.get_results()
wri.write(outfile, sol.get_results(), dev, sce)
```

Publications List

Journal Articles

- J. Popp, J. Stowasser, M. A. Schreiber, L. Seitner, F. Hitzelhammer, M. Haider, G. Slavcheva, and C. Jirauschek, "Modeling of fluctuations in dynamical optoelectronic device simulations within a Maxwell-density matrix Langevin approach", *APL Quantum*, vol. 1, no. 1, p. 016 109, 2024. DOI: 10.1063/5.0183 828.
- C. Jirauschek, J. Popp, M. Haider, M. Franckié, and J. Faist, "Ensemble Monte Carlo modeling of quantum cascade detectors", *J. Appl. Phys.*, vol. 130, no. 20, p. 203 103, 2021. DOI: 10.1063/5.0065540.
- W. Kaiser, J. Popp, M. Rinderle, T. Albes, and A. Gagliardi, "Generalized kinetic Monte Carlo framework for organic electronics", *Algorithms*, vol. 11, no. 4, p. 37, 2018. DOI: 10.3390/a11040037.
- J. Popp, W. Kaiser, and A. Gagliardi, "Impact of phosphorescent sensitizers and morphology on the photovoltaic performance in organic solar cells", *Adv. Theory Sim.*, vol. 2, no. 1, p. 1 800 114, 2019. DOI: 10.1002/adts.201800114.
- J. Popp, M. Haider, M. Franckié, J. Faist, and C. Jirauschek, "Bayesian optimization of quantum cascade detectors", *Opt. Quant. Electron.*, vol. 53, no. 5, p. 287, 2021. DOI: 10.1007/s11082-021-02885-0.
- J. Popp, L. Seitner, M. A. Schreiber, M. Haider, L. Consolino, A. Sorgi, F. Cappelli, P. De Natale, K. Fujita, and C. Jirauschek, "Self-consistent simulations of intracavity terahertz comb difference frequency generation by mid-infrared quantum cascade lasers", *J. Appl. Phys.*, vol. 133, no. 23, p. 233 103, 2023. DOI: 10.1063/5.0151036.
- J. Popp, L. Seitner, F. Naunheimer, G. Janowski, M. Haider, and C. Jirauschek, "Multi-domain modeling of free-running harmonic frequency comb formation in terahertz quantum cascade lasers", *IEEE Photonics J.*, vol. 16, no. 2, p. 0600711, 2024. DOI: 10.1109/JPHOT.2024.3370189.
- L. Seitner, J. Popp, I. Heckelmann, R.-E. Vass, B. Meng, M. Haider, J. Faist, and C. Jirauschek, "Backscattering-induced dissipative solitons in ring quantum cascade lasers", *Phys. Rev. Lett.*, vol. 132, p. 043 805, 2024. DOI: 10.1103/PhysRevLett.132.043805.
- L. Seitner, J. Popp, M. Haider, S. S. Dhillon, M. S. Vitiello, and C. Jirauschek, "Theoretical model of passive mode-locking in terahertz quantum cascade lasers with distributed saturable absorbers", *Nanophotonics*, vol. 13, no. 10, pp. 1823–1834, 2024. DOI: doi:10.1515/nanoph-2023-0657.

Conference Proceedings

- J. Popp, M. Haider, M. Franckié, J. Faist, and C. Jirauschek, "Monte Carlo modeling of a short wavelength strain compensated quantum cascade detector", in 2021 Conference on Lasers and Electro-Optics Europe & European Quantum Electronics Conference (CLEO/Europe-EQEC), 2021, pp. 1–1. DOI: 10.1109 /CLEO/Europe-EQEC52157.2021.9542111.
- J. Popp, W. Kaiser, and A. Gagliardi, "Simulation of enhanced exciton diffusion in organic solar cells with phosphorescent sensitizers", in 2018 IEEE 18th International Conference on Nanotechnology (IEEE-NANO), IEEE, 2018, pp. 420–425. DOI: 10.1109/NANO.2018.8626281.

- J. Popp, M. Haider, M. Franckié, J. Faist, and C. Jirauschek, "Monte Carlo modeling of terahertz quantum cascade detectors", in 2020 XXXIIIrd General Assembly and Scientific Symposium of the International Union of Radio Science, 2020, pp. 1–3. DOI: 10.23919/URSIGASS49373.2020.9232167.
- J. Popp, M. Haider, M. Franckié, J. Faist, and C. Jirauschek, "Numerical optimization of quantum cascade detector heterostructures", in 2020 International Conference on Numerical Simulation of Optoelectronic Devices (NUSOD), IEEE, 2020, pp. 1–2. DOI: 10.1109/NUSOD49422.2020.9217784.
- J. Popp, L. Seitner, M. Schreiber, M. Haider, L. Consolino, F. Cappelli, P. De Natale, K. Fujita, and C. Jirauschek, "Modeling of THz comb emission in difference-frequency quantum cascade lasers", in 2022 International Conference on Numerical Simulation of Optoelectronic Devices (NUSOD), 2022, pp. 63–64. DOI: 10.1109/NUSOD54938.2022.9894839.
- J. Popp, L. Seitner, M. Haider, and C. Jirauschek, "Reducing the reflection error of PML absorbing boundary conditions within a generalized Maxwell-Bloch framework", in 2022 3rd URSI Atlantic and Asia Pacific Radio Science Meeting (AT-AP-RASC), 2022, pp. 1–4. DOI: 10.23919/AT-AP-RASC54737 .2022.9814330.
- J. Popp, L. Seitner, F. Naunheimer, M. Haider, and C. Jirauschek, "Influence of eigenstate basis sets on self-starting harmonic comb simulations in THz QCLs", in *International Conference on Numerical Simulation of Optoelectronic Devices (NUSOD)*, (**TOP 10%**), 2023, pp. 11–12. DOI: 10.1109/NUSOD5 9562.2023.10273518.
- M. A. Schreiber, J. Popp, L. Seitner, M. Haider, and C. Jirauschek, "Implementation of partially reflecting boundary conditions in the generalized Maxwell-Bloch equations", in 2022 International Conference on Numerical Simulation of Optoelectronic Devices (NUSOD), 2022, pp. 99–100. DOI: 10.1109/NUSOD54 938.2022.9894802.
- L. Seitner, J. Popp, M. Riesch, M. Haider, and C. Jirauschek, "Group velocity dispersion in terahertz frequency combs within a generalized Maxwell-Bloch framework", *J. Phys.: Conf. Ser.*, vol. 2090, no. 1, p. 012 082, 2021. DOI: 10.1088/1742-6596/2090/1/012082.
- L. Seitner, J. Popp, F. Naunheimer, G. Janowski, M. Haider, and C. Jirauschek, "Modeling the influence of charge carrier diffusion on harmonic comb formation in quantum cascade lasers", in *2023 International Conference on Electromagnetics in Advanced Applications (ICEAA)*, 2023, pp. 590–592. DOI: 10.1109 /ICEAA57318.2023.10297844.
- L. Seitner, J. Popp, M. A. Schreiber, M. Haider, and C. Jirauschek, "Theoretical investigation of harmonic frequency comb formation dynamics in defect-engineered THz quantum cascade lasers", in *Terahertz Photonics III*, M. Jarrahi, S. Preu, and D. Turchinovich, Eds., International Society for Optics and Photonics, vol. 12994, SPIE, 2024, p. 1 299 406. DOI: 10.1117/12.3017516.
- L. Seitner, J. Popp, I. Heckelmann, R.-E. Vass, B. Meng, M. Haider, J. Faist, and C. Jirauschek, "Modeling optical solitons in ring quantum cascade lasers in the presence of backscattering", in *Novel In-Plane Semiconductor Lasers XXIII*, A. A. Belyanin and P. M. Smowton, Eds., International Society for Optics and Photonics, vol. 12905, SPIE, 2024, p. 1 290 508. DOI: 10.1117/12.3003654.

Conference Talks and Poster

- J. Popp, L. Seitner, M. A. Schreiber, M. Haider, and C. Jirauschek, "Modeling of self-starting harmonic mode-locking in THz quantum cascade lasers", in *Infrared Terahertz Quantum Workshop (ITQW 2023)*, Jun. 2023.
- M. Franckié, J. Popp, M. Haider, C. Jirauschek, and J. Faist, "Numerical optimization of mid-IR QCL frequency combs", in *Infrared Terahertz Quantum Workshop (ITQW 2019)*, Sep. 2019.

- M. Haider, J. Stowasser, J. Popp, M. Schreiber, L. Seitner, F. Hitzelhammer, U. Hohenester, G. Slavcheva, and C. Jirauschek, "Decay-induced noise modeling of quantum cascade laser frequency combs within a Maxwell-density matrix Langevin approach", in *International Quantum Cascade Lasers School & Workshop (IQCLSW 2024)*, Aug. 2024.
- C. Jirauschek and J. Popp, "Modeling of phase-locked quantum cascade lasers", in *Perspectives on Quantum Simulation and Technologies The Qombs Project Final Workshop*, Jun. 2022.
- J. Popp, L. Seitner, M. Schreiber, M. Haider, and C. Jirauschek, "Modeling of THz difference-frequency comb generation in mid-infrared quantum cascade lasers", in *International Quantum Cascade Lasers School & Workshop (IQCLSW 2022)*, Aug. 2022.
- L. Seitner, J. Popp, M. Haider, M. Franckié, J. Faist, and C. Jirauschek, "Towards self-consistent simulation of mid-infrared kerr solitons in ring-cavity quantum cascade lasers", in *International Quantum Cascade Lasers School & Workshop (IQCLSW 2022)*, Aug. 2022.

Bibliography

- [1] R. Rediker, "Semiconductor diode luminescence and lasers. a perspective", *IEEE J. Sel. Top. Quantum Electron.*, vol. 6, no. 6, pp. 1355–1362, 2000. DOI: 10.1109/2944.902189.
- [2] A. R. Adams, C. T. Elliott, A. Krier, B. N. Murdin, and M. Tacke, "Lead–salt lasers", *Philos. Trans. Royal Soc. A*, vol. 359, no. 1780, pp. 547–566, 2001. DOI: 10.1098/rsta.2000.0742.
- [3] R. F. Curl, F. Capasso, C. Gmachl, A. A. Kosterev, B. McManus, R. Lewicki, M. Pusharsky, G. Wysocki, and F. K. Tittel, "Quantum cascade lasers in chemical physics", *Chem. Phys. Lett.*, vol. 487, no. 1, pp. 1–18, 2010. DOI: 10.1016/j.cplett.2009.12.073.
- [4] F. Capasso, "High-performance midinfrared quantum cascade lasers", *Opt. Eng.*, vol. 49, no. 11, p. 111 102, 2010. DOI: 10.1117/1.3505844.
- [5] J. Faist, F. Capasso, D. L. Sivco, C. Sirtori, A. L. Hutchinson, and A. Y. Cho, "Quantum cascade laser", Science, vol. 264, no. 5158, pp. 553–556, 1994. DOI: 10.1126/science.264.5158.553.
- [6] B. S. Williams, "Terahertz quantum-cascade lasers", *Nature Photon.*, vol. 1, no. 9, pp. 517–525, 2007. DOI: 10.1038/nphoton.2007.166.
- [7] G. Scalari, C. Walther, M. Fischer, R. Terazzi, H. Beere, D. Ritchie, and J. Faist, "THz and sub-THz quantum cascade lasers", *Laser Photonics Rev.*, vol. 3, no. 1-2, pp. 45–66, 2009. DOI: 10.1002/lpor.200 810030.
- [8] I. Vurgaftman, R. Weih, M. Kamp, J. R. Meyer, C. L. Canedy, C. S. Kim, M. Kim, W. W. Bewley, C. D. Merritt, J. Abell, and S. Höfling, "Interband cascade lasers", *J. Phys. D*, vol. 48, no. 12, p. 123 001, 2015. DOI: 10.1088/0022-3727/48/12/123001.
- [9] J. R. Meyer, W. W. Bewley, C. L. Canedy, C. S. Kim, M. Kim, C. D. Merritt, and I. Vurgaftman, "The interband cascade laser", *Photonics*, vol. 7, no. 3, p. 75, 2020. DOI: 10.3390/photonics7030075.
- [10] B. Schwarz, J. Hillbrand, M. Beiser, A. M. Andrews, G. Strasser, H. Detz, A. Schade, R. Weih, and S. Höfling, "Monolithic frequency comb platform based on interband cascade lasers and detectors", *Optica*, vol. 6, no. 7, pp. 890–895, 2019. DOI: 10.1364/OPTICA.6.000890.
- [11] R. Kazarinov and R. Suris, "Possibility of the amplification of electromagnetic waves in a semiconductor with a superlattice", *Sov. Phys. Semicond.*, vol. 5, p. 707, 1971.
- [12] J. Faist, G. Villares, G. Scalari, M. Rösch, C. Bonzon, A. Hugi, and M. Beck, "Quantum cascade laser frequency combs", *Nanophotonics*, vol. 5, no. 2, pp. 272–291, 2016. DOI: doi:10.1515/nanoph-2016-0 015.
- [13] C. Silvestri, X. Qi, T. Taimre, K. Bertling, and A. D. Rakić, "Frequency combs in quantum cascade lasers: An overview of modeling and experiments", *APL Photonics*, vol. 8, no. 2, p. 020 902, 2023. DOI: 10.1063/5.0134539.
- [14] D. Burghoff, T.-Y. Kao, N. Han, C. W. I. Chan, X. Cai, Y. Yang, D. J. Hayton, J.-R. Gao, J. L. Reno, and Q. Hu, "Terahertz laser frequency combs", *Nature Photon.*, vol. 8, no. 6, pp. 462–467, 2014. DOI: 10.1038/nphoton.2014.85.
- [15] A. Hugi, G. Villares, S. Blaser, H. C. Liu, and J. Faist, "Mid-infrared frequency comb based on a quantum cascade laser", *Nature*, vol. 492, no. 7428, pp. 229–233, 2012. DOI: 10.1038/nature11620.
- [16] T. Udem, R. Holzwarth, and T. W. Hänsch, "Optical frequency metrology", *Nature*, vol. 416, no. 6877, pp. 233–237, 2002. DOI: 10.1038/416233a.

- [17] A. Daničić, J. Radovanović, V. Milanović, D. Indjin, and Z. Ikonić, "Optimization and magnetic-field tunability of quantum cascade laser for applications in trace gas detection and monitoring", *J. Phys. D*, vol. 43, no. 4, p. 045 101, 2010. DOI: 10.1088/0022-3727/43/4/045101.
- [18] A. Bismuto, R. Terazzi, B. Hinkov, M. Beck, and J. Faist, "Fully automatized quantum cascade laser design by genetic optimization", *Appl. Phys. Lett.*, vol. 101, no. 2, p. 021 103, 2012. DOI: 10.1063/1.47 34389.
- [19] A. Mátyás, R. Chashmahcharagh, I. Kovacs, P. Lugli, K. Vijayraghavan, M. A. Belkin, and C. Jirauschek, "Improved terahertz quantum cascade laser with variable height barriers", *J.Appl. Phys.*, vol. 111, no. 10, p. 103 106, 2012. DOI: 10.1063/1.4719071.
- [20] J. M. Wolf, "Quantum cascade laser: From 3 to 26 μ m", Ph.D. dissertation, ETH Zurich, 2017. DOI: 10.3929/ethz-b-000213855.
- [21] L. Bosco, M. Franckié, G. Scalari, M. Beck, A. Wacker, and J. Faist, "Thermoelectrically cooled THz quantum cascade laser operating up to 210 K", *Appl. Phys. Lett.*, vol. 115, no. 1, p. 010 601, 2019. DOI: 10.1063/1.5110305.
- [22] M. Franckié and J. Faist, "Bayesian optimization of terahertz quantum cascade lasers", *Phys. Rev. Appl.*, vol. 13, p. 034 025, 2020. DOI: 10.1103/PhysRevApplied.13.034025.
- [23] J. Popp, M. Haider, M. Franckié, J. Faist, and C. Jirauschek, "Numerical optimization of quantum cascade detector heterostructures", in 2020 International Conference on Numerical Simulation of Optoelectronic Devices (NUSOD), IEEE, 2020, pp. 1–2. DOI: 10.1109/NUSOD49422.2020.9217784.
- [24] J. Popp, M. Haider, M. Franckié, J. Faist, and C. Jirauschek, "Bayesian optimization of quantum cascade detectors", *Opt. Quant. Electron.*, vol. 53, no. 5, p. 287, 2021. DOI: 10.1007/s11082-021-02885-0.
- [25] D. Hofstetter, M. Beck, and J. Faist, "Quantum-cascade-laser structures as photodetectors", *Appl. Phys. Lett.*, vol. 81, no. 15, pp. 2683–2685, 2002. DOI: 10.1063/1.1512954.
- [26] L. Gendron, M. Carras, A. Huynh, V. Ortiz, C. Koeniguer, and V. Berger, "Quantum cascade photodetector", *Appl. Phys. Lett.*, vol. 85, no. 14, pp. 2824–2826, 2004. DOI: 10.1063/1.1781731.
- [27] A. Harrer, "Quantum cascade intersubband devices for mid-infrared sensing", Ph.D. dissertation, Technische Universität Wien, 2017. DOI: 10.34726/hss.2017.45040.
- [28] B. Schwarz, "Monolithic integration of mid-infrared photonics", Ph.D. dissertation, Technische Universität Wien, 2015. DOI: 10.34726/hss.2015.34238.
- [29] C. Jirauschek and T. Kubis, "Modeling techniques for quantum cascade lasers", *Appl. Phys. Rev.*, vol. 1, no. 1, p. 011 307, 2014. DOI: 10.1063/1.4863665.
- [30] P. Borowik, J.-L. Thobel, and L. Adamowicz, "Monte Carlo modeling applied to studies of quantum cascade lasers", *Opt. Quantum Electron.*, vol. 49, no. 3, p. 96, 2017. DOI: 10.1007/s11082-017-0931-9.
- [31] R. C. Iotti, E. Ciancio, and F. Rossi, "Quantum transport theory for semiconductor nanostructures: A density-matrix formulation", *Phys. Rev. B*, vol. 72, p. 125 347, 2005. DOI: 10.1103/PhysRevB.72.1253 47.
- [32] R. Terazzi and J. Faist, "A density matrix model of transport and radiation in quantum cascade lasers", *New J. Phys.*, vol. 12, no. 3, p. 033 045, 2010. DOI: 10.1088/1367-2630/12/3/033045.
- [33] S.-C. Lee and A. Wacker, "Nonequilibrium Green's function theory for transport and gain properties of quantum cascade structures", *Phys. Rev. B*, vol. 66, p. 245 314, 2002. DOI: 10.1103/PhysRevB.66.2453 14.
- [34] A. Wacker, M. Lindskog, and D. O. Winge, "Nonequilibrium Green's function model for simulation of quantum cascade laser devices under operating conditions", *IEEE J. Sel. Top. Quantum Electron.*, vol. 19, no. 5, p. 1 200 611, 2013. DOI: 10.1109/JSTQE.2013.2239613.
- [35] C. Jirauschek, "Density matrix Monte Carlo modeling of quantum cascade lasers", *J. Appl. Phys.*, vol. 122, p. 133 105, 2017. DOI: 10.1063/1.5005618.

- [36] H. Callebaut and Q. Hu, "Importance of coherence for electron transport in terahertz quantum cascade lasers", *J. Appl. Phys.*, vol. 98, no. 10, p. 104 505, 2005. DOI: 10.1063/1.2136420.
- [37] O. Baumgartner, Z. Stanojevic, K. Schnass, M. Karner, and H. Kosina, "VSP–A quantum-electronic simulation framework", *J. Comput. Electron.*, vol. 12, no. 4, pp. 701–721, 2013. DOI: 10.1007/s10825-013-0535-y.
- [38] A. Harrer, B. Schwarz, S. Schuler, P. Reininger, A. Wirthmüller, H. Detz, D. MacFarland, T. Zederbauer, A. Andrews, M. Rothermund, H. Oppermann, W. Schrenk, and G. Strasser, "4.3 μm quantum cascade detector in pixel configuration", *Opt. Express*, vol. 24, no. 15, pp. 17 041–17 049, 2016. DOI: 10.1364 /OE.24.017041.
- [39] C. Koeniguer, G. Dubois, A. Gomez, and V. Berger, "Electronic transport in quantum cascade structures at equilibrium", *Phys. Rev. B*, vol. 74, p. 235 325, 2006. DOI: 10.1103/PhysRevB.74.235325.
- [40] P. Reininger, B. Schwarz, H. Detz, D. MacFarland, T. Zederbauer, A. M. Andrews, W. Schrenk, O. Baumgartner, H. Kosina, and G. Strasser, "Diagonal-transition quantum cascade detector", *Appl. Phys. Lett.*, vol. 105, no. 9, p. 091 108, 2014. DOI: 10.1063/1.4894767.
- [41] J. Popp, M. Haider, M. Franckié, J. Faist, and C. Jirauschek, "Monte Carlo modeling of terahertz quantum cascade detectors", in 2020 XXXIIIrd General Assembly and Scientific Symposium of the International Union of Radio Science, 2020, pp. 1–3. DOI: 10.23919/URSIGASS49373.2020.9232167.
- [42] C. Jirauschek, J. Popp, M. Haider, M. Franckié, and J. Faist, "Ensemble Monte Carlo modeling of quantum cascade detectors", *J. Appl. Phys.*, vol. 130, no. 20, p. 203 103, 2021. DOI: 10.1063/5.0065540.
- [43] L. Allen and J. H. Eberly, *Optical Resonance and Two-Level Atoms*. New York: Courier Corporation, 1987, vol. 28.
- [44] G. Slavcheva, J. Arnold, and R. Ziolkowski, "FDTD simulation of the nonlinear gain dynamics in active optical waveguides and semiconductor microcavities", *IEEE J. Sel. Top. Quantum Electron.*, vol. 10, no. 5, pp. 1052–1062, 2004. DOI: 10.1109/JSTQE.2004.836023.
- [45] A. Gordon, C. Y. Wang, L. Diehl, F. X. Kärtner, A. Belyanin, D. Bour, S. Corzine, G. Höfler, H. C. Liu, H. Schneider, T. Maier, M. Troccoli, J. Faist, and F. Capasso, "Multimode regimes in quantum cascade lasers: From coherent instabilities to spatial hole burning", *Phys. Rev. A*, vol. 77, p. 053 804, 2008. DOI: 10.1103/PhysRevA.77.053804.
- [46] R. W. Boyd, Nonlinear Optics, 4th ed. Academic Press, 2020.
- [47] C. Jirauschek, M. Riesch, and P. Tzenov, "Optoelectronic device simulations based on macroscopic Maxwell-Bloch equations", *Adv. Theory Simul.*, vol. 2, no. 8, p. 1900018, 2019. DOI: 10.1002/adts.20 1900018.
- [48] N. Opačak, "The origin of frequency combs in free-running quantum cascade lasers", Ph.D. dissertation, Technische Universität Wien, 2022. DOI: 10.34726/hss.2022.103442.
- [49] C. Ning, R. Indik, and J. Moloney, "Effective Bloch equations for semiconductor lasers and amplifiers", *IEEE J. Quantum Electron.*, vol. 33, no. 9, pp. 1543–1550, 1997. DOI: 10.1109/3.622635.
- [50] L. L. Columbo, S. Barbieri, C. Sirtori, and M. Brambilla, "Dynamics of a broad-band quantum cascade laser: From chaos to coherent dynamics and mode-locking", *Opt. Express*, vol. 26, no. 3, pp. 2829–2847, 2018. DOI: 10.1364/OE.26.002829.
- [51] C. Silvestri, L. L. Columbo, M. Brambilla, and M. Gioannini, "Coherent multi-mode dynamics in a quantum cascade laser: Amplitude- and frequency-modulated optical frequency combs", *Opt. Express*, vol. 28, no. 16, pp. 23 846–23 861, 2020. DOI: 10.1364/OE.396481.
- [52] C. Silvestri, X. Qi, T. Taimre, and A. D. Rakić, "Multimode dynamics of terahertz quantum cascade lasers: Spontaneous and actively induced generation of dense and harmonic coherent regimes", *Phys. Rev. A*, vol. 106, p. 053 526, 2022. DOI: 10.1103/PhysRevA.106.053526.
- [53] C. Silvestri, X. Qi, T. Taimre, and A. D. Rakić, "Harmonic active mode locking in terahertz quantum cascade lasers", *Phys. Rev. A*, vol. 108, p. 013 501, 2023. DOI: 10.1103/PhysRevA.108.013501.

- [54] C. Jirauschek, "Theory of hybrid microwave–photonic quantum devices", *Laser Photonics Rev.*, vol. 17, no. 12, p. 2 300 461, 2023. DOI: 10.1002/lpor.202300461.
- [55] P. Tzenov, D. Burghoff, Q. Hu, and C. Jirauschek, "Time domain modeling of terahertz quantum cascade lasers for frequency comb generation", *Opt. Express*, vol. 24, no. 20, pp. 23232–23247, 2016. DOI: 10.1364/OE.24.023232.
- [56] P. Tzenov, D. Burghoff, Q. Hu, and C. Jirauschek, "Analysis of operating regimes of terahertz quantum cascade laser frequency combs", *IEEE Trans. Terahertz Sci. Technol.*, vol. 7, no. 4, pp. 351–359, 2017. DOI: 10.1109/TTHZ.2017.2693822.
- [57] G. Slavcheva, M. Koleva, and A. Rastelli, "Ultrafast pulse phase shifts in a charged-quantum-dot-micropillar system", *Phys. Rev. B*, vol. 99, p. 115 433, 2019. DOI: 10.1103/PhysRevB.99.115433.
- [58] [SW] Computational Photonics Group of the Technical University of Munich, *mbsolve: An open-source solver tool for the full wave 1D Maxwell-Bloch equations* 2023, vcs: https://github.com/cph-tum/mbsolve.
- [59] J. Popp, J. Stowasser, M. A. Schreiber, L. Seitner, F. Hitzelhammer, M. Haider, G. Slavcheva, and C. Jirauschek, "Modeling of fluctuations in dynamical optoelectronic device simulations within a Maxwell-density matrix Langevin approach", APL Quantum, vol. 1, no. 1, p. 016 109, 2024. DOI: 10.1063/5.018 3828.
- [60] C. R. Menyuk and M. A. Talukder, "Self-induced transparency modelocking of quantum cascade lasers", *Phys. Rev. Lett.*, vol. 102, p. 023 903, 2009. DOI: 10.1103/PhysRevLett.102.023903.
- [61] A. K. Wójcik, P. Malara, R. Blanchard, T. S. Mansuripur, F. Capasso, and A. Belyanin, "Generation of picosecond pulses and frequency combs in actively mode locked external ring cavity quantum cascade lasers", *Appl. Phys. Lett.*, vol. 103, no. 23, p. 231 102, 2013. DOI: 10.1063/1.4838275.
- [62] M. A. Talukder and C. R. Menyuk, "Quantum coherent saturable absorption for mid-infrared ultra-short pulses", *Opt. Express*, vol. 22, no. 13, pp. 15608–15617, 2014. DOI: 10.1364/OE.22.015608.
- [63] Y. Wang and A. Belyanin, "Active mode-locking of mid-infrared quantum cascade lasers with short gain recovery time", *Opt. Express*, vol. 23, no. 4, pp. 4173–4185, 2015. DOI: 10.1364/OE.23.004173.
- [64] P. Tzenov, I. Babushkin, R. Arkhipov, M. Arkhipov, N. Rosanov, U. Morgner, and C. Jirauschek, "Passive and hybrid mode locking in multi-section terahertz quantum cascade lasers", *New J. Phys.*, vol. 20, no. 5, p. 053 055, 2018. DOI: 10.1088/1367-2630/aac12a.
- [65] F. Wang, V. Pistore, M. Riesch, H. Nong, P.-B. Vigneron, R. Colombelli, O. Parillaud, J. Mangeney, J. Tignon, C. Jirauschek, *et al.*, "Ultrafast response of harmonic modelocked THz lasers", *Light Sci. Appl.*, vol. 9, p. 51, 2020. DOI: 10.1038/s41377-020-0288-x.
- [66] E. Riccardi, M. A. J. Guerrero, V. Pistore, L. Seitner, C. Jirauschek, L. Li, A. G. Davies, E. H. Linfield, and M. S. Vitiello, "Sculpting harmonic comb states in terahertz quantum cascade lasers by controlled engineering", *Optica*, vol. 11, no. 3, pp. 412–419, 2024. DOI: 10.1364/OPTICA.509929.
- [67] L. Seitner, J. Popp, M. Haider, S. S. Dhillon, M. S. Vitiello, and C. Jirauschek, "Theoretical model of passive mode-locking in terahertz quantum cascade lasers with distributed saturable absorbers", *Nanophotonics*, vol. 13, no. 10, pp. 1823–1834, 2024. DOI: doi:10.1515/nanoph-2023-0657.
- [68] C. Y. Wang, L. Diehl, A. Gordon, C. Jirauschek, F. X. Kärtner, A. Belyanin, D. Bour, S. Corzine, G. Höfler, M. Troccoli, J. Faist, and F. Capasso, "Coherent instabilities in a semiconductor laser with fast gain recovery", *Phys. Rev. A*, vol. 75, p. 031 802, 2007. DOI: 10.1103/PhysRevA.75.031802.
- [69] N. N. Vuković, J. Radovanović, V. Milanović, and D. L. Boiko, "Low-threshold RNGH instabilities in quantum cascade lasers", *IEEE J. Sel. Top. Quantum Electron.*, vol. 23, no. 6, p. 1 200 616, 2017. DOI: 10.1109/JSTQE.2017.2699139.
- [70] N. Opačak and B. Schwarz, "Theory of frequency-modulated combs in lasers with spatial hole burning, dispersion, and Kerr nonlinearity", *Phys. Rev. Lett.*, vol. 123, p. 243 902, 2019. DOI: 10.1103/PhysRev Lett.123.243902.

- [71] C. Jirauschek and P. Tzenov, "Self-consistent simulations of quantum cascade laser structures for frequency comb generation", *Opt. Quant. Electron.*, vol. 49, no. 12, p. 414, 2017. DOI: 10.1007/s11082 -017-1253-7.
- [72] M. Riesch and C. Jirauschek, "mbsolve: An open-source solver tool for the Maxwell-Bloch equations", *Comput. Phys. Commun.*, vol. 268, p. 108 097, 2021. DOI: 10.1016/j.cpc.2021.108097.
- [73] A. Forrer, Y. Wang, M. Beck, A. Belyanin, J. Faist, and G. Scalari, "Self-starting harmonic comb emission in THz quantum cascade lasers", *Appl. Phys. Lett.*, vol. 118, no. 13, p. 131112, 2021. DOI: 10.1063/5.0041339.
- [74] M. Piccardo, B. Schwarz, D. Kazakov, M. Beiser, N. Opačak, Y. Wang, S. Jha, J. Hillbrand, M. Tamagnone, W. T. Chen, *et al.*, "Frequency combs induced by phase turbulence", *Nature*, vol. 582, no. 7812, pp. 360–364, 2020. DOI: 10.1038/s41586-020-2386-6.
- [75] Y. Wang and A. Belyanin, "Harmonic frequency combs in quantum cascade lasers: Time-domain and frequency-domain theory", *Phys. Rev. A*, vol. 102, p. 013519, 2020. DOI: 10.1103/PhysRevA.102.013519.
- [76] F. P. Mezzapesa, K. Garrasi, J. Schmidt, L. Salemi, V. Pistore, L. Li, A. G. Davies, E. H. Linfield, M. Riesch, C. Jirauschek, T. Carey, F. Torrisi, A. C. Ferrari, and M. S. Vitiello, "Terahertz frequency combs exploiting an on-chip, solution-processed, graphene-quantum cascade laser coupled-cavity", ACS Photonics, vol. 7, no. 12, pp. 3489–3498, 2020. DOI: 10.1021/acsphotonics.0c01523.
- [77] I. Heckelmann, M. Bertrand, A. Dikopoltsev, M. Beck, G. Scalari, and J. Faist, "Quantum walk comb in a fast gain laser", *Science*, vol. 382, no. 6669, pp. 434–438, 2023. DOI: 10.1126/science.adj3858.
- [78] L. Seitner, J. Popp, I. Heckelmann, R.-E. Vass, B. Meng, M. Haider, J. Faist, and C. Jirauschek, "Backscattering-induced dissipative solitons in ring quantum cascade lasers", *Phys. Rev. Lett.*, vol. 132, p. 043 805, 2024. DOI: 10.1103/PhysRevLett.132.043805.
- [79] D. Kazakov, M. Piccardo, Y. Wang, P. Chevalier, T. S. Mansuripur, F. Xie, C.-E. Zah, K. Lascola, A. Belyanin, and F. Capasso, "Self-starting harmonic frequency comb generation in a quantum cascade laser", *Nature Photon.*, vol. 11, no. 12, pp. 789–792, 2017. DOI: 10.1038/s41566-017-0026-y.
- [80] Q. Lu and M. Razeghi, "Recent advances in room temperature, high-power terahertz quantum cascade laser sources based on difference-frequency generation", *Photonics*, vol. 3, no. 3, p. 42, 2016. DOI: 10.3390/photonics3030042.
- [81] M. Piccardo, P. Chevalier, T. S. Mansuripur, D. Kazakov, Y. Wang, N. A. Rubin, L. Meadowcroft, A. Belyanin, and F. Capasso, "The harmonic state of quantum cascade lasers: Origin, control, and prospective applications [Invited]", *Opt. Express*, vol. 26, no. 8, pp. 9464–9483, 2018. DOI: 10.1364 /OE.26.009464.
- [82] K. Fujita, S. Jung, Y. Jiang, J. H. Kim, A. Nakanishi, A. Ito, M. Hitaka, T. Edamura, and M. A. Belkin, "Recent progress in terahertz difference-frequency quantum cascade laser sources", *Nanophotonics*, vol. 7, no. 11, pp. 1795–1817, 2018. DOI: doi:10.1515/nanoph-2018-0093.
- [83] T. Gabbrielli, N. Bruno, N. Corrias, S. Borri, L. Consolino, M. Bertrand, M. Shahmohammadi, M. Franckié, M. Beck, J. Faist, A. Zavatta, F. Cappelli, and P. De Natale, "Intensity correlations in quantum cascade laser harmonic frequency combs", *Adv. Photonics Res.*, vol. 3, no. 10, p. 2 200 162, 2022. DOI: 10.1002/adpr.202200162.
- [84] M. S. Vitiello and P. De Natale, "Terahertz quantum cascade lasers as enabling quantum technology", *Adv. Quantum Technol.*, vol. 5, no. 1, p. 2100082, 2022. DOI: 10.1002/qute.202100082.
- [85] C. Gardiner and P. Zoller, *Quantum Noise: A Handbook of Markovian and non-Markovian Quantum Stochastic Methods with Applications to Quantum Optics*. New York: Springer Science & Business Media, 2004, vol. 56.
- [86] M. Sargent III, M. O. Scully, and J. W. E. Lamb, *Laser Physics*. Reading, MA: Addison-Wesley, 1974.
- [87] W. H. Louisell, Quantum Statistical Properties of Radiation. New York, NY: Wiley, 1973.

- [88] M. Lax, "Quantum noise. IV. Quantum theory of noise sources", *Phys. Rev.*, vol. 145, pp. 110–129, 1966. DOI: 10.1103/PhysRev.145.110.
- [89] P. D. Drummond and M. G. Raymer, "Quantum theory of propagation of nonclassical radiation in a near-resonant medium", *Phys. Rev. A*, vol. 44, no. 3, pp. 2072–2085, 1991. DOI: 10.1103/PhysRevA.44.2072.
- [90] J. Popp, L. Seitner, M. A. Schreiber, M. Haider, L. Consolino, A. Sorgi, F. Cappelli, P. De Natale, K. Fujita, and C. Jirauschek, "Self-consistent simulations of intracavity terahertz comb difference frequency generation by mid-infrared quantum cascade lasers", *J. Appl. Phys.*, vol. 133, no. 23, p. 233 103, 2023. DOI: 10.1063/5.0151036.
- [91] A. Bismuto, R. Terazzi, M. Beck, and J. Faist, "Electrically tunable, high performance quantum cascade laser", *Appl. Phys. Lett.*, vol. 96, no. 14, p. 141 105, 2010. DOI: 10.1063/1.3377008.
- [92] C. Gmachl, F. Capasso, D. L. Sivco, and A. Y. Cho, "Recent progress in quantum cascade lasers and applications", *Rep. Prog. Phys.*, vol. 64, no. 11, p. 1533, 2001. DOI: 10.1088/0034-4885/64/11/204.
- [93] R. Köhler, A. Tredicucci, F. Beltram, H. E. Beere, E. H. Linfield, A. G. Davies, D. A. Ritchie, R. C. Iotti, and F. Rossi, "Terahertz semiconductor-heterostructure laser", *Nature*, vol. 417, no. 6885, pp. 156–159, 2002. DOI: 10.1038/417156a.
- [94] J. Faist, F. Capasso, D. L. Sivco, A. L. Hutchinson, S.-N. G. Chu, and A. Y. Cho, "Short wavelength ($\lambda \sim 3.4 \,\mu\text{m}$) quantum cascade laser based on strained compensated InGaAs/AlInAs", *Appl. Phys. Lett.*, vol. 72, no. 6, pp. 680–682, 1998. DOI: 10.1063/1.120843.
- [95] J. Devenson, D. Barate, O. Cathabard, R. Teissier, and A. N. Baranov, "Very short wavelength (λ = 3.1–3.3 μ m) quantum cascade lasers", *Appl. Phys. Lett.*, vol. 89, no. 19, p. 191 115, 2006. DOI: 10.1063 /1.2387473.
- [96] M. P. Semtsiv, M. Wienold, S. Dressler, and W. T. Masselink, "Short-wavelength ($\lambda \approx 3.05 \ \mu m$) InP-based strain-compensated quantum-cascade laser", *Appl. Phys. Lett.*, vol. 90, no. 5, p. 051 111, 2007. DOI: 10.1063/1.2437108.
- [97] T. Gresch, "Gain and waveguide engineering in mid-infrared quantum cascade lasers", Ph.D. dissertation, ETH Zurich, 2009. DOI: 10.3929/ethz-a-006032243.
- [98] Y. Bai, S. Slivken, S. Kuboya, S. R. Darvish, and M. Razeghi, "Quantum cascade lasers that emit more light than heat", *Nature Photon.*, vol. 4, no. 2, pp. 99–102, 2010. DOI: 10.1038/nphoton.2009.263.
- [99] P. Q. Liu, A. J. Hoffman, M. D. Escarra, K. J. Franz, J. B. Khurgin, Y. Dikmelik, X. Wang, J.-Y. Fan, and C. F. Gmachl, "Highly power-efficient quantum cascade lasers", *Nature Photon.*, vol. 4, no. 2, pp. 95–98, 2010. DOI: 10.1038/nphoton.2009.262.
- [100] Y. Yao, A. J. Hoffman, and C. F. Gmachl, "Mid-infrared quantum cascade lasers", *Nature Photon.*, vol. 6, no. 7, pp. 432–439, 2012. DOI: 10.1038/nphoton.2012.143.
- [101] M. S. Vitiello, G. Scalari, B. Williams, and P. D. Natale, "Quantum cascade lasers: 20 years of challenges", *Opt. Express*, vol. 23, no. 4, pp. 5167–5182, 2015. DOI: 10.1364/OE.23.005167.
- [102] A. Mátyás, P. Lugli, and C. Jirauschek, "Photon-induced carrier transport in high efficiency midinfrared quantum cascade lasers", *J. Appl. Phys.*, vol. 110, no. 1, p. 013 108, 2011. DOI: 10.1063/1.3608116.
- [103] C. Sirtori, "Terahertz race heats up", *Nature Photon.*, vol. 15, no. 1, pp. 1–2, 2021. DOI: 10.1038/s4156 6-020-00740-4.
- [104] M. A. Belkin, F. Capasso, F. Xie, A. Belyanin, M. Fischer, A. Wittmann, and J. Faist, "Room temperature terahertz quantum cascade laser source based on intracavity difference-frequency generation", *Appl. Phys. Lett.*, vol. 92, no. 20, p. 201 101, 2008. DOI: 10.1063/1.2919051.
- [105] A. Khalatpour, A. K. Paulsen, C. Deimert, Z. R. Wasilewski, and Q. Hu, "High-power portable terahertz laser systems", *Nature Photon.*, vol. 15, no. 1, pp. 16–20, 2021.
- [106] A. Khalatpour, M. C. Tam, S. J. Addamane, J. Reno, Z. Wasilewski, and Q. Hu, "Enhanced operating temperature in terahertz quantum cascade lasers based on direct phonon depopulation", *Appl. Phys. Lett.*, vol. 122, no. 16, p. 161 101, 2023. DOI: 10.1063/5.0144705.

- [107] K. Garrasi, F. P. Mezzapesa, L. Salemi, L. Li, L. Consolino, S. Bartalini, P. De Natale, A. G. Davies, E. H. Linfield, and M. S. Vitiello, "High dynamic range, heterogeneous, terahertz quantum cascade lasers featuring thermally tunable frequency comb operation over a broad current range", *ACS Photonics*, vol. 6, no. 1, pp. 73–78, 2019. DOI: 10.1021/acsphotonics.8b01483.
- [108] M. Rösch, G. Scalari, M. Beck, and J. Faist, "Octave-spanning semiconductor laser", *Nature Photon.*, vol. 9, no. 1, pp. 42–47, 2015.
- [109] M. Rösch, M. Beck, M. J. Süess, D. Bachmann, K. Unterrainer, J. Faist, and G. Scalari, "Heterogeneous terahertz quantum cascade lasers exceeding 1.9 THz spectral bandwidth and featuring dual comb operation", *Nanophotonics*, vol. 7, no. 1, pp. 237–242, 2018. DOI: doi:10.1515/nanoph-2017-0024.
- [110] E. Riccardi, V. Pistore, L. Consolino, A. Sorgi, F. Cappelli, R. Eramo, P. De Natale, L. Li, A. G. Davies, E. H. Linfield, and M. S. Vitiello, "Terahertz sources based on metrological-grade frequency combs", *Laser & Photonics Rev.*, vol. 17, no. 2, p. 2 200 412, 2023. DOI: 10.1002/lpor.202200412.
- [111] L. Consolino, M. Nafa, F. Cappelli, K. Garrasi, F. P. Mezzapesa, L. Li, A. G. Davies, E. H. Linfield, M. S. Vitiello, P. De Natale, *et al.*, "Fully phase-stabilized quantum cascade laser frequency comb", *Nat. Commun.*, vol. 10, p. 2938, 2019. DOI: 10.1038/s41467-019-10913-7.
- [112] S. A. Diddams, K. Vahala, and T. Udem, "Optical frequency combs: Coherently uniting the electromagnetic spectrum", *Science*, vol. 369, no. 6501, eaay3676, 2020. DOI: 10.1126/science.aay3676.
- [113] L. Chang, S. Liu, and J. E. Bowers, "Integrated optical frequency comb technologies", *Nature Photon.*, vol. 16, no. 2, pp. 95–108, 2022. DOI: 10.1038/s41566-021-00945-1.
- [114] D. Burghoff, Y. Yang, D. J. Hayton, J.-R. Gao, J. L. Reno, and Q. Hu, "Evaluating the coherence and time-domain profile of quantum cascade laser frequency combs", *Opt. Express*, vol. 23, no. 2, pp. 1190–1202, 2015. DOI: 10.1364/OE.23.001190.
- [115] M. Singleton, P. Jouy, M. Beck, and J. Faist, "Evidence of linear chirp in mid-infrared quantum cascade lasers", *Optica*, vol. 5, no. 8, pp. 948–953, 2018. DOI: 10.1364/OPTICA.5.000948.
- [116] F. Cappelli, L. Consolino, G. Campo, I. Galli, D. Mazzotti, A. Campa, M. Siciliani de Cumis, P. Cancio Pastor, R. Eramo, M. Rösch, *et al.*, "Retrieval of phase relation and emission profile of quantum cascade laser frequency combs", *Nature Photon.*, vol. 13, no. 8, pp. 562–568, 2019. DOI: 10.1038/s41566-019-0451-1.
- [117] J. Hillbrand, A. M. Andrews, H. Detz, G. Strasser, and B. Schwarz, "Coherent injection locking of quantum cascade laser frequency combs", *Nature Photon.*, vol. 13, no. 2, pp. 101–104, 2019. DOI: 10.1038/s41566-018-0320-3.
- [118] U. Senica, A. Dikopoltsev, A. Forrer, S. Cibella, G. Torrioli, M. Beck, J. Faist, and G. Scalari, "Frequency-modulated combs via field-enhancing tapered waveguides", *Laser Photonics Rev.*, vol. 17, no. 12, p. 2 300 472, 2023. DOI: 10.1002/lpor.202300472.
- [119] J. B. Khurgin, Y. Dikmelik, A. Hugi, and J. Faist, "Coherent frequency combs produced by self frequency modulation in quantum cascade lasers", *Appl. Phys. Lett.*, vol. 104, no. 8, p. 081 118, 2014. DOI: 10.1063/1.4866868.
- [120] N. Henry, D. Burghoff, Q. Hu, and J. B. Khurgin, "Temporal characteristics of quantum cascade laser frequency modulated combs in long wave infrared and THz regions", *Opt. Express*, vol. 26, no. 11, pp. 14201–14212, 2018. DOI: 10.1364/OE.26.014201.
- [121] N. Henry, D. Burghoff, Q. Hu, and J. B. Khurgin, "Study of spatio-temporal character of frequency combs generated by quantum cascade lasers", *IEEE J. Sel. Top. Quantum Electron.*, vol. 25, no. 6, p. 1200209, 2019. DOI: 10.1109/JSTQE.2019.2929222.
- [122] D. Burghoff, "Unraveling the origin of frequency modulated combs using active cavity mean-field theory", *Optica*, vol. 7, no. 12, pp. 1781–1787, 2020. DOI: 10.1364/OPTICA.408917.

- [123] L. Humbard and D. Burghoff, "Analytical theory of frequency-modulated combs: Generalized mean-field theory, complex cavities, and harmonic states", *Opt. Express*, vol. 30, no. 4, pp. 5376–5401, 2022. DOI: 10.1364/OE.445570.
- [124] F. Giorgetta, "Design, fabrication, and testing of intersubband infrared photodetectors operating at wavelengths between 2 μ m and 17 μ m", Ph.D. dissertation, Université de Neuchâtel, 2007.
- [125] A. Buffaz, M. Carras, L. Doyennette, A. Nedelcu, P. Bois, and V. Berger, "State of the art of quantum cascade photodetectors", in *Infrared Technology and Applications XXXVI*, B. F. Andresen, G. F. Fulop, and P. R. Norton, Eds., International Society for Optics and Photonics, vol. 7660, SPIE, 2010, 76603Q. DOI: 10.1117/12.853525.
- [126] F. R. Giorgetta, E. Baumann, M. Graf, Q. Yang, C. Manz, K. Kohler, H. E. Beere, D. A. Ritchie, E. Linfield, A. G. Davies, *et al.*, "Quantum cascade detectors", *IEEE J. Quantum Electron.*, vol. 45, no. 8, pp. 1039–1052, 2009. DOI: 10.1109/JQE.2009.2017929.
- [127] B. F. Levine, K. K. Choi, C. G. Bethea, J. Walker, and R. J. Malik, "New 10 μm infrared detector using intersubband absorption in resonant tunneling GaAlAs superlattices", *Appl. Phys. Lett.*, vol. 50, no. 16, pp. 1092–1094, 1987. DOI: 10.1063/1.97928.
- [128] H. Liu, "Dependence of absorption spectrum and responsivity on the upper state position in quantum well intersubband photodetectors", *J. Appl. Phys.*, vol. 73, no. 6, pp. 3062–3067, 1993. DOI: 10.1063/1 .352989.
- [129] D. Hofstetter, M. Graf, T. Aellen, J. Faist, L. Hvozdara, and S. Blaser, "23 GHz operation of a room temperature photovoltaic quantum cascade detector at 5.35 μm", *Appl. Phys. Lett.*, vol. 89, no. 6, p. 061 119, 2006. DOI: 10.1063/1.2269408.
- [130] D. Hofstetter, F. R. Giorgetta, E. Baumann, Q. Yang, C. Manz, and K. Köhler, "Mid-infrared quantum cascade detectors for applications in spectroscopy and pyrometry", *Appl. Phys. B*, vol. 100, no. 2, pp. 313–320, 2010. DOI: 10.1007/s00340-010-3965-2.
- [131] B. Schwarz, P. Reininger, H. Detz, T. Zederbauer, A. Maxwell Andrews, S. Kalchmair, W. Schrenk, O. Baumgartner, H. Kosina, and G. Strasser, "A bi-functional quantum cascade device for same-frequency lasing and detection", *Appl. Phys. Lett.*, vol. 101, no. 19, p. 191 109, 2012. DOI: 10.1063/1.4767128.
- [132] B. Schwarz, P. Reininger, D. Ristanić, H. Detz, A. M. Andrews, W. Schrenk, and G. Strasser, "Monolithically integrated mid-infrared lab-on-a-chip using plasmonics and quantum cascade structures", *Nat. Commun.*, vol. 5, no. 1, p. 4085, 2014. DOI: 10.1038/ncomms5085.
- [133] T. Dougakiuchi, K. Fujita, T. Hirohata, A. Ito, M. Hitaka, and T. Edamura, "High photoresponse in room temperature quantum cascade detector based on coupled quantum well design", *Appl. Phys. Lett.*, vol. 109, no. 26, p. 261 107, 2016. DOI: 10.1063/1.4973582.
- [134] B. Schwarz, D. Ristanic, P. Reininger, T. Zederbauer, D. MacFarland, H. Detz, A. M. Andrews, W. Schrenk, and G. Strasser, "High performance bi-functional quantum cascade laser and detector", *Appl. Phys. Lett.*, vol. 107, no. 7, p. 071 104, 2015. DOI: 10.1063/1.4927851.
- [135] A. Harrer, R. Szedlak, B. Schwarz, H. Moser, T. Zederbauer, D. MacFarland, H. Detz, A. M. Andrews, W. Schrenk, B. Lendl, *et al.*, "Mid-infrared surface transmitting and detecting quantum cascade device for gas-sensing", *Sci. Rep.*, vol. 6, no. 1, p. 21795, 2016. DOI: 10.1038/srep21795.
- [136] M. Wienold, B. Röben, L. Schrottke, and H. Grahn, "Evidence for frequency comb emission from a Fabry-Pérot terahertz quantum-cascade laser", *Opt. Express*, vol. 22, no. 25, pp. 30410–30424, 2014. DOI: 10.1364/OE.22.030410.
- [137] L. Consolino, F. Cappelli, M. S. de Cumis, and P. De Natale, "QCL-based frequency metrology from the mid-infrared to the THz range: A review", *Nanophotonics*, vol. 8, no. 2, pp. 181–204, 2019. DOI: 10.1515/nanoph-2018-0076.
- [138] M. Piccardo and F. Capasso, "Laser frequency combs with fast gain recovery: Physics and applications", *Laser Photonics Rev.*, vol. 16, no. 2, p. 2 100 403, 2022. DOI: 10.1002/lpor.202100403.

- [139] E. U. Rafailov, M. A. Cataluna, W. Sibbett, N. D. Il'inskaya, Y. M. Zadiranov, A. E. Zhukov, V. M. Ustinov, D. A. Livshits, A. R. Kovsh, and N. N. Ledentsov, "High-power picosecond and femtosecond pulse generation from a two-section mode-locked quantum-dot laser", *Appl. Phys. Lett.*, vol. 87, no. 8, p. 081 107, 2005. DOI: 10.1063/1.2032608.
- [140] E. U. Rafailov, M. A. Cataluna, and W. Sibbett, "Mode-locked quantum-dot lasers", *Nature Photon.*, vol. 1, no. 7, pp. 395–401, 2007. DOI: 10.1038/nphoton.2007.120.
- [141] Z. Lu, J. Liu, S. Raymond, P. Poole, P. Barrios, and D. Poitras, "312-fs pulse generation from a passive c-band InAs/InP quantum dot mode-locked laser", *Opt. Express*, vol. 16, pp. 10835–10840, 2008. DOI: 10.1364/OE.16.010835.
- [142] J. Liu, Z. Lu, S. Raymond, P. J. Poole, P. J. Barrios, and D. Poitras, "Dual-wavelength 92.5 GHz self-mode-locked InP-based quantum dot laser", *Opt. Lett.*, vol. 33, no. 15, pp. 1702–1704, 2008. DOI: 10.1364/OL.33.001702.
- [143] R. Rosales, K. Merghem, A. Martinez, A. Akrout, J.-P. Tourrenc, A. Accard, F. Lelarge, and A. Ramdane, "InAs/InP quantum-dot passively mode-locked lasers for 1.55-μm applications", *IEEE J. Sel. Top. Quantum Electron.*, vol. 17, no. 5, pp. 1292–1301, 2011. DOI: 10.1109/JSTQE.2011.2116772.
- [144] S. Liu, D. Jung, J. C. Norman, M. J. Kennedy, A. C. Gossard, and J. E. Bowers, "490 fs pulse generation from passively mode-locked single section quantum dot laser directly grown on on-axis GaP/Si", *Electron. Lett.*, vol. 54, no. 7, pp. 432–433, 2018. DOI: 10.1049/el.2017.4639.
- [145] J. C. Norman, D. Jung, Y. Wan, and J. E. Bowers, "Perspective: The future of quantum dot photonic integrated circuits", *APL Photonics*, vol. 3, no. 3, p. 030 901, 2018. DOI: 10.1063/1.5021345.
- [146] S. Liu, X. Wu, D. Jung, J. C. Norman, M. J. Kennedy, H. K. Tsang, A. C. Gossard, and J. E. Bowers, "High-channel-count 20 GHz passively mode-locked quantum dot laser directly grown on Si with 4.1 Tbit/s transmission capacity", *Optica*, vol. 6, no. 2, pp. 128–134, 2019. DOI: 10.1364/OPTICA.6.000128.
- [147] C. Weber, L. L. Columbo, M. Gioannini, S. Breuer, and P. Bardella, "Threshold behavior of optical frequency comb self-generation in an InAs/InGaAs quantum dot laser", *Opt. Lett.*, vol. 44, no. 14, pp. 3478–3481, 2019. DOI: 10.1364/OL.44.003478.
- [148] R. Pawlus, L. L. Columbo, P. Bardella, S. Breuer, and M. Gioannini, "Intensity noise behavior of an InAs/InGaAs quantum dot laser emitting on ground states and excited states", *Opt. Lett.*, vol. 43, no. 4, pp. 867–870, 2018. DOI: 10.1364/OL.43.000867.
- [149] J. Hillbrand, D. Auth, M. Piccardo, N. Opačak, E. Gornik, G. Strasser, F. Capasso, S. Breuer, and B. Schwarz, "In-phase and anti-phase synchronization in a laser frequency comb", *Phys. Rev. Lett.*, vol. 124, p. 023 901, 2020. DOI: 10.1103/PhysRevLett.124.023901.
- [150] K. Merghem, A. Akrout, A. Martinez, G. Aubin, A. Ramdane, F. Lelarge, and G.-H. Duan, "Pulse generation at 346 GHz using a passively mode locked quantum-dash-based laser at 1.5 μm", *Appl. Phys. Lett.*, vol. 94, no. 2, p. 021 107, 2009. DOI: 10.1063/1.3070544.
- [151] R. Rosales, S. G. Murdoch, R. Watts, K. Merghem, A. Martinez, F. Lelarge, A. Accard, L. P. Barry, and A. Ramdane, "High performance mode locking characteristics of single section quantum dash lasers", *Opt. Express*, vol. 20, no. 8, pp. 8649–8657, 2012. DOI: 10.1364/OE.20.008649.
- [152] K. Merghem, C. Calò, R. Rosales, X. Lafosse, G. Aubin, A. Martinez, F. Lelarge, and A. Ramdane, "Stability of optical frequency comb generated with InAs/InP quantum-dash-based passive mode-locked lasers", *IEEE J. Quantum Electron.*, vol. 50, no. 4, pp. 275–280, 2014. DOI: 10.1109/JQE.2014.2308323.
- [153] E. Sooudi, S. Sygletos, A. D. Ellis, G. Huyet, J. G. McInerney, F. Lelarge, K. Merghem, R. Rosales, A. Martinez, A. Ramdane, and S. P. Hegarty, "Optical frequency comb generation using dual-mode injection-locking of quantum-dash mode-locked lasers: Properties and applications", *IEEE J. Quantum Electron.*, vol. 48, no. 10, pp. 1327–1338, 2012. DOI: 10.1109/JQE.2012.2210389.

- [154] V. Panapakkam, A. P. Anthur, V. Vujicic, R. Zhou, Q. Gaimard, K. Merghem, G. Aubin, F. Lelarge, E. A. Viktorov, L. P. Barry, and A. Ramdane, "Amplitude and phase noise of frequency combs generated by single-section InAs/InP quantum-dash-based passively and actively mode-locked lasers", *IEEE J. Quantum Electron.*, vol. 52, no. 11, p. 1300 207, 2016. DOI: 10.1109/JQE.2016.2608800.
- [155] J. N. Kemal, P. Marin-Palomo, V. Panapakkam, P. Trocha, S. Wolf, K. Merghem, F. Lelarge, A. Ramdane, S. Randel, W. Freude, and C. Koos, "Coherent WDM transmission using quantum-dash mode-locked laser diodes as multi-wavelength source and local oscillator", *Opt. Express*, vol. 27, no. 22, pp. 31 164–31 175, 2019. DOI: 10.1364/OE.27.031164.
- [156] M. Bagheri, C. Frez, L. A. Sterczewski, I. Gruidin, M. Fradet, I. Vurgaftman, C. L. Canedy, W. W. Bewley, C. D. Merritt, C. S. Kim, *et al.*, "Passively mode-locked interband cascade optical frequency combs", *Sci. Rep.*, vol. 8, no. 1, p. 3322, 2018. DOI: 10.1038/s41598-018-21504-9.
- [157] L. A. Sterczewski, J. Westberg, M. Bagheri, C. Frez, I. Vurgaftman, C. L. Canedy, W. W. Bewley, C. D. Merritt, C. S. Kim, M. Kim, J. R. Meyer, and G. Wysocki, "Mid-infrared dual-comb spectroscopy with interband cascade lasers", *Opt. Lett.*, vol. 44, no. 8, pp. 2113–2116, 2019. DOI: 10.1364/OL.44.002113.
- [158] M. Gioannini, P. Bardella, and I. Montrosset, "Time-domain traveling-wave analysis of the multimode dynamics of quantum dot Fabry–Perot lasers", *IEEE J. Sel. Top. Quantum Electron.*, vol. 21, no. 6, pp. 698–708, 2015. DOI: 10.1109/JSTQE.2015.2425537.
- [159] P. Bardella, L. L. Columbo, and M. Gioannini, "Self-generation of optical frequency comb in single section quantum dot Fabry-Perot lasers: A theoretical study", *Opt. Express*, vol. 25, no. 21, pp. 26234–26252, 2017. DOI: 10.1364/OE.25.026234.
- [160] M. Dong, N. M. Mangan, J. N. Kutz, S. T. Cundiff, and H. G. Winful, "Traveling wave model for frequency comb generation in single-section quantum well diode lasers", *IEEE J. Quantum Electron.*, vol. 53, no. 6, p. 2 500 311, 2017. DOI: 10.1109/JQE.2017.2756641.
- [161] M. Rossetti, P. Bardella, and I. Montrosset, "Time-domain travelling-wave model for quantum dot passively mode-locked lasers", *IEEE J. Quantum Electron.*, vol. 47, no. 2, pp. 139–150, 2011. DOI: 10.1109/JQE.2010.2055550.
- [162] F. Cappelli, G. Villares, S. Riedi, and J. Faist, "Intrinsic linewidth of quantum cascade laser frequency combs", *Optica*, vol. 2, no. 10, pp. 836–840, 2015. DOI: 10.1364/OPTICA.2.000836.
- [163] Y. Li, N. Yang, Y. Xie, W. Chu, W. Zhang, S. Duan, and J. Wang, "Basic phase-locking, noise, and modulation properties of optically mutual-injected terahertz quantum cascade lasers", *Opt. Express*, vol. 27, no. 3, pp. 3146–3160, 2019. DOI: 10.1364/OE.27.003146.
- [164] J. Duan, X.-G. Wang, Y.-G. Zhou, C. Wang, and F. Grillot, "Carrier-noise-enhanced relative intensity noise of quantum dot lasers", *IEEE J. Quantum Electron.*, vol. 54, no. 6, p. 2001407, 2018. DOI: 10.1109/JQE.2018.2880452.
- [165] Y. Zhou, J. Duan, F. Grillot, and C. Wang, "Optical noise of dual-state lasing quantum dot lasers", *IEEE J. Quantum Electron.*, vol. 56, no. 6, p. 2 001 207, 2020. DOI: 10.1109/JQE.2020.3026090.
- [166] A. I. Borodkin, A. V. Kovalev, M. Giudici, G. Huyet, A. Ramdane, M. Marconi, and E. A. Viktorov, "Noise-induced broadening of a quantum-dash laser optical frequency comb", *Appl. Phys. Lett.*, vol. 123, no. 4, p. 041 105, 2023. DOI: 10.1063/5.0157209.
- [167] T. Gabbrielli, F. Cappelli, N. Bruno, N. Corrias, S. Borri, P. D. Natale, and A. Zavatta, "Mid-infrared homodyne balanced detector for quantum light characterization", *Opt. Express*, vol. 29, no. 10, pp. 14536–14547, 2021. DOI: 10.1364/OE.420990.
- [168] Y. Mao, Z. Lu, J. Liu, P. J. Poole, and G. Liu, "Pulse timing jitter estimated from optical phase noise in mode-locked semiconductor quantum dash lasers", *J. Light. Technol.*, vol. 38, no. 17, pp. 4787–4793, 2020. DOI: 10.1109/JLT.2020.2996424.
- [169] Z. Lu, J. Liu, P. J. Poole, Y. Mao, J. Weber, G. Liu, and P. Barrios, "InAs/InP quantum dash semiconductor coherent comb lasers and their applications in optical networks", *J. Lightwave Technol.*, vol. 39, no. 12, pp. 3751–3760, 2021. DOI: 10.1109/JLT.2020.3043284.

- [170] U. Senica, A. Forrer, T. Olariu, P. Micheletti, S. Cibella, G. Torrioli, M. Beck, J. Faist, and G. Scalari, "Planarized THz quantum cascade lasers for broadband coherent photonics", *Light Sci. Appl.*, vol. 11, no. 1, p. 347, 2022. DOI: 10.1038/s41377-022-01058-2.
- [171] T. S. Mansuripur, C. Vernet, P. Chevalier, G. Aoust, B. Schwarz, F. Xie, C. Caneau, K. Lascola, C.-e. Zah, D. P. Caffey, T. Day, L. J. Missaggia, M. K. Connors, C. A. Wang, A. Belyanin, and F. Capasso, "Single-mode instability in standing-wave lasers: The quantum cascade laser as a self-pumped parametric oscillator", *Phys. Rev. A*, vol. 94, p. 063 807, 2016. DOI: 10.1103/PhysRevA.94.063807.
- [172] H. Li, W. Wan, Z. Li, J. C. Cao, S. Lepillet, J.-F. Lampin, K. Froberger, L. Columbo, M. Brambilla, and S. Barbieri, "Real-time multimode dynamics of terahertz quantum cascade lasers via intracavity self-detection: Observation of self mode-locked population pulsations", *Opt. Express*, vol. 30, no. 3, pp. 3215–3229, 2022. DOI: 10.1364/OE.444295.
- [173] D. Kazakov, N. Opačak, M. Beiser, A. Belyanin, B. Schwarz, M. Piccardo, and F. Capasso, "Defect-engineered ring laser harmonic frequency combs", *Optica*, vol. 8, no. 10, pp. 1277–1280, 2021. DOI: 10.1364/OPTICA.430896.
- [174] M. Jaidl, N. Opačak, M. A. Kainz, S. Schönhuber, D. Theiner, B. Limbacher, M. Beiser, M. Giparakis, A. M. Andrews, G. Strasser, B. Schwarz, J. Darmo, and K. Unterrainer, "Comb operation in terahertz quantum cascade ring lasers", *Optica*, vol. 8, no. 6, pp. 780–787, 2021. DOI: 10.1364/OPTICA.420674.
- [175] E. Riccardi, M. A. J. Guerrero, V. Pistore, L. Seitner, C. Jirauschek, L. Li, A. G. Davies, E. H. Linfield, and M. S. Vitiello, "Sculpting harmonic comb states in terahertz quantum cascade lasers by controlled engineering", *Optica*, vol. 11, no. 3, pp. 412–419, 2024. DOI: 10.1364/OPTICA.509929.
- [176] C. Silvestri, X. Qi, T. Taimre, and A. D. Rakić, "Frequency combs induced by optical feedback and harmonic order tunability in quantum cascade lasers", *APL Photonics*, vol. 8, no. 11, p. 116 102, 2023. DOI: 10.1063/5.0164597.
- [177] M. Piccardo, P. Chevalier, S. Anand, Y. Wang, D. Kazakov, E. A. Mejia, F. Xie, K. Lascola, A. Belyanin, and F. Capasso, "Widely tunable harmonic frequency comb in a quantum cascade laser", *Appl. Phys. Lett.*, vol. 113, no. 3, p. 031 104, 2018. DOI: 10.1063/1.5039611.
- [178] J. Popp, L. Seitner, F. Naunheimer, G. Janowski, M. Haider, and C. Jirauschek, "Multi-domain modeling of free-running harmonic frequency comb formation in terahertz quantum cascade lasers", *IEEE Photonics J.*, vol. 16, no. 2, p. 0 600 711, 2024. DOI: 10.1109/JPHOT.2024.3370189.
- [179] J. Popp, L. Seitner, F. Naunheimer, M. Haider, and C. Jirauschek, "Influence of eigenstate basis sets on self-starting harmonic comb simulations in THz QCLs", in 2023 International Conference on Numerical Simulation of Optoelectronic Devices (NUSOD), 2023, pp. 11–12. DOI: 10.1109/NUSOD59562.2023.1 0273518.
- [180] M. I. Amanti, G. Scalari, R. Terazzi, M. Fischer, M. Beck, J. Faist, A. Rudra, P. Gallo, and E. Kapon, "Bound-to-continuum terahertz quantum cascade laser with a single-quantum-well phonon extraction/injection stage", *New J. Phys.*, vol. 11, no. 12, p. 125 022, 2009. DOI: 10.1088/1367-2630/11/12/125022.
- [181] A. Forrer, M. Franckié, D. Stark, T. Olariu, M. Beck, J. Faist, and G. Scalari, "Photon-driven broadband emission and frequency comb RF injection locking in THz quantum cascade lasers", *ACS Photonics*, vol. 7, no. 3, pp. 784–791, 2020. DOI: 10.1021/acsphotonics.9b01629.
- [182] A. D. Gaspare, L. Viti, H. E. Beere, D. D. Ritchie, and M. S. Vitiello, "Homogeneous quantum cascade lasers operating as terahertz frequency combs over their entire operational regime", *Nanophotonics*, vol. 10, no. 1, pp. 181–186, 2021. DOI: 10.1515/nanoph-2020-0378.
- [183] C. Jirauschek, "Accuracy of transfer matrix approaches for solving the effective mass Schrödinger equation", *IEEE J. Quantum Electron.*, vol. 45, no. 9, pp. 1059–1067, 2009. DOI: 10.1109/JQE.2009.2 020998.
- [184] V. Rindert, E. Önder, and A. Wacker, "Analysis of high-performing terahertz quantum cascade lasers", *Phys. Rev. Appl.*, vol. 18, no. 4, p. L041001, 2022. DOI: 10.1103/PhysRevApplied.18.L041001.

- [185] M. Wienold, B. Röben, L. Schrottke, R. Sharma, A. Tahraoui, K. Biermann, and H. Grahn, "High-temperature, continuous-wave operation of terahertz quantum-cascade lasers with metal-metal waveguides and third-order distributed feedback", *Opt. Express*, vol. 22, no. 3, pp. 3334–3348, 2014. DOI: 10.1364/OE.22.003334.
- [186] C. A. Curwen, S. J. Addamane, J. L. Reno, M. Shahili, J. H. Kawamura, R. M. Briggs, B. S. Karasik, and B. S. Williams, "Thin THz QCL active regions for improved continuous-wave operating temperature", *AIP Adv.*, vol. 11, no. 12, p. 125 018, 2021. DOI: 10.1063/5.0071953.
- [187] M. Razeghi, Q. Lu, N. Bandyopadhyay, W. Zhou, D. Heydari, Y. Bai, and S. Slivken, "Quantum cascade lasers: From tool to product", *Opt. Express*, vol. 23, no. 7, pp. 8462–8475, 2015. DOI: 10.1364/OE.23 .008462.
- [188] M. A. Belkin and F. Capasso, "New frontiers in quantum cascade lasers: High performance room temperature terahertz sources", *Phys. Scr.*, vol. 90, no. 11, p. 118 002, 2015. DOI: 10.1088/0031-8949 /90/11/118002.
- [189] M. A. Belkin, F. Capasso, A. Belyanin, D. L. Sivco, A. Y. Cho, D. C. Oakley, C. J. Vineis, and G. W. Turner, "Terahertz quantum-cascade-laser source based on intracavity difference-frequency generation", *Nature Photon.*, vol. 1, pp. 288–292, 2007. DOI: 10.1038/nphoton.2007.70.
- [190] K. Fujita, M. Hitaka, A. Ito, T. Edamura, M. Yamanishi, S. Jung, and M. A. Belkin, "Terahertz generation in mid-infrared quantum cascade lasers with a dual-upper-state active region", *Appl. Phys. Lett.*, vol. 106, no. 25, p. 251 104, 2015. DOI: 10.1063/1.4923203.
- [191] K. Fujita, M. Hitaka, A. Ito, M. Yamanishi, T. Dougakiuchi, and T. Edamura, "Ultra-broadband room-temperature terahertz quantum cascade laser sources based on difference frequency generation", *Opt. Express*, vol. 24, no. 15, pp. 16357–16365, 2016. DOI: 10.1364/OE.24.016357.
- [192] Q. Lu, D. Wu, S. Sengupta, S. Slivken, and M. Razeghi, "Room temperature continuous wave, monolithic tunable THz sources based on highly efficient mid-infrared quantum cascade lasers", *Sci. Rep.*, vol. 6, p. 23 595, 2016. DOI: 10.1038/srep23595.
- [193] K. Fujita, A. Ito, M. Hitaka, T. Dougakiuchi, and T. Edamura, "Low-threshold room-temperature continuous-wave operation of a terahertz difference-frequency quantum cascade laser source", *Appl. Phys. Express*, vol. 10, no. 8, p. 082 102, 2017. DOI: 10.7567/APEX.10.082102.
- [194] Q. Lu, N. Bandyopadhyay, S. Slivken, Y. Bai, and M. Razeghi, "Room temperature single-mode terahertz sources based on intracavity difference-frequency generation in quantum cascade lasers", *Appl. Phys. Lett.*, vol. 99, no. 13, p. 131 106, 2011. DOI: 10.1063/1.3645016.
- [195] K. Vijayraghavan, R. W. Adams, A. Vizbaras, M. Jang, C. Grasse, G. Boehm, M. C. Amann, and M. A. Belkin, "Terahertz sources based on Čerenkov difference-frequency generation in quantum cascade lasers", *Appl. Phys. Lett.*, vol. 100, no. 25, p. 251 104, 2012. DOI: 10.1063/1.4729042.
- [196] Q. Lu, N. Bandyopadhyay, S. Slivken, Y. Bai, and M. Razeghi, "Continuous operation of a monolithic semiconductor terahertz source at room temperature", *Appl. Phys. Lett.*, vol. 104, no. 22, p. 221 105, 2014. DOI: 10.1063/1.4881182.
- [197] A. Jiang, S. Jung, Y. Jiang, K. Vijayraghavan, J. H. Kim, and M. A. Belkin, "Widely tunable terahertz source based on intra-cavity frequency mixing in quantum cascade laser arrays", *Appl. Phys. Lett.*, vol. 106, no. 26, p. 261 107, 2015. DOI: 10.1063/1.4923374.
- [198] Q. Lu, S. Slivken, N. Bandyopadhyay, Y. Bai, and M. Razeghi, "Widely tunable room temperature semiconductor terahertz source", *Appl. Phys. Lett.*, vol. 105, no. 20, p. 201 102, 2014. DOI: 10.1063/1.4 902245.
- [199] S. Jung, A. Jiang, Y. Jiang, K. Vijayraghavan, X. Wang, M. Troccoli, and M. A. Belkin, "Broadly tunable monolithic room-temperature terahertz quantum cascade laser sources", *Nat. Commun.*, vol. 5, p. 4267, 2014. DOI: 10.1038/ncomms5267.

- [200] K. Vijayraghavan, Y. Jiang, M. Jang, A. Jiang, K. Choutagunta, A. Vizbaras, F. Demmerle, G. Boehm, M. C. Amann, and M. A. Belkin, "Broadly tunable terahertz generation in mid-infrared quantum cascade lasers", *Nat. Commun.*, vol. 4, p. 2021, 2013. DOI: 10.1038/ncomms3021.
- [201] Y. Jiang, K. Vijayraghavan, S. Jung, F. Demmerle, G. Boehm, M. C. Amann, and M. A. Belkin, "External cavity terahertz quantum cascade laser sources based on intra-cavity frequency mixing with 1.2–5.9 THz tuning range", *J. Opt.*, vol. 16, no. 9, p. 094 002, 2014. DOI: 10.1088/2040-8978/16/9/094002.
- [202] Y. Jiang, K. Vijayraghavan, S. Jung, A. Jiang, J. H. Kim, F. Demmerle, G. Boehm, M. C. Amann, and M. A. Belkin, "Spectroscopic study of terahertz generation in mid-infrared quantum cascade lasers", *Sci. Rep.*, vol. 6, p. 21 169, 2016. DOI: 10.1038/srep21169.
- [203] L. Consolino, S. Jung, A. Campa, M. D. Regis, S. Pal, J. H. Kim, K. Fujita, A. Ito, M. Hitaka, S. Bartalini, P. D. Natale, M. A. Belkin, and M. S. Vitiello, "Spectral purity and tunability of terahertz quantum cascade laser sources based on intracavity difference-frequency generation", *Sci. Adv.*, vol. 3, no. 9, e1603317, 2017. DOI: 10.1126/sciadv.1603317.
- [204] K. Fujita, S. Hayashi, A. Ito, M. Hitaka, and T. Dougakiuchi, "Sub-terahertz and terahertz generation in long-wavelength quantum cascade lasers", *Nanophotonics*, vol. 8, no. 12, pp. 2235–2241, 2019. DOI: doi:10.1515/nanoph-2019-0238.
- [205] Q. Lu, F. Wang, D. Wu, S. Slivken, and M. Razeghi, "Room temperature terahertz semiconductor frequency comb", *Nat. Commun.*, vol. 10, p. 2403, 2019. DOI: 10.1038/s41467-019-10395-7.
- [206] L. Consolino, M. Nafa, M. De Regis, F. Cappelli, S. Bartalini, A. Ito, M. Hitaka, T. Dougakiuchi, T. Edamura, P. De Natale, and F. Kazuue, "Direct observation of terahertz frequency comb generation in difference-frequency quantum cascade lasers", *Appl. Sci.*, vol. 11, no. 4, p. 1416, 2021. DOI: 10.3390/a pp11041416.
- [207] J. Popp, L. Seitner, M. Schreiber, M. Haider, L. Consolino, F. Cappelli, P. De Natale, K. Fujita, and C. Jirauschek, "Modeling of THz comb emission in difference-frequency quantum cascade lasers", in 2022 International Conference on Numerical Simulation of Optoelectronic Devices (NUSOD), 2022, pp. 63–64. DOI: 10.1109/NUSOD54938.2022.9894839.
- [208] M. Aichhorn, M. Hohenadler, C. Tahan, and P. B. Littlewood, "Quantum fluctuations, temperature, and detuning effects in solid-light systems", *Phys. Rev. Lett.*, vol. 100, p. 216 401, 2008. DOI: 10.1103/Phys RevLett.100.216401.
- [209] V. Giovannetti, S. Lloyd, and L. Maccone, "Advances in quantum metrology", *Nature Photon.*, vol. 5, no. 4, pp. 222–229, 2011. DOI: 10.1038/nphoton.2011.35.
- [210] P. Krantz, M. Kjaergaard, F. Yan, T. P. Orlando, S. Gustavsson, and W. D. Oliver, "A quantum engineer's guide to superconducting qubits", *Appl. Phys. Rev.*, vol. 6, no. 2, p. 021318, 2019. DOI: 10.1063/1.5089550.
- [211] R. Hanai, A. Edelman, Y. Ohashi, and P. B. Littlewood, "Non-hermitian phase transition from a polariton Bose-Einstein condensate to a photon laser", *Phys. Rev. Lett.*, vol. 122, p. 185 301, 2019. DOI: 10.1103 /PhysRevLett.122.185301.
- [212] M. Erhard, M. Krenn, and A. Zeilinger, "Advances in high-dimensional quantum entanglement", *Nat. Rev. Phys.*, vol. 2, no. 7, pp. 365–381, 2020. DOI: 10.1038/s42254-020-0193-5.
- [213] A. J. Daley, I. Bloch, C. Kokail, S. Flannigan, N. Pearson, M. Troyer, and P. Zoller, "Practical quantum advantage in quantum simulation", *Nature*, vol. 607, no. 7920, pp. 667–676, 2022. DOI: 10.1038/s4158 6-022-04940-6.
- [214] H. J. Kimble, "The quantum internet", *Nature*, vol. 453, no. 7198, pp. 1023–1030, 2008. DOI: 10.1038 /nature07127.
- [215] S. Wehner, D. Elkouss, and R. Hanson, "Quantum internet: A vision for the road ahead", *Science*, vol. 362, no. 6412, eaam9288, 2018. DOI: 10.1126/science.aam9288.

- [216] T. D. Ladd, F. Jelezko, R. Laflamme, Y. Nakamura, C. Monroe, and J. L. O'Brien, "Quantum computers", *Nature*, vol. 464, no. 7285, pp. 45–53, 2010. DOI: 10.1038/nature08812.
- [217] H.-S. Zhong, H. Wang, Y.-H. Deng, M.-C. Chen, L.-C. Peng, Y.-H. Luo, J. Qin, D. Wu, X. Ding, Y. Hu, P. Hu, X.-Y. Yang, W.-J. Zhang, H. Li, Y. Li, X. Jiang, L. Gan, G. Yang, L. You, Z. Wang, L. Li, N.-L. Liu, C.-Y. Lu, and J.-W. Pan, "Quantum computational advantage using photons", *Science*, vol. 370, no. 6523, pp. 1460–1463, 2020. DOI: 10.1126/science.abe8770.
- [218] N. Gisin and R. Thew, "Quantum communication", *Nature Photon.*, vol. 1, no. 3, pp. 165–171, 2007. DOI: 10.1038/nphoton.2007.22.
- [219] C. L. Degen, F. Reinhard, and P. Cappellaro, "Quantum sensing", *Rev. Mod. Phys.*, vol. 89, p. 035 002, 2017. DOI: 10.1103/RevModPhys.89.035002.
- [220] E. Polino, M. Valeri, N. Spagnolo, and F. Sciarrino, "Photonic quantum metrology", *AVS Quantum Sci.*, vol. 2, no. 2, p. 024 703, 2020. DOI: 10.1116/5.0007577.
- [221] M. Barbieri, "Optical quantum metrology", *PRX Quantum*, vol. 3, p. 010202, 2022. DOI: 10.1103 /PRXQuantum.3.010202.
- [222] I. Bloch, J. Dalibard, and S. Nascimbene, "Quantum simulations with ultracold quantum gases", *Nat. Phys.*, vol. 8, no. 4, pp. 267–276, 2012. DOI: 10.1038/nphys2259.
- [223] I. M. Georgescu, S. Ashhab, and F. Nori, "Quantum simulation", *Rev. Mod. Phys.*, vol. 86, pp. 153–185, 2014. DOI: 10.1103/RevModPhys.86.153.
- [224] M. Kues, C. Reimer, J. M. Lukens, W. J. Munro, A. M. Weiner, D. J. Moss, and R. Morandotti, "Quantum optical microcombs", *Nature Photon.*, vol. 13, no. 3, pp. 170–179, 2019. DOI: 10.1038/s41566-019-03 63-0.
- [225] Z. Yang, M. Jahanbozorgi, D. Jeong, S. Sun, O. Pfister, H. Lee, and X. Yi, "A squeezed quantum microcomb on a chip", *Nat. Commun.*, vol. 12, no. 1, p. 4781, 2021. DOI: 10.1038/s41467-021-25054-z.
- [226] M. A. Guidry, D. M. Lukin, K. Y. Yang, R. Trivedi, and J. Vučković, "Quantum optics of soliton microcombs", *Nature Photon.*, vol. 16, no. 1, pp. 52–58, 2022. DOI: 10.1038/s41566-021-00901-z.
- [227] F. Rana and R. J. Ram, "Current noise and photon noise in quantum cascade lasers", *Phys. Rev. B*, vol. 65, p. 125 313, 2002. DOI: 10.1103/PhysRevB.65.125313.
- [228] O. Hess and T. Kuhn, "Maxwell-Bloch equations for spatially inhomogeneous semiconductor lasers. I. theoretical formulation", *Phys. Rev. A*, vol. 54, pp. 3347–3359, 1996. DOI: 10.1103/PhysRevA.54.3347.
- [229] N. Majer, K. Lüdge, and E. Schöll, "Cascading enables ultrafast gain recovery dynamics of quantum dot semiconductor optical amplifiers", *Phys. Rev. B*, vol. 82, p. 235 301, 2010. DOI: 10.1103/PhysRev B.82.235301.
- [230] E. Gehrig and O. Hess, "Mesoscopic spatiotemporal theory for quantum-dot lasers", *Phys. Rev. A*, vol. 65, p. 033 804, 2002. DOI: 10.1103/PhysRevA.65.033804.
- [231] D. Polder, M. F. H. Schuurmans, and Q. H. F. Vrehen, "Superfluorescence: Quantum-mechanical derivation of Maxwell-Bloch description with fluctuating field source", *Phys. Rev. A*, vol. 19, pp. 1192–1203, 1979. DOI: 10.1103/PhysRevA.19.1192.
- [232] K. Wódkiewicz, "Stochastic incoherences of optical Bloch equations", *Phys. Rev. A*, vol. 19, pp. 1686–1696, 1979. DOI: 10.1103/PhysRevA.19.1686.
- [233] J. Andreasen and H. Cao, "Finite-difference time-domain formulation of stochastic noise in macroscopic atomic systems", *J. Light. Technol.*, vol. 27, no. 20, pp. 4530–4535, 2009. DOI: 10.1109/JLT.2009.202 4627.
- [234] J. E. Kim, E. Malic, M. Richter, A. Wilms, and A. Knorr, "Maxwell-Bloch equation approach for describing the microscopic dynamics of quantum-dot surface-emitting structures", *IEEE J. Quantum Electron.*, vol. 46, no. 7, pp. 1115–1126, 2010. DOI: 10.1109/JQE.2010.2043923.

- [235] S. Wilkinson, B. Lingnau, J. Korn, E. Schoell, and K. Luedge, "Influence of noise on the signal quality of quantum-dot semiconductor optical amplifiers", *IEEE J. Sel. Top. Quantum Electron.*, vol. 19, no. 4, p. 1900 106, 2012. DOI: 10.1109/JSTQE.2012.2233464.
- [236] E. Gehrig and O. Hess, "Spatio-temporal dynamics of light amplification and amplified spontaneous emission in high-power tapered semiconductor laser amplifiers", *IEEE J. Quantum Electron.*, vol. 37, no. 10, pp. 1345–1355, 2001. DOI: 10.1109/3.952547.
- [237] E. Gehrig and O. Hess, *Spatio-Temporal Dynamics and Quantum Fluctuations in Semiconductor Lasers*. Berlin, Heidelberg: Springer Berlin Heidelberg, 2003.
- [238] H. F. Hofmann and O. Hess, "Quantum Maxwell-Bloch equations for spatially inhomogeneous semi-conductor lasers", *Phys. Rev. A*, vol. 59, pp. 2342–2358, 1999. DOI: 10.1103/PhysRevA.59.2342.
- [239] A. Cerjan, A. Pick, Y. D. Chong, S. G. Johnson, and A. D. Stone, "Quantitative test of general theories of the intrinsic laser linewidth", *Opt. Express*, vol. 23, no. 22, pp. 28316–28340, 2015. DOI: 10.1364/OE.23.028316.
- [240] A. Benediktovitch, V. P. Majety, and N. Rohringer, "Quantum theory of superfluorescence based on two-point correlation functions", *Phys. Rev. A*, vol. 99, p. 013 839, 2019. DOI: 10.1103/PhysRevA.99.0 13839.
- [241] H. Haken, Laser Theory. Berlin, Heidelberg: Springer, 1984.
- [242] H. Haken and W. Weidlich, "Quantum noise operators for the N-level system", *Z. Phys.*, vol. 189, no. 1, pp. 1–9, 1966. DOI: 10.1007/BF01343315.
- [243] R. Graham and H. Haken, "Quantum theory of light propagation in a fluctuating laser-active medium", *Z. Phys.*, vol. 213, no. 5, pp. 420–450, 1968. DOI: 10.1007/BF01405384.
- [244] M. Lax and W. Louisell, "Quantum noise. XII. Density-operator treatment of field and population fluctuations", *Phys. Rev.*, vol. 185, no. 2, pp. 568–591, 1969. DOI: 10.1103/PhysRev.185.568.
- [245] H. Haug and H. Haken, "Theory of noise in semiconductor laser emission", *Z. Phys.*, vol. 204, no. 3, pp. 262–275, 1967. DOI: 10.1007/BF01326200.
- [246] T. Liu, K. E. Lee, and Q. J. Wang, "Effects of resonant tunneling and dynamics of coherent interaction on intrinsic linewidth of quantum cascade lasers", *Opt. Express*, vol. 20, no. 15, pp. 17145–17159, 2012. DOI: 10.1364/OE.20.017145.
- [247] X.-G. Wang, F. Grillot, and C. Wang, "Rate equation modeling of the frequency noise and the intrinsic spectral linewidth in quantum cascade lasers", *Opt. Express*, vol. 26, no. 3, pp. 2325–2334, 2018. DOI: 10.1364/OE.26.002325.
- [248] D. E. Essebe, A. D. Mengue, and B. Z. Essimbi, "Stochastic behavior of an external optically injected single-mode semiconductor laser including Langevin noise sources", *Phys. Scr.*, vol. 94, no. 11, p. 115 501, 2019. DOI: 10.1088/1402-4896/ab0c27.
- [249] T. Gensty and W. Elsäßer, "Semiclassical model for the relative intensity noise of intersubband quantum cascade lasers", *Opt. Commun.*, vol. 256, no. 1, pp. 171–183, 2005. DOI: 10.1016/j.optcom.2005.07.020.
- [250] P. D. Drummond and D. F. Walls, "Quantum theory of optical bistability. II. atomic fluorescence in a high-Q cavity", *Phys. Rev. A*, vol. 23, pp. 2563–2579, 1981. DOI: 10.1103/PhysRevA.23.2563.
- [251] A. Pusch, S. Wuestner, J. M. Hamm, K. L. Tsakmakidis, and O. Hess, "Coherent amplification and noise in gain-enhanced nanoplasmonic metamaterials: A Maxwell-Bloch Langevin approach", *ACS Nano*, vol. 6, no. 3, pp. 2420–2431, 2012. DOI: 10.1021/nn204692x.
- [252] M. Fang, Z. Huang, W. E. I. Sha, and C. M. Soukoulis, "Modelling of the fluctuation and coherent dynamics in active metamaterial devices", *IEEE Trans. Nanotechnol.*, vol. 20, pp. 543–551, 2021. DOI: 10.1109/TNANO.2021.3092059.
- [253] J. Andreasen, H. Cao, A. Taflove, P. Kumar, and C.-Q. Cao, "Finite-difference time-domain simulation of thermal noise in open cavities", *Phys. Rev. A*, vol. 77, p. 023810, 2008. DOI: 10.1103/PhysRevA.77.023810.

- [254] [SW] Computational Photonics Group of the Technical University of Munich, *monacoQC: An object-oriented Matlab-based device engineering tool for quantum cascade (QC) structures* 2023, vcs: https://github.com/cph-tum/monacoQC.
- [255] J. Snoek, H. Larochelle, and R. P. Adams, "Practical Bayesian optimization of machine learning algorithms", in *Advances in Neural Information Processing Systems*, 2012, pp. 2951–2959.
- [256] P. I. Frazier, A tutorial on Bayesian optimization, arXiv: 1807.02811, 2018.
- [257] J. A. Van Vechten and T. K. Bergstresser, "Electronic structures of semiconductor alloys", *Phys. Rev. B*, vol. 1, pp. 3351–3358, 1970. DOI: 10.1103/PhysRevB.1.3351.
- [258] I. Vurgaftman, J. R. Meyer, and L. R. Ram-Mohan, "Band parameters for III–V compound semiconductors and their alloys", *J. Appl. Phys.*, vol. 89, no. 11, pp. 5815–5875, 2001. DOI: 10.1063/1.1368156.
- [259] J. M. Luttinger and W. Kohn, "Motion of electrons and holes in perturbed periodic fields", *Phys. Rev.*, vol. 97, pp. 869–883, 1955. DOI: 10.1103/PhysRev.97.869.
- [260] E. O. Kane, "Band structure of indium antimonide", *J. Phys. Chem. Solids*, vol. 1, no. 4, pp. 249–261, 1957. DOI: 10.1016/0022-3697(57)90013-6.
- [261] E. O. Kane, "Energy band theory", *Handb. Semicond.*, vol. 1, pp. 193–217, 1982.
- [262] G. Bastard, *Wave Mechanics Applied to Semiconductor Heterostructures*. Paris: Les Editons de Physique, 1988.
- [263] J. H. Davies, *The physics of low-dimensional semiconductors: an introduction*. Cambridge university press, 1998.
- [264] Y. A. Goldberg and N. M. Schmidt, in *Handbook Series on Semiconductor Parameters*. World Scientific, 1999, vol. 2, pp. 62–88. DOI: 10.1142/9789812832085_0003.
- [265] M. Sugawara, N. Okazaki, T. Fujii, and S. Yamazaki, "Conduction-band and valence-band structures in strained In_{1-x}Ga_xAs/InP quantum wells on (001) InP substrates", *Phys. Rev. B*, vol. 48, pp. 8102–8118, 1993. DOI: 10.1103/PhysRevB.48.8102.
- [266] B. A. Foreman, "Elimination of spurious solutions from eight-band **k** · **p** theory", *Phys. Rev. B*, vol. 56, R12748–R12751, 1997. DOI: 10.1103/PhysRevB.56.R12748.
- [267] P. Enders and M. Woerner, "Exact block diagonalization of the eight-band hamiltonian matrix for tetrahedral semiconductors and its application to strained quantum wells", *Semicond. Sci. Technol.*, vol. 11, no. 7, p. 983, 1996. DOI: 10.1088/0268-1242/11/7/002.
- [268] U. Rössler, "Nonparabolicity and warping in the conduction band of GaAs", *Solid State Commun.*, vol. 49, no. 10, pp. 943–947, 1984. DOI: 10.1016/0038-1098(84)90299-0.
- [269] U. Ekenberg, "Nonparabolicity effects in a quantum well: Sublevel shift, parallel mass, and Landau levels", *Phys. Rev. B*, vol. 40, pp. 7714–7726, 1989. DOI: 10.1103/PhysRevB.40.7714.
- [270] Y. Varshni, "Temperature dependence of the energy gap in semiconductors", *Physica*, vol. 34, no. 1, pp. 149–154, 1967. DOI: 10.1016/0031-8914(67)90062-6.
- [271] C. G. Van de Walle, "Band lineups and deformation potentials in the model-solid theory", *Phys. Rev. B*, vol. 39, pp. 1871–1883, 1989. DOI: 10.1103/PhysRevB.39.1871.
- [272] Y. Ando and T. Itoh, "Calculation of transmission tunneling current across arbitrary potential barriers", *J. Appl. Phys.*, vol. 61, no. 4, pp. 1497–1502, 1987. DOI: 10.1063/1.338082.
- [273] B. Jonsson and S. Eng, "Solving the Schrödinger equation in arbitrary quantum-well potential profiles using the transfer matrix method", *IEEE J. Quantum Electron.*, vol. 26, no. 11, pp. 2025–2035, 1990. DOI: 10.1109/3.62122.
- [274] E. Cassan, "On the reduction of direct tunneling leakage through ultrathin gate oxides by a one-dimensional Schrödinger–Poisson solver", *J. Appl. Phys.*, vol. 87, no. 11, pp. 7931–7939, 2000. DOI: 10.1063/1.373477.

- [275] C. Juang, K. J. Kuhn, and R. B. Darling, "Stark shift and field-induced tunneling in $Al_xGa_{1-x}As/GaAs$ quantum-well structures", *Phys. Rev. B*, vol. 41, pp. 12 047–12 053, 1990. DOI: 10.1103/PhysRevB.41 .12047.
- [276] W. R. Frensley, "VLSI electronics: Microstructure science", in *Heterostructures and Quantum Devices*, F. W. R. and E. N. G., Eds. Academic Press, 2014.
- [277] S. Vatannia and G. Gildenblat, "Airy's functions implementation of the transfer-matrix method for resonant tunneling in variably spaced finite superlattices", *IEEE J. Quantum Electron.*, vol. 32, no. 6, pp. 1093–1105, 1996. DOI: 10.1109/3.502388.
- [278] J.-G. S. Demers and R. Maciejko, "Propagation matrix formalism and efficient linear potential solution to Schrödinger's equation", *J. Appl. Phys.*, vol. 90, no. 12, pp. 6120–6129, 2001. DOI: 10.1063/1.1412584.
- [279] H. Li, J. C. Cao, and H. C. Liu, "Effects of design parameters on the performance of terahertz quantum-cascade lasers", *Semicond. Sci. Technol.*, vol. 23, no. 12, p. 125 040, 2008. DOI: 10.1088/0268-1242/23 /12/125040.
- [280] G. Scalari, L. Ajili, J. Faist, H. Beere, E. Linfield, D. Ritchie, and G. Davies, "Far-infrared ($\lambda \approx 87 \mu m$) bound-to-continuum quantum-cascade lasers operating up to 90 K", *Appl. Phys. Lett.*, vol. 82, no. 19, pp. 3165–3167, 2003. DOI: 10.1063/1.1571653.
- [281] M. Graf, G. Scalari, D. Hofstetter, J. Faist, H. Beere, E. Linfield, D. Ritchie, and G. Davies, "Terahertz range quantum well infrared photodetector", *Appl. Phys. Lett.*, vol. 84, no. 4, pp. 475–477, 2004. DOI: 10.1063/1.1641165.
- [282] O. Bonno and J.-L. Thobel, "Monte Carlo modeling of carrier-carrier scattering in semiconductors with nonparabolic bands", *J. Appl. Phys.*, vol. 104, no. 5, p. 053719, 2008. DOI: 10.1063/1.2976170.
- [283] H. Tanimoto, N. Yasuda, K. Taniguchi, and C. Hamaguchi, "Monte Carlo study of hot electron transport in quantum wells", *Jpn. J. Appl. Phys.*, vol. 27, no. 4R, p. 563, 1988. DOI: 10.1143/JJAP.27.563.
- [284] C. E. Rasmussen, "Gaussian Processes in Machine Learning", in *Advanced Lectures on Machine Learning*, O. Bousquet, U. von Luxburg, and G. Rätsch, Eds., Berlin, Heidelberg: Springer Berlin Heidelberg, 2004, pp. 63–71.
- [285] M. A. Gelbart, J. Snoek, and R. P. Adams, *Bayesian optimization with unknown constraints*, arXiv: 1403.5607, 2014.
- [286] T. Kuhn and F. Rossi, "Monte Carlo simulation of ultrafast processes in photoexcited semiconductors: Coherent and incoherent dynamics", *Phys. Rev. B*, vol. 46, pp. 7496–7514, 1992. DOI: 10.1103/PhysRe vB.46.7496.
- [287] D. O. Winge, M. Franckié, C. Verdozzi, A. Wacker, and M. F. Pereira, "Simple electron-electron scattering in non-equilibrium Green's function simulations", in *J. Phys.: Conf. Ser.*, IOP Publishing, vol. 696, 2016, p. 012 013. DOI: 10.1088/1742-6596/696/1/012013.
- [288] T. Schmielau and J. Pereira M. F., "Nonequilibrium many body theory for quantum transport in terahertz quantum cascade lasers", *Appl. Phys. Lett.*, vol. 95, no. 23, p. 231 111, 2009. DOI: 10.1063/1.3272675.
- [289] T. Kuhn, "Density matrix theory of coherent ultrafast dynamics", in *Theory of Transport Properties of Semiconductor Nanostructures*, E. Schöll, Ed. Boston, MA: Springer US, 1998, pp. 173–214. DOI: 10.1007/978-1-4615-5807-1_6.
- [290] R. C. Iotti and F. Rossi, "Nature of charge transport in quantum-cascade lasers", *Phys. Rev. Lett.*, vol. 87, p. 146 603, 2001. DOI: 10.1103/PhysRevLett.87.146603.
- [291] R. C. Iotti and F. Rossi, "Microscopic theory of semiconductor-based optoelectronic devices", *Rep. Prog. Phys.*, vol. 68, no. 11, p. 2533, 2005. DOI: 10.1088/0034-4885/68/11/R02.
- [292] C. Weber, A. Wacker, and A. Knorr, "Density-matrix theory of the optical dynamics and transport in quantum cascade structures: The role of coherence", *Phys. Rev. B*, vol. 79, p. 165 322, 2009. DOI: 10.1103/PhysRevB.79.165322.

- [293] S. Fathololoumi, E. Dupont, C. Chan, Z. Wasilewski, S. Laframboise, D. Ban, A. Mátyás, C. Jirauschek, Q. Hu, and H. C. Liu, "Terahertz quantum cascade lasers operating up to ~ 200 K with optimized oscillator strength and improved injection tunneling", *Opt. Express*, vol. 20, no. 4, pp. 3866–3876, 2012. DOI: 10.1364/OE.20.003866.
- [294] S. Kumar and Q. Hu, "Coherence of resonant-tunneling transport in terahertz quantum-cascade lasers", *Phys. Rev. B*, vol. 80, p. 245 316, 2009. DOI: 10.1103/PhysRevB.80.245316.
- [295] E. Dupont, S. Fathololoumi, and H. C. Liu, "Simplified density-matrix model applied to three-well terahertz quantum cascade lasers", *Phys. Rev. B*, vol. 81, p. 205 311, 2010. DOI: 10.1103/PhysRevB.81.205311.
- [296] J. R. Freeman, J. Maysonnave, S. Khanna, E. H. Linfield, A. G. Davies, S. S. Dhillon, and J. Tignon, "Laser-seeding dynamics with few-cycle pulses: Maxwell-Bloch finite-difference time-domain simulations of terahertz quantum cascade lasers", *Phys. Rev. A*, vol. 87, p. 063 817, 2013. DOI: 10.1103/Phys RevA.87.063817.
- [297] P. Harrison and A. Valavanis, *Quantum wells, wires and dots: theoretical and computational physics of semiconductor nanostructures.* John Wiley & Sons, 2016.
- [298] H. Callebaut, S. Kumar, B. S. Williams, Q. Hu, and J. L. Reno, "Importance of electron-impurity scattering for electron transport in terahertz quantum-cascade lasers", *Appl. Phys. Lett.*, vol. 84, no. 5, pp. 645–647, 2004. DOI: 10.1063/1.1644337.
- [299] R. Nelander and A. Wacker, "Temperature dependence of the gain profile for terahertz quantum cascade lasers", *Appl. Phys. Lett.*, vol. 92, no. 8, p. 081 102, 2008. DOI: 10.1063/1.2884686.
- [300] R. Nelander and A. Wacker, "Temperature dependence and screening models in quantum cascade structures", *J. Appl. Phys.*, vol. 106, no. 6, p. 063 115, 2009. DOI: 10.1063/1.3226072.
- [301] C. Jirauschek and P. Lugli, "Monte-Carlo-based spectral gain analysis for terahertz quantum cascade lasers", *J. Appl. Phys.*, vol. 105, no. 12, p. 123 102, 2009. DOI: 10.1063/1.3147943.
- [302] T. Kubis, S. R. Mehrotra, and G. Klimeck, "Design concepts of terahertz quantum cascade lasers: Proposal for terahertz laser efficiency improvements", *Appl. Phys. Lett.*, vol. 97, no. 26, p. 261 106, 2010. DOI: 10.1063/1.3524197.
- [303] C. Deutsch, H. Detz, T. Zederbauer, A. M. Andrews, P. Klang, T. Kubis, G. Klimeck, M. E. Schuster, W. Schrenk, G. Strasser, and K. Unterrainer, "Probing scattering mechanisms with symmetric quantum cascade lasers", *Opt. Express*, vol. 21, no. 6, pp. 7209–7215, 2013. DOI: 10.1364/OE.21.007209.
- [304] M. Franckié, D. O. Winge, J. Wolf, V. Liverini, E. Dupont, V. Trinité, J. Faist, and A. Wacker, "Impact of interface roughness distributions on the operation of quantum cascade lasers", *Opt. Express*, vol. 23, no. 4, pp. 5201–5212, 2015. DOI: 10.1364/OE.23.005201.
- [305] B. S. Williams, H. Callebaut, S. Kumar, Q. Hu, and J. L. Reno, "3.4-THz quantum cascade laser based on longitudinal-optical-phonon scattering for depopulation", *Appl. Phys. Lett.*, vol. 82, no. 7, pp. 1015–1017, 2003. DOI: 10.1063/1.1554479.
- [306] M. Moško, A. Mošková, and V. Cambel, "Carrier-carrier scattering in photoexcited intrinsic GaAs quantum wells and its effect on femtosecond plasma thermalization", *Phys. Rev. B*, vol. 51, pp. 16860–16866, 1995. DOI: 10.1103/PhysRevB.51.16860.
- [307] S. M. Goodnick and P. Lugli, "Effect of electron-electron scattering on nonequilibrium transport in quantum-well systems", *Phys. Rev. B*, vol. 37, pp. 2578–2588, 1988. DOI: 10.1103/PhysRevB.37.2578.
- [308] R. C. Iotti and F. Rossi, "Carrier thermalization versus phonon-assisted relaxation in quantum-cascade lasers: A Monte Carlo approach", *Appl. Phys. Lett.*, vol. 78, no. 19, pp. 2902–2904, 2001. DOI: 10.1063/1.1370537.
- [309] C. Jirauschek, A. Mátyás, and P. Lugli, "Modeling bound-to-continuum terahertz quantum cascade lasers: The role of Coulomb interactions", *J. Appl. Phys.*, vol. 107, no. 1, p. 013104, 2010. DOI: 10.1063/1.3276160.

- [310] C. Jirauschek, "Universal quasi-level parameter for the characterization of laser operation", *IEEE Photonics J.*, vol. 10, no. 4, p. 1503 209, 2018. DOI: 10.1109/JPHOT.2018.2863025.
- [311] A. Delga, L. Doyennette, M. Carras, V. Trinité, and P. Bois, "Johnson and shot noises in intersubband detectors", *Appl. Phys. Lett.*, vol. 102, no. 16, p. 163 507, 2013. DOI: 10.1063/1.4803447.
- [312] A. Buffaz, A. Gomez, M. Carras, L. Doyennette, and V. Berger, "Role of subband occupancy on electronic transport in quantum cascade detectors", *Phys. Rev. B*, vol. 81, no. 7, p. 075 304, 2010. DOI: 10.1103/PhysRevB.81.075304.
- [313] M. S. Vitiello, G. Scamarcio, V. Spagnolo, B. S. Williams, S. Kumar, Q. Hu, and J. L. Reno, "Measurement of subband electronic temperatures and population inversion in THz quantum-cascade lasers", *Appl. Phys. Lett.*, vol. 86, no. 11, p. 111 115, 2005. DOI: 10.1063/1.1886266.
- [314] T. Ando, "Broadening of inter-subband transitions in image-potential-induced surface states outside liquid Helium", *J. Phys. Soc. Jpn.*, vol. 44, no. 3, pp. 765–773, 1978. DOI: 10.1143/JPSJ.44.765.
- [315] T. Ando, "Line width of inter-subband absorption in inversion layers: Scattering from charged ions", *J. Phys. Soc. Jpn.*, vol. 54, no. 7, pp. 2671–2675, 1985. DOI: 10.1143/JPSJ.54.2671.
- [316] T. Unuma, M. Yoshita, T. Noda, H. Sakaki, and H. Akiyama, "Intersubband absorption linewidth in GaAs quantum wells due to scattering by interface roughness, phonons, alloy disorder, and impurities", *J. Appl. Phys.*, vol. 93, no. 3, pp. 1586–1597, 2003. DOI: 10.1063/1.1535733.
- [317] W. Freeman, "Self-consistent calculation of dephasing in quantum cascade structures within a density matrix method", *Phys. Rev. B*, vol. 93, p. 205 301, 2016. DOI: 10.1103/PhysRevB.93.205301.
- [318] C. Jirauschek, H. Okeil, and P. Lugli, "Monte Carlo analysis of the terahertz difference frequency generation susceptibility in quantum cascade laser structures", *Opt. Express*, vol. 23, no. 2, pp. 1670–1678, 2015. DOI: 10.1364/OE.23.001670.
- [319] C. Jirauschek, A. Mátyás, P. Lugli, and M.-C. Amann, "Monte Carlo study of terahertz difference frequency generation in quantum cascade lasers", *Opt. Express*, vol. 21, no. 5, pp. 6180–6185, 2013. DOI: 10.1364/OE.21.006180.
- [320] M. O. Scully and M. S. Zubairy, *Quantum Optics*. Cambridge, UK: Cambridge University Press, 1997.
- [321] D. Marcuse, "Computer simulation of laser photon fluctuations: Theory of single-cavity laser", *IEEE J. Quantum Electron.*, vol. 20, no. 10, pp. 1139–1148, 1984. DOI: 10.1109/JQE.1984.1072276.
- [322] M. Lax and H. Yuen, "Quantum noise. XIII. Six-classical-variable description of quantum laser fluctuations", *Phys. Rev.*, vol. 172, pp. 362–371, 1968. DOI: 10.1103/PhysRev.172.362.
- [323] P. D. Drummond and M. Hillery, "Phase-space distributions", in *The Quantum Theory of Nonlinear Optics*. Cambridge University Press, 2014, pp. 217–255. DOI: 10.1017/CBO9780511783616.009.
- [324] S. Mandt, D. Sadri, A. A. Houck, and H. E. Türeci, "Stochastic differential equations for quantum dynamics of spin-boson networks", *New J. Phys.*, vol. 17, no. 5, p. 053 018, 2015. DOI: 10.1088/1367-2630/17/5/053018.
- [325] P. D. Drummond and C. W. Gardiner, "Generalised P-representations in quantum optics", *J. Phys. A: Math. Gen.*, vol. 13, no. 7, p. 2353, 1980. DOI: 10.1088/0305-4470/13/7/018.
- [326] L. Seitner, J. Popp, M. Riesch, M. Haider, and C. Jirauschek, "Group velocity dispersion in terahertz frequency combs within a generalized Maxwell-Bloch framework", *J. Phys.: Conf. Ser.*, vol. 2090, no. 1, p. 012 082, 2021. DOI: 0.1088/1742-6596/2090/1/012082.
- [327] M. Riesch, *Qclsip: The quantum cascade laser stock image project*, Jul. 2019. DOI: 10.5281/zenodo.32 65933.
- [328] M. Riesch and C. Jirauschek, "Analyzing the positivity preservation of numerical methods for the Liouville-von Neumann equation", *J. Comput. Phys.*, vol. 390, pp. 290–296, 2019. DOI: 10.1016/j.jcp .2019.04.006.

- [329] M. Riesch, N. Tchipev, S. Senninger, H.-J. Bungartz, and C. Jirauschek, "Performance evaluation of numerical methods for the Maxwell–Liouville–von Neumann equations", *Opt. Quant. Electron.*, vol. 50, no. 2, p. 112, 2018. DOI: 10.1007/s11082-018-1377-4.
- [330] M. Riesch, T. D. Nguyen, and C. Jirauschek, "Bertha: Project skeleton for scientific software", *PLOS ONE*, vol. 15, no. 3, e0230557, 2020. DOI: 10.1371/journal.pone.0230557.
- [331] M. Riesch, "On the modeling and simulation of the dynamical behavior of quantum cascade lasers", Ph.D. dissertation, Technische Universität München, 2023.
- [332] R. W. Ziolkowski, J. M. Arnold, and D. M. Gogny, "Ultrafast pulse interactions with two-level atoms", *Phys. Rev. A*, vol. 52, pp. 3082–3094, 1995. DOI: 10.1103/PhysRevA.52.3082.
- [333] G. Slavcheva, J. M. Arnold, I. Wallace, and R. W. Ziolkowski, "Coupled Maxwell-pseudospin equations for investigation of self-induced transparency effects in a degenerate three-level quantum system in two dimensions: Finite-difference time-domain study", *Phys. Rev. A*, vol. 66, p. 063418, 2002. DOI: 10.1103/PhysRevA.66.063418.
- [334] R. Marskar and U. Österberg, "Multilevel Maxwell-Bloch simulations in inhomogeneously broadened media", *Opt. Express*, vol. 19, no. 18, pp. 16784–16796, 2011. DOI: 10.1364/OE.19.016784.
- [335] B. Bidégaray, "Time discretizations for Maxwell-Bloch equations", *Numer. Methods for Partial Differ. Equ.*, vol. 19, no. 3, pp. 284–300, 2003. DOI: 10.1002/num.10046.
- [336] A. Bourgeade and O. Saut, "Numerical methods for the bidimensional Maxwell-Bloch equations in nonlinear crystals", *J. Comput. Phys.*, vol. 213, no. 2, pp. 823–843, 2006. DOI: 10.1016/j.jcp.2005.09.0 03.
- [337] B. Hellsing and H. Metiu, "An efficient method for solving the quantum Liouville equation: Applications to electronic absorption spectroscopy", *Chem. Phys. Lett.*, vol. 127, no. 1, pp. 45–49, 1986. DOI: 10.10 16/S0009-2614(86)80206-8.
- [338] M. Berman, R. Kosloff, and H. Tal-Ezer, "Solution of the time-dependent Liouville-von Neumann equation: Dissipative evolution", *J. Phys. A: Math. Gen.*, vol. 25, no. 5, p. 1283, 1992. DOI: 10.1088/03 05-4470/25/5/031.
- [339] W. Cartar, J. Mørk, and S. Hughes, "Self-consistent Maxwell-Bloch model of quantum-dot photonic-crystal-cavity lasers", *Phys. Rev. A*, vol. 96, p. 023 859, 2017. DOI: 10.1103/PhysRevA.96.023859.
- [340] M. Sukharev and A. Nitzan, "Numerical studies of the interaction of an atomic sample with the electromagnetic field in two dimensions", *Phys. Rev. A*, vol. 84, p. 043 802, 2011. DOI: 10.1103/Phys RevA.84.043802.
- [341] A. Deinega and T. Seideman, "Self-interaction-free approaches for self-consistent solution of the Maxwell-Liouville equations", *Phys. Rev. A*, vol. 89, p. 022501, 2014. DOI: 10.1103/PhysRevA.8 9.022501.
- [342] M. E. Songolo and B. Bidégaray-Fesquet, "Nonstandard finite-difference schemes for the two-level Bloch model", *Int. J. Model. Simul. Sci. Comput.*, vol. 09, no. 04, p. 1850033, 2018. DOI: 10.1142/S17 93962318500332.
- [343] B. Bidégaray, A. Bourgeade, and D. Reignier, "Introducing physical relaxation terms in Bloch equations", *J. Comput. Phys.*, vol. 170, no. 2, pp. 603–613, 2001. DOI: 10.1006/jcph.2001.6752.
- [344] F. T. Hioe and J. H. Eberly, "*N*-level coherence vector and higher conservation laws in quantum optics and quantum mechanics", *Phys. Rev. Lett.*, vol. 47, pp. 838–841, 1981. DOI: 10.1103/PhysRevLett.47.838.
- [345] A. Klaedtke and O. Hess, "Ultrafast nonlinear dynamics of whispering-gallery mode micro-cavity lasers", *Opt. Express*, vol. 14, no. 7, pp. 2744–2752, 2006. DOI: 10.1364/OE.14.002744.
- [346] K. Lopata and D. Neuhauser, "Nonlinear nanopolaritonics: Finite-difference time-domain Maxwell-Schrödinger simulation of molecule-assisted plasmon transfer", *J. Chem. Phys.*, vol. 131, no. 1, p. 014 701, 2009. DOI: 10.1063/1.3167407.

- [347] M. Dridi and G. C. Schatz, "Model for describing plasmon-enhanced lasers that combines rate equations with finite-difference time-domain", *J. Opt. Soc. Am. B*, vol. 30, no. 11, pp. 2791–2797, 2013. DOI: 10.1364/JOSAB.30.002791.
- [348] S. Hughes, "Breakdown of the area theorem: Carrier-wave Rabi flopping of femtosecond optical pulses", *Phys. Rev. Lett.*, vol. 81, pp. 3363–3366, 1998. DOI: 10.1103/PhysRevLett.81.3363.
- [349] G. Slavcheva, J. Arnold, and R. Ziolkowski, "Ultrashort pulse lossless propagation through a degenerate three-level medium in nonlinear optical waveguides and semiconductor microcavities", *IEEE J. Sel. Top. Quantum Electron.*, vol. 9, no. 3, pp. 929–938, 2003. DOI: 10.1109/JSTQE.2003.818844.
- [350] F. Schlottau, M. Piket-May, and K. Wagner, "Modeling of femtosecond pulse interaction with inhomogeneously broadened media using an iterative predictor corrector FDTD method", *Opt. Express*, vol. 13, no. 1, pp. 182–194, 2005. DOI: 10.1364/OPEX.13.000182.
- [351] S. Krishnamoorthy, M. Baskaran, U. Bondhugula, J. Ramanujam, A. Rountev, and P. Sadayappan, "Effective automatic parallelization of stencil computations", *SIGPLAN Not.*, vol. 42, no. 6, pp. 235–244, 2007. DOI: 10.1145/1273442.1250761.
- [352] M. Riesch, N. Tchipev, H.-J. Bungartz, and C. Jirauschek, "Numerical simulation of the quantum cascade laser dynamics on parallel architectures", in *Proceedings of the Platform for Advanced Scientific Computing Conference*, Zurich, Switzerland: ACM, 2019. DOI: 10.1145/3324989.3325715.
- [353] A. Taflove and S. C. Hagness, *Computational Electrodynamics: The Finite-Difference Time-Domain Method*, 3rd ed. Artech House, Boston, 2005.
- [354] J.-P. Berenger, "A perfectly matched layer for the absorption of electromagnetic waves", *J. Comput. Phys.*, vol. 114, no. 2, pp. 185–200, 1994.
- [355] J. Fang and Z. Wu, "Generalized perfectly matched layer-an extension of Berenger's perfectly matched layer boundary condition", *IEEE Microw. Wirel. Compon. Lett.*, vol. 5, no. 12, pp. 451–453, 1995. DOI: 10.1109/75.481858.
- [356] J. Fang and Z. Wu, "Generalized perfectly matched layer for the absorption of propagating and evanescent waves in lossless and lossy media", *IEEE Trans. Microw. Theory Tech.*, vol. 44, no. 12, pp. 2216–2222, 1996. DOI: 10.1109/22.556449.
- [357] S. D. Gedney, "An anisotropic perfectly matched layer-absorbing medium for the truncation of FDTD lattices", *IEEE Trans. Antennas Propag.*, vol. 44, no. 12, pp. 1630–1639, 1996. DOI: 10.1109/8.546249.
- [358] S. D. Gedney, "An anisotropic PML absorbing media for the FDTD simulation of fields in lossy and dispersive media", *Electromagnetics*, vol. 16, no. 4, pp. 399–415, 1996. DOI: 10.1080/0272634960890 8487.
- [359] Q. Wang and S.-T. Ho, "Implementation of perfectly matched layer boundary condition for finite-difference time-domain simulation truncated with gain medium", *J. Lightwave Technol.*, vol. 29, no. 10, pp. 1453–1459, 2011. DOI: 10.1109/JLT.2011.2126559.
- [360] J. Popp, L. Seitner, M. Haider, and C. Jirauschek, "Reducing the reflection error of PML absorbing boundary conditions within a generalized Maxwell-Bloch framework", in 2022 3rd URSI Atlantic and Asia Pacific Radio Science Meeting (AT-AP-RASC), 2022, pp. 1–4. DOI: 10.23919/AT-AP-RASC5473 7.2022.9814330.
- [361] M. A. Schreiber, J. Popp, L. Seitner, M. Haider, and C. Jirauschek, "Implementation of partially reflecting boundary conditions in the generalized Maxwell-Bloch equations", in *2022 International Conference on Numerical Simulation of Optoelectronic Devices (NUSOD)*, IEEE, 2022, pp. 99–100. DOI: 10.1109/NUSOD54938.2022.9894839.
- [362] H. Choi, J.-W. Baek, and K.-Y. Jung, "Comprehensive study on numerical aspects of modified Lorentz model-based dispersive FDTD formulations", *IEEE Trans. Antennas Propag.*, vol. 67, no. 12, pp. 7643–7648, 2019. DOI: 10.1109/TAP.2019.2934779.

- [363] J. Chochol, K. Postava, M. Čada, M. Vanwolleghem, M. Mičica, L. Halagačka, J.-F. Lampin, and J. Pištora, "Plasmonic behavior of III-V semiconductors in far-infrared and terahertz range", *J. Eur. Opt. Soc.-Rapid Publ.*, vol. 13, no. 13, p. 13, 2017. DOI: 10.1186/s41476-017-0044-x.
- [364] [SW] The HDF Group, *Hierarchical Data Format, version 5*, vcs: https://github.com/HDFGroup/hdf5.
- [365] [SW] The Blue Brain Project, *HighFive HDF5 header-only C++ Library* 2024, vcs: https://github.com/BlueBrain/HighFive.
- [366] K. Yee, "Numerical solution of initial boundary value problems involving Maxwell's equations in isotropic media", *IEEE Trans. Antennas Propag.*, vol. 14, no. 3, pp. 302–307, 1966. DOI: 10.1109 /TAP.1966.1138693.
- [367] G. Strang, "On the construction and comparison of difference schemes", SIAM J. Numer. Anal., vol. 5, no. 3, pp. 506–517, 1968. DOI: 10.1137/0705041.
- [368] R. Courant and D. Hilbert, Methods of Mathematical Physics. Wiley-VCH, Weilheim, 2004, vol. 1.
- [369] [SW] G. Guennebaud, B. Jacob, et al., Eigen v3 2010, vcs: https://gitlab.com/libeigen/eigen.
- [370] [SW] M. Lee et al., EigenRand: The Fastest C++11-compatible random distribution generator for Eigen 2023, vcs: https://github.com/bab2min/EigenRand.
- [371] F. Haake, H. King, G. Schröder, J. Haus, and R. Glauber, "Fluctuations in superfluorescence", *Phys. Rev. A*, vol. 20, pp. 2047–2063, 1979. DOI: 10.1103/PhysRevA.20.2047.
- [372] M. S. Malcuit, J. J. Maki, D. J. Simkin, and R. W. Boyd, "Transition from superfluorescence to amplified spontaneous emission", *Phys. Rev. Lett.*, vol. 59, pp. 1189–1192, 1987. DOI: 10.1103/PhysRevLett.59 .1189.
- [373] J. J. Maki, M. S. Malcuit, M. G. Raymer, R. W. Boyd, and P. D. Drummond, "Influence of collisional dephasing processes on superfluorescence", *Phys. Rev. A*, vol. 40, pp. 5135–5142, 1989. DOI: 10.1103 /PhysRevA.40.5135.
- [374] D. P. Burghoff, "Broadband terahertz photonics", Ph.D. dissertation, Massachusetts Institute of Technology, 2014.
- [375] N. Jukam, S. Dhillon, Z.-Y. Zhao, G. Duerr, J. Armijo, N. Sirmons, S. Hameau, S. Barbieri, P. Filloux, C. Sirtori, X. Marcadet, and J. Tignon, "Gain measurements of THz quantum cascade lasers using THz time-domain spectroscopy", *IEEE J. Sel. Top. Quantum Electron.*, vol. 14, no. 2, pp. 436–442, 2008. DOI: 10.1109/JSTQE.2007.911761.
- [376] M. Martl, J. Darmo, C. Deutsch, M. Brandstetter, A. M. Andrews, P. Klang, G. Strasser, and K. Unterrainer, "Gain and losses in THz quantum cascade laser with metal-metal waveguide", *Opt. Express*, vol. 19, no. 2, pp. 733–738, 2011. DOI: 10.1364/OE.19.000733.
- [377] S. Adachi, *Optical Properties of Crystalline and Amorphous Semiconductors: Materials and Fundamental Principles.* Springer Science & Business Media, New York, 1999. DOI: 10.1007/978-1-4615-5241-3.
- [378] D. Burghoff, Y. Yang, D. J. Hayton, J.-R. Gao, J. L. Reno, and Q. Hu, "Evaluating the coherence and time-domain profile of quantum cascade laser frequency combs", *Opt. Express*, vol. 23, no. 2, pp. 1190–1202, 2015. DOI: 10.1364/OE.23.001190.
- [379] F. R. Giorgetta, E. Baumann, R. Théron, M. Pellaton, D. Hofstetter, M. Fischer, and J. Faist, "Short wavelength (4 μm) quantum cascade detector based on strain compensated InGaAs/InAlAs", *Appl. Phys. Lett.*, vol. 92, no. 12, p. 121 101, 2008. DOI: 10.1063/1.2902301.
- [380] D. Hofstetter, F. R. Giorgetta, E. Baumann, Q. Yang, C. Manz, and K. Köhler, "Mid-infrared quantum cascade detectors for applications in spectroscopy and pyrometry", in *Proc. Of SPIE*, International Society for Optics and Photonics, vol. 7608, 2010, 76081N. DOI: 10.1117/12.853351.
- [381] N. Mott, "Electrons in disordered structures", *Adv. Phys.*, vol. 16, no. 61, pp. 49–144, 1967. DOI: 10.1080/00018736700101265.

- [382] J. Palmier, H. Le Person, C. Minot, A. Chomette, A. Regreny, and D. Calecki, "Hopping mobility in semiconductor superlattices", *Superlattices Microst.*, vol. 1, no. 1, pp. 67–72, 1985. DOI: 10.1016/0749 -6036(85)90031-X.
- [383] O. Bonno, J.-L. Thobel, and F. Dessenne, "Modeling of electron-electron scattering in Monte Carlo simulation of quantum cascade lasers", *J. Appl. Phys.*, vol. 97, no. 4, p. 043702, 2005. DOI: 10.1063/1.1840100.
- [384] H. Willenberg, G. H. Döhler, and J. Faist, "Intersubband gain in a Bloch oscillator and quantum cascade laser", *Phys. Rev. B*, vol. 67, p. 085315, 2003. DOI: 10.1103/PhysRevB.67.085315.
- [385] J. Popp, M. Haider, M. Franckié, J. Faist, and C. Jirauschek, "Monte Carlo modeling of a short wavelength strain compensated quantum cascade detector", in 2021 Conference on Lasers and Electro-Optics Europe & European Quantum Electronics Conference (CLEO/Europe-EQEC), 2021, pp. 1–1. DOI: 10.1109/CLEO/Europe-EQEC52157.2021.9542111.
- [386] M. Lindskog, J. Wolf, V. Trinite, V. Liverini, J. Faist, G. Maisons, M. Carras, R. Aidam, R. Ostendorf, and A. Wacker, "Comparative analysis of quantum cascade laser modeling based on density matrices and non-equilibrium Green's functions", *Appl. Phys. Lett.*, vol. 105, no. 10, p. 103 106, 2014. DOI: 10.1063/1.4895123.
- [387] M. Franckié, L. Bosco, M. Beck, C. Bonzon, E. Mavrona, G. Scalari, A. Wacker, and J. Faist, "Two-well quantum cascade laser optimization by non-equilibrium Green's function modelling", *Appl. Phys. Lett.*, vol. 112, no. 2, p. 021 104, 2018. DOI: 10.1063/1.5004640.
- [388] G. Pegolotti, A. Vasanelli, Y. Todorov, and C. Sirtori, "Quantum model of coupled intersubband plasmons", *Phys. Rev. B*, vol. 90, p. 035 305, 2014. DOI: 10.1103/PhysRevB.90.035305.
- [389] H. Beere, J. Fowler, J. Alton, E. Linfield, D. Ritchie, R. Köhler, A. Tredicucci, G. Scalari, L. Ajili, J. Faist, *et al.*, "MBE growth of terahertz quantum cascade lasers", *J. Cryst. Growth*, vol. 278, no. 1-4, pp. 756–764, 2005.
- [390] C. Henry, "Theory of the linewidth of semiconductor lasers", *IEEE J. Quantum Electron.*, vol. 18, no. 2, pp. 259–264, 1982. DOI: 10.1109/JQE.1982.1071522.
- [391] C. Jirauschek, "Monte Carlo study of intrinsic linewidths in terahertz quantum cascade lasers", *Opt. Express*, vol. 18, no. 25, pp. 25 922–25 927, 2010. DOI: 10.1364/OE.18.025922.
- [392] M. Franckié, M. Bertrand, and J. Faist, "Sensitive dependence of the linewidth enhancement factor on electronic quantum effects in quantum cascade lasers", *Appl. Phys. Lett.*, vol. 122, no. 2, p. 021 107, 2023. DOI: 10.1063/5.0111599.
- [393] X. Qi, K. Bertling, T. Taimre, G. Agnew, Y. L. Lim, T. Gillespie, A. Robinson, M. Brünig, A. Demić, P. Dean, L. H. Li, E. H. Linfield, A. G. Davies, D. Indjin, and A. D. Rakić, "Observation of optical feedback dynamics in single-mode terahertz quantum cascade lasers: Transient instabilities", *Phys. Rev. A*, vol. 103, p. 033 504, 2021. DOI: 10.1103/PhysRevA.103.033504.
- [394] Y. Leng Lim, P. Dean, M. Nikolić, R. Kliese, S. P. Khanna, M. Lachab, A. Valavanis, D. Indjin, Z. Ikonić, P. Harrison, E. H. Linfield, A. Giles Davies, S. J. Wilson, and A. D. Rakić, "Demonstration of a self-mixing displacement sensor based on terahertz quantum cascade lasers", *Appl. Phys. Lett.*, vol. 99, no. 8, p. 081 108, 2011. doi: 10.1063/1.3629991.
- [395] T. Aellen, R. Maulini, R. Terazzi, N. Hoyler, M. Giovannini, J. Faist, S. Blaser, and L. Hvozdara, "Direct measurement of the linewidth enhancement factor by optical heterodyning of an amplitude-modulated quantum cascade laser", *Appl. Phys. Lett.*, vol. 89, no. 9, p. 091 121, 2006. DOI: 10.1063/1.2345035.
- [396] S. Kohen, B. S. Williams, and Q. Hu, "Electromagnetic modeling of terahertz quantum cascade laser waveguides and resonators", *J. Appl. Phys.*, vol. 97, no. 5, p. 053 106, 2005. DOI: 10.1063/1.1855394.
- [397] K. Fujita, S. Furuta, A. Sugiyama, T. Ochiai, A. Ito, T. Dougakiuchi, T. Edamura, and M. Yamanishi, "High-performance quantum cascade lasers with wide electroluminescence (~ 600 cm⁻¹), operating in continuous-wave above 100 °C", *Appl. Phys. Lett.*, vol. 98, no. 23, p. 231 102, 2011. DOI: 10.1063/1.35 96706.

- [398] S. Tsujino, A. Borak, E. Müller, M. Scheinert, C. Falub, H. Sigg, D. Grützmacher, M. Giovannini, and J. Faist, "Interface-roughness-induced broadening of intersubband electroluminescence in p-SiGe and n-GaInAs/ AlInAs quantum-cascade structures", *Appl. Phys. Lett.*, vol. 86, no. 6, p. 062 113, 2005. DOI: 10.1063/1.1862344.
- [399] A. Wittmann, Y. Bonetti, J. Faist, E. Gini, and M. Giovannini, "Intersubband linewidths in quantum cascade laser designs", *Appl. Phys. Lett.*, vol. 93, no. 14, p. 141 103, 2008. DOI: 10.1063/1.2993212.
- [400] K. Fujita, S. Furuta, A. Sugiyama, T. Ochiai, T. Edamura, N. Akikusa, M. Yamanishi, and H. Kan, "High-performance $\lambda \sim 8.6\,\mu m$ quantum cascade lasers with single phonon-continuum depopulation structures", *IEEE J. Quantum Electron.*, vol. 46, no. 5, pp. 683–688, 2010. DOI: 10.1109/JQE.2010.20 48015.
- [401] C. Gmachl, F. Capasso, J. Faist, A. L. Hutchinson, A. Tredicucci, D. L. Sivco, J. N. Baillargeon, S. G. Chu, and A. Y. Cho, "Continuous-wave and high-power pulsed operation of index-coupled distributed feedback quantum cascade laser at $\lambda \approx 8.5 \ \mu m$ ", *Appl. Phys. Lett.*, vol. 72, no. 12, pp. 1430–1432, 1998. DOI: 10.1063/1.120585.
- [402] H. Kogelnik and C. Shank, "Coupled-wave theory of distributed feedback lasers", *J. Appl. Phys.*, vol. 43, no. 5, pp. 2327–2335, 1972. DOI: 10.1063/1.1661499.
- [403] H. Li, P. Laffaille, D. Gacemi, M. Apfel, C. Sirtori, J. Leonardon, G. Santarelli, M. Rösch, G. Scalari, M. Beck, J. Faist, W. Hänsel, R. Holzwarth, and S. Barbieri, "Dynamics of ultra-broadband terahertz quantum cascade lasers for comb operation", *Opt. Express*, vol. 23, no. 26, pp. 33 270–33 294, 2015. DOI: 10.1364/OE.23.033270.
- [404] T. Herr, K. Hartinger, J. Riemensberger, C. Wang, E. Gavartin, R. Holzwarth, M. Gorodetsky, and T. Kippenberg, "Universal formation dynamics and noise of Kerr-frequency combs in microresonators", *Nature Photon.*, vol. 6, no. 7, pp. 480–487, 2012. DOI: 10.1038/nphoton.2012.127.

List of Symbols and Acronyms

 α Linewidth enhancement factor

 α, β Strain parameters

 α', β' Nonparabolicity parameters

 α_0 Linear loss term

 $\alpha_{\rm p}$ Power absorption coefficient

 $\alpha_{\rm V}, \beta_{\rm V}$ Varshni parameters

 $\chi, \chi^{(2)}, \chi^{(3)}$ Nonlinear susceptibility, second- and third-order

Δ Standard deviation of interface roughness

 Δ_E Energy subintervals

 Δ_{ij} Energy separation between levels i and j

 ΔN , ΔN_i Population inversion density (of level i)

 Δn Modulation of the modal refractive index $n_{\rm eff}$

 Δ_n Length of the *n*th segment

 $\Delta\Omega/\Omega$ Volume change arising from biaxial strain

 Δ_{SO} Spin-orbit splitting

 $\Delta \hat{V}_{tb}$ Coupling of electron states in two adjacent periods within the tight-binding model

 Δt Temporal discretization size

 Δx Spatial discretization size

 Δ_z Uniform grid spacing

 δ Damping constant

 δE Electric field values of the thermal noise sources

 δ_{th} RMS amplitude of the noise field

 $\epsilon,\,\epsilon_\parallel,\,\epsilon_\perp$ Strain tensor, in-plane and perpendicular strain

 ϵ_i Energy of level i

 $\epsilon_{\rm n}$ Gaussian noise term

 ε Permittivity, $\varepsilon = \varepsilon_0 \varepsilon_r$

 ε_0 Vacuum permittivity

 $\varepsilon_{\rm r}, \varepsilon_{\rm r,s}, \varepsilon_{\rm r,\infty}$ Relative permittivity, static, infinite frequency, effective relative permittivity $\varepsilon_{\rm r,eff}$

 η_0 Free-space wave impedance

 η_{abs} Absorption efficiency

 Γ Confinement factor

 γ_i Level broadening of level i

 Γ_{ij} Total dephasing energy between level i and j

 γ_{ij} Dephasing rate between level i and j

 $\gamma_{ij,p}$ Pure dephasing rate between level i and j

 γ_p Inverse of the pole relaxation time

 κ Cavity decay rate; imaginary part of the complex refractive index n

 κ_{DFB} Coupling constant

Λ Interface roughness correlation length

 $\Lambda_{\rm DFB}$ DFB period length

 λ Wavelength

 $\lambda_{\rm B}$ Bragg wavelength

 $\lambda_{\rm P}$ Peak wavelength

 μ Permeability, $\mu = \mu_0 \mu_r$, effective relative permeability $\mu_{r,eff}$

 $\mu(x)$ Mean or expectation of the Gaussian distribution

 μ_0 Vacuum permeability

 $\mu_{\rm c}$ Chemical potential

 ∇ Nabla operator

 Ω Rabi frequency

 ω Angular frequency, $2\pi c/\lambda$

 ω_0 Single mode lasing angular frequency

 $\omega_{\rm c}$ Center frequency

 ω_{ij} Resonance frequency for transition from subband i to j, $(E_i - E_j)/\hbar$

 ω_{LO} LO phonon frequency

 ϕ Angle in xy-plane (Bloch sphere)

 $\phi_{i,k}$ Slowly varying envelope wavefunction of level i

Ψ Atomic wavefunction

 $\Psi_{n,k}$ Bloch theorem state

1D wavefunction of level i $\psi_{i,k}$

 $\hat{\rho}$ Density matrix

Density matrix element, ρ_{ii} is the occupation of level i ρ_{ii}

Bloch vector $\rho_{\rm B}$

Space charge ρ

 $\sigma_{\rm n}$

Population operator, $|i\rangle\langle i|$ $\hat{\sigma}_{ii}$ Coherence operator, $|i\rangle\langle j|$ $\hat{\sigma}_{ii}$

 σ Material conductivity

 σ_0^2 Covariance amplitude

Conductance per unit area between subband i and j σ_{ij}

 σ_1^2 Characteristic length scale Noise standard deviation

Conductance per unit area of a single QCD period σ_{p}

Conductivity in the PML layer σ_{x}

 θ Propagation angle; hyperparameter GP; tipping angle (Bloch sphere)

Cherenkov emission angle $\theta_{\rm c}$

Lifetime of level i τ_i

Simulation time $au_{
m sim}$

 $\boldsymbol{\xi}(t)$ Vector with real, independent Gaussian random numbers

Real and complex Gaussian random numbers ξ_{ij}

 \boldsymbol{A} In-plane cross-sectional area of the quantum wells

 $A_{\rm d}$ Detector area

 $\hat{a}^{\dagger}(\hat{a})$ Creation (annihilation) operator of the radiation field

a(x)Acquisition function

 $a_{\rm c}, a_{\rm v}$ Hydrostatic deformation potential in conduction and valence band

 \boldsymbol{B} Noise matrix

Shear deformation potential $b_{\rm s}$

Ĉ Linear chosen ordering operator

 \boldsymbol{C} Courant number; bowing parameter (ternary alloys)

Speed of light, c_0/n c

 c_0 Speed of light in vacuum

 $\hat{D}_{\mu}, \hat{D}_{\mu}^{c}$ Drift operator, c highlights the chosen order

 $2\langle \hat{D}_{\mu\nu}\rangle_{\rm R}$ Diffusion coefficient in the quantum Langevin equations

D Diffusion matrix

 D, D_z Electric flux density

D* Specific detectivity

 $2\langle D_{\mu\nu}\rangle_{\rm R}$ Diffusion coefficient in the c-number Langevin equations

 $D_{\mu}(t)$ C-number drift term

 D_n Normalized energy density of the blackbody radiation

 \mathcal{D} Dissipation superoperator

 $\hat{d}, \hat{d}_z, \hat{d}$ Dipole moment operator

d Dipole length

 $d_{ij}, d_{ij,z}$ Dipole matrix element for transition from level i to j, $-ez_{ij}$

 $\boldsymbol{E}, \boldsymbol{E}_z$ Electric field

 $E_{\rm act}$ Activation energy

 $E_{\rm c}$ Conduction band edge energy

 $E_{\rm g}$ Bandgap energy

 $E_{\rm in}, E_{\rm out}$ Electric field of the injected seed pulse, recorded electric field

 $E_{\rm p}$ Bias drop over a single QC device period

 $E_{
m v}^{
m HH},\,E_{
m v}^{
m LH},\,E_{
m v}^{
m SO},\,E_{
m V}\,$ Heavy-hole, light-hole and split-off valence band energy

 E_i Eigenenergy of state i

 e_z Unit vector in z direction

e Elementary charge

 $e_{\rm r}$ Reflection error

 $\hat{F}_{\mu}, \hat{F}^{c}_{\mu}$ Fluctuation operator, c highlights the chosen order

F Kane parameter

 F_{ii} , F_{ij} Diagonal and off-diagonal fluctuation terms

 $F_{\mu}(t)$ C-number fluctuation term

 \mathcal{F} Langevin fluctuation superoperator

 $f_{\rm c}$ Center frequency

 f_i Carrier distribution function in subband i

 $f_{\rm rt}$ Roundtrip rate

G Conductance matrix

g Dipole coupling constant

 $g(\omega)$ Power gain coefficient

 g_{ij} Conductance matrix elements

g_p Peak gain value

 \hat{H}' Perturbation Hamiltonian

 \hat{H}_0 Unperturbed Hamiltonian

 $\hat{H}_{\rm F}$ Hamiltonian of the optical field

 \hat{H}_{I} Interaction Hamiltonian

 \hat{H}_{s} System Hamiltonian

 H, H_y Magnetic field

ħ Reduced Planck constant

*I*_{out} Detector photocurrent

K Covariance matrix

k 3D bulk/2D in-plane wavevector

 k, k_x, k_y Wavenumber, x- and y-direction

*k*_B Boltzmann constant

k(x, x') Covariance function

 k_n Wavenumber in segment n

 \tilde{k}_n k_n/m_n^*

 $L_{\mu}(t)$ C-number coherent term corresponding to the commutation of $\hat{A}_{\mu}(t)$ with the system

Hamiltonian \hat{H}_{s}

 $L_{\rm p}$ Length of a single QC device period

L Cavity length

 \mathcal{L} Liouville superoperator

 $M_{\mu}(t) \qquad \qquad L_{\mu}(t) + D_{\mu}(t)$

 m^* Γ -valley effective mass

 $m_{\perp}^{*}, m_{\parallel}^{*}$ Perpendicular and in-plane effective mass

 m_0 Electron mass

 $N_{\rm BL}$ Number of gridpoints in the boundary layer

 N_{cell} Number of carriers in one grid cell

 $N_{\rm p}$ Number of periods

Number of temporal gridpoints

 $N_{\rm x}$ Number of spatial gridpoints

<u>n</u> Complex refractive index, $n + i\kappa$

 n_{3D} Carrier number density

 $n_{\rm D}$ Donor concentration

 n, n_{eff} Refractive index, effective refractive index

 $n_{\rm g}$ Group effective refractive index

 n_i^{2D} 2D density of states per unit area and energy

 $n_{\rm p}$ Number of passes of the optical field through the absorbing region

n^s Total sheet density per QC device period

 $n_i^{\rm s}$ Electron sheet density of level i

 $n_{\rm th}$ Number of thermal photons in the lasing mode

 P, P_z Polarization, macroscopic polarization, classical polarization $P_{z, \text{class}} = \epsilon_0 \chi E_z$

 $P_{z,qm}$ Quantummechanical polarization

P Momentum matrix element

 $P_{\rm all}$ Total optical power

 $P_{\epsilon}^{c}, P_{\epsilon}^{v}$ Relative shift in conduction and valence band energy due to strain

 P_i Optical power of lasing mode i

 $P_{\rm in}$ Incident optical power

 \hat{p} Momentum operator

p Occupation probability vector

*p*_e Extraction efficiency

 p_i Occupation probability of subband i

 \hat{Q}_{μ} Function of system operators

Q Transition rate matrix

Q Phonon wave vector

 Q_{ϵ} Energy shift parameter due to biaxial strain, $-b_{\rm s}(\epsilon_{\parallel} - \epsilon_{\perp})$

q Carrier charge

R Period in a bulk semiconductor crystal

R Facet reflectance

 $R_{\rm d}$ Total device resistance

R_p Responsivity

r Microscopic position vector

 r_{ij} Transition rate from subband j to i

r_p Photon-induced rate

S In-plane cross-sectional area

T Temperature

 T_1 Excited state lifetime

*T*₂ Dephasing time

 $T_{\rm f}$ Facet transmittance

te Simulation endtime

 $u_{n,k}$ Periodic Bloch function of band n

*u*_p Voltage drop per period

 \hat{V}_{ext} Extended conduction band potential

V Potential energy

 \tilde{V} Electrostatic potential energy

 $V_{jk',ik}$ Potential matrix element for elastic scattering processes

 $V^{\pm}_{jk',ik}$ Potential matrix elements for inelastic scattering processes

 $V_{\rm p}$ Volume of a QC device period

 $V_{\rm tb}, \hat{V}_{\rm tb}$ Tight-binding potential

 V_z^i, W_z^i Non-physical quantities for the ADE-FDTD update step

V Update superoperator

v_g Group velocity

 $W_{jk',ik}$ Transition rate from an initial state $|ik\rangle$ to the final state $|jk'\rangle$

*w*₀ Equilibrium inversion

 w^{\pm} Reservoir spectral densities

 \hat{z} Position operator in growth direction

z Coordinate in growth direction

ABC Absorbing boundary conditions

ADE Auxiliary differential equation

Al Aluminum

AM Amplitude-modulated

API Application programming interface

As Arsenic

ASE Amplified spontaneous emission

BO Bayesian optimization

BTC Bound-to-continuum

CBO Conduction band offset

CN Crank-Nicolson

Cu Copper

CW Continuous wave

DAU Dual-upper state

DFB Distributed feedback

DFG Difference-frequency generation

DM Density matrix

DM-EMC Density matrix Ensemble Monte Carlo

DP Depopulation level

EC External cavity

EI Expected improvement

EL Electroluminescence

EMC Ensemble Monte Carlo

ESMB Effective semiconductor Maxwell–Bloch

eV Electronvolt

FACE Fourier-transform analysis of comb emission

fcc Face-centered cubic

FDTD Finite-difference time-domain

FFT Fast Fourier transform

FM Frequency-modulated

FP Fabry-Perot

FSR Free spectral range

FWM Four-wave-mixing

Ga Gallium

GP Gaussian Process

GVD Group velocity dispersion

HDF Hierarchical Data Format

HFC Harmonic frequency comb

HH Heavy-hole

HR High-reflection

IAPT Information algorithm with parallel trials

ICL Interband cascade laser

IF Interface roughness

In Indium

INJ Injection level

IR Infrared

LEF Linewidth enhanced factor

LH Light-hole

LLL Lower laser level

LO Longitudinal optical

MB Maxwell-Bloch

MBE Molecular beam epitaxy

ME Matrix exponentials

MOCVD Metalorganic chemical vapor deposition

NEGF Nonequilibrium Green's function

NEP Noise equivalent power

OFC Optical frequency comb

PC Phosphorus

PC Predictor corrector

PEC Perfectly electric conductor

PMC Perfectly magnetic conductor

PML Perfectly matched layer

PRL Partially reflecting layer

PSTD Pseudo-spectral time-domain

QC Quantum cascade

QCD Quantum cascade detector

QCL Quantum cascade laser

QCRF Quadratic complex rational function

QD Quantum dot

QDash Quantum dash

QS Quantum system

QW Quantum well

QWIP Quantum well infrared photodetector

RF Radio frequency

RIN Relative intensity noise

RK Runge-Kutta

rt Roundtrip

RWA Rotating wave approximation

SCL Semiconductor laser

SDE Stochastic differential equation

SF Superfluorescence

SHB Spatial hole burning

SI Semi-insulating

SIT Self-induced transparency

SO Split-off

SP Schrödinger-Poisson

SPR Single-phonon resonance depopulation

STL Standard template library in C++

SWIFTS Shifted-wave interference Fourier-transform spectroscopy

TDS Time domain spectroscopy

THz Terahertz

TMM Transfer matrix method

ULL Upper laser level

UPML Uniaxial perfectly matched layer

VCA Virtual crystal approximation

Acknowledgments

I would like to express my deepest gratitude to my research supervisor, Prof. Christian Jirauschek, for giving me the opportunity to work under his guidance. His meticulous and subtle approach to complex physical problems on the one hand, and the pragmatism he has probably acquired over the years for administrative tasks on the other, impressed me very much. I learned a lot from him, even if I probably won't be able to put everything into practice to the same extent. Furthermore, he always took the time to discuss issues and helped to work out a solution. This attitude is surely not the standard in a university environment.

Special thanks go to the Akademische Rat in our group, Dr. Michael Haider, who was a great support to me with his knowledge and commitment, especially at the beginning of my doctorate. Some project reports and submissions could certainly not have been completed to this extent and with this quality. Through him, I learned to keep calm under time pressure and to break down a difficult problem and tackle it piece by piece - an invaluable skill that I hope to keep for the rest of my life. I would also like to thank my colleague Lukas Seitner with whom I was allowed to share a room, first in the city center and then in Garching. By working on similar topics, we were able to support each other and create new ideas. The spirit that developed over time helped to motivate each other and resulted in several publications.

In this context, I would also like to thank the entire team at the Professorship of Computational Photonics. Thanks to my office mates Jesus Humberto Abundis Patino, Tim Albes, Michael Riesch and Mark Schmidt, who were always available for discussions, both about science and life in general. My thanks also goes to all other former and current colleagues for providing a stimulating and supportive work environment, including Özüm Asirim, Michael Schreiber, Takuma Sato, Johannes Stowasser and Yongjie Yuan, as well as the colleagues Waldemar Kaiser, Martina Kiechle, Simon Mendisch and Michael Rinderle from other groups. I would also like to thank Bianca Ertl, Susanne Maier and Rosi Mittermeier for their help with countless administrative matters. My special thanks go to my mentor Prof. Alessio Gagliardi, who put me in touch with my current supervisor during my Master's thesis and always supported me during my doctorate.

It was a great chance for me to collaborate on the Qombs Project funded by the EU-H2020-FET Flagship on Quantum Technologies (Grant No. 820419). The project began on October 1, 2018, and was extended until July 31, 2022, due to COVID-19. The pandemic has also affected the scientific work at the university, where lectures, conferences and project meetings were transformed into contactless online formats. Within this project, I worked in close collaboration with Dr. Martin Franckié and Prof. Jérôme Faist from the Quantum Optoelectronics group at ETH Zurich on the simulation and optimization of intersubband quantum cascade devices. Together with Dr. Luigi Consolino and his group from CNR-INO and LENS in Sesto Fiorentino, Italy, and with Dr. Kazuue Fujita from the Central Research Laboratory, Hamamatsu Photonics K.K., Japan, we have focused on the modeling of THz DFG OFC combs in mid-IR QCLs. In the field of quantum fluctuation theory, we have established a fruitful cooperation with Dr. Gabriela Slavcheva and Felix Hitzelhammer from the Institute of Physics at the University of Graz.

During my time at the university, I also had the opportunity to take part in some lecture courses and supervise several students. It was an informative and insightful experience and I enjoyed it a lot to work with motivated Bachelor and Master students. Here, I would like to thank my students Andreas Britz, Markus Fitz, Yassine Hamilla, Georg Janowski, Jeremy Kua, Matthias Lederle, Aden Lee, Stephan Matthies, Felix Naunheimer, Filip Osana, Khalil Ouni, Michael Schreiber and Bogdan Stamenic for their cooperation and help in developing the simulation tools *monacoQC* and *mbsolve*. I hope that they enjoyed the time at our group and were able to learn a few things.

In addition, I just want to thank my parents, Hans and Anna and my sister Katharina. Thank you for all the love and support I have received from you during the last few years and throughout my whole life. Last but not least, I would like to thank my beloved wife Franziska Popp for her unwavering support over the years and for always bringing me back to real life when I was lost in thought.